TECHNICAL NOTE

D-1669

GODDARD SPACE FLIGHT CENTER
CONTRIBUTIONS TO THE COSPAR MEETING
MAY 1962

Goddard Space Flight Center
Greenbelt, Maryland

NATIONAL AERONAUTICS AND SPACE ADMINISTRATION

WASHINGTON   May 1963

GODDARD SPACE FLIGHT CENTER
CONTRIBUTIONS TO THE COSPAR MEETING
MAY 1962

FOREWORD

The Committee on Space Research (COSPAR) held its third International Space Science Symposium in May 1962 in Washington, D. C. This volume presents a collection of 14 papers co-authored or presented at the meeting by personnel of NASA's Goddard Space Flight Center, Greenbelt, Maryland.

There has been no attempt to arrange the papers in any particular sequence, nor to cross-reference those which are closely related. Their publication within a single NASA Technical Note, rather than as separate ones, was prompted by recognition of the growing need for more inter-disciplinary communication. It is to be hoped, therefore, that readers of any of these papers will find material of interest in all of them.

<div align="right">

Technical Information Division
Goddard Space Flight Center
Greenbelt, Maryland

</div>

Page Intentionally Left Blank

TABLE OF CONTENTS

Page Intentionally Left Blank

STRUCTURE OF THE UPPER ATMOSPHERE DEDUCED FROM CHARGED PARTICLE MEASUREMENTS ON ROCKETS AND THE EXPLORER VIII SATELLITE

by

R. E. Bourdeau and S. J. Bauer

Goddard Space Flight Center

SUMMARY

The ion composition measured directly at altitudes above the F2 peak by the Explorer VIII satellite (1960 ξ1) is compared with the ion composition inferred indirectly from recent rocket measurements of charged particle densities. These data show that there are two transition regions (from O^+ to He^+ and from He^+ to H^+) in the upper ionosphere rather than a single transition from O^+ to H^+ as was previously believed. The results place the altitude at which $O^+/He^+ = 1$ between 800 and 1400 km depending on the atmospheric temperature. The measured temperature in the upper ionosphere was found to be constant with altitude within a few percent and consistent with a previously developed empirical relation which predicts the temperature as a function of diurnal time and of solar activity. The determined altitudes of the ion transition levels are in good agreement with a theoretical model which predicts these altitudes as a function of atmospheric temperature.

Langmuir probe measurements of electron temperature made on the Explorer VIII satellite, together with those obtained on recent rocket flights, are compared herein with reference atmospheres. This comparison favors the concept of temperature equilibrium in all but the lower F region of the quiet daytime ionosphere. A revision of theoretical considerations, based on present knowledge of ionizing radiation and energy transfer mechanisms, is offered to explain the observed detailed altitude dependence of the difference between electron and neutral gas temperatures. From a comparison of Explorer VIII data and several rocket measurements of charged particle densities, a diurnal temperature variation of about 80 percent is indicated in the isothermal altitude region of the upper atmosphere.

INTRODUCTION

The structure of the upper atmosphere is defined in terms of its density, temperature, and chemical composition. This paper presents results of studies on the structure of the *ionized* atmosphere. The value of the charged particle data is enhanced when, as is done here, the data are compared with recent reference atmospheres and solar radiation observations.

To establish a basis for discussion of the most recent results, it will be helpful to summarize our knowledge of upper atmosphere ionic composition as it existed a year ago. The ions formed in the greatest numbers in the lower ionosphere are N_2^+, O_2^+, and O^+. The N_2 ions disappear very rapidly at low pressures by dissociative recombination (Reference 1), so that their concentration is small. Chemical reactions of O^+ with molecular nitrogen produce NO^+, and the principal ions which exist below the F2 peak are O^+, NO^+, and O_2^+. Early flights of a Bennett RF mass spectrometer in the auroral zone showed that the ions below 200 km are principally diatomic, O_2^+ predominating at the lower altitudes (Reference 2). More recently, flights of the same experiment at middle latitudes have shown that, of the two molecular ions, NO^+ was predominant below 200 km (Reference 3). In both sets of data, the ionic composition measured above 200 km was essentially atomic in nature — mainly O^+. Results from RF spectrometer (Reference 4) and ion trap (Reference 5) experiments flown on Sputnik III (1958 δ2) showed that O^+ remains predominant up to at least 800 km. In the early reporting of data (References 6 and 7) from a retarding-potential experiment flown on the NASA Explorer VIII satellite (1960 ξ1), it was demonstrated that O^+ predominates at 1000 km in the daytime ionosphere.

In the absence of experimental results, it has been generally believed that at an altitude of approximately 1300 km the ionic composition would change directly from atomic oxygen to protons. One of the important results of the NASA ionospheric physics program has been the conclusion, drawn from several experimental observations, *that an additional transition region must be considered and that a "helium layer" is interposed between the regions where O^+ and H^+ predominate.* Nicolet (Reference 8) had previously deduced from observations of drag on the NASA Echo I satellite (1960 ι1) that neutral helium is an important constituent at very high altitudes. His estimates of the neutral helium number density have subsequently been verified by ground-based optical experiments conducted in the USSR (Reference 9).

Even though the discovery of the ionized helium layer is recent, it is already possible to deduce a preliminary relationship between the atmospheric temperature and the altitudes of the O^+ to He^+ and He^+ to H^+ transition regions. Throughout this paper, we define the transition altitudes as those altitudes where the ratios O^+/He^+ and He^+/H^+ equal unity. Four separate measurements of the lower transition altitude and one of the upper transition altitude are available.

IONIC COMPOSITION

We shall consider first the data from the Explorer VIII retarding-potential experiment, which is illustrated schematically in Figure 1. This experiment is based on the proposition that, because of the high satellite velocity, the kinetic energy (relative to the vehicle) of an ion is proportional to its mass. A measurement of this kinetic energy can be derived from the behavior of the collected ion current as a function of an applied retarding potential. Specifically, the potential of the collector, relative to the plasma, at which one half of the ions of mass M_+ are retarded is given by

$$\phi_R = \frac{M_+ (V \cos \theta)^2}{2e} ,$$

(1)
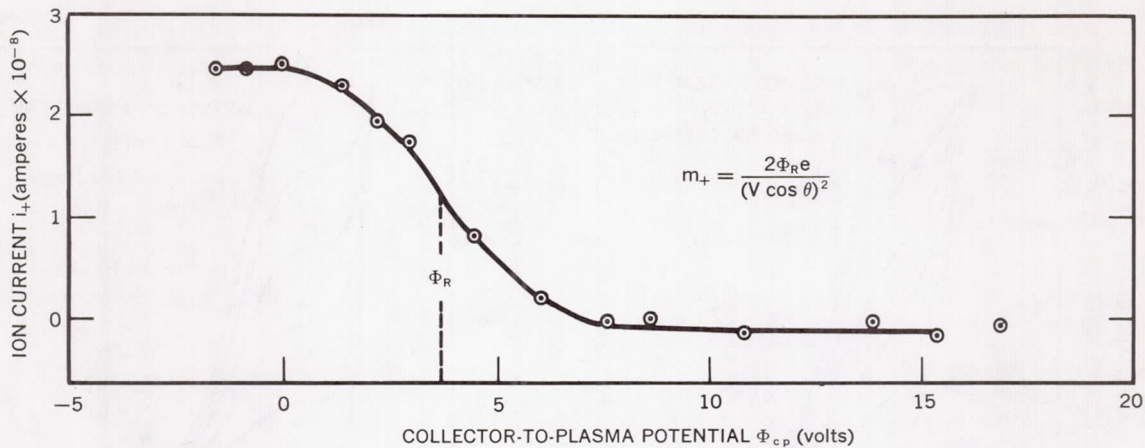
Figure 1—Results of the Explorer VIII retarding-potential experiment at an altitude of 1000 km under daytime conditions. The instrument is shown schematically at the left

$$m_+ = \frac{2\Phi_R e}{(V \cos \theta)^2}$$

where V is the satellite velocity, θ is the angle of the sensor relative to the velocity vector, and e is the electronic charge. To give accurate ratios of the ionic constituents, the sensor must be pointed in the direction of motion — a condition which, because of the short active life of the satellite, did not prevail except in the altitude region between 700 and 1600 km, and then under daytime conditions only. Experimental points for an altitude of 1000 km are shown in Figure 1. The monotonically decreasing nature of the curve is characteristic of a single ionic constituent which, by substituting into Equation 1 the known satellite velocity and orientation and the value of ϕ_R from Figure 1, is identified as O^+. The abscissa in Figure 1 is the collector-to-plasma potential ϕ_{cp} which is the algebraic sum of the applied collector potential ϕ_c and the satellite-to-plasma potential ϕ_{sp} measured separately by a Langmuir probe.

Theoretical retarding-potential curves computed from an expression given by Whipple (Reference 10) for binary mixtures of helium and oxygen and of hydrogen and oxygen are presented in Figures 2 and 3, respectively. It is seen that an oxygen-helium mixture is characteristically identified by an inflection point, and an oxygen-hydrogen mixture by distinguishable plateaus. The shapes of these curves are relatively insensitive to the ion temperature T_+. Since the Explorer VIII data at altitudes of about 1600 km are characterized by inflection points, it was concluded that the predominant ions at this altitude are O^+ and He^+ (Reference 11). By fitting the experimental points to the family of oxygen-helium curves shown in Figure 3, it was found that the lower transition altitude (O^+ to He^+) was about 1400 km for an atmospheric temperature of approximately 1750°K.

3
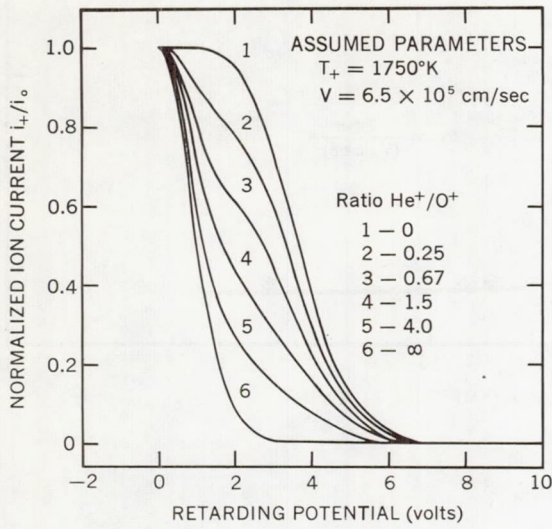
Figure 2—Theoretical retarding-potential curves for a binary mixture of helium and oxygen ions
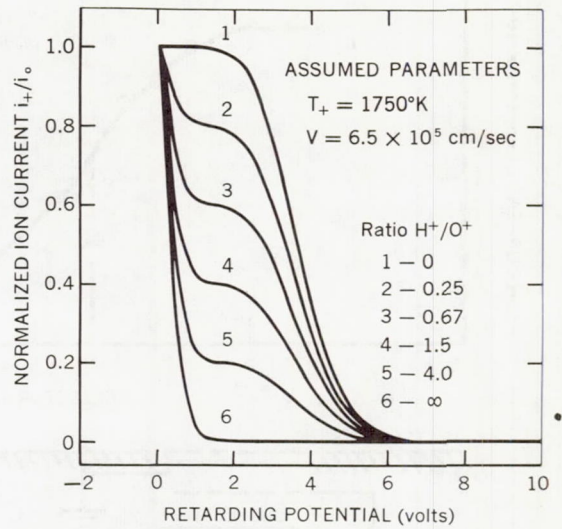
Figure 3—Theoretical retarding-potential curves for a binary mixture of hydrogen and oxygen ions

$$H' = \frac{k(T_e + T_i)}{m_+ g}$$
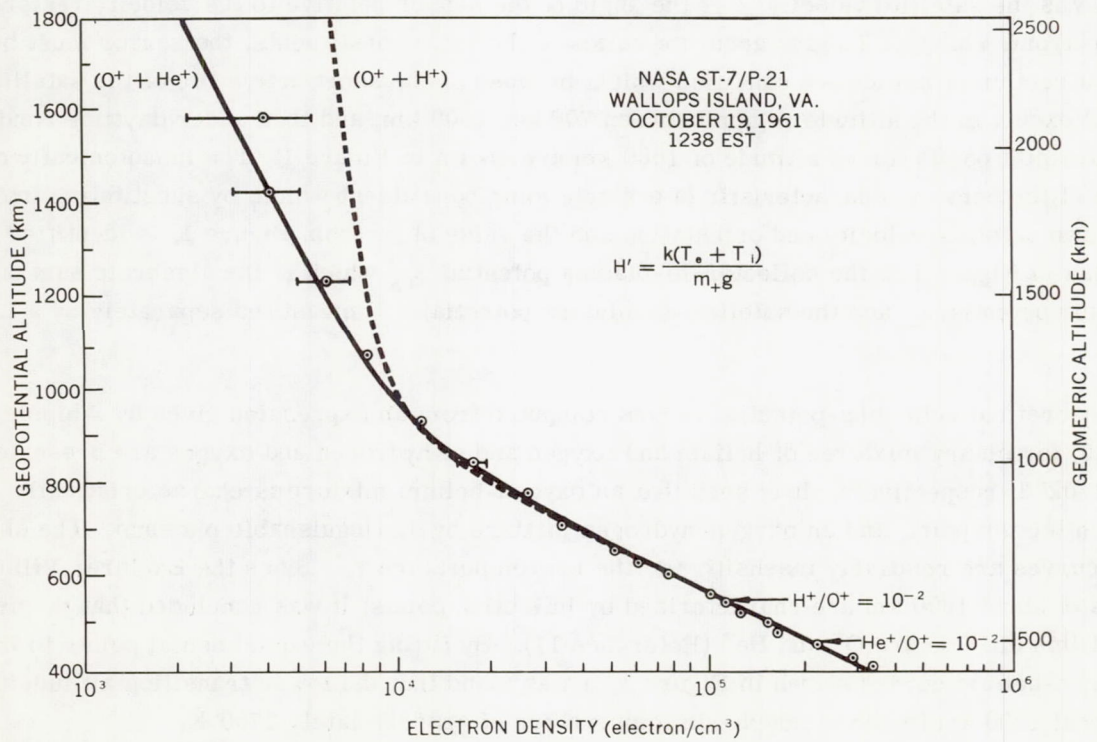
Figure 4—Comparison of the electron density profile obtained by a radio propagation experiment with that of a theoretical model

Hanson (Reference 12), who first reported on upper atmosphere helium ions, has indirectly determined both transition altitudes from the changes in scale height of an ion density profile obtained by Hale (Reference 13) in an ion trap experiment flown on NASA Scout ST-2. The atmospheric temperature derived from the scale height of the electron-ion gas in the region between 1600 and 3400 km, on the assumption of a mean ionic mass of 4 amu, was $1600°$ K. The transition altitudes from O^+ to He^+ and from He^+ to H^+ which Hanson estimated are 1150 and 3500 km, respectively. Figure 4 shows an electron density profile obtained by Bauer and Jackson (Reference 14) from a radio propagation experiment flown on NASA Scout ST-7. The right-hand ordinate scale is the true or geometric altitude, while the left-hand scale is the geopotential height which takes into account the altitude variation of the acceleration of gravity. As illustrated, the experimental data are more consistent with a transition from O^+ to He^+ (solid line) than from O^+ to H^+ (dashed line). In this case, the inferred atmospheric temperature is $1350°K$ and the transition altitude (O^+ to He^+) is 1050 km.

Most recently, Donley (private communication) has made a direct measurement of He^+/O^+ from a retarding-potential experiment flown on NASA Scout ST-9 into a nighttime ionosphere. From a preliminary data analysis, the transition altitude appears to be below 800 km at a time when the atmospheric temperature was approximately $800°$ K.

Figure 5 illustrates the atmospheric temperature dependence of the transition altitudes as determined from Bauer's theoretical model (Reference 15) for the electron density distribution in an isothermal, three-constituent i o n o s p h e r e in diffusive equilibrium. Three curves are shown: two for the upper transition altitude ($H^+ = He^+$) and one for the lower ($He^+ = O^+$). For the latter case, the prediction assumes that the ratio $He^+/O^+ \equiv \eta_{21}$ has the value 10^{-2} at 500 km, in accordance with the experimental results of Bauer and Jackson (Reference 14). Plotted on the graph are the four experimental results referred to earlier, which show reasonably good agreement with the theoretical curve when we consider that the relative concentrations of these ionic constituents may also vary with temperature at the reference altitude.

The upper theoretical curve assumes that the ratio $H^+/O^+ \equiv \eta_{31}$ has the value 2×10^{-4} at 500 km, a value representative of Hanson's current estimates of proton concentration in the upper ionosphere. The other upper transition altitude curve ($\eta_{31} = 10^{-3}$) is included to illustrate the radical reduction in the thickness of the helium layer which would result if the relative proton concentration were increased by a factor of 5 at the reference altitude.
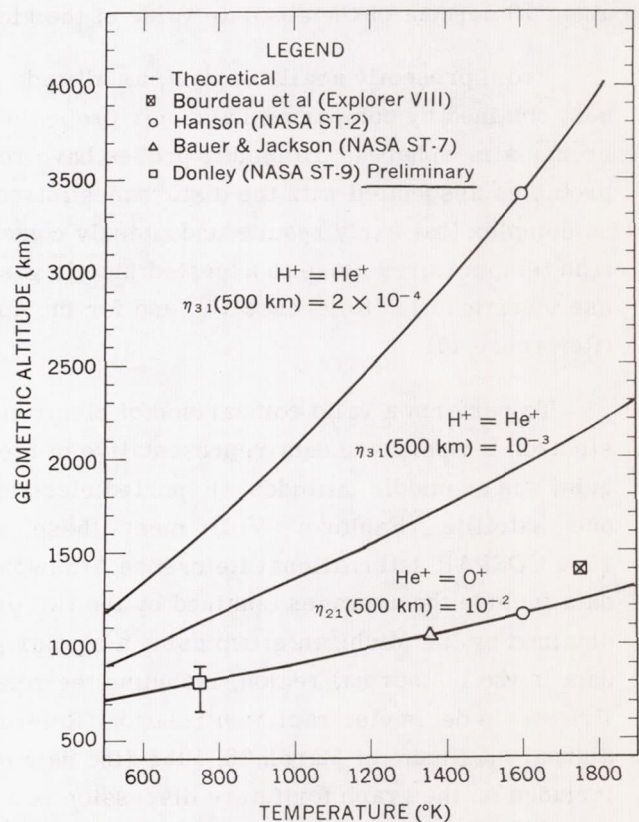

Figure 5—Ion transition altitudes as functions of atmospheric temperature

ALTITUDE COMPARISON OF EXPERIMENTALLY OBTAINED ELECTRON
TEMPERATURES WITH REFERENCE ATMOSPHERES

It is of considerable importance to compare electron and neutral gas temperatures, since their relationship depends upon many parameters essential to the quantitative confirmation of present theories regarding the formation of the various ionospheric regions. Because direct and indirect measurements of charged particle temperatures have been made under radically different conditions, and because of the limitations of the kinetic gas temperature models, various investigators have provided conflicting answers to the important question of temperature equilibrium between electrons and heavy constituents. As this paper will show, a consistent pattern can be found in the temperature ratio of charged particles to neutral gas by carefully separating the reported data in altitude and possibly in latitude, and more importantly by treating conditions of quiet and enhanced solar activity as separate cases.

Before proceeding, it is important to define our use of the term "temperature equilibrium." Actually, because in the ionization process the electrons are liberated with high initial energies, their temperature T_e will be higher than that of the neutral gas T but will approach it asymptotically in time, depending on the efficiency of the energy transfer mechanisms. We shall define temperature equilibrium as existing when the difference between T_e and T is smaller than the estimated uncertainties in reference atmospheres and in experimental methods of measuring charged particle temperatures. We can estimate, perhaps optimistically, that for most cases these uncertainties together are about 10 percent of the absolute value of the kinetic gas temperature.

From presently available data, an altitude comparison of electron and kinetic gas temperature is best obtained by comparing Langmuir probe measurements of electron temperatures with recent reference atmospheres. Langmuir probes have required considerable development in order to overcome problems associated with the disturbance introduced into the medium by a conducting body — problems so complex that early results undoubtedly contain first-order errors. It was not until 1961 that electron temperatures close to accepted kinetic gas values were first reported for the E region, by Japanese investigators (Reference 16), and for the upper ionosphere, from the NASA Explorer VIII satellite (Reference 17).

To perform a valid comparison of electron and kinetic gas temperatures, it is necessary to select electron temperature data representative of the characteristic reference atmosphere conditions of a quiet sun at middle latitudes. Reported electron temperature results from only two rocket flights and one satellite (Explorer VIII) meet these requirements. These data are compared with the 1961 COSPAR International Reference Atmosphere (CIRA) in Figure 6. The rocket Langmuir probe data include the averages obtained by the two probes flown simultaneously by the Japanese, and results obtained by the Michigan group using a bipolar probe flown on NASA Rocket 6.04 (Reference 18). All data in the isothermal region, including the reference atmosphere, have been normalized according to Priester's decimeter radiation relation (Reference 19) to the solar activity conditions prevailing at the diurnal maximum of March 26, 1961 (the data of both the Japan and Michigan rocket flights). Also included on the graph for future discussion is a measurement of the kinetic gas temperature inferred on the basis of temperature equilibrium from a measured electron density profile (Reference 20).

In view of the status of Langmuir probe technology and the limitations (imposed by the necessity to assume a neutral composition) of reference atmospheres, the foregoing comparison supports the expectation — based on theoretical considerations of ionizing radiation and energy transfer mechanisms — of temperature equilibrium in all but the lower F region of the quiet daytime ionosphere (Reference **21**). The Japanese data actually show lower electron temperatures than the generally accepted kinetic gas temperatures below 170 km. The Michigan values and the reference atmosphere are virtually identical between 140 and 190 km. The Michigan group reports that their values below 140 km have larger uncertainties than their other data. Taken together, then, the two sets of rocket data indicate equilibrium between 100 and about 190 km.

In the F region between 250 and 360 km, the Michigan electron temperature values are sufficiently higher than those of the neutral gas that the difference cannot be ascribed to inade-

Figure 6—Comparison of the kinetic gas and experimental electron temperatures for a quiet daytime ionosphere at middle latitudes

quacies of the reference atmosphere or to experimental electron temperature errors. Consequently, this is a definite indication that departure from temperature equilibrium has been established for the F region, with the maximum electron temperature values occurring at about the altitude of maximum absorption of solar radiation.

The data obtained at apogee of the Michigan flight, which occurred at 360 km (just above the F2 peak), show a trend toward a return to temperature equilibrium. As the next section of this paper will show, it can be predicted by quantitative revisions to the Hanson-Johnson hypothesis that the electron and neutral gas become virtually identical at altitudes between 400 and 500 km. This is indicated by the dashed extrapolation of the Michigan results in Figure 6. There are several experimental justifications for temperature equilibrium well above the F2 peak. Explorer VIII data yield electron temperature values within 15 percent of those of the neutral gas models. Although this small indicated departure from equilibrium could be real, it is equally likely that it represents inadequacies in the electron temperature measurements. A second justification is the observation from ground-based radar incoherent backscatter experiments (Reference 22) — which directly measure the ratio T_e/T_i of electron and ion temperature — that temperature equilibrium prevails near the F2 peak throughout the day except at sunrise and during disturbed ionospheric conditions. The third justification comes from the general agreement of temperatures computed from measured scale-heights of the electron-ion gas above the F2 peak with accepted values of neutral gas temperature in the isothermal region. These data are discussed
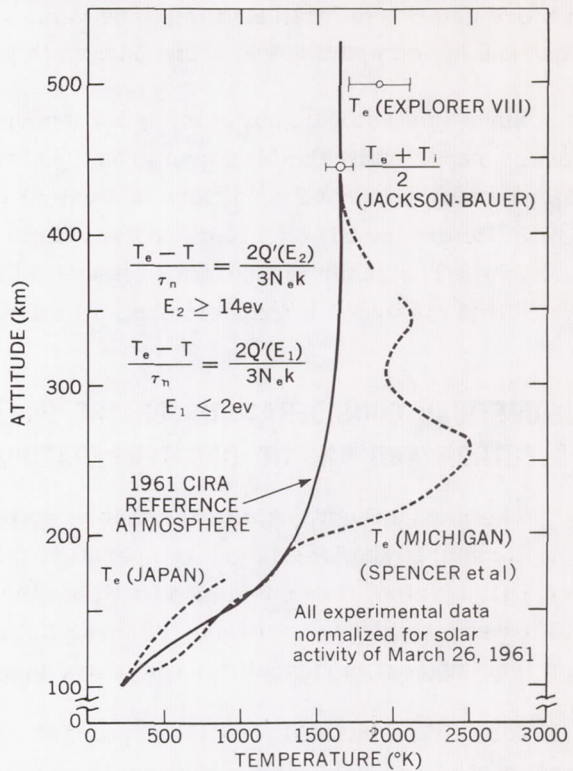
in more detail in a later section. The value given by Jackson and Bauer (Reference 20) is included in Figure 6 for comparison with the Langmuir probe data.

Since this comparison is for quiet ionospheric conditions at middle latitudes, it does not include results reported by the Michigan group (Reference 18) on three other NASA rocket flights, two obtained under disturbed conditions and one in the auroral region. Also excluded are the results of Smith (Reference 23) on a NASA rocket flight made within 24 hours of the onset of a geomagnetic disturbance. The radar incoherent backscatter results (Reference 22) have provided experimental evidence that disturbed ionospheric conditions result in values of T_e/T_i of the order of 2.

THEORETICAL CONSIDERATIONS OF THE DIFFERENCE BETWEEN ELECTRON AND KINETIC GAS TEMPERATURES

The most recent quantitative theoretical study of the ionospheric electron temperature and its relationship to the kinetic gas temperature was made by Hanson and Johnson (Reference 21). As Figure 7 illustrates, they concluded that the electron and neutral gas temperatures are virtually identical except at altitudes between 160 and 325 km. In this section we shall summarize their hypotheses and then suggest modifications which are more consistent with the data presented in Figure 6.

Just after ionization has taken place the newly liberated photoelectrons, which comprise less than 1 percent of the total electron population, have energies exceeding that of the neutral gas by at least 14 ev. The process by which this excess energy is transferred to upper atmosphere constituents is an altitude-dependent phenomenon which may be described as follows:

Below 225 km, inelastic collisions with neutral particles reduce the photoelectron energy to 2 ev, the cutoff point of the excitation cross-section of atomic oxygen. The 2 ev electrons then share their energy with the ambient electrons, thus raising the temperature of the latter above that of the heavy constituents. Because this process is very fast, the electrons have a Maxwellian energy distribution — a conclusion verified experimentally by the shapes of the volt-ampere curves of those Langmuir probes whose potentials are permitted to reach the plasma potential.

After a Maxwellian distribution of electron energy is established, the temperature difference is calculated by relating the heat input to the electrons to the heat lost by elastic collisions with heavy particles:

Figure 7—Theoretical considerations of temperature equilibrium for quiet daytime conditions

$$\frac{2Q'(E_1)}{3N_e k} = \frac{T_e - T}{\tau_n}, \quad z < 225 \text{ km}, \tag{2}$$

where Q' is the rate at which photoelectrons of energy E_1 (2 ev or less for this case) are released, N_e is the electron density, k is Boltzmann's constant, and τ_n is the time needed for electrons of energy E_1 to transfer their excess energy to neutral particles.

Between 225 and 350 km, the process is the same except that the time τ_i needed for 2 ev electrons to transfer their excess energies to ions is shorter than τ_n; thus,

$$\frac{2Q'(E_1)}{2N_e k} = \frac{T_e - T}{\tau_i}, \quad 225 \text{ km} < z < 350 \text{ km}. \tag{3}$$

Above 350 km, the inelastic collision process is no longer efficient, and the photoelectrons transfer their energy directly to the ambient electrons, raising the value of E_1 to E_2, that is, to 14 ev or more depending upon whether two or one photoelectrons are released per incoming photon:

$$\frac{2Q'(E_2)}{3N_e k} = \frac{T_e - T}{\tau_i}, \quad z > 350 \text{ km}. \tag{4}$$

Hanson and Johnson calculated from available atmospheric models that temperature equilibrium as we have defined it would prevail except between 160 and 325 km, a region where high solar radiation absorption is accompanied by moderate values for the respective equipartition times. The principal uncertainties in their computations result from corresponding uncertainties in cross sections and densities of the atmospheric constituents. They noted, in proof of this, that an overestimated excitation cross section of atomic oxygen caused them to overestimate the altitude at which inelastic collisions become ineffective; and we shall note below that this radically affects the altitude domains in which the various energy transfer mechanisms come into play. The rearrangement offers one explanation for the experimental results presented in Figure 6.

The major effect of lowering the altitude above which inelastic collisions are unimportant is that the efficiency of energy transfer by elastic collisions with ions is greatly reduced. If we must consider equipartition times τ_i based on electrons with energies of 14 ev or greater rather than 2 ev at all altitudes, we estimate that energy transfer to ions does not control the electron temperature below about 600 km.

Following this reasoning, we must now consider two altitude domains below 600 km: an upper portion where energetic electrons of 14 ev or greater transfer their energy directly to the ambient electrons; and a lower portion where, because of the intervening inelastic collision process, there are only 2 ev of energy available for selective electron heating. In both domains the temperature difference $(T_e - T)$ is finally controlled by elastic collisions with neutral constituents.

In order to provide new estimates of $(T_e - T)$ at all altitudes, $Q'(E)$ was calculated with $(T_e - T)$ values from Figure 6 in the altitude region where the difference is measurable (200-360 km);

equilibration times τ_n in accordance with Hanson and Johnson; and electron densities measured during the Michigan flight by an ionosonde and by a rocket-borne propagation experiment. In these calculations, a discontinuity appears in the $Q'(E)$ function at 325 km. This discontinuity may be attributed to the transition altitude where inelastic collisions are no longer efficient: Above that altitude more energy (E_2) is available for selective electron heating; and the secondary maximum in the Michigan electron temperature profile (Figure 6) in the 300-350 km region may possibly be explained in this fashion. The new equations which seem to apply below and above 325 km are included as part of Figure 6.

By an extrapolation of the $Q'(E)$ function, and of the τ_n values given by Hanson and Johnson (now *reduced* above 325 km), and of the electron density profile, we conclude for the ionospheric conditions represented by Figure 6 that the electron and kinetic gas temperatures are virtually identical below about 190 and above about 450 km. Below 190 km, the justification is the reduction of photoelectron energy by inelastic collisions together with high collision frequencies. In the higher altitude region, it appears that the heat input to the electrons is decreasing more rapidly with altitude than is the combined effect of an increasing equipartition time and a decreasing electron density. This does require a somewhat more rapid decrease in $Q'(E)$ at the higher altitudes than would be inferred from a recent study by Watanabe and Hinteregger (Reference 24); but, as they point out, their analysis is a first approximation which can be refined as the atmospheric composition and some photoionization and absorption cross sections become better known.

DIURNAL AND SOLAR ACTIVITY VARIATION OF UPPER IONOSPHERE TEMPERATURES

Neutral gas temperatures above 200 km are generally derived from an assumed atmospheric composition together with atmospheric densities computed from satellite drag observations. The drag observations show that density variations are correlated with solar activity. Although not the source of upper atmosphere heating, solar decimeter radiation — which is observable at the earth's surface — is an indicator of this interrelationship. Different empirical equations relating the 10.7 and 20 cm solar radiation to atmospheric temperature in the isothermal altitude region have been derived by Jacchia (Reference 25) and Priester (Reference 19). Jacchia's equations are based on an atmospheric model by Nicolet (Reference 26) which includes the presence of helium and in which the mean molecular weight is computed on the basis of diffusive equilibrium of the atmospheric constituents. Priester's model, on the other hand, makes use of a molecular mass variation typical of the 1961 CIRA reference atmosphere.

Theories of upper atmospheric heating can be improved by comparing such models of the diurnal and solar activity variations of neutral gas temperatures with charged particle temperatures obtained from measurements in the isothermal altitude region. To do so, it is necessary to assume temperature equilibrium well above the F2 peak; this assumption was justified theoretically and experimentally in the previous sections.

One method of deducing charged particle temperatures above the F2 peak is to measure accurately the electron or ion density profile. From theoretical considerations as well as experimental evidence, it is now well established that the distribution of electrons and ions at these altitudes

10

generally corresponds to a diffusive equilibrium distribution. One such experimental evidence, a daytime electron profile measured by a radio propagation method (Reference 20), is illustrated in Figure 8. In such cases the slope of the charged particle distribution is a unique measure of the scale height of the electron-ion gas; and for regions where one ionic constituent predominates it is also a measure of the sum of the electron (T_e) and ion (T_i) temperatures. In general, the scale-height of the electron-ion gas is given by

$$H' = \frac{k\left(T_e + T_i\right)}{m_+ g} = \left[\frac{d}{dz}\left(\ln N\right)\right]^{-1}, \tag{5}$$

where m_+ is the mean ionic mass, g is the acceleration of gravity, N is the charged particle density, and z the altitude. Thus, H' is a measure of $\left(T_e + T_i\right)$ or, in the case of temperature equilibrium, of the neutral gas temperature $T = \left(T_e + T_i\right)\big/2$.

Parenthetically, the high degree of isothermality in $\left(T_e + T_i\right)$ evidenced by the experimental results in Figure 8 provides additional support for the assumption of temperature equilibrium well above the F2 peak. For this isothermality to occur with radical differences between T_e and T_i requires the rather unlikely condition that the energy input to the electrons $Q'(E)$ decreases with altitude identically as the combined rate of increase in equipartition time and of decrease in electron density.
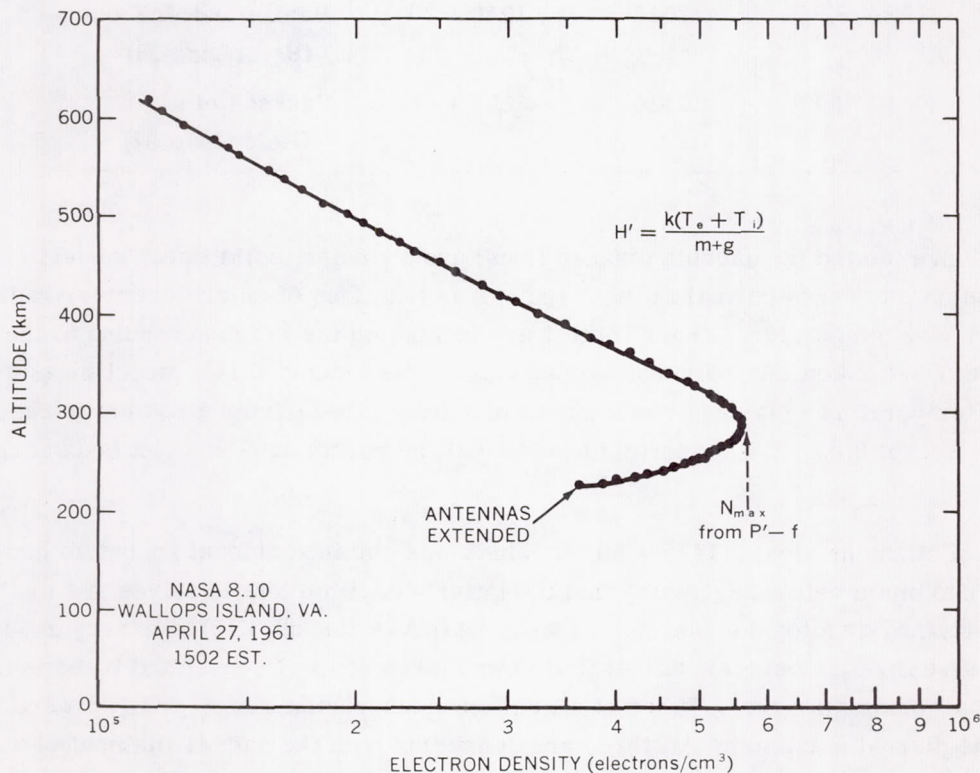

Figure 8—Electron density profile from a radio-propagation experiment, illustrating the isothermality of the upper ionosphere

Six rocket measurements of the altitude profile of charged particle densities above the F2 peak have been reported during the last year. In addition to those presented in Figures 3 and 7, two electron density profiles were obtained from the NASA topside sounder program (Reference 27), and the remaining two are ion density profiles. The six sets of data are listed in Table 1 along with the kinetic gas temperature inferred from an assumption of temperature equilibrium.

Table 1

Rocket Measurements of Atmospheric Temperature above the F2 Peak

Rocket Flight	Local Time (hours)	Temperature (°K)	Source of Data
NASA ST-7	1238	1350 ± 100	Bauer and Jackson (Reference 14)
NASA ST-2	1500	1600 ± 100	Hanson (Reference 12)
NASA 8.10	1502	1640 ± 90	Jackson and Bauer (Reference 20)
NASA 8.15	1812	1200 ± 60	Jackson et al. (Reference 27)
NASA 8.04	2044	1240 ± 70	Hanson and McKibbin (Reference 28)
NASA 8.17	2326	800 ± 40	Jackson et al. (Reference 27)

In Figure 9 are plotted the Jacchia (dashed lines) and Priester (solid lines) models of the atmospheric temperature in the isothermal altitude regions as functions of solar decimeter radiation flux. For comparison, the temperatures from Table 1 are located on the graph according to the solar decimeter radiation observed on the individual launch dates. Also included is a direct measurement of the neutral gas temperature obtained by Blamont et al. (Reference 29) from a sodium release experiment flown on NASA Rocket 8.05. It is important to note that the rocket data have not been normalized for diurnal time.

The value of Blamont et al., $1475 \pm 40°K$, which was obtained at local sunset, is higher than Jacchia's diurnal maximum value, suggesting that the latter's daytime temperatures are too low. One value of $(T_e + T_i)/2$ obtained by a topside sounder experiment (NASA Rocket 8.15) is in very good agreement with the value given by Blamont et al. in that it also was taken at local sunset and it too is higher than Jacchia's diurnal maximum curve. Three of the rocket measurements of $(T_e + T_i)/2$ were taken within two hours of the diurnal maximum. All three are consistent with the data of Blamont et al. in that they are higher than the temperatures in Jacchia's model but lower than or equal to Priester's values for the diurnal maximum. The remaining measurements of $(T_e + T_i)/2$ are for nighttime conditions. One

taken close to midnight (NASA Rocket 8.17) agrees quite well with both Jacchia's and Priester's values for diurnal minimum. This should be expected since little cooling will occur between midnight and the diurnal minimum. The other nighttime value (NASA Rocket 8.04) was taken about two hours after sunset when the atmosphere was cooling toward diurnal minimum. As expected, this value falls between the diurnal maximum and minimum values.

Considering that both Jacchia's and Priester's kinetic gas temperatures are inferred rather than measured, the general agreement of the various charged particle measurements with their temperature models is reasonably good. It appears from the daytime values of temperatures deduced from charged particle observations, as well as from the direct measurement of neutral gas temperature given by Blamont et al., that the diurnal variation of temperature in the isothermal region is closer to the 80 percent suggested by Priester than to the 35 percent suggested by Jacchia.

Figure 9—Upper ionosphere temperature as a function of solar activity

Inasmuch as the rocket temperature measurements are in somewhat closer agreement with Priester's model than with Jacchia's, they are plotted in Figure 10 as a function of local mean time to illustrate further the agreement with his implied diurnal variation (Reference 30). Electron temperatures reported from the Explorer VIII satellite are also included. All of these data have been normalized to the average 10.7-cm flux for the month of November 1960. It should be emphasized that the individual electron temperature values from Explorer VIII have a 200° K error spread which is not indicated on the graph. Assuming temperature equilibrium, it would appear from the Explorer VIII data that Priester's daytime values are too low. However, there is a possibility of second-order errors in these Langmuir probe measurements of electron temperature (Reference 31). There is fair agreement between indirect measurements of charged particle temperatures and Priester's values, with a possible implication that the diurnal maximum is broader than indicated.

13

Figure 10—Diurnal variation of upper ionosphere temperatures

VARIABILITY EXTREMES OF ELECTRON DENSITIES IN THE UPPER IONOSPHERE

It has been brought out indirectly in the preceding section that electron densities in the upper ionosphere are controlled by the atmospheric temperature and ion composition. They are, of course, additionally controlled by N_{max} values at the F2 peak, which are in turn governed by absorption of solar radiation and by recombination processes in the lower F region. In this section, to illustrate the variability extremes which these factors produce in upper ionosphere electron densities, we shall compare ionosonde data with electron density measurements by J. A. Kane (private communication) using an RF probe experiment flown on Explorer VIII.

With ionosonde data for N_{max} values and with the then prevailing diurnal variation of atmospheric density, Figure 11 shows the extreme theoretical electron density profiles which — assuming diffusive equilibrium and temperature equilibrium — would be expected during Explorer VIII's active lifetime. The shaded areas indicate the variability of electron densities observed by the RF impedance probe. Each segment plotted at the nearest 100 km level represents about 50 data points.

In the RF probe experiment, which was originally developed by Jackson and Kane (Reference 32), the inflight capacitance C of a shortened dipole antenna is compared to the latter's free space capacitance C_0 at a radio frequency f. The electron density is computed from the simplified Appleton-Hartree formula which relates N_e to the dielectric constant K of the medium as follows:

$$K = \frac{C}{C_0} = 1 - \frac{81N_e}{f^2} , \qquad (6)$$

where f is in kilocycles:

14
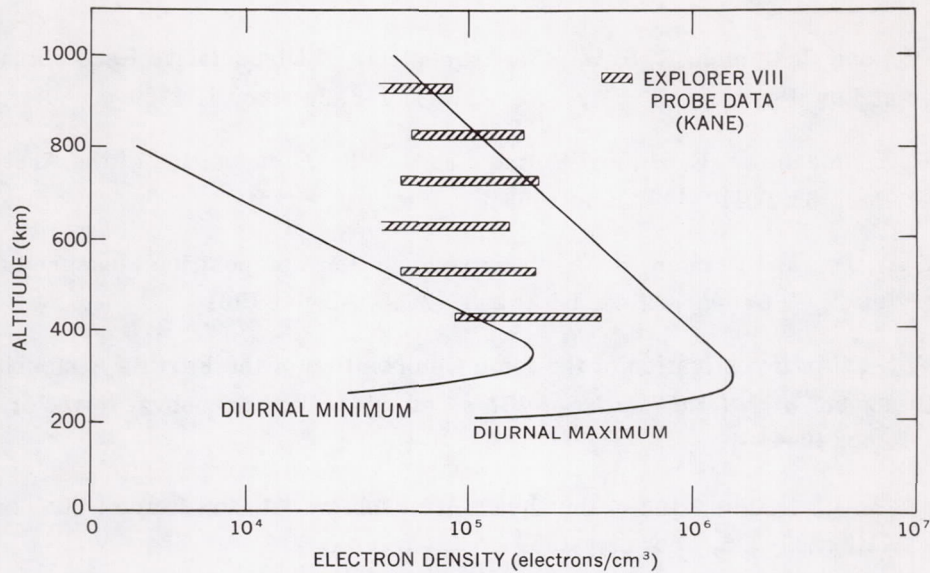
Figure 11—Comparison of electron densities from the Explorer VIII RF impedance probe
with theoretical models

The principal uncertainty in this measurement is due to the ion sheath which forms about the antenna; the error can be estimated from a knowledge of the potential that the spacecraft acquires relative to the medium (Reference 33). In the case of Explorer VIII, where satellite potentials varied between approximately zero for daytime conditions and −1 volt at night, Kane estimates that the uncertainties due to the ion sheath correspond to electron densities of the order of 2×10^4 electrons/cm^3. For this reason, values below 4×10^4 electrons/cm^3 were not considered in the data recorded in Figure 11.

It was observed that whenever the satellite, *at perigee* (425 km), was within one degree of latitude and longitude of an ionosonde, the electron density observed on the satellite was consistent with what would be expected from the N_{max} value. On some perigee transits occurring near local midnight it was noted that fluctuations in the electron density were less than 10 percent over a distance of the order of 500 km along the direction of the satellite orbit.

As would be expected, the experimental values at the lower altitudes, which correspond to a nighttime condition, are in close agreement with the theoretical diurnal minimum curve. The values which exceed those of the model above 700 km are attributed to the fact that in this region the satellite was passing either into a sunrise or sunset condition; in the former case diffusive and probably temperature equilibrium may not apply.

ACKNOWLEDGMENTS

REFERENCES

1. Faire, A. C., and Champion, K. S. W., "Measurements of Dissociative Recombination and Diffusion in Nitrogen at Low Pressures," *Phys. Rev.* 113(1):1-6, January 1, 1959

2. Johnson, C. Y., Meadows, E. B., and Holmes, J. C., "Ion Composition of the Arctic Ionosphere," *J. Geophys. Res.* 63(2):443-444, June 1958

3. Taylor, H. A., Jr., and Brinton, H. C., "Atmospheric Ion Composition Measured above Wallops Island, Virginia," *J. Geophys. Res.* 66(8):2587-2588, August 1961

4. Istomin, V. G., "An Investigation of the Ionic Composition of the Earth's Atmosphere Using Rockets and Satellites," in: *Artificial Earth Satellites,* ed. by L. V. Kurnosova, New York: Plenum Press, 1960, Vol. 2, pp. 40-44

5. Krassovsky, V. I., "Exploration of the Upper Atmosphere with the Help of the Third Soviet Sputnik," *Proc. IRE,* 41(2):289-296, February 1959

6. Bourdeau, R. E., "Ionospheric Results with Sounding Rockets and the Explorer VIII Satellite," in: *Space Research II: Proc. 2nd Internat. Space Sci. Sympos., Florence, April 1961,* ed. by H. C. van de Hulst, C. de Jager, and A. F. Moore, Amsterdam: North-Holland Publ. Co., 1961, pp. 554-573

7. Bourdeau, R. E., Donley, J. L., and Whipple, E. C., Jr., "Instrumentation of the Ionosphere Direct Measurements Satellite (Explorer VIII)" NASA Technical Note D-414, April 1962

8. Nicolet, M., "Helium, an Important Constituent in the Lower Exosphere," *J. Geophys. Res.* 66(7):2263-2264, July 1961

9. Shefov, N. N., "Émission de l'Hélium dans la haute Atmosphère," *Annales de Géophysique* 17(4): 395-402, 1961

10. Whipple, E. C., Jr., "The Ion-Trap Results in'Exploration of the Upper Atmosphere with the Help of the Third Soviet Sputnik'," *Proc. IRE,* 47(11):2023-2024, November 1959

11. Bourdeau, R. E., Whipple, E. C., Jr., et al., "Experimental Evidence for the Presence of Helium Ions Based on Explorer VIII Satellite Data," *J. Geophys. Res.* 67(2):467-475, February 1962

12. Hanson, W. B., "Upper-Atmosphere Helium Ions," *J. Geophys. Res.* 67(1):183-188, January 1962

13. Hale, L. C., "Ionospheric Measurements with a Multigrid Potential Analyzer," *J. Geophys. Res.* 66(5):1554, May 1961 (Abstract)

14. Bauer, S. J., and Jackson, J. E., "Rocket Measurement of the Electron-Density Distribution in the Topside Ionosphere," *J. Geophys. Res.* 67(4):1675-1677, April 1962

15. Bauer, S. J., "On the Structure of the Topside Ionosphere," *J. Atmos. Sci.* 19(3):276-278, May 1962

16

16. Aono, Y., Hirao, K., and Miyazaki, S., "Positive Ion Density, Electron Density and Electron Temperature in the Ionosphere by the Kappa-8-5 and -6 Rockets," *J. Radio Res. Labs.* (Japan) 8(40): 453-465, November 1961

17. Serbu, G. P., Bourdeau, R. E., and Donley, J. L., "Electron Temperature Measurements on the Explorer VIII Satellite," *J. Geophys. Res.* 66(12):4313-4315, December 1961

18. Spencer, N. W., Brace, L. H., and Carignan, G. R., "Electron Temperature Evidence for Nonthermal Equilibrium in the Ionosphere, *J. Geophys. Res.* 67(1):157-175, January 1962

19. Priester, W., "Solar Activity Effect and Diurnal Variation in the Upper Atmosphere," *J. Geophys. Res.* 66(12):4143-4148, December 1961

20. Jackson, J. E., and Bauer, S. J., "Rocket Measurement of a Daytime Electron-Density Profile up to 620 Kilometers," *J. Geophys. Res.*, 66(9):3055-3057, September 1961

21. Hanson, W. B., and Johnson, F. S., "Electron Temperatures in the Ionosphere," *Mémoires de la Société Royale des Sciences de Liège* 4:390-424, 1961

22. Bowles, K. L., Ochs, G. R., and Green, J. L., "On the Absolute Intensity of Incoherent Scatter Echoes from the Ionosphere," *J. Res. NBS* 66D(4):395-407, July-August 1962

23. Smith, L. G., "Electron Density Measurements by the Asymmetrical Bipolar Probe," *J. Geophys. Res.* 66(8):2562, August 1961 (Abstract)

24. Watanabe, K., and Hinteregger, H. E., "Photoionization Rates in the E and F Regions," *J. Geophys. Res.* 67(3):999-1006, March 1962

25. Jacchia, L. G., "A Working Model for the Upper Atmosphere," *Nature*, 192(4808):1147-1148, December 23, 1961

26. Nicolet, M., "Density of the Heterosphere Related to Temperature," Smithsonian Institution, Astrophys. Observ., Res. in Space Sci., Spec. Rept. No. 75, September 19, 1961

27. Jackson, J. E., Knecht, R. W., and Russell, S., "First Results in NASA Topside Sounder Satellite Program," Paper presented at 8th Annual Meeting of the American Astronautical Society, Washington, January 1962 (To be published)

28. Hanson, W. B., and McKibbin, D. D., "An Ion-Trap Measurement of the Ion Concentration Profile above the F2 Peak," *J. Geophys. Res.* 66(6):1667-1671, June 1961

29. Blamont, J. E., Lory, M. L., and Schneuler, J. P., "Mesure de la Température de la haute Atmosphère à l'Altitude de 370 km," in: *Space Research II: Proc. 2nd Internat. Space Sci. Sympos., Florence, April 1961,* ed. by H. C. van de Hulst, C. de Jager, and A. F. Moore, Amsterdam: North-Holland Publ. Co., 1961, pp. 974-980

30. Jastrow, R., "Results of Experiments in Space," *J. Aerospace Sci.* 29(4):377-388, 409, April 1962

31. Bourdeau, R. E., Donley, J. L., et al., "Measurements of Sheath Currents and Equilibrium Potential on the Explorer VIII Satellite," *J. Astronautical Sci.*, 8(3):65-73, Fall, 1961

32. Jackson, J. E., and Kane, J. A., "Measurement of Ionospheric Electron Densities Using an RF Probe Technique, *J. Geophys. Res.*, 64(8):1074-1075, August 1959

33. Kane, J. A., Jackson, J. E., and Whale, H. A., "The Simultaneous Measurement of Ionospheric Electron Densities by CW Propagation and RF Impedance Probe Techniques," NASA Technical Note D-1098, January 1962

ELECTRON LOSS RATE FROM
THE OUTER ELECTRON BELT

by

W. N. Hess

Goddard Space Flight Center

and

S. D. Bloom, L. G. Mann, F. D. Seward, and H. I. West, Jr.

Lawrence Radiation Laboratory

SUMMARY

Present experimental information permits a reasonable picture to
be formed of the electrons in the outer radiation belt. The lifetime of
the trapped particles is very important to a complete understanding of
the belts; and for a known steady-state population the only easy way to
determine this is to measure the loss rate. This paper discusses the
mechanism and rate of the loss of high energy electrons from the outer
belt.

Three separate groups of radiation belt electrons have been ob-
served in the Discoverer satellite flights. The first group has a spec-
trum that falls off sharply with increasing energy, does not extend
above 125 kev, and shows large time fluctuations; its source is not un-
derstood. The second group has a spectrum similar to that of the
auroral electrons. Most of the electrons in the belts are of the third
group; their spectrum somewhat resembles a neutron β-decay spec-
trum but extends to higher energies. They are lost from the belt by
coulomb scattering. The calculated loss rate and residence time of
these electrons in the outer belt are consistent with the proposition
that they are neutron decay products.

INTRODUCTION

Enough experimental information is now available that a reasonable picture can be formed of the
electrons in the outer Van Allen radiation belt. From Explorer XII (1961 v) we now know that there are
typically about 10^7 electrons/cm^2-sec in the energy region 40 kev to 1 Mev in the outer belt (Refer-
ence 1); this is a considerably lower flux than earlier estimates had given. The *flux* does not vary much
with position in the outer belt from 25,000 to 65,000 km nor does it vary much with time. *Intensity* vari-
ations by a factor of 2 or 3 with time are seen in the 100 kev energy range, occasionally reaching a

factor of 5 to 7 during August and September (J. A. Van Allen, private communication). These variations might be due only to changes in the magnetic field and the associated effects on particles, rather than to changes in the particle population. The large time variations in flux seen in several earlier experiments are seen only in the high energy ($E > 1.6$ Mev) group of electrons in the case of Explorer XII. Very likely the large time variations on several earlier experiments involved the high energy electrons also. At the times of magnetic storms the 100 kev flux changes by as much as a factor of 7, but returns to roughly the prestorm flux in a few days at the end of the storm (J. A. Van Allen, private communication). All of these features seem to indicate a particle population that has quite a long lifetime.

It is very important to a complete understanding of the radiation belt to know the lifetime of the trapped particles. When dealing with a steady-state population, the only easy way to determine particle lifetimes is to measure the loss rate from the belt. The total population of the belt then yields the average lifetime.

In this paper we will consider the mechanism and the rate of the loss of high energy electrons from the outer radiation belt.

DATA FROM EXPERIMENTS ON DISCOVERER SATELLITES

We now have information that bears on the lifetime of the outer belt electrons in the 100 kev to 1 Mev energy range. Several particle-detecting instruments have recently been flown on Discoverer satellites. These vehicles orbit at altitudes of a few hundred kilometers and at orbital inclinations of approximately 82 degrees, so the earth is quite well covered by measurements from these satellites. The instruments that have been flown are: (1) a thin *CsI* scintillator covered by 2 mils of *Be*, which counted electrons of $E_e > 100$ kev and protons above about 3 Mev; (2) a thick plastic scintillator that counted electrons of $E_e > 2$ Mev and protons of $E_p > 15$ Mev; and (3) a ten channel magnetic electron spectrometer (Reference 2) that counted electrons from 80 kev to 1.25 Mev.

The count rates of the *CsI* detector are shown in Figure 1 for the Southern Hemisphere. Three types of features are seen here. First, off the coast of Brazil a high count rate is observed which is related to the loss of particles from the inner radiation belt. In this region the earth's surface magnetic field is weak, so that the inner belt particles come closest to the earth here. Secondly, irregular pulses of particles are seen in the auroral zones. From the electron spectrometer we know that these particles are electrons of $E_e < 200$ kev and a considerable fraction of them come essentially directly down the field lines. That is, the electrons are not trapped and drifting down in altitude but, rather, they are on their way to earth in one single bounce.

The third group of particles is the most interesting. At about 10 or 15 degrees subauroral in the South Atlantic we see a large population of particles. These particles are not uniquely identified as electrons, but no protons of $E > 3$ Mev are known to exist in this region of space, so they are almost certainly electrons. These particles show a reasonably consistent spatial distribution from pass to pass. They are the leakage from the outer radiation belt being lost in the Capetown Anomaly (Reference 3). They showed a roll modulation when one of the Discoverer vehicles tumbled,
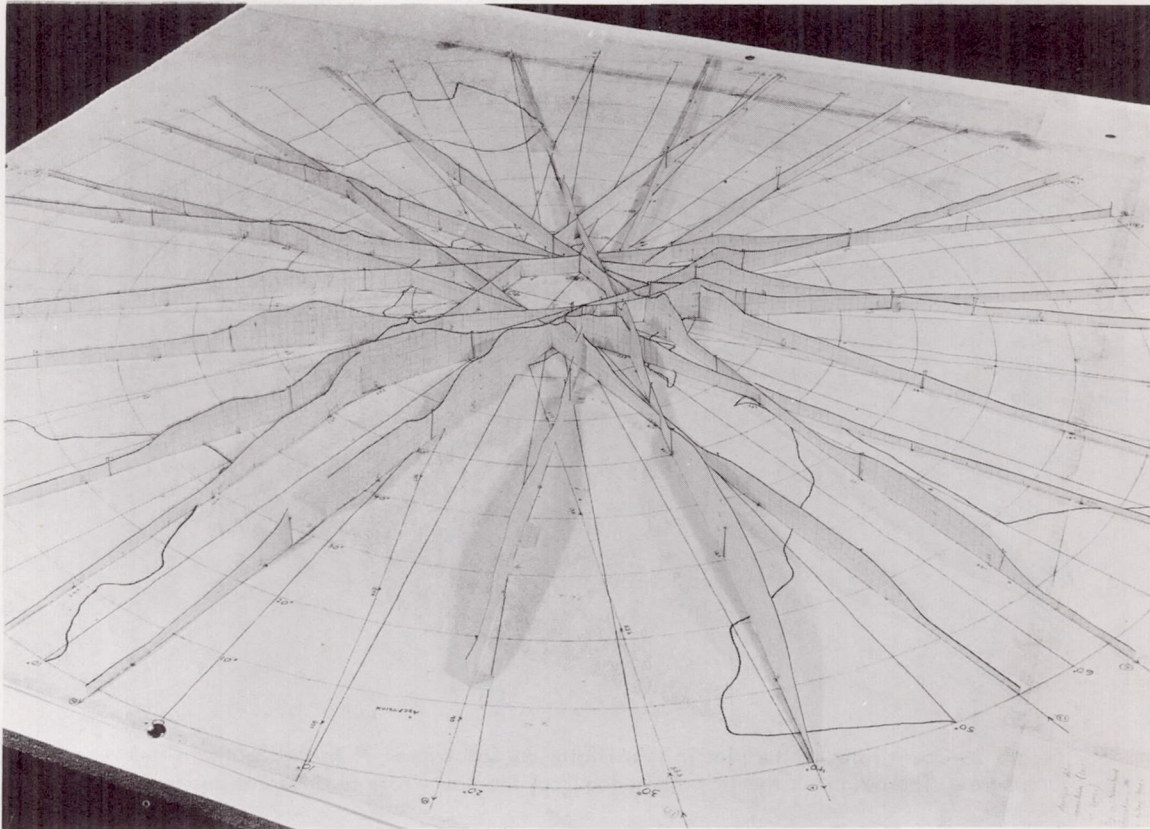
Figure 1—Count rates of the *CsI* detector on Discoverer 31 in the Southern Hemisphere. The height of the strip gives $\log_{10}$ of the count rate at different positions. The highest count rate is above 10^4 counts/sec and the lowest is about 10 counts/sec

indicating that they are almost certainly trapped particles. These particles were slowly being lost in an orderly way, quite differently from auroral particles which are lost in squirts.

The plastic scintillator shows quite similar behavior in the Southern Hemisphere (Figure 2). The losses from the inner belt off Brazil and the loss from the outer belt off Capetown are quite apparent. The auroral spikes are, however, not seen; this indicates that the auroral particles are below the threshold of this detector.

In the Northern Hemisphere the Discoverer results are quite different. Auroral pulses are seen by the *CsI* detector (Figure 3) but the other features are not. The scintillator count rate (see Figure 4) shows no high count rate regions such as those in the South Atlantic. Count rate contours for the high count rate regions in the South Atlantic are shown in Figures 5 and 6 for the two detectors.

These features of the radiation belts were first seen on a low altitude Soviet satellite (References 4 and 5). Vernov et al. observed both the high intensity region off Brazil which they identified as mostly protons and related to the inner belt (Reference 4) and a high intensity region in the South Atlantic identified as mostly electrons related to the outer radiation belt (Reference 5).

21
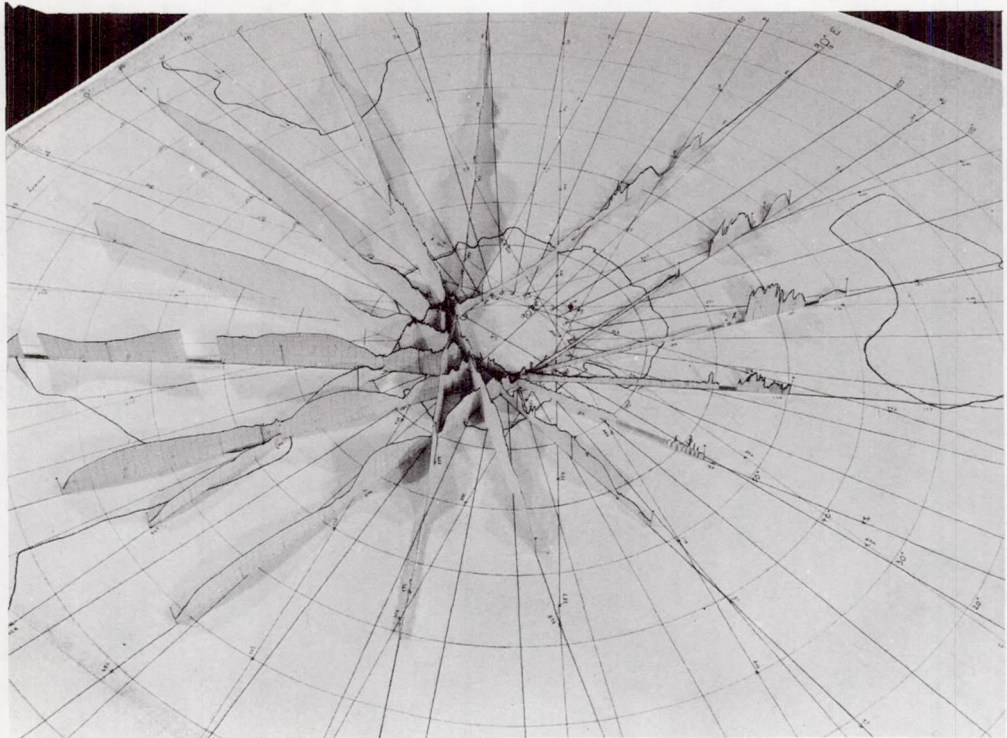
Figure 2—Count rates of the plastic scintillator on Discoverer 31 in the Southern Hemisphere. The height of the strip gives $\log_{10}$ of the count rate at different positions
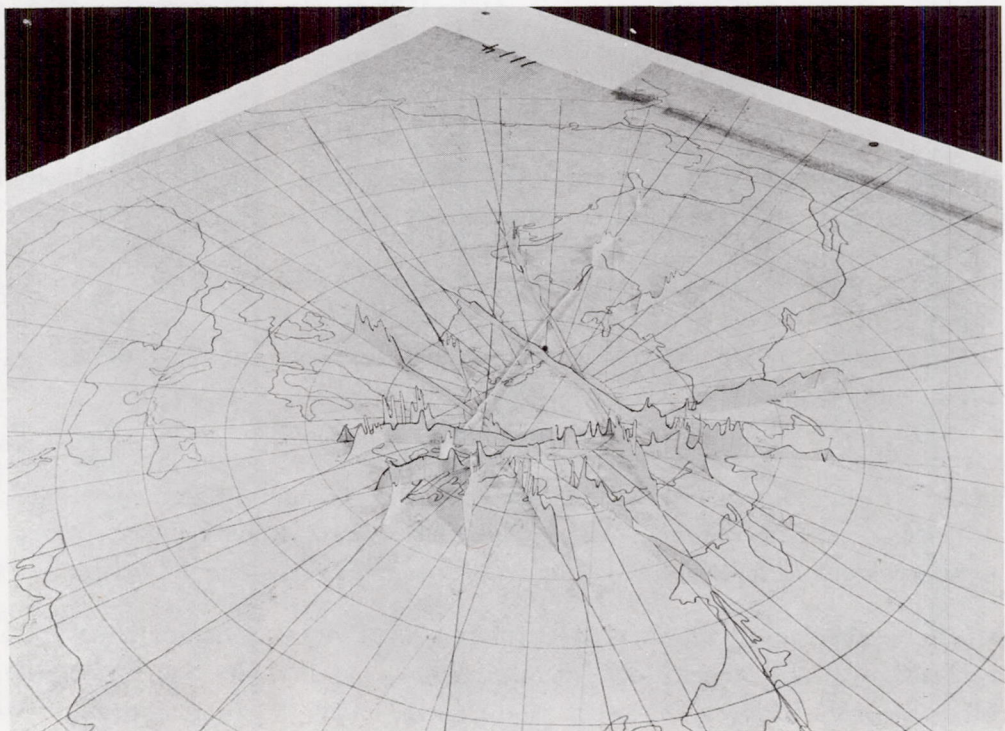

Figure 3—Count rate of the *CsI* detector on Discoverer 31 in the Northern Hemisphere. The height of the strip gives $\log_{10}$ of the count rate at different positions
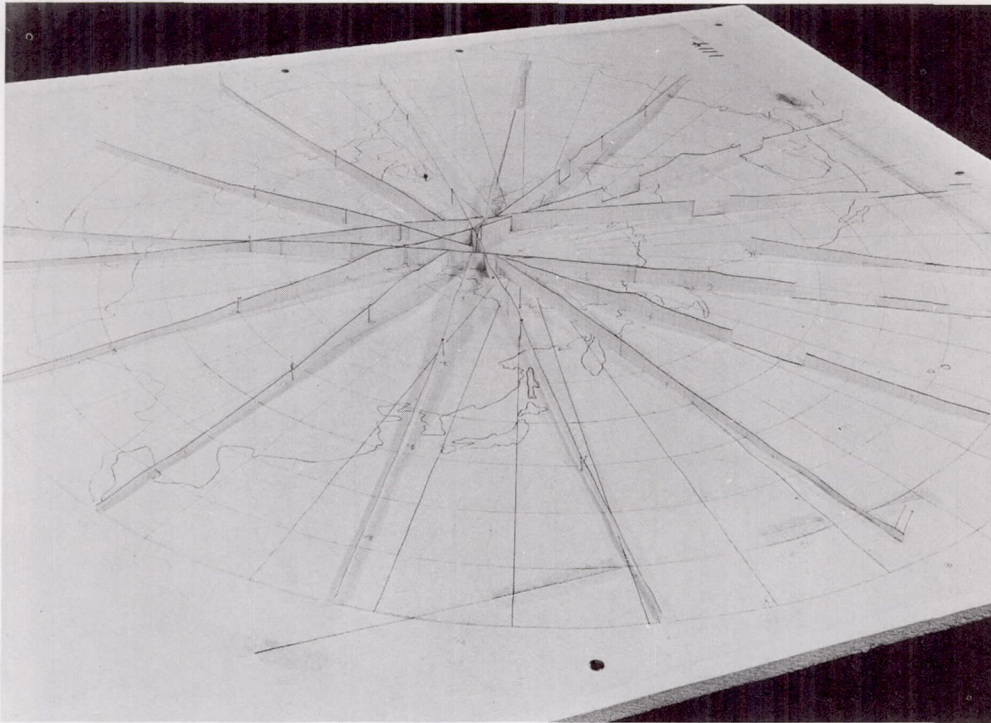
Figure 4—Count rate of the plastic scintillator on Discoverer 31 in the Northern Hemisphere. The height of the strip gives $\log_{10}$ of the count rate at different positions
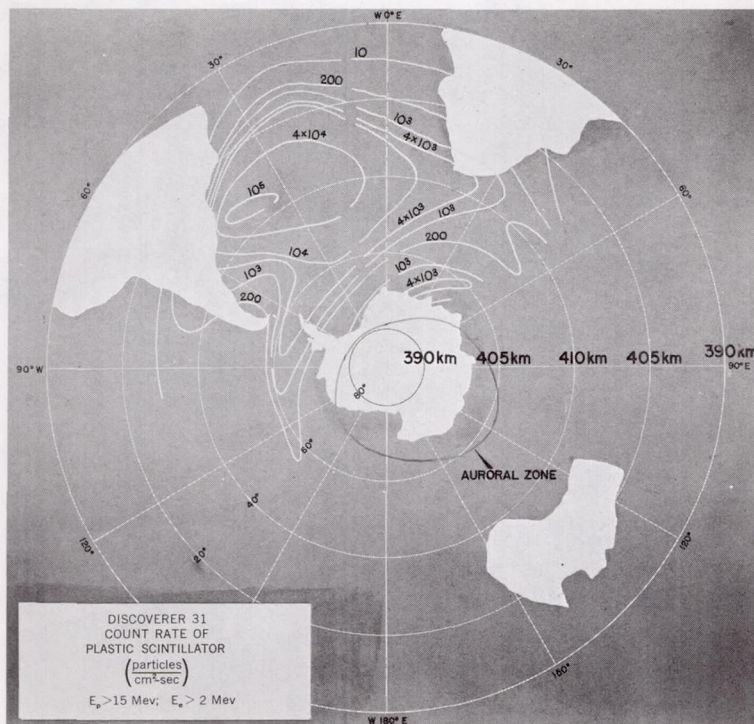
Figure 5—Count rate contours for the plastic scintillator on Discoverer 31 for the Southern Hemisphere
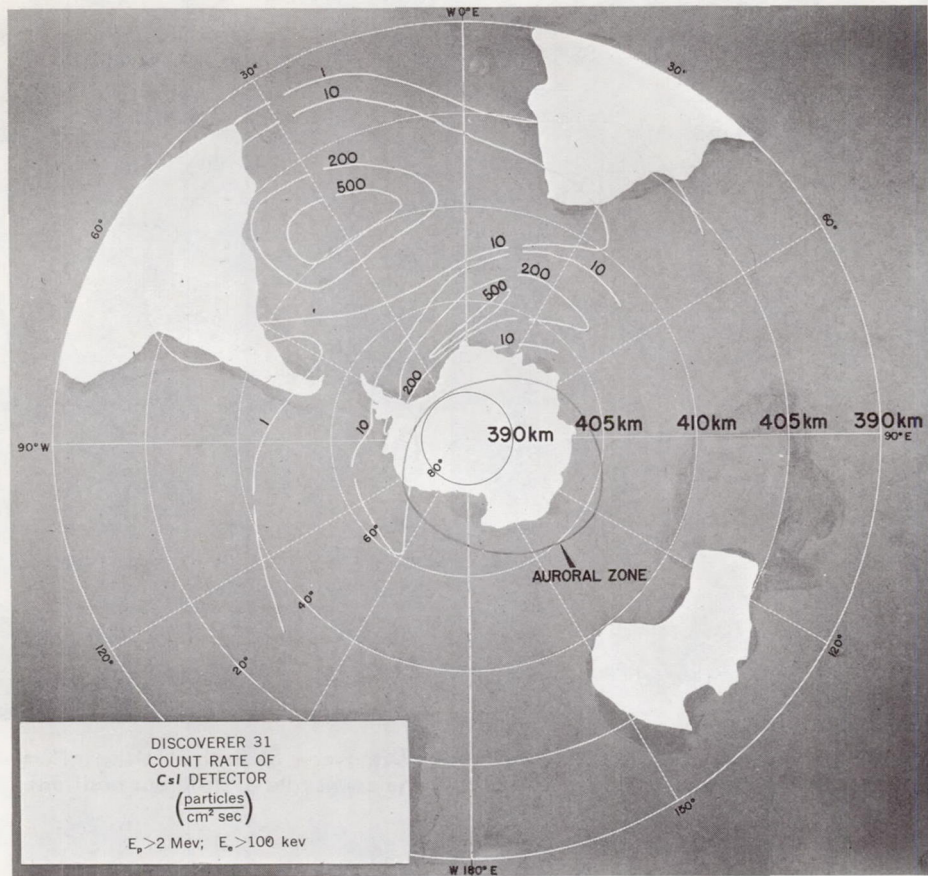
Figure 6—Count rate contours for the *CsI* detector on Discoverer 31 for the Southern Hemisphere

CALCULATION OF THE LOSS RATE

From these low altitude measurements on the outer belt electrons, we can calculate the rate of loss of particles from the radiation belt. Cladis and Dessler (Reference 6) suggested studying the bremsstrahlung of electrons in the atmosphere in the region of the Capetown Magnetic Anomaly to get the loss rate from the belt. The present study uses the more direct method of observing the electrons themselves. If we have steady state in the radiation belt, then the situation depicted in Figure 7 occurs. Particles are
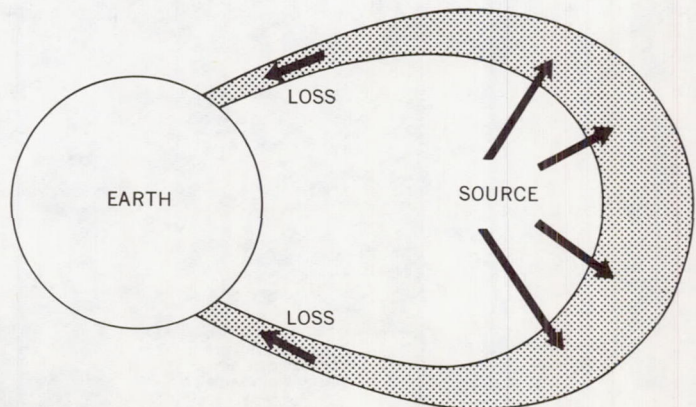
Figure 7—The steady-state picture of the radiation belt. Particles are injected into the belt at a rate s which must equal the loss rate l

continually injected into the belt. If, as is commonly thought, radial diffusion is a slow process, then the particles are lost from the belt down into the atmosphere in the manner shown in the figure. This loss rate can be described in terms of a motion of particles down into the loss cones and their eventual collision with the earth.

In this calculation of the loss rate, we must assume that coulomb scattering is the dominant loss process. We have measured the particle flux Φ at altitude h. From this we can get the net motion of particles downwards, the drift flux D, by

$$D = \left(\frac{\Phi}{v}\right)U ,$$

where v is the particle's velocity and U is a downward drift velocity. The drift velocity U describes the process of particles gradually leaking out of the loss cone as the result of coulomb scattering. This is, of course, an average concept; a given particle does not move smoothly downwards in altitude. The first attempts to describe this loss process (References 7 and 8) introduced the concept of the velocity of lowering of mirror points W. Later it was shown that this description of the process was incomplete (Reference 9) and a second term Y was needed which would describe the diffusion of the particles. W. McDonald has shown (private communication) that for the case of the exponential atmosphere the two terms can be written as

$$U = W + Y = W \left[1 + \frac{H}{\Phi\rho} \frac{\partial}{\partial h} (\Phi\rho)\right] ,$$

where H is the scale height of the atmosphere and ρ is the air density.

If the electron flux Φ varies inversely with the air density ρ, then $Y = 0$. We know that this situation is roughly true for protons, but there are no good data on electrons to evaluate Y. For lack of better information we will take $W = Y$ and $U = 2W$. It would be quite surprising if the altitude dependence of Φ were such that $Y \gg W$, but we must wait for final information on this.

Using the value of $U = 1.5 \times 10^5$ cm/sec for $E = 200$ kev at an altitude of 400 km, we can obtain D as a function of position from the *CsI* detector data. From D we can determine the total loss rate L from the radiation belt by

$$L = \oint D \, da .$$

To get L we integrate D along two lines of constant integral invariant I, one in the Northern Hemisphere and one in the Southern. This sums up the loss from one lunoid of the belt (a *lunoid* is a figure of revolution whose cross section is a lune, the region between two neighboring field lines, as shown in Figure 8). We will take two strips 1 cm wide around the earth in order to evaluate L. The volume of the lunoid whose base is 1 cm wide for $r_0 = 2.8 \ r_e$ is $V = 1.4 \times 10^{20}$ cm^3. The total loss rate L evaluated this way is 2.5×10^7 electrons/sec and the volume loss rate is $l = L/V = 1.5 \times 10^{-13}$ electrons/cm^3-sec. The only contribution to the integral for L is from the region of the South Atlantic. For a steady-state situation the volume loss rate l is equal to s, the strength of the source that is populating the radiation belt. The source strength s calculated (Reference 10) for neutron decay is
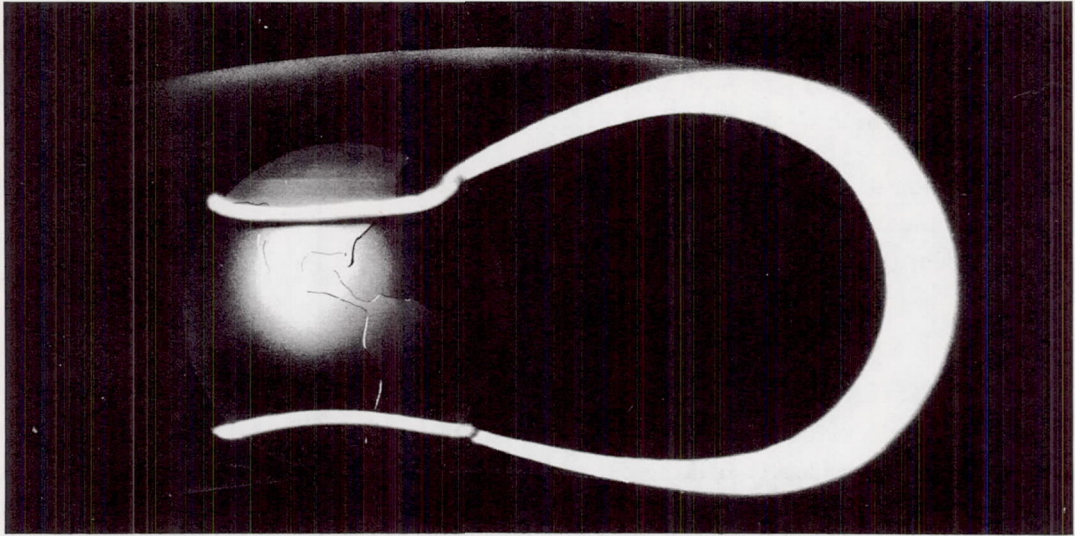
Figure 8—A lunoid of the outer radiation belt. This is a volume whose cross section is the region between two neighboring field lines. The lines on the earth at the base of the lunoid are lines of constant integral invariant which represent the loci of the loss zones for the particles in the lunoid

about 10^{-13} electrons/cm^3-sec for the outer belt. This value of s looks very similar to the calculated value of l; thus the neutron decay source seems adequate in strength to produce the outer belt electrons.

We can also get from this the average residence time τ of an electron in the radiation belt by assuming a steady state and using $L = Q/\tau$, where

$$Q = \left[\frac{10^7 \text{ electrons/cm}^2\text{-sec}}{(2 \times 10^{10} \text{ cm/sec})} \right] 1.4 \times 10^{20} \text{ cm}^3 = 0.7 \times 10^{17} \text{ electrons} .$$

Q is the total number of electrons in the lunoid. We get $\tau = Q/L = 0.7 \times 10^{17}/2.5 \times 10^7 = 3 \times 10^9$ sec. This time τ is about the same as the estimates of lifetimes (References 11, 12, and 13) for outer belt electrons, based on coulomb scattering.

It is somewhat surprising that the loss rate is as small as it seems to be from this calculation. We might expect, on the basis of other experiments, that polar-cap neutrons would substantially increase the strength of the neutron source due because of galactic cosmic rays. If this were the case, the source strength would be increased above the value of $s = 10^{-13}$.

COMPARISON OF OTHER EXPERIMENTS WITH THE DISCOVERER RESULTS

One other experiment measures the outer belt electron loss rate directly and can be compared with our calculation. The count rate of the 213 GM counter on the Injun satellite (Reference 14) determines the loss rate of electrons of $E > 40$ kev. Sometimes the angular distribution of the particles

observed by this counter over North America is so wide that the particles are obviously being lost directly into the atmosphere. A determination of the loss rate from these observations yields a figure much larger than the one calculated here. According to the Injun analysis, the average residence time τ of an outer belt electron is about 10^4 seconds. The loss of electrons as observed on Injun must be considered to be the result of a catastrophic process; that is, the electron mirror altitude is changed by a large amount in a single bounce period. This must be due to some process other than coulomb scattering.

This comparison of Injun and Discoverer results seems inconsistent, but with the help of the Discoverer electron spectrometer experiment (Reference 2) we can understood both experiments.

The spectrometer detects three different and distinct spectra of electrons:

Spectrum A is a very sharply falling off function of energy. The intensity decreases by a factor of e with an increase in energy of about 5 kev, and is only present below 125 kev. This spectrum is seen almost world-wide at some times and other times is not seen at all. At some times, fluxes greater than 10^6 electrons/cm²-sec-ster are seen in a 28 kev wide channel centered at 94 kev.

Spectrum B e-folds with a change in energy of from 25 to 40 kev and goes up to about 200 kev. It is seen prominently in the auroral zone and shows large time fluctuations. A group of particles of $90 < E < 245$ kev, with a similar energy spectrum and considerably lower intensity, is seen in the inner belt loss zone off Brazil and is seen sometimes in the outer belt loss zone off Capetown.

Spectrum C usually has a maximum intensity at about 600 kev and goes up beyond 1.2 Mev. At 200 kev it is down about a factor of 2 from the maximum intensity. This spectrum is always seen in the inner belt loss zone off Brazil and with lower intensity in the outer belt loss zone off Capetown. The detection of lower intensities of the C spectrum in the outer belt loss zone than off Brazil may be due to the fact that the spectrometer's look direction is closer to the direction of the field line. If the angular distribution is pancake shaped, it would be seen less near the direction of the field line. The C spectrum is also seen in certain small areas of the Pacific Ocean. It shows a smooth spatial variation and is quite constant in time. The intensity at one place normally is constant to within a factor of 2 for long periods.

The fact that there are three different spectra of electrons apparently produced by different processes helps explain other experiments. The Injun experiment (Reference 14) that observed catastrophic dumping over North America is quite consistent in spatial extent, time variations, energy, and flux with the A spectrum of electrons seen by the Discoverer. The fact that these electrons are almost all of $E < 100$ kev means that the *CsI* detector on Discoverer will not see these particles.

The C spectrum observed by the Discoverer looks somewhat like the equilibrium electron energy spectrum expected (References 15, 16, and 17) from neutron β-decay, except that it extends to higher energies. This spectrum is rather similar to the outer belt electron spectrum seen (Reference 18) on Explorer XII in that it is quite flat at about 100 kev and extends up beyond 1 Mev. This population of particles shows smooth spatial variations and roll modulation, indicating that the particles are trapped, and the flux is quite constant in time. All of these facts and also the fact that this spectrum is seen essentially only in the magnetic field anomalies in the South Altantic strongly indicate that

these particles are being lost by coulomb scattering. If other processes were responsible for the particle loss, there would be no reason for the measured flux to be largest in the South Atlantic. The fact that the fluxes of the C spectrum are concentrated in the South Atlantic strongly indicates that the atmosphere controls the loss process. The particles' mirror points come closest to the earth in this region, and the particles encounter the densest atmosphere here. This shows that coulomb scattering is the dominant loss process.

One other experiment has given information on the loss of electrons from the outer radiation belt. Cladis and Dessler (Reference 6) analyzed the results of the experiment of Walt et al. (Reference 19) who flew a magnetic spectrometer to 1000 km to measure electrons. From this analysis a drift flux D of 320 electrons/cm^2-sec was obtained. Assuming the magnetic anomaly is 1000 km wide, this gives a loss rate of L = 3 $\times$ 10^{10} electrons/sec. This is 1000 times larger than the loss rate obtained in the present paper. It is not understood what causes the difference in these values. The electron energy spectrum measured by Walt et al. (Reference 19) is not very similar to the C spectrum seen by the Discoverer over the South Atlantic; it more resembles the B spectrum. Possibly the Walt experiment was not seeing trapped outer-belt electrons (Reference 18), but some population more like the Injun electrons. This question cannot be answered now. For the present, we must leave this question about the difference of the L values unresolved.

CONCLUSIONS

The following points have come out of this analysis:

1. There are three separate groups of electrons observed on the Discoverer flights.

2. The A spectrum falls off sharply with increasing energy and does not extend above 125 kev. It shows large time fluctuations. The Injun experiment that observed direct dumping was quite likely seeing this flux of particles. The source of these particles is not understood.

3. The B spectrum is the spectrum of auroral electrons. A similar spectrum also appears at low energies in some of the particles lost from the radiation belts, indicating that some of the belt electrons of E < 200 kev may have been accelerated by auroral processes.

4. Most of the electrons in the radiation belt are of the C spectrum type, which looks rather like a neutron β-decay spectrum but extends to higher energies. These particles are lost from the radiation belt by coulomb scattering.

5. The average residence time of an electron in the outer radiation belt is calculated on the basis of coulomb scattering to be 3 $\times$ 10^9 seconds. The analysis here is uncertain by a factor of 2 or more in a few instances, but the results are probably good to within a factor of 5.

6. The data on the C spectrum electrons concerning their energy spectrum, loss rate, and lifetime are all consistent with the proposition that these particles, which constitute most of the inner and outer radiation belt electrons, are the result of neutron decay.

REFERENCES

1. Rosser, W. G. V., O'Brien, B. J., et al., "Electrons in the Earth's Outer Radiation Zone," paper presented at 43rd Annual Meeting Amer. Geophys. Union, Washington, April 1962

2. Mann, L. G., Bloom, S. D., and West, H. I., Jr., "The Electron Spectrum from 80 to 1258 Kev Observed on Discoverer Satellites 29 and 31," paper presented at the 3rd Interna. Space Sci. Sympos., Washington, May 1962

3. Dessler, A. J., "Effect of Magnetic Anomaly on Particle Radiation Trapped in Geomagnetic Field," J. Geophys. Res. 64(7):713-715, July 1959

4. Vernov, S. N., Savenko, I. A., et al., "Discovery of the Internal Radiation Belt at a Height of 320 km in the Region of the South Atlantic Magnetic Anomaly," Doklady Akademii Nauk SSSR 140(5):1041-1044, October 11, 1961. Translation in Soviet Phys. - Doklady 6 (10):893-896, April 1962

5. Vernov, S. N., Savenko, I. A., Shavrin, P. I., "The External Radiation Belt About The Earth at an Altitude of 320 Kilometers," Doklady Akademii Nauk SSSR 140(4):787-790, October 1961

6. Cladis, J. B., and Dessler, A. J., "X Rays From Van Allen Belt Electrons," J. Geophys. Res. 66(2):343-350, February 1961

7. Christofilos, N. C., "Trapping and Lifetime of Charged Particles in the Geomagnetic Field," Univ. Calif. Radiation Lab. Rept. UCRL-5407, November 28, 1958

8. Welch, J. A., and Whitaker, W. A., "Theory of Geomagnetically Trapped Electrons from an Artificial Source," J. Geophys. Res. 64(8)909-922, August 1959

9. Kellog, P. J., "Possible Explanation of the Radiation observed by Van Allen at High Altitudes in Satellites," Nuobo Cimento 11W:48-66, January 1, 1959

10. Hess, W. N., Canfield, E. H. and Lingenfelter, R. E., "Cosmic-Ray Neutron Demography," J. Geophys. Res. 66(3):665-677, March 1961

11. Wentworth, R. C., "Lifetimes of Geomagnetically Trapped Particles Determined by Coulomb Scattering," PH.D. Thesis, University of Maryland 1960

12. Wentworth, R. C., MacDonald, W. W. and Singer, S. F., "Lifetimes of Trapped Radiation Belt Particles Determined by Coulomb Scattering," Physics of Fluids 2(5):499-509, September-October 1959

13. Hess, W. N., and Killeen, J., "Spatal Distribution of Electrons from Nelltron Decay in the Outer Radiation Belt," J. Geophys. Res. 66(11):3671-3680, November 1961

14. O'Brien, B. J., "Direct Observations of Dumping of Electrons at 1000 km Altitude and High Altitudes," State Univ. of Iowa, SUI-62-2 January 10, 1962

15. Kellogg, P. J., "Electrons of the Van Allen Radiation, J. Geophys. Res. 65(9):2705-2713, September 1960

16. Lenchek, A. M., Singer, S. F. and Wentworth, R. C., "Geomagnetically Trapped Electrons from Cosmic Ray Albedo Neutrons," J. Geophys. Res. 66(12): 4027-4046, December 1961

17. Hess, W. N. and Poirier, J. A., "Energy Spectrum of Electrons in the Outer Radiation Belt," J. Geophys. Res. 67(5):1699-1709, May 1962

18. O'Brien, B. J., Van Allen, J. A., et al., "Absolute Electron Intensities in the Heart of the Earth's Outer Radiation Zone," J. Geophys. Res. 67(1):397-402, January 1962

PRELIMINARY SOLAR FLARE OBSERVATIONS WITH THE SOFT X-RAY SPECTROMETER ON ORBITING SOLAR OBSERVATORY I

by

William E. Behring, Werner M. Neupert, and John C. Lindsay

Goddard Space Flight Center

SUMMARY

A spectrometer carried by Orbiting Solar Observatory I (1962 ζ 1) and used for observing the solar spectrum from 10 to 400A is described. The instrument utilizes a concave grating mounted in grazing incidence, and an open-window photomultiplier. Resolution of approximately 1A is obtained throughout the wavelength region covered. Solar spectra obtained with this instrument during a rocket flight are shown, and tentative identification of the origins of observed spectral lines is listed. Preliminary satellite results obtained during a solar flare are discussed.

INTRODUCTION

The primary experiment on Orbiting Solar Observatory I (1962 ζ 1) was a soft x-ray spectrometer designed specifically to make satellite measurements of the solar spectrum in the wavelength range from 10 to 400A. As a result of the successful launching of the satellite into a nearly circular earth orbit (550 km perigee and 600 km apogee) and the subsequent successful operation of the experiment, the first long term measurements of the soft x-ray solar spectrum have been obtained. The purpose of this paper is to briefly describe the instrument, to illustrate its performance with data obtained from a rocket launch, and to present some preliminary satellite data obtained before and during the solar flare of March 13, 1962.

THE SPECTROMETER

The angular aperture of the spectrometer is approximately 1.2 by 2.2 degrees. Hence, with moderately accurate pointing (within a few angular minutes of the center of the solar disc) the spectrometer responds to the total light intensity emitted by the sun. The instrument's orientation is such that sunlight is incident perpendicularly on the front face, passes through the entrance slit, and strikes a concave grating mounted in grazing incidence, the angle of incidence being 88 degrees

(Figure 1). The grating, an original which was lightly ruled in a special glass by the Nobel Institute in Stockholm, has 576 lines/mm on a blank with a radius of curvature of 1 meter. No reflecting coatings were used on this grating. The diffracted rays continue on to the exit slit in front of the detector. The detector is mounted on a carriage which is driven on a circular rail so that the exit slit scans along the Rowland circle from 10 to 400A. The plane of the exit slit stays approximately perpendicular to the diffracted ray at all positions along the rail, thereby keeping the spectral passband nearly constant for all angles of diffraction. The 50 micron entrance and exit slits provide a spectral passband of 1.7A and permit resolution of lines 0.85A apart.

The detector used was an open-window multiplier phototube developed by the Bendix Corporation specifically for use in this spectrometer and now commercially designated M-306. Photoelectrons from the tungsten cathode move along cycloidal paths in crossed electric and magnetic fields between two glass strips, each coated with a semiconducting secondary-emitting oxide layer. One of the glass strips serves as a continuous dynode. Each photoelectron is multiplied into a pulse of approximately 10^6 electrons at the anode. These electrical pulses are amplified and, after coding to compress bandwidth, are recorded on a tape recorder for later transmission to a ground station.

The spectrometer uses about 1.3 watts supplied by the satellite at 18 volts dc. About 1 watt of this goes to the oscillator powering the three-phase synchronous motor, which requires about 300 mw at 137 cps to yield 100 mw of mechanical output power. The remainder of the power is used in the multiplier and pulse handling circuitry.

All of the materials exposed inside the spectrometer were tested at a pressure of about 10^{-6} mm Hg in order to eliminate any material that had a high vapor pressure. Because the electronic circuits were potted in a compound having a high vapor pressure, they were enclosed in sealed boxes vented to the outside through holes in the spectrometer base plate. During assembly all the parts exposed
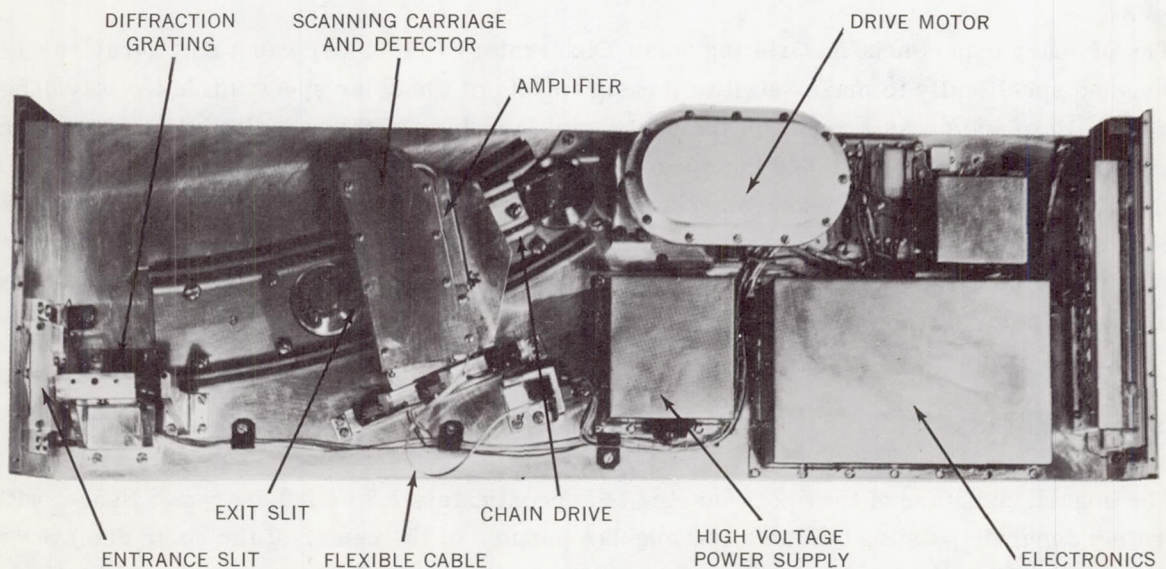
Figure 1—OSO I Spectrometer

to the interior were carefully cleaned so that they would be free of oil, grease, and other contaminants. The temperature of the instrument was controlled by the radiation balance. Most of the outer case was polished. The central section was painted black in order to keep the temperature close to that of the satellite.

Alignment of the spectrometer was accomplished with the use of only visible light by means of a fixture with a radius rod pivoted at the center of the Rowland circle; this procedure was developed on the basis of the method described by Rathenau and Peerlkamp (Reference 1). Alignment tests were performed with a source of carbon K radiation. A separate photomultiplier was used to provide a monitor on the stability of this source. The response to scattered hydrogen Lyman-alpha radiation was checked with a closed hydrogen discharge lamp. The specific grating used was selected by means of comparative tests performed on several gratings.

THE ROCKET FLIGHT

Figure 2 shows the solar spectrum obtained with a similar instrument and a rocket pointing control during an Aerobee rocket flight. In this spectrum the wavelength regions of 120 to 170A and 220 to 240A represent the average of data taken in three different scans in an attempt to improve the reliability of faint lines and provide continuity in the region originally containing wavelength marker pulses. In the region below 100A evidence of spectral lines is inconclusive. Comparison of the observed counting rates with laboratory scattered-light measurements indicates that for the rocket flight the signal attributable to the first order spectrum becomes lost in the scattered light below about 60A.
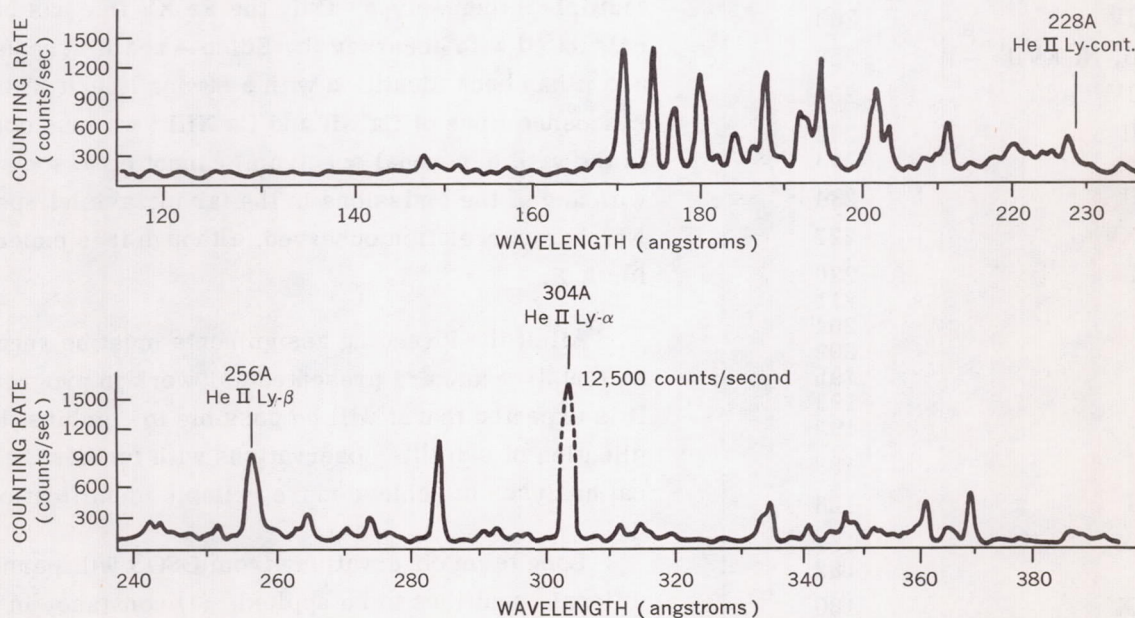
Figure 2—The solar spectrum from 120 to 400A as recorded near peak altitude (201-216 km) during an Aerobee rocket flight at 1433 GMT on September 30, 1961

Table 1

Tentative Identification of Various Strong Emission Lines in the Solar Spectrum

| Element	Wavelength (angstroms)
Fe XIV, Fe XII	370
Fe X	366
	365
Fe XVI	361
Fe XII	360
Ni XV, Fe X	347
Fe XIV	345
	341
Fe XVI	335
Ni XV	333
	320
Ni XV	316
	315
	312
He II	304
	293
Fe XV	284
Cu XIX	274
	271
S X	264
A XIV	263
He II, Ni XVII	256
A XIV	250
He II	244
	243
He II	234
Ca XV	227
S IX	220
	211
	204
	202
	195
	193
	192
A XI	188
A XI	186
Cl IX	184
	182
Cl IX	180
	177
	174
	171

An attempt has been made to identify the resonance lines of highly ionized atoms of the heavier elements. Lines produced by several stages of ionization of C, N, and O, and also by Mg, Si, Ne, and Fe have already been found at wavelengths greater than 400A. The extension of isoelectronic sequences to heavier elements leads to resonance lines with wavelengths below 400A. The wavelengths of some of the strong lines observed are shown in Table 1, along with tentative identification of their origin. The tabulation of emissions compiled by Varsavsky (Reference 2) was used in this work. The criteria for assigning values were: (1) agreement with theoretically extrapolated values of the spacing and relative intensities of members of a multiplet, with the assumption, for the intensities, of an optically thin corona; (2) approximate agreement in wavelength with theory for lines not yet observed under laboratory conditions; (3) observation of more than one stage of ionization.

A preliminary analysis of the spectrum was made for ions known to exist in the solar atmosphere. These are ions of Fe, Ni, and, with lesser abundances, Ca and A. Identification of iron multiplets on the basis of one observation is difficult because of the presence of strong second-order lines as well as the superposition of the multiplets themselves. Only the Fe XV line has been calculated with accuracy (by Edlen — see Reference 3), and it has been identified with a strong line at 284A. The resonance lines of Ca XII and Ca XIII (two ions observed in the visible coronal spectrum) cannot be associated with any of the emissions in the far ultraviolet spectrum. Nor is a correlation observed, although it is expected, for A X.

All of the foregoing assignments must be regarded as tentative and are presented as "work in progress." It is expected that it will be possible to combine the application of satellite observations with further theoretical analyses to achieve more reliable identifications.

Long term observations from OSO I will permit additional conditions to be applied: (1) constancy in time of the ratio of intensities of the members of a multiplet, under the assumption that the opacity of the corona does

not change with time; (2) regularity in the variations of intensity throughout the observed stages of ionizations; (3) for each stage of ionization, agreement of intensity variation with the corresponding variation in the visual coronal line(s) for that stage.

PRELIMINARY SATELLITE OBSERVATIONS

The Orbiting Solar Observatory I was launched at 1606 UT on March 7, 1962, during a period of low solar activity. The first flares observed after launch were in McMath plage 6366, with heliographic coordinates N10E66. The flares were of importance 1 and 2+ and occurred at 1407 and 1444 UT, respectively. Figure 3 is an H-alpha photograph of the sun showing the 2+ flare as it appeared at 1543:22, considerably after maximum (which occurred at about 1450 UT). The total duration of this flare was about two hours. Ionospheric effects were recorded during the entire life of the visible flare, and included an SWF (short-wave fadeout) of importance 3, a 99 percent SPA (sudden phase anomaly), SCNA (sudden cosmic noise absorption) of importance 1 (20 percent), and SEA (sudden enhancement of atmospherics) of importance 2. Type III spectral radio bursts were observed on 21-41 Mc from 1514 to 1632 UT, and continuum bursts from 1519 to 1550 UT. Major bursts were also observed on the single frequencies of 108 and 2800 Mc. There was no evidence of energetic particle fluxes (Reference 4).

In the time available, it has been possible to reduce only partially the satellite data for the six orbits encompassing the visual flare. Two spectral lines were chosen for analysis: He II Lyman-alpha at 304A; and a line at 284A (tentatively identified as an Fe XV line). These data are shown in Figure 4, from which we observe two points.
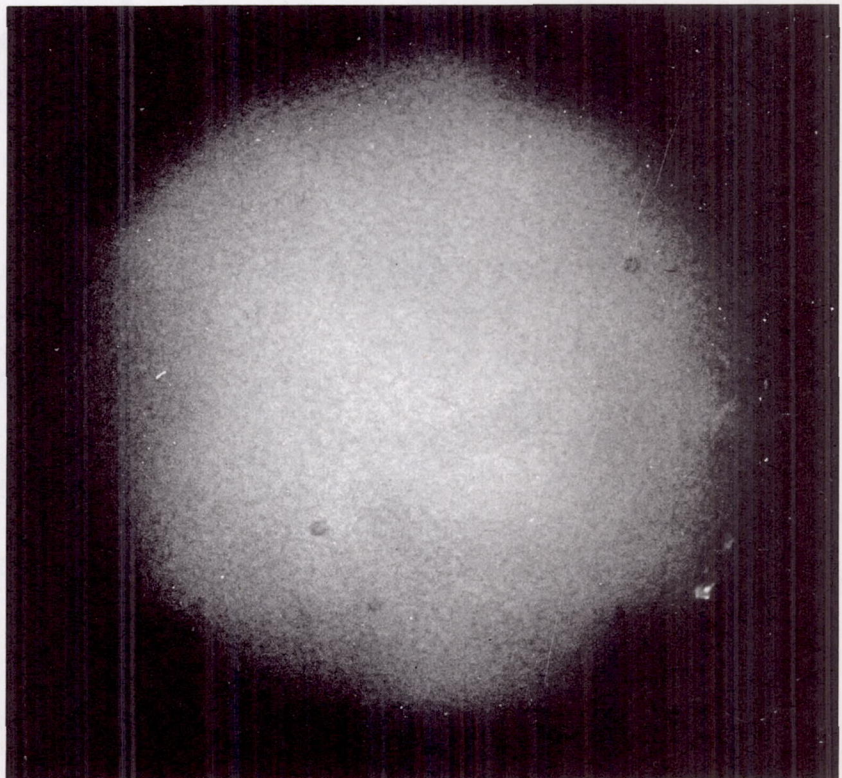
Figure 3—Picture of H-alpha flare at 1543:22, March 13, 1962; picture presented through the courtesy of the High Altitude Observatory (HAO), Boulder, Colorado
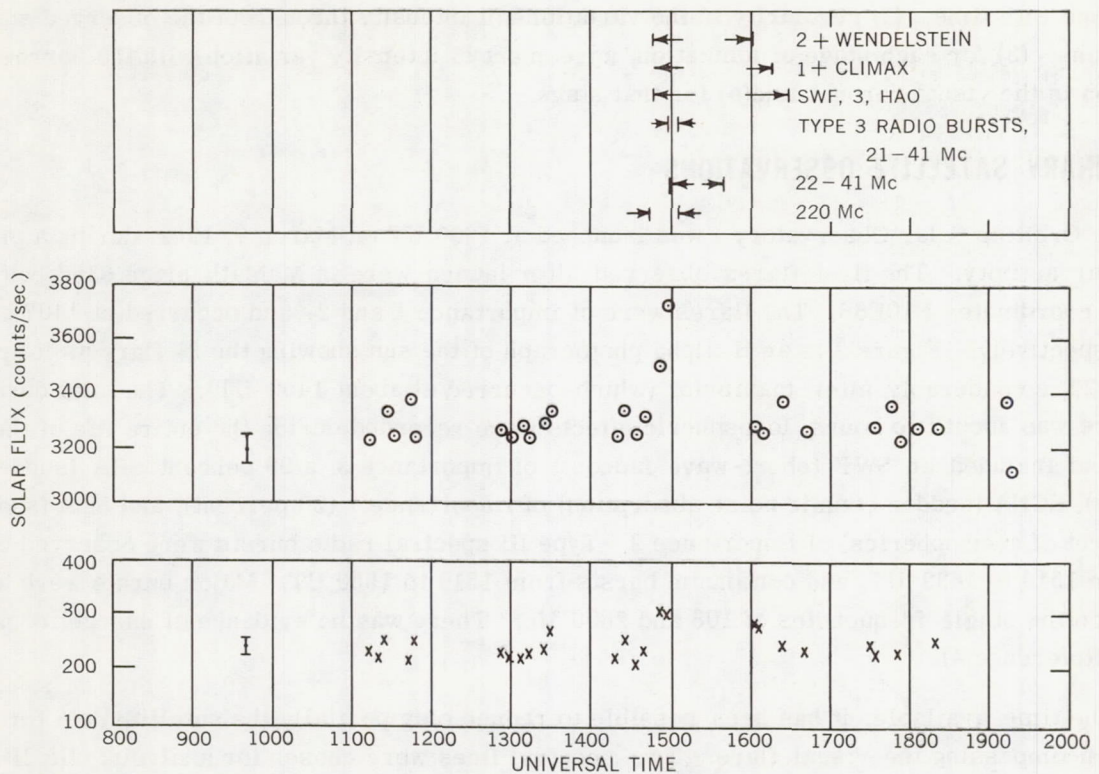
Figure 4—Relative solar flux at 304A (middle) and 284A (bottom) during the March 13, 1962, flare (Wendelstein and Climax are observatories.)

1. Increased emission coinciding with or preceding visual observations or other indicators.

2. Possible continued enhancement after the cessation of other indicators.

Using values for these two lines before the onset of the flare and during the flare, we find the maximum enhancements for the lines were 15 percent for 304A and 28 percent for 284A. Typical error flags are shown to the left on the figure. Practically all the error is statistical, and is due to the relatively small number of photons counted. The changes in the observed line intensities are larger than the expected errors and are believed to represent real changes associated with the flare.

CONCLUSION

As of April 13, 1962, OSO I had made approximately 550 orbits of the earth, and 3500 spectra of the sun in the 10-400A region had been collected. During this time fourteen flares of varying importance occurred—the largest one, of importance 3, on March 22. It is believed that the OSO data will:

1. Aid in identifying the spectral lines;

2. Allow limits to be placed on the continua in this wavelength region, for a quiet sun as well as during solar activity;

3. Allow quiet-sun line intensity measurements to be made with some certainty;

4. Determine line intensity enhancement, if any, before, during, and after visual flare activity;

5. Determine enhancement, if any, associated with other solar activities such as plage areas and spot groups;

6. Determine short time fluctuations in line intensities not associated with other easily observable phenomena.

Analysis and interpretation of these results should throw light on the energy transport in the corona and the relaxation time of the corona, as well as form the basis for a more complete model of the chromosphere.

ACKNOWLEDGMENTS

REFERENCES

1. Rathenau, G., and Peerlkamp, P. K., "Zur Justierung des Konkavgitters in streifender Inzidenz," *Physica,* Vol. 2, Part 1, pp. 125-143, 1935

2. Varsavsky, C. M., "Some Atomic Parameters for Ultraviolet Lines," *Astrophys. J. Suppl. Ser.* 6(53):75-108, March 1961

3. Firor, J., and Zirin, H., "Observations of Five Ionization Stages of Iron in the Solar Corona," *Astrophys. J.* 135(1):122-137, January 1962

4. "CRPL-F, Part B, Solar-Geophysical Data," issued monthly by the Nat. Bur. Standards, Central Radio Propagation Lab., Boulder, Colorado

REVIEW OF DIRECT MEASUREMENTS OF INTERPLANETARY
DUST FROM SATELLITES AND PROBES

by
W. M. Alexander, C. W. McCracken, L. Secretan, and O. E. Berg
Goddard Space Flight Center

SUMMARY

Interplanetary dust particle experiments have been flown on various types of spacecraft. Measurements of dust particle momentum, kinetic energy, and impact damage have been obtained from a variety of sensors.

More than 10,000 dust particle impacts have been measured by acoustical and light flash detectors. A cumulative mass distribution curve valid for average conditions in the vicinity of the earth has been derived from the direct measurements for dust particles with masses between about 10^{-13} and 10^{-6} gm.

The results of direct measurements from various penetration and fracture experiments are presented here. Comparison of these data with the average mass distribution curve shows no major discrepancies among the measurements from all of the different sensor systems used. Two satellite experiments, Vanguard III (1959 η) and Explorer I (1958 α), give evidence for dust particle streams. Vanguard III measured 2800 events in a 70-hour interval coincident in time with the expected return of the Leonid meteor shower. The average influx rate during the dust particle shower was more than one order of magnitude greater than the non-shower influx rate measured with the same satellite. There were rapid fluctuations during the shower when the influx rates increased by as much as three orders of magnitude above the non-shower average rate. For a 10-hour period, Explorer I detected a dust particle shower with impact rates as high as 25 times the average impact rate during the satellite's lifetime.

The distribution curve obtained with the direct measurements differs from that expected on the basis of extrapolations of meteor observations. Small dust particles dominate the accretion by the earth of interplanetary matter; the accretion rate is of the order of 10^4 tons per day.

INTRODUCTION

An important constituent of the solar system is the cloud of dust surrounding the sun. Knowledge concerning the orgin, composition, and dynamic properties of these dust particles is fundamental to considerations of the solar system.

Various techniques have been used in studying the distributions and physical properties of dust particles in the zodiacal cloud. These include: ground-based visual, photographic, and radar meteor observations; photometric observations of the zodiacal light and solar F corona; and various types of collection techniques and laboratory analyses.

From observations of collisions of individual meteoroids with the earth's atmosphere, vector velocity, mass, density, and composition have been measured. These studies are limited, in most cases, to particle masses greater than 10^{-4} gm. Additional information has been obtained from the collection of remnants of meteoroidal and dust particle material which have survived passage through the atmosphere. Composition, age, and gross accretion rates have also been determined from these analyses. Zodiacal light observations represent the only ground-based technique which has been used to measure the size distribution of interplanetary dust particles with masses less than 10^{-6} gm.

Another technique for measuring the physical characteristics and dynamic properties of dust particles became a reality with the advent of vehicles capable of placing experiments in space. Detectors have been developed which are capable of measurements on individual dust particles with masses as small as 10^{-13} gm. The dust particle measurements in space started with experiments borne by sounding rockets in 1949. Subsequent to the successful launching of Explorer I (1958 α), results have been obtained from experiments on fourteen United States and Soviet Union satellites and space probes. Six different types of sensors have been used to measure the following particle parameters: momentum, kinetic energy, penetration, and fracture properties. The results of these rocket and satellite measurements are presented in the following sections.

DIRECT MEASUREMENTS FROM MICROPHONE SYSTEMS

The microphone type of dust particle sensor has basically consisted of a piezoelectric crystal microphone attached to a metallic sounding board. The electrical signal generated as an impacting dust particle delivers a mechanical impulse to the sounding board is amplified and pulse-height analyzed in order to obtain information about the particle. Analog calibrations, performed in the laboratory by dropping carefully selected glass spheres onto the sounding boards, have consistently shown (for low velocities) that the microphone system is sensitive to the momentum of an impacting particle. Hypervelocity studies with microparticles from shaped charges (Reference 1) tend to confirm that the microphone systems are also sensitive to the momentum of a particle impacting at hypervelocity. An energy dependence can be obtained by the use of the theoretical results of Stanyukovich (Reference 2). Lavrentyev (Reference 3) theoretically finds that the sensitivity lies somewhere between momentum and energy.

The direct measurements can presently be expressed in terms of the particle mass, subject only to minor uncertainties. These uncertainties include the choice of an average speed (relative to the satellite) for the particles; the determination of an effective coefficient of restitution for hypervelocity microparticle impacts; and the computation of the appropriate correction factors for shielding by the earth, for the solid viewing angle of the sensor, and for the orientation of the solid viewing angle relative to the apex of the earth's motion. The various correction factors have been chosen in such a way that the minor corrections which will most probably become necessary will leave the results of this analysis essentially unchanged.

Microphone systems have provided the greatest quantity of information about the interplanetary dust particles. These systems have flown on more vehicles and over a greater range of geocentric distances than any of the other systems. In addition, they are more nearly calibrated than other types of dust particle sensors. It will be assumed, for the present analysis, that the microphone systems are momentum-sensitive and that the ratio of the mechanical impulse to the impact momentum of a particle is unity. A small correction, estimated to be a factor of 2 or 3, can be introduced later when the appropriate hypervelocity laboratory studies have been completed.

The microphone system on Explorer VIII (1960 ξ) used two metallic sounding boards attached to a conical section of the spin-stabilized satellite. The solid viewing angle of the system was 2π steradians and remained almost centered on the antapex of the earth's motion during the lifetime of the experiment. From an analog calibration performed in the laboratory, the limiting sensitivities for the three ranges of sensitivity were found to be 2.5×10^{-3}, 2.5×10^{-2}, and 2.5×10^{-1} dyne second. These may be expressed in terms of particle mass as 1.0×10^{-9}, 1.0×10^{-8}, and 1.0×10^{-7} gm, respectively, if an average speed (relative to the satellite) of 25 km/sec is assumed. The large separations of the limiting sensitivities used in the Explorer VIII microphone system are of particular importance in view of the excellent data sample which was obtained. The magnitude of the total range of sensitivity allows not only a definition of the influx rates within the three ranges but also the establishment of the shape of a segment of an average mass distribution curve.

The fine structure in the influx rate measured with the Explorer VIII microphone system is presently being analyzed. The large variations (at least plus or minus an order of magnitude from the mean, within intervals of a few hours, for particle masses of about 10^{-9} gm) are being studied to determine their physical significance. The preliminary readouts of the total numbers of impacts used in establishing the average mass distribution curves that were reported earlier (References 4 and 5) have been confirmed. Exact specification of these numbers awaits completion of the analyses which are in progress, but "revised preliminary" numbers may be given. They are: 3726 dust particles with momenta of 2.5×10^{-3} dyne-sec and greater, 76 with momenta of 2.5×10^{-2} dyne-sec and greater, and 1 or 2 with momenta of 2.5×10^{-1} dyne-sec and greater. (The corresponding limits on particle mass were given above.) The area of the sounding boards was 7.0×10^{-2} m^2, and the lifetime of the experiment was 3.47×10^6 seconds.

A correction factor of 2 is applied to convert the influx rates to omnidirectional values before the data are plotted as the cumulative mass distribution curve shown in Figure 1. Although the data point for the scale of lowest sensitivity is not very significant, it lies on the straight line segment indicated by the two data points which are significant. The equation of a straight line segment which approximately fits the data points shown in Figure 1 is:

$$\log I = -17.0 - 1.70 \log m, \tag{1}$$

where I is the cumulative omnidirectional influx rate in particles/m^2-sec and m is the particle mass in grams.

The spacecraft from which direct measurements with microphone systems have been obtained in the United States are listed, together with the relevant data, in Table 1. Average particle speeds of
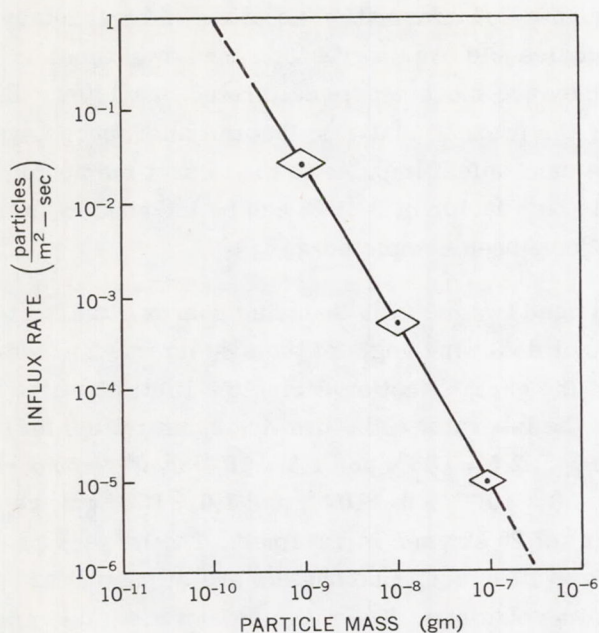
Figure 1—Cumulative mass distribution established by the microphone system on Explorer VIII. The largest symbol represents the data point of highest significance, and the diminished size of the symbols indicates lower significance

30 km/sec have been used for the omnidirectional sensors and for sensors mounted on spinning or tumbling vehicles which viewed most of the celestial sphere. An attempt has been made to apply correction factors for shielding by the earth and lack of omnidirectionality of the sensors. All data were converted to omnidirectional influx rates.

Reading of the telemetered data from Vanguard III (1959 η) has now been completed and is in the final stages of analysis. More than 6000 impacts were recorded during the 80-day lifetime of the experiment. Of this number, approximately 2800 impacts occurred in a 70-hour interval on November 16 to 18, which coincides in time with the expected annual return of the Leonid meteor shower. An average influx rate has been computed from the Vanguard III data on the basis of approximately 3500 impacts. A factor of 1.5 was used to correct for shielding by the earth.

Table 1

Direct Measurements Obtained with Microphone Systems on United States Satellites and Space Probes.

Spacecraft	Momentum Sensitivity (dyne-sec)	Mass Sensitivity (gm)	Effective Area (m²)	Exposure Time (sec)	Exposure (m²-sec)	Number of Particles	Cumulative Influx Rate $\left(\frac{particles}{m^2\text{-}sec}\right)$	
							Observed	Corrected
Explorer VIII	$2.5 \times 10^{-3} - 2.5 \times 10^{-2}$	$1.0 \times 10^{-9} - 1.0 \times 10^{-8}$	7.0×10^{-2}	3.5×10^{6}	2.4×10^{5}	~3650	1.5×10^{-2}	3.0×10^{-2}
	$2.5 \times 10^{-2} - 2.5 \times 10^{-1}$	$1.0 \times 10^{-8} - 1.0 \times 10^{-7}$				~75	3.1×10^{-4}	6.2×10^{-4}
	$>2.5 \times 10^{-1}$	$>1.0 \times 10^{-7}$				1 or 2	~5.0×10^{-6}	~1.0×10^{-5}
Vanguard III	$>1.0 \times 10^{-2}$	$>3.3 \times 10^{-9}$	4.0×10^{-1}	6.9×10^{6}	2.8×10^{6}	~3500	1.3×10^{-3}	2.0×10^{-3}
Explorer I	$>2.5 \times 10^{-3}$	$>8.3 \times 10^{-10}$	2.3×10^{-1}	7.9×10^{4}	1.8×10^{4}	145	8.4×10^{-3}	1.7×10^{-2}
Pioneer I	$>1.5 \times 10^{-4}$	$>5.0 \times 10^{-11}$	3.9×10^{-2}	1.1×10^{5}	4.2×10^{3}	17	4.0×10^{-3}	1.6×10^{-2}
Ranger I	$>3.0 \times 10^{-5}$	$>1.0 \times 10^{-11}$	8.0×10^{-4}	1.1×10^{4}	8.8	64	7.3	4.0×10
Midas II	$>3 \times 10^{-4}$	$>1 \times 10^{-10}$	6.9×10^{-2}	4.0×10^{3}	2.7×10^{2}	67	2.5×10^{-1}	5.0×10^{-1}
Samos II	$\gtrsim 3 \times 10^{-4}$	$\gtrsim 1 \times 10^{-10}$	6.9×10^{-2}	?	?	?	3.4×10^{-1}	6.8×10^{-1}
SLV-1	$\gtrsim 9 \times 10^{-3}$	$\gtrsim 3 \times 10^{-9}$	8.0×10^{-1}	9.5×10^{2}	7.6×10^{2}	10	1.3×10^{-2}	2.6×10^{-2}

The data given for Explorer I and Pioneer I are those reported by Dubin (References 6 and 7). The total number of impacts (145) for Explorer I was used in computing an average influx rate even though more than half of the impacts probably represented an interplanetary dust particle event (References 8 and 9). The high influx rates during this event were nearly counterbalanced by an interval of low rates, so an influx rate computed from the total number of impacts serves very well in the

present analysis. A factor of 2 was used in correcting for shielding by the earth and in allowing for the fact that the sensor was not completely omnidirectional. The microphone system on Pioneer I registered 25 impacts, of which 17 are considered to represent impacting dust particles. No correction for shielding by the earth was made, because Pioneer I spent most of its time at large geocentric distances (2 to 19 earth radii). A factor of 4 was used in converting to an omnidirectional influx rate.

A preliminary readout of the data from the microphone and coated photomultiplier systems on Ranger I (1961 ϕ) has been reported by Alexander and Berg (Reference 10). In this system, the two sensors were capable of operating in coincidence as well as independently. The data for the microphone system alone are given in Table 1.

The results from the microphone system on Midas II (1960 ζ1) and preliminary results from a similar system on Samos II (1961 α1) have been reported by Soberman and Della Lucca (Reference 11). The data were obtained — as in the case of Explorer I — in real time as the satellite passed over telemetry stations.

The data from a microphone system on SLV-1 (a Vanguard satellite that failed to achieve orbit) have been reported by LaGow, Schaefer, and Schaffert (Reference 12). A data point which is of use in the present analysis can be obtained if the sensitivity of the system is computed on the basis of momentum rather than energy. The bursts of counts observed were most likely produced when the expended third stage motor sputtered and bumped the separated payload (LaGow, private communication). Therefore, only 10 of the 17 impacts are used in computing an influx rate. The value of the mass sensitivity assumed for this system has been computed from calibration data which were given (Reference 12).

Some of the earliest direct measurements of quantitative value were obtained with microphone systems on a series of seven successful high altitude rockets instrumented and flown by Oklahoma State University, hereafter referred to as OSU (References 5, 13, and 14). The data from these rockets are summarized in Table 2. Average particle speeds have been assumed for each sensor of each rocket until the distribution of orbits of dust particles can be determined. Most of the sensors on the rockets were possibly exposed to a high speed component of dust particle influx; hence, higher particle speeds have been assumed for these sensors.

The direct measurements obtained with microphone systems on rockets, satellites, and spacecraft of the Soviet Union have been reported by Nazarova (References 15 and 16) and are summarized in Table 3. Some of the quantities in Table 3 have been computed on the basis of information given by Nazarova in order that data from space vehicles of both the United States and the Soviet Union can be included in the same analysis.

The sensitivities for the microphone systems on the Soviet spacecraft were expressed by Nazarova in terms of particle mass. The microphone system was assumed to be energy sensitive, and an average particle speed of 40 km/sec was assumed by her in converting to particle mass. An average particle speed of 40 km/sec was used in an early analysis by McCracken (Reference 13), but this value is now regarded as being too high. A value of 30 km/sec seems more reasonable and will be used until information on the velocity distribution of the dust particles has been obtained. The

Table 2
Direct Measurements Obtained with Microphone Systems on the OSU Rockets.

Rocket	Momentum Sensitivity (dyne-sec)	Particle Speed (km/sec)	Mass Sensitivity (gm)	Number of Impacts	Exposure h > 110 km. (m²-sec)	Cumulative Influx Rate $\left(\dfrac{particles}{m^2\text{-}sec}\right)$
Aerobee No. 80	$>6.0 \times 10^{-4}$	70	$>8.6 \times 10^{-11}$	49	5.0	9.8
	$>3.0 \times 10^{-3}$	70	$>4.3 \times 10^{-10}$	10	5.0	2.0
	$>1.0 \times 10^{-3}$	40	$>2.5 \times 10^{-10}$	3	50	6.0×10^{-2}
	$>3.0 \times 10^{-3}$	40	$>7.5 \times 10^{-10}$	1	50	2.0×10^{-2}
Aerobee No. 88	$>1.3 \times 10^{-4}$	20	$>6.5 \times 10^{-11}$	6	3.0	2.0
	$>2.0 \times 10^{-3}$	20	$>1.0 \times 10^{-9}$	1	3.0	3.3×10^{-1}
	$>4.7 \times 10^{-4}$	35	$>1.3 \times 10^{-10}$	17	30	5.7×10^{-1}
	$>1.0 \times 10^{-3}$	35	$>2.9 \times 10^{-10}$	7	30	2.3×10^{-1}
Nike-Cajun AF-2	$>6.0 \times 10^{-4}$	40	$>1.5 \times 10^{-10}$	45	31	1.5
	$>1.2 \times 10^{-3}$		$>3.0 \times 10^{-10}$	15		4.8×10^{-1}
	$>4.0 \times 10^{-3}$		$>1.0 \times 10^{-9}$	3		9.7×10^{-2}
Nike-Cajun AA6.203	$>3.0 \times 10^{-4}$	35	$>8.6 \times 10^{-11}$	55	37	1.5
	$>3.0 \times 10^{-3}$		$>8.6 \times 10^{-10}$	3		8.1×10^{-2}
Nike-Cajun AA6.204	$>7.0 \times 10^{-4}$	40	$>1.8 \times 10^{-10}$	32	33	9.7×10^{-1}
	$>3.0 \times 10^{-3}$		$>7.5 \times 10^{-10}$	1		3.0×10^{-2}
Nike-Cajun AA6.206	$>1.5 \times 10^{-4}$	35	$>4.3 \times 10^{-11}$	12	24	5.0×10^{-1}
	$>1.0 \times 10^{-3}$		$>2.9 \times 10^{-10}$	1		4.2×10^{-2}
	$>7.0 \times 10^{-4}$		$>2.0 \times 10^{-10}$	6		2.5×10^{-1}
Spaerobee 10.01	$>5.0 \times 10^{-4}$	60	$>8.3 \times 10^{-11}$	20	8.1	2.5

Table 3
Direct Measurements Obtained with Microphone Systems on the Soviet Union Rockets, Satellites, and Space Probes.

Vehicle	Mass Sensitivity (gm)		Effective Area (m²)	Exposure Time (sec)	Exposure (m²-sec)	Number of Particles	Influx Rate $\left(\dfrac{particles}{m^2\text{-}sec}\right)$	
	v = 40 km/sec	v = 30 km/sec					(Nazarova)	Cumulative
Sputnik III	$8.0 \times 10^{-9} - 2.7 \times 10^{-8}$	$1.4 \times 10^{-8} - 4.8 \times 10^{-8}$	0.34	$\sim 8 \times 10^5$	3×10^5	?	(see text)	$<1 \times 10^{-4}$
	$2.7 \times 10^{-8} - 1.5 \times 10^{-7}$	$4.8 \times 10^{-8} - 2.7 \times 10^{-7}$						
	$1.5 \times 10^{-7} - 5.6 \times 10^{-6}$	$2.7 \times 10^{-7} - 1.0 \times 10^{-5}$						
	$>5.6 \times 10^{-6}$	$>1.0 \times 10^{-5}$						
Lunik I	$2.5 \times 10^{-9} - 1.5 \times 10^{-8}$	$4.4 \times 10^{-9} - 2.7 \times 10^{-8}$	0.2	3.6×10^4	7.2×10^3	<16	$<2 \times 10^{-3}$	$<2.9 \times 10^{-3}$
	$1.5 \times 10^{-8} - 2.0 \times 10^{-7}$	$2.7 \times 10^{-8} - 3.6 \times 10^{-7}$				< 4	$<5 \times 10^{-4}$	$<7.0 \times 10^{-4}$
	$>2.0 \times 10^{-7}$	$>3.6 \times 10^{-7}$				< 1	$<1 \times 10^{-4}$	$<1.4 \times 10^{-4}$
Lunik II	$2.0 \times 10^{-9} - 6.0 \times 10^{-9}$	$3.6 \times 10^{-9} - 1.1 \times 10^{-8}$	0.2	1.1×10^5	2.2×10^4	0	$<5 \times 10^{-5}$	
	$6.0 \times 10^{-9} - 1.5 \times 10^{-8}$	$1.1 \times 10^{-8} - 2.7 \times 10^{-8}$				0	$<5 \times 10^{-5}$	
	$>1.5 \times 10^{-8}$	$>2.7 \times 10^{-8}$				2	9×10^{-5}	9.1×10^{-5}
Interplanetary Station	$1.0 \times 10^{-9} - 3.0 \times 10^{-9}$	$1.8 \times 10^{-9} - 5.3 \times 10^{-9}$	0.1	2.3×10^4	2.3×10^3	1	4×10^{-4}	3.0×10^{-3}
	$3.0 \times 10^{-9} - 8.0 \times 10^{-9}$	$5.3 \times 10^{-9} - 1.4 \times 10^{-8}$				5	2×10^{-3}	2.6×10^{-3}
	$>8.0 \times 10^{-9}$	$>1.4 \times 10^{-8}$				1	4×10^{-4}	4.3×10^{-4}
Geophysical Rocket I	—	$\geq 2.5 \times 10^{-9}$	4	1.3×10^2	5.4×10^2	?	6×10^{-2}	6×10^{-2}
Geophysical Rocket II	—	$\geq 2.5 \times 10^{-9}$	4	1.5×10^2	5.9×10^2	?	5×10^{-2}	5×10^{-2}
Geophysical Rocket III	—	$\geq 2.5 \times 10^{-9}$	4	8.5×10	3.4×10^2	?	7.5×10^{-1}	7.5×10^{-1}

mass sensitivities for the microphone systems on the Soviet spacecraft are therefore reduced by the square of 40/30 to compensate for the difference in the assumed particle speeds. The average particle speed assumed in computing the mass sensitivities of the microphone systems on the Soviet geophysical rockets was 15 km/sec, so the mass sensitivities given by Nazarova are increased by a factor of 4 when converting to 30 km/sec.

The influx rates measured by Sputnik III (1958 δ2) underwent tremendous changes during the first three days of operation of the equipment. The influx rates, as reported by Nazarova (References 15 and 17), were 4 to 11 particles/m²-sec on May 15 (day of launch), 5×10^{-4} particles/m²-sec on May 16 and 17, and less than 10^{-4} particles/m²-sec during the interval May 18 to 26. Nazarova attributes the high influx rates during the first few days to a meteoroid shower, but her conclusion is open to question. In any case, only the influx rate given for the last nine days of operation can be used in establishing an average mass distribution curve. It is not clear whether or not Nazarova corrected the influx rate from Sputnik III for shielding by the earth, so the influx rate is left in Table 3 as it was given.

The method of encoding information into the telemetered signal on Lunik I was such that only very crude upper limits to the influx rates can be specified. Only that influx rate measured by the scale of highest sensitivity is of any value in the present analysis. Lunik I (1959 μ), Lunik II (1959 ξ), and Lunik III (Interplanetary Station, 1959 θ) operated at large geocentric distances, obviating corrections for shielding by the earth. No attempt has been made to correct the influx rates from the three geophysical rockets to omnidirectional values, because the orientations of the rockets and solid viewing angles of the sensors have not been reported.

DIRECT MEASUREMENTS FROM PHOTOMULTIPLIER AND ROCKET COLLECTION SYSTEMS

Experiments for measuring the kinetic energy of micron-size dust particles were flown on three rockets (References 9, 18, and 19) and two satellites (References 9 and 10). The sensors measured the intensity of the visible light emitted in each impact of a dust particle with a speed greater than 5 km/sec. Light emitted from impacts of microparticles with speeds between 4 and 11 km/sec has been observed in laboratory experiments (Reference 19). Measurements of the intensity and duration of the light flash provide a means for determining the kinetic energy of an impacting particle. Results of the laboratory studies indicate that the light flash sensor detected particles with masses greater than 10^{-13} gm.

The configuration of the sensors in each of the five experiments was different, but the principle of light flash detection was the same. The basic detector unit was a photomultiplier tube. The surfaces exposed to impacts in the experiments were Lucite (References 18 and 19) and glass (References 9 and 10). A few thousand angstroms of aluminum were evaporated on the impact surfaces to shield the photocathodes from background light. When a dust particle penetrated the aluminum during an impact, light from the impact flash could reach the photocathodes. The rocket experiments exposed larger impact areas than did the satellite experiments to compensate for the shorter exposure times

of the rocket flights. The impact surface for each of the two satellite detectors was the face of an end-on type photomultiplier tube. An intensive effort was made to make the sensors insensitive to Cerenkov radiation and to energetic particles.

The results of the measurements with the light flash detector are given in Table 4. The cone of vision of the detector, the exposure, and the total number of impacts are given for each experiment.

Table 4

Direct Measurements from Photomultiplier Systems on
United States Rockets and Satellites.

Vehicle	Half-Angle of Detector Cone of Vision (degrees)	Exposure (m²-sec)	Number of Particles	Influx Rate $\left(\dfrac{particles}{m^2\text{-sec}}\right)$	Omnidirectional Influx Rate $\left(\dfrac{particles}{m^2\text{-sec}}\right)$
Aerobee NRL-25	80	0.63	101	160	390
Jupiter AM-28	80	2.2	4	1.63	4
Explorer VIII (preliminary)	60	4.3	110	25	200
Ranger I (preliminary)	75	8.5	179	21	114

An impact rate is computed and then normalized to 4π steradians. (These computations also include correction factors for earth shielding.)

Aerobee NRL-25, launched at 0200 local time, exposed the light flash detector to the high-speed component of the dust particle influx; and Jupiter AM-28, at 1900 local time, to the low speed component. The results may be normalized to 30 km/sec for purposes of comparison if the average particle speeds are taken as 45 and 12 km/sec, respectively. Since the detector sensitivity is a function of the square of the particle speed, the omnidirectional influx rates for the Aerobee and Jupiter — respectively 390 and 4 particles/m²-sec (Table 4) — become 173 and 25 particles/m²-sec (assuming a linear relation between influx rate and mass sensitivity).

The Skylark rocket flown by Lovering (Reference 20) carried a light flash experiment very similar to that on Aerobee NRL-25. No events were observed, but because of the following circumstances, there is a possibility that the experiment did not survive launch. The sensor was a 1P21 photomultiplier, and the rocket was a Skylark, which has a solid propellant motor. The system was subjected to a 70-g acceleration test in a centrifuge. A meaningful environmental qualification test should have also included severe shock and vibration tests, since the 1P21 is not ruggedized. An inflight sensor calibration with a light source would have verified the launch survival of the detector. The Jupiter AM-28 experiment and both satellite experiments contained this feature in the instrumentation.

The measurements from the satellites are corrected for earth shielding and normalized to 4π steradians. The data from the Explorer VIII and Ranger I experiments are restricted to satellite

46

nighttime measurements in order to eliminate any extraneous counts caused by sunlight. The average omnidirectional influx rates for these measurements are 200 and 114 particles/m^2-sec, respectively, for particles with masses of 10^{-13} gm and greater.

Another estimate of the influx rates for dust particles somewhat smaller than those covered by the direct measurements obtained with microphone systems has been reported by Soberman, Hemenway, et al., (Reference 21). A recoverable high-altitude rocket was used in obtaining a very interesting collection of particles at altitudes greater than 88 km. An influx rate of 300 particles/m^2-sec was estimated for particles with diameters equal to or greater than 3 μ. The cumulative influx rate (plotted as a function of particle diameter) has a negative slope of 1.3 and applies to particles with diameters as small as 0.2 μ. If a mass density of 3 gm/cm^3 is used (Reference 21), the influx rates estimated from this collection may be compared to those obtained from the other direct measurements. No shielding corrections are introduced, since the collectors faced in the general direction of the apex of the earth's motion.

CUMULATIVE MASS DISTRIBUTION CURVE FROM DIRECT MEASUREMENTS

The direct measurements obtained with the microphone, photomultiplier, and rocket collection systems are plotted as a cumulative mass distribution curve in Figure 2. Two characteristics of the data used in establishing the curve should be emphasized. First, the influx rates are expressed as omnidirectional values, and secondly, the curve is the result of a series of experiments in the vicinity of the earth. How well the curve applies to other regions of space is not presently known.

All of the microphone data for the mass range of 10^{-10} to 10^{-7} gm are compared in Figure 2 with the Explorer VIII results (presented in Figure 1). A study of the data points in Figure 2 demonstrates the degree of consistency with which the average influx rates derived from all microphone measurements fit the curve.

The photomultiplier results allow an extension, to approximately 10^{-13} gm, of the distribution curve obtained with microphone systems. The reported influx rates from the rocket collection experiment (Reference 21) are somewhat
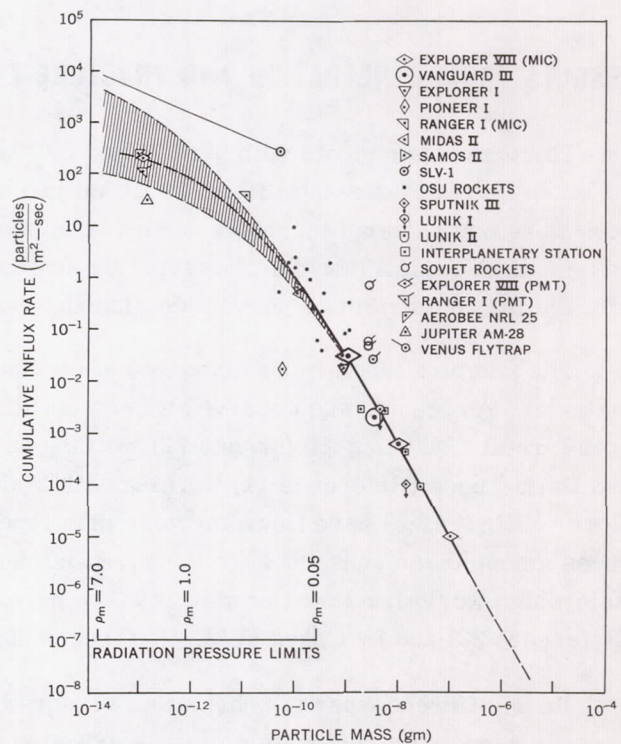
Figure 2—An average cumulative mass distribution curve for the vicinity of earth derived from all the available direct measurements obtained with microphone and photomultiplier systems. The influx rates are omnidirectional values. A dust particle of mass density ρ_m is expelled from the solar system by radiation pressure if its mass is less than that shown on the lower abscissa opposite the particular value of ρ_m

higher than the photomultiplier detector results. The 80 to 150 km altitude range of the collection experiment probably contains an abundance of decelerated microparticles; hence, this is a possible explanation for the high influx rate of microparticles reported from the collection results.

The radiation pressure limits, in terms of particle mass density ρ_m, are also shown in Figure 2 and subsequent figures above the particle mass abscissa. Each value of ρ_m determines a "cutoff" radius; all dust particles of this radius having masses smaller than that read below on the abscissa will be swept out of the solar system by radiation pressure. (The above statements are true only to the extent to which geometrical optics may be used in place of the more complex Mie theory of light scattering. The differences are not important in the present analysis.)

The cumulative mass distribution curve is not a constant mass-to-magnitude curve, and the slope appears to change rapidly with decreasing particle size. On a cumulative mass distribution curve, the slope should approach zero as the radiation pressure limits are reached. The results for particles with masses between 10^{-13} and 10^{-10} gm represent initial measurements which are inherently more uncertain than the microphone data. As the number of measurements increase for this range of particle size, the mechanisms controlling the distributions of these dust particles will be better understood.

RESULTS FROM PENETRATION AND FRACTURE EXPERIMENTS

Thirteen experiments with penetration or fracture types of dust particle sensors have been flown on seven United States satellites. In all but two cases, the numbers of events detected by these sensors were one or zero; therefore, a measured average influx rate for dust particles cannot be determined. A comparison can, however, be made between the results of these experiments and the average mass distribution curve established by measurements with microphone systems.

The fracture type sensor consisted of continuous wire wrapped around an insulating support material. An impact was observed when a colliding dust particle fractured the wire and caused an open circuit. Manring (Reference 22) working with Explorer I and Explorer III (1958 γ), Soberman and Della Lucca (Reference 11) working with Midas II and Samos II, and Secretan working with Explorer XIII (1961 χ) have flown the wire grid type sensor on these five satellites. The major differences among these sensors were the wire size and the total exposed area. The mass of the dust particle which would fracture the wire is taken here as being comparable to that reported by Manring (Reference 22) and by Cohen et al. (Reference 23).

Four different types of penetration sensors have been flown on three satellites. Three of the sensors required a perforation of the exposed surface, and one sensor required a crater with a diameter sufficient to destroy the sensing element. LaGow and Secretan (References 24 and 25) developed three of these sensors for Vanguard III.

The first type of sensor consisted of a chromium strip 300 μ wide and 1 to 3 μ thick, evaporated onto Pyrex glass. The resistance of the strip was monitored, and a complete break of the chromium was required to register an impact. The threshold sensitivity in terms of particle mass was

determined by computing the diameter of the crater necessary to produce an open circuit. The second type of sensor consisted of two hermetically sealed and pressurized zones of which the exposed surface was 0.162 m² of the 26-mil thick magnesium skin of the satellite. A transducer constantly monitored the differential pressure between the two zones, so that a puncture of either or both could be detected. The third sensor consisted of a CdS cell covered by a 1/4-mil Mylar film which was made opaque by evaporating aluminum onto both sides of the film. As penetrations occurred, the admitted sunlight changed the resistance of the CdS cell permitting measurement of the effective hole size. More than one penetration could have been observed with this sensor. This experiment was also flown on Explorer VII (1959 ι).

Davison (References 26 and 27) has flown the fourth type of penetration experiment on Explorer XIII. A plate of stainless steel was mounted in front of a foil gage consisting of a continuous strip of gold deposited on silicone rubber. The foil gage was separated from the metallic plate by a mylar insulator. Two thicknesses of stainless steel (75 and 150μ) were used in two separate sensors. A particle sufficiently large to penetrate the metal plate and fracture the gold foil would have led to an open circuit and detection of an impact.

Using 1/4-mil mylar film and micron-size particles with speeds as high as 11 km/sec, Friichtenicht (Reference 20) has found that the diameter of the hole is 1.5 ± 0.5 times the diameter of the impacting particle for speeds greater than 3.5 km/sec. Secretan and Berg (unreported results), using the same accelerator, have found no marked deviation from the above results. These results are the basis for the sensitivity used in the interpretation of the mylar-film CdS experiment. The other three penetration sensors (magnesium and stainless steel) required a perforation or a crater. An extensive series of penetration experiments has been performed by Summers, et al. (References 28 and 29). The penetration equation developed empirically in these studies was used to compute the threshold mass sensitivity for the three sensors.

The pertinent information concerning the penetration and fracture experiments is summarized in Table 5. The exposure (area-time product) includes a consideration of earth shielding, except for the two measurements by Soberman and Della Lucca (Reference 11). The influx rates for Explorer III and Samos II were computed from the numbers of impacts and the corresponding exposures. One event was observed on Explorer VII, but no events were observed in the ten remaining experiments. An average influx rate can be predicted for these latter experiments by computing the influx rate necessary for a probability of 0.99 for at least one impact. This is done in the following manner: an omnidirectional distribution of particles was assumed and the equation given below (based on Poisson statistics) was used to find the average influx rate:

$$P_1 = 1 - e^{-atr},$$

where

P_1 = 0.99 = probability of at least one impact,

at = exposure (m²-sec),

r = average influx rate (particles/m²-sec).

INFLUX RATE $\left(\dfrac{\text{particles}}{\text{m}^2 - \text{sec}}\right)$

PARTICLE MASS (gm)

VANGUARD III (1, 2, 3, 4)
EXPLORER VII (5)
EXPLORER XIII (6, 7, 8, 9)
EXPLORER I (10)
EXPLORER III (11)
MIDAS II (12)
SAMOS II (13)
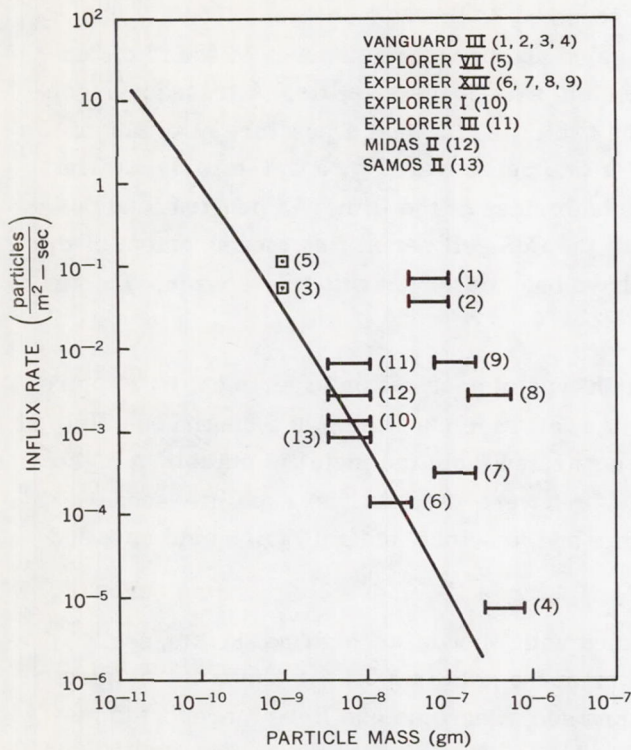
Figure 3—Average influx rates computed (on the basis of a probability of 0.99 of at least one impact) from penetration and fracture experiments and compared with those given by the cumulative mass distribution curve. The numbers following the names of the vehicles identify the data points with the data given in Table 5

The results derived from these experiments are compared in Figure 3 with the average mass distribution curve established by measurements from microphone systems.

The indicated uncertainties represent a consideration of the major variations known at present concerning the parameters (particle speed and mass density) involved in hyper-velocity impacts. The data show that some of the experiments had insufficient exposure to yield significant information. Within the uncertainties shown, the measurements do support the average mass distribution curve, especially within the mass range of 10^{-8} to 10^{-6} gm. The curve shown in Figure 3 predicts the wire grid fractures which occurred on Explorer III (Reference 22) and Samos II (Reference 11) and the survival (without puncture) of the penetration experiments on Vanguard III (Reference 24) and Explorer XIII (Reference 26).

The analysis of all of the direct measurements has shown no significant departures from the average mass distribution curve derived

Table 5

Direct Measurements from Penetration and Fracture Experiments on United States Satellites.

Satellite	Type of Dust Particle Sensor	Critical Dimension for Penetration or Fracture	Range of Threshold Particle Mass (gm)	Exposure (Corrected) (m²-sec)	Number of Particles	Predicted Influx Rate $P_1 = 0.99$ $\left(\dfrac{\text{particles}}{\text{m}^2\text{-sec}}\right)$	Data Point Shown in Figure 3
Vanguard III	Pyrex-Chromium Strip	300μ	$4.0 \times 10^{-8} - 1.2 \times 10^{-7}$	7.0×10^1	0	6.2×10^{-2}	1
	Pyrex-Chromium Strip	300μ	$4.0 \times 10^{-8} - 1.2 \times 10^{-7}$	1.4×10^2	0	3.3×10^{-2}	2
	Mylar-CdS Cell	1/4 mil	1.2×10^{-9}	8.7×10^1	0	5.3×10^{-2}	3
	Magnesium Pressure Zones	26 mil	$3.0 \times 10^{-7} - 9.0 \times 10^{-7}$	7.2×10^5	0	6.4×10^{-6}	4
Explorer VII	Mylar - CdS Cell	1/4 mil	1.2×10^{-9}	3.9×10^1	1	1.2×10^{-1}	5
Explorer XIII	Stainless Steel-Gold Foil	75μ	$1.1 \times 10^{-8} - 3.3 \times 10^{-8}$	3.4×10^4	0	1.4×10^{-4}	6
	Stainless Steel-Gold Foil	150μ	$8.8 \times 10^{-8} - 2.6 \times 10^{-7}$	8.5×10^3	0	5.6×10^{-4}	7
	Wire Grids	75μ	$2.0 \times 10^{-7} - 6.0 \times 10^{-7}$	1.7×10^3	0	2.7×10^{-3}	8
	Wire Grids	50μ	$6.7 \times 10^{-8} - 1.8 \times 10^{-7}$	7.7×10^2	0	6.0×10^{-3}	9
Explorer I	Wire Grids	17μ	$4.2 \times 10^{-9} - 1.2 \times 10^{-8}$	3.6×10^3	0	1.3×10^{-3}	10
Explorer III	Wire Grids	17μ	$4.2 \times 10^{-9} - 1.2 \times 10^{-8}$	2.4×10^2	2	6.4×10^{-3}	11
Midas II	Wire Grids	20μ	$4.2 \times 10^{-9} - 1.5 \times 10^{-8}$	$2.0 \times 10^3 *$	0	2.3×10^{-3}	12
Samos II	Wire Grids	20μ	$4.2 \times 10^{-9} - 1.5 \times 10^{-8}$	$1.1 \times 10^4 *$	8	8.0×10^{-4}	13

*Not corrected for earth shielding.

from the microphone experiment on Explorer VIII. Now that it has been demonstrated that the direct measurements are quite self-consistent, comparisons of the direct measurements with results obtained by other observational techniques can be attempted. Information deserving special attention in such a comparison comes from the observations of meteors, the zodiacal light, and the solar F corona.

COMPARISON OF DIRECT MEASUREMENTS WITH RESULTS FROM METEOR OBSERVATIONS

Extrapolating the results from meteor observations toward smaller particles represented a major method of estimating influx rates for dust particles before the advent of the direct measurements technique. The tabulation by Watson (Reference 30) of influx rates of meteors followed the constant-mass-per-magnitude relationship, rendering the extrapolation to smaller particles relatively easy. Such extrapolations have been made in the past, the most commonly used ones being those of Grimminger (Reference 31) and Whipple (Reference 32).

Even the earliest of the rockets in the OSU series (Reference 13) gave influx rates several orders of magnitude higher than those expected on the basis of the extrapolations of meteor data. Meanwhile, an observation of coasting in the train of a double station photographic meteor led to the hypothesis of a very low value of mass density ($\rho_m = 0.05$ gm/cm^3) for meteoroids (Reference 33). Whipple (Reference 34)—using this low value of mass density together with the corresponding change in the mass-to-magnitude relationship, the influx rates reported by Millman and Burland (Reference 35), and an average speed of 28 km/sec for the meteoroids—proposed a constant-mass-per-magnitude extrapolation. This new distribution, showing much higher influx rates than are shown by the Watson distribution for particles of a given mass, did not agree with the early direct measurements.

The results of Millman and Burland (Reference 35) and of Hawkins and Upton (Reference 36) showed that the constant-mass-per-magnitude relationship was not valid, even for meteoroids. If the distribution curve given by Hawkins and Upton had been extrapolated into the direct measurements range of particle mass, it would have shown some degree of compatibility with the early results from the OSU rockets. Such an extrapolation was not in agreement with the direct measurements from the early satellites (References 37 and 38).

On the basis of this early evidence of disagreement between the direct measurements and the extrapolated meteor results, McCracken (together with Alexander) first suggested that a constant-mass-per-magnitude law did not apply in the direct measurements range of particle mass (Reference 13). The direct measurements then available were not sufficient to confirm this hypothesis, nor did sufficient data become available until measurements were obtained with Explorer VIII. Actually, two interpretations of the direct measurements were possible at the time the suggestion was first made. They were: (1) the mass distribution curve obtained from the direct measurements departed significantly from those obtained by extrapolating results from meteor observations, or (2) the direct measurements were indicating the presence of a geocentric concentration of dust particles. Although the first interpretation seemed to be in better agreement with the early data, quantitative arguments for its validity were not possible until the data sample was obtained with the microphone system on Explorer VIII.

VISUAL MAGNITUDE
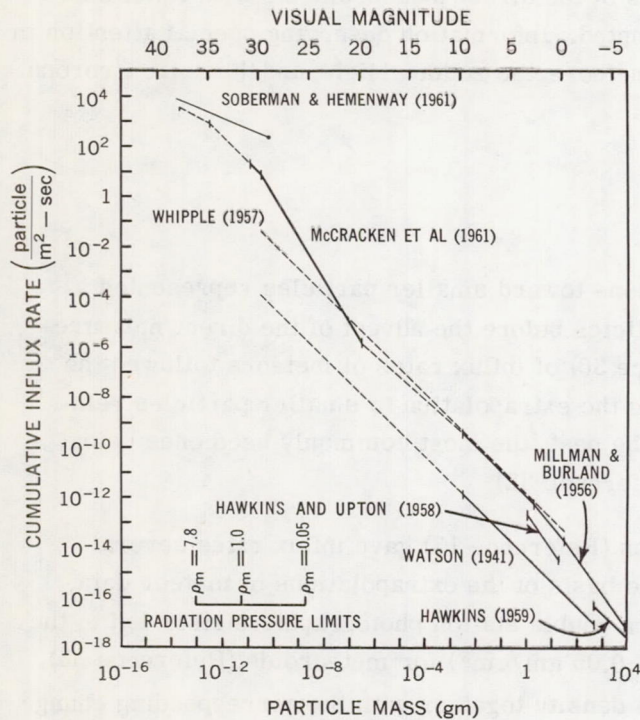
Figure 4—Segmented cumulative mass distribution curve for omnidirectional influx rates of dust particles and meteoroids. The portions of the curve derived from the direct measurements of dust particles are known only to be valid for average conditions in the vicinity of the earth. The equations for the curve labeled "Millman and Burland" were given by McKinley (Reference 39).

A segmented approximation to the cumulative mass distribution curve (Figure 2) is shown, together with several model distributions and observational results from the meteor studies, in Figure 4. The cumulative influx rates obtained by the various observational methods are plotted as a function of particle mass or visual magnitude, with the approximate radiation pressure limits for selected values of mass density being given as an auxiliary abscissa.

Visual magnitude has been introduced as an abscissa because the results from meteor observations can be placed on a mass distribution curve only within the limits set by the uncertainty (≈ 200) in the mass-to-magnitude relationship. Visual magnitude is related to particle mass in Figure 4 by assuming that the luminosity of meteors with a given speed depends linearly on the mass of the meteoroid and that a meteoroid with a mass of 25 gm and a speed of 28 km/sec will produce a meteor of zero visual magnitude (Reference 34). Use of a mass density greater than the value of 0.05 gm/cm³ used by Whipple (Reference 34) shifts the influx rate for meteoroids of a given mass toward a lower value.

The distribution curves for meteors given by Whipple (Reference 34), McKinley (Reference 39), and Hawkins and Upton (Reference 36) are plotted in Figure 4 as functions of visual magnitude; a mass distribution given by Hawkins (Reference 40) for asteroids and fireballs is also included. The distribution given by Watson (Reference 30) is plotted in terms of particle mass. This is done so that the difference between the Watson and Whipple distributions can be used to illustrate the uncertainty in the influx rate of meteoroids of a given mass resulting from the poorly known mass-to-magnitude relationship for meteors. The direct measurements are not affected by this uncertainty. The uncertainties encountered in placing the direct measurements on a cumulative mass distribution curve are about two orders of magnitude smaller than those for meteoroids.

As Figure 4 shows, the mass distribution curve obtained from the direct measurements departs markedly from those obtained by extrapolating results from meteor observations. It is evident that the constant-mass-per-magnitude relation does not hold for dust particles in the vicinity of the earth. There is, in fact, little evidence that the relation holds for more than a few magnitudes within any range of particle mass, except possibly for fireballs and asteroids (Reference 40). Thus, there is no particular reason for trying to force the direct measurements to fit a constant-mass-per-magnitude curve.

The mass distribution of small dust particles was not known before the data were obtained with Explorer VIII. Several analyses (using best guesses, such as a constant-mass-per-magnitude relation) for the distribution curve in the direct measurements range of particle mass led to the conclusion that the direct measurements confirmed the existence of a geocentric concentration of dust particles. The results from Explorer VIII and the good agreement of all the other direct measurements with the Explorer VIII data show that these analyses are incorrect, because the measured mass distribution curve differs significantly from those assumed in the various analyses.

Some of the more subtle points shown in Figure 4 can be illustrated more clearly by deriving from the incremental mass distribution the mass influx curve shown in Figure 5. To remove the effects of using the segmented cumulative mass distribution (Figure 4) as a basis for deriving the incremental mass influx curve, the latter has been smoothed. It is given in terms of the accretion rate by the earth of dust particles or meteoroids in a given mass range as a function of particle mass or visual magnitude.

The most important conclusion which can be reached on the basis of the distribution curve shown in Figure 5 is that the earth's accretion of interplanetary material is dominated by the small dust particles. The integrated accretion rate amounts to about 1×10^4 tons per day.

It must be realized that in both Figure 4 and Figure 5, the distribution curves for particles with masses less than about 10^{-11} gm are more uncertain than the segments of the curves derived from microphone results. Dust particles with masses less than about 10^{-9} gm are subject to the
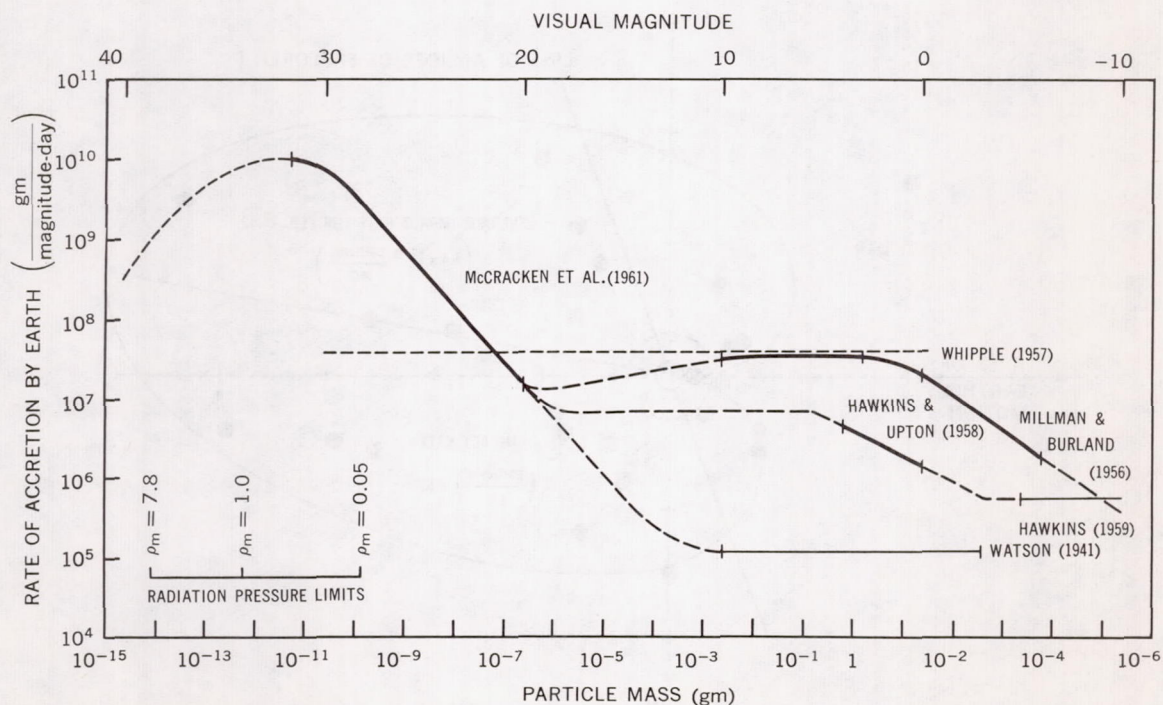

Figure 5—Incremental mass influx curve derived from the cumulative mass distribution curve for interplanetary material accreted by the earth

perturbative effects of radiation pressure. The shape of the distribution curves in the submicron range of particle size depends critically on the locations of the sources, on the distribution of orbits, and on the mass densities of the dust particles.

Gallagher and Eshleman (Reference 41) have found that the influx rates of faint radar meteors show large fluctuations with time. The observed grouping of radiants suggests that the faint radar meteors are members of "sporadic showers" rather than dispersed members of major meteor streams. Large fluctuations in the influx rate also seem to be the rule rather than the exception in the case of direct measurements. Dubin (References 7 and 8) has reported on the large fluctuations observed with Explorer I. Large fluctuations in the influx rate have also been reported for Vanguard III (References 42 and 43) and for Sputnik III (References 15 and 17), although there is still some question about the latter case. (The fluctuations in influx rate observed on Vanguard III and Explorer VIII are presently under analysis.) It appears, on the basis of both the direct measurements and the data for faint radar meteors, that the dust particles are not nearly so uniformly distributed as are the sporadic meteoroids.

The interplanetary dust particle event detected by Explorer I on February 2 and 3, (shown in Figure 6) may be evidence of a "sporadic shower" of small dust particles, since it bears no relation to a known meteor shower. The large increases in influx rate which occurred during the November 16 to 18 interplanetary dust particle event observed with Vanguard III are shown in Figure 7. The coincidence in time with the Leonids suggests that large numbers of small dust particles are being generated in the Leonid stream. The microphone system was almost omnidirectional, so it is not possible to establish the radiants of these dust particles. If they did belong to the Leonid stream,
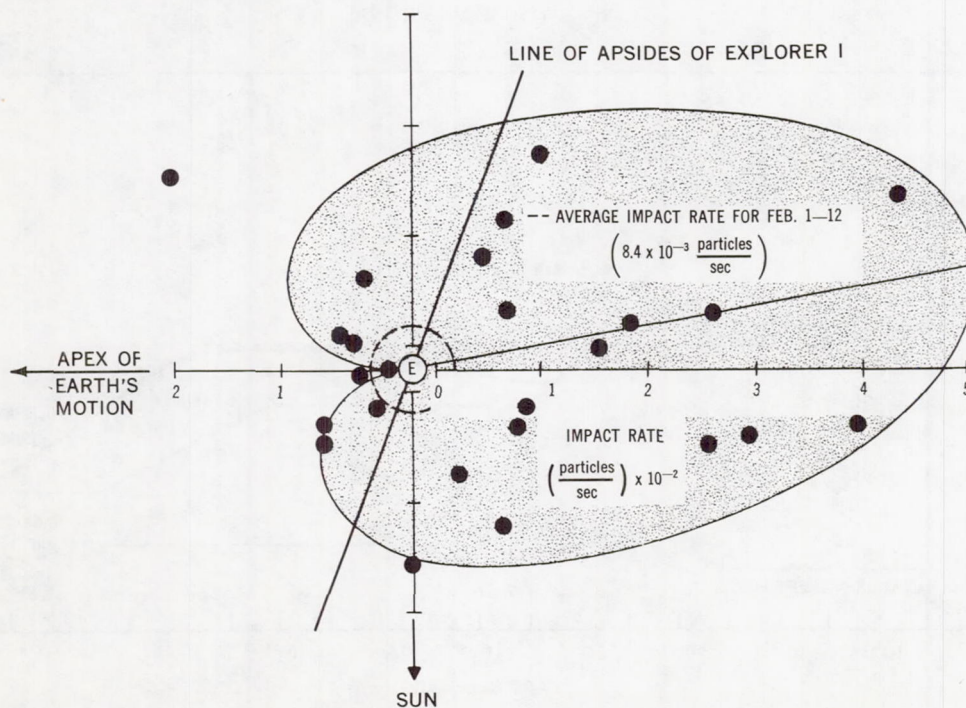

Figure 6—Impact rates during the February 1958 interplanetary dust particle event plotted as a function of the position of the satellite relative to the earth
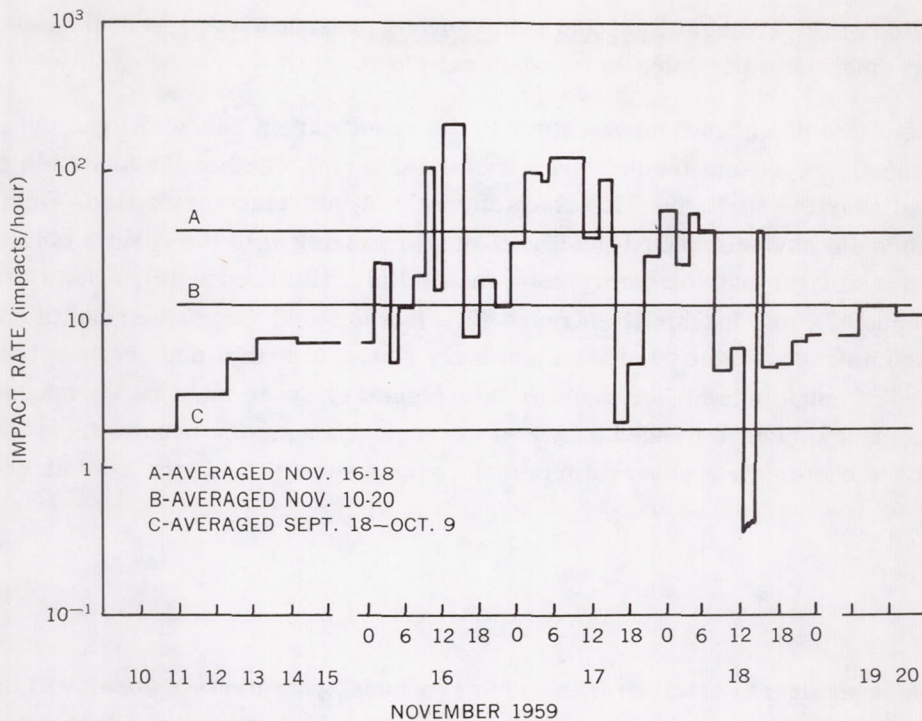
Figure 7—Impact rates during the November 1959 interplanetary dust particle event.
The impact rates during the three days of peak activity are shown on an expanded
time scale

the improbability of such dust particles remaining in the stream for one orbital period would require
that they were released from larger meteoroids as they approached perihelion passage.

Eshleman (Reference 44) has reported that the influx rates of the faint radar meteors seem to
increase rather than decrease as the limiting sensitivity of the equipment is approached. This may
be evidence that the distribution curve obtained from the direct measurements can be extrapolated to
join onto a distribution curve for meteoroids at about 15th visual magnitude (see Figure 4 or 5).

COMPARISON OF DIRECT MEASUREMENTS WITH RESULTS FROM ZODIACAL LIGHT AND SOLAR CORONA OBSERVATIONS

Photometric observations of the zodiacal light and the solar corona have yielded considerable
information about the material in the zodiacal cloud surrounding the sun. The results obtained by
analyzing the observations are generally expressed in terms of the spatial densities (and variations
in the spatial densities) of electrons and dust particles with distance from the sun. Incremental size
distributions for the dust particles are also obtained in such analyses.

Direct measurements of the spatial density, mass distribution, and selected physical parameters
of interplanetary dust particles have not yet been obtained for regions of space removed from the
earth-moon system. The spatial densities and size distributions of dust particles inferred from

photometric studies of the zodiacal light and solar corona presently represent the only available information about small dust particles in the zodiacal cloud.

Comparisons of the direct measurements with the results from zodiacal light and solar corona observations presently represent the only means of determining whether the available direct measurements obtained near the earth are also characteristic of interplanetary space. Dubin and Mc-Cracken (Reference 45) have compared the direct measurements with the results obtained in investigations of the zodiacal light and solar corona by van de Hulst (Reference 46), Allen (Reference 47), Elsässer (Reference 48), and Ingham (Reference 49). It was found that if the results obtained by Ingham were taken as representative of interplanetary space, a spatial density near the earth at least three orders of magnitude higher than for interplanetary space must be introduced in order to remove the discrepancy. There is such a lack of agreement among the results from the various investigations of the photometric observations that comparisons of this kind are, at best, only qualitative.

CONCLUSIONS

The direct measurements obtained with the microphone system on Explorer VIII have provided a basis for analyzing all the available direct measurements of interplanetary dust particles. An average cumulative mass distribution curve, subject only to very minor uncertainties, has been established for dust particles in the vicintiy of the earth. This average distribution is valid, within an order of magnitude or less, for particles with masses between 10^{-13} and 10^{-6} gm. The irregular shape of the distribution curve precludes the possibility of writing its equation in a simple analytical form.

The mass distribution curve obtained from the direct measurements differs markedly from those expected on the basis of extrapolations of results from meteor observations. Consequently, the earth's accretion of interplanetary matter may be said to be dominated by dust particles with masses less than about 10^{-6} gm. A conservative estimate of the accretion rate is 10^4 tons per day.

The influx rates obtained from the direct measurements undergo large fluctuations and, in one case, show a correlation in time with the expected annual return of a major meteor shower. These fluctuations suggest that the dust particles are not predominantly in long-lived orbits about the earth.

Discrepancies as large as 10^4 are found when the direct measurements in the vicinity of the earth are compared with the spatial densities of dust particles in interplanetary space inferred from photometric studies of the zodiacal light and the solar corona. However, such comparisons are uncertain because of the large discrepancies among the photometric data.

The available direct measurements are not sufficient to define either an average geocentric speed or an average mass density. These measurements encompass a range of particle mass which extends well past the radiation pressure limit for particles in heliocentric orbits with mass densities of 0.05 gm/cm³. Mass densities of approximately 1 gm/cm³ seem more reasonable for the direct measurements range of particle size. In view of the uncertainties concerning the probable

origin (or origins) of the particles, the distribution of their orbits, and the mass densities of those of micron size, it does not seem wise to extrapolate results from the meteoroidal range of particle size to the smaller sizes of dust particles.

The various departures of the direct measurements from expectations based on other methods of observation shows the feasibility of using the direct measurements technique to study material in the zodiacal cloud. Appropriate direct measurements will serve to answer most of the questions left unanswered in this analysis, and will represent an important means of determining the predominant source of the dust particles observed in the vicinity of the earth.

REFERENCES

1. Anderson, G. D., Burkdoll, F. B., et al., "Experimental Techniques Developed for Impact Studies of Microparticles," in: *Proc. 3rd Sympos. on Hypervelocity Impact, Chicago, October 1958,* ed. by F. Genevese, Illinois Inst. Tech., Armour Res. Found., February 1959, Vol. 1, pp. 361-384

2. Stanyukovich, K. P., "Elements of the Theory of the Impact of Solid Bodies with High (Cosmic) Velocities," in: *Artificial Earth Satellites,* ed. by L. V. Kurnosova, New York: Plenum Press, 1961, Vol. 4, pp. 292-333

3. Lavrent'ev, M. A., "The Problem of Piercing at Cosmic Velocities," in: *Artificial Earth Satellites,* ed. by L. V. Kurnosova, New York: Plenum Press, 1961, Vol. 3, pp. 85-91

4. McCracken, C. W., Alexander, W. M., and Dubin, M., "Direct Measurement of Interplanetary Dust Particles in the Vicinity of Earth," NASA Technical Note D-1174, December 1961; also published in Nature, 192(4801):441-442, November 4, 1961

5. McCracken, C. W., and Alexander, W. M., "The Distribution of Small Interplanetary Dust Particles in the Vicinity of Earth," NASA Technical Note D-1349, July 1962; also published in *Proc. Internat. Sympos. on the Astronomy and Physics of Meteors,* Cambridge, Mass., August-September 1961 *Smithsonian Contrib. Astrophys.* (To be published)

6. Dubin, M., "IGY Micrometeorite Measurements," in: *Space Research: Proc. 1st Internat. Space Sci. Sympos., Nice, January 1960,* ed. by H. K. Bijl, Amsterdam: North-Holland Publ. Co., 1960, pp. 1042-1058

7. Dubin, M., "Meteoritic Dust Measured from Explorer I," *Planetary and Space Sci.* 2(2/3): 121-129, April 1960

8. Dubin, M., "Remarks on the Article by A. R. Hibbs, 'The Distribution of Micrometeorites near the Earth'," *J. Geophys. Res.* 66(8):2592-2594, August 1961

9. Dubin, M., Alexander, W. M., and Berg, O. E., "Cosmic Dust Showers by Direct Measurements," in: *Proc. Internat. Sympos. on the Astronomy and Physics of Meteors,* Cambridge, Mass., August-September 1961 *Smithsonian Contrib. Astrophys.* (To be published)

10. Alexander, W. M., and Berg, O. E., "Microparticle Hypervelocity Impacts from Ranger I," Paper presented at the 5th Hypervelocity Sympos., Colorado School of Mines, Golden, Colorado, November 1961 (To be published)

11. Soberman, R. K., and Della Lucca, L., "Micrometeorite Measurements from the Midas II Satellite (1960 ζ 1)," Air Force Cambridge Res. Labs., Geophys. Res. Directorate, GRD Res. Notes No. 72 (AFCRL 1053) November 1961

12. LaGow, H. E., Schaefer, D. H., and Schaffert, J. C., "Micrometeorite Impact Measurements on a 20 in. Diameter Sphere at 700 to 2500 km Altitude," in: *Annals of the International Geophysical Year,* London: Pergamon Press, 1961, Vol. 12, Part 2, pp. 465-472

13. McCracken, C. W., "An Analysis of Rocket and Earth Satellite Measurements of Micrometeoric Influx," M. S. Thesis, Oklahoma State Univ., 1959; Also Oklahoma State Univ., Res. Found., Final Rept. Contract AF 19(604)-1908, Appendix B, April 14, 1960

14. Buck, R. F., "Acoustic Detection of Meteoric Particles," Oklahoma State Univ., Res. Found., Final Rept. Contract AF 19(604)-1908, April 14, 1960

15. Nazarova, T. N., "The Results of Studies of Meteoric Dust by Means of Sputnik III and Space Rockets," in: *Space Research: Proc. 1st Internat. Space Sci. Sympos., Nice, January 1960,* ed. by H. K. Bijl, Amsterdam: North-Holland Publ. Co., 1960, pp. 1059-1062

16. Nazarova, T. N., "Rocket and Satellite Meteoric Dust Investigations," *Proc. 12th Internat. Astronautical Congress, Washington, 1961,* ed. by R. M. L. Baker, Jr. and M. W. Makemson, Vienna: Springer-Verlag, 1962 (In Press)

17. Nazarova, T. N., "Results of Exploring Meteoric Matter with Instrumentation of Sputnik III and Space Probes," in: *Proc. 11th Internat. Astronautical Congress, Stockholm, 1960,* ed. by C. W. P. Reuterswärd, Vienna: Springer-Verlag, 1961, Vol. 1, p. 625 (Abstract)

18. Berg, O. E., and Meredith, L. H., "Meteorite Impacts to Altitude of 103 Kilometers," *J. Geophys. Res.* 61(4):751-754, December 1956

19. Friichtenicht, J. E., "Experiments with a Two Million Volt Electrostatic Generator," Paper presented at the 5th Hypervelocity Sympos., Colorado School of Mines, Golden, Colorado, November 1961 (To be published)

20. Lovering, J. F., "Micrometeorite Impacts to an Altitude of 135 Km," *Planetary and Space Sci.* 2(1):75-77, October 1959

21. Soberman, R. K. (Ed.) "Micrometeorite Collection from a Recoverable Sounding Rocket," Air Force Cambridge Res. Labs., Geophys. Res. Directorate, GRD Res. Notes No. 71 (AFCRL 1049) November 1961

22. Manring, E. R., "Micrometeorite Measurements from 1958 Alpha and Gamma Satellites," *Planetary and Space Sci.* 1(1):27-31, January 1959

23. Cohen, H. A., Corman, A., and Dubin, M., "Calibration of Micrometeoritic Detectors Used in Satellites and Rockets," in: *Proc. 3rd Sympos. on Hypervelocity Impact, Chicago, October 1958,* ed. by F. Genevese, Illinois Inst. Tech., Armour Res. Found., February 1959, Vol. 1, pp. 405-424

24. LaGow, H. E., Secretan, L., and Giuliani, J., "Experiments for Satellite Environmental Measurements," in: *Annals of the International Geophysical Year,* London: Pergamon Press, 1958, Vol. 6, Parts 1-5, pp. 319-321

25. LaGow, H. E., and Secretan, L., "The Micrometeorite Penetration Experiment," in: *Juno II Summary Project Rept. Vol. 1. Explorer VII Satellite,* NASA Technical Note D-608, July 1961, pp. 263-272

26. Davison, E. H., and Winslow, P. C., Jr., "Direct Evaluation of Meteoroid Hazard," *Aerospace Eng.* 21(2):24-33, February 1962

27. Davison, E. H., and Winslow, P. C., Jr., "Space Debris Hazard Evaluation," NASA Technical Note D-1105, December 1961

28. Summers, J. L., "Investigation of High-Speed Impact: Regions of Impact and Impact at Oblique Angles," NASA Technical Note D-94, October 1959

29. Nysmith, C. R., and Summers, J. L., "Preliminary Investigation of Impact on Multiple-Sheet Structures and an Evaluation of the Meteoroid Hazard to Space Vehicles," NASA Technical Note D-1039, September 1961

30. Watson, F. G., "Between the Planets," Philadelphia: Blackiston, 1941 (Rev. Ed., Cambridge, Mass.: Harvard University Press, 1956)

31. Grimminger, G., "Probability That a Meteorite Will Hit or Penetrate a Body Situated in the Vicinity of Earth," *J. Appl. Phys.* 19(10):947-956, October 1948

32. Whipple, F. L., "Meteoritic Phenomena and Meteorites," in: *Physics and Medicine of the Upper Atmosphere,* ed. by C. S. White and O. O. Benson, Jr., Albuquerque: University of New Mexico, 1952, pp. 137-170

33. Whipple, F. L., "Some Problems of Meteor Astronomy," in: *Radio Astronomy,* ed. by H. C. van de Hulst, Cambridge: The University Press, 1957, pp. 375-389

34. Whipple, F. L., "The Meteoritic Risk to Space Vehicles," in: *Proc. 8th Internat. Astronautical Congress, Barcelona,* 1957, ed. by F. Hecht, Vienna: Springer-Verlag, 1958, pp. 418-428

35. Millman, P. M., and Burland, M. S., "The Magnitude Distribution of Visual Meteors," Paper presented at the 96th meeting of the American Astronomical Society, New York, December 1956

36. Hawkins, G. S., and Upton, E. K. L., "The Influx Rate of Meteors in the Earth's Atmosphere," *Astrophys. J.* 128(3):727-735, November 1958

37. Dubin, M., "Direct Measurement of Meteoric Dust Using Rockets and Satellites," in: *Trans. 10th General Assembly Internat. Astronom. Union, Moscow, August 1958,* ed. by D. H. Sadler, Cambridge: The University Press, 1960, pp. 714-715

38. Nazarova, T. N., "Rocket and Satellite Investigation of Meteors," in: *Trans. 10th General Assembly Internat. Astronom. Union, Moscow, August 1958,* ed. by D. H. Sadler, Cambridge: The University Press, 1960, pp. 713-714

39. McKinley, D. W. R., *Meteor Science and Engineering,* New York: McGraw-Hill, 1961

40. Hawkins, G. S., "The Relation Between Asteroids, Fireballs, and Meteorites," *Astronom. J.* 64(10):450-454, December 1959

41. Gallagher, P. B., and Eshleman, V. R., "'Sporadic Shower' Properties of Very Small Meteors," *J. Geophys. Res.* 65(6):1846-1847, June 1960

42. LaGow, H. E. and Alexander, W. M., "Recent Direct Measurements of Cosmic Dust in the Vicinity of the Earth Using Satellites," in: *Proc. 1st Internat. Space Sci. Sympos., Nice, January 1960,* ed. by H. K. Bijl, Amsterdam: North-Holland Publ. Co., pp. 1033-1041

43. Alexander, W. M., McCracken, C. W., and LaGow, H. E., "Interplanetary Dust Particles of Micron-Size Probably Associated with the Leonid Meteor Stream," NASA Technical Note D-1154, December 1961; also published in *J. Geophys. Res.* 66(11):3970-3973, November 1961

44. Eshleman, V. R., and Gallagher, P. B., "Radar Studies of 15th-Magnitude Meteors," *Astronom. J.* 67(5):245-248, June 1962

45. Dubin, M., and McCracken, C. W., "Measurements of Distributions of Interplanetary Dust," *Astronom. J.* 67(5):248-256, June 1962

46. van de Hulst, H. C., "Zodiacal Light in the Solar Corona," *Astrophys. J.* 105(3):471-488, May 1947

47. Allen, C. W., "The Spectrum of the Corona at the Eclipse of 1940 October 1," *Monthly Not. Roy. Astronom. Soc.* 106(2):137-150, 1946

48. Elsässer, H., "Fraunhoferkorona and Zodiakallicht," *Zeitschrift für Astrophysik* 37(2):114-124, July 13, 1955

49. Ingham, M. F., "Observations of the Zodiacal Light from a Very High Altitude Station. IV. The Nature and Distribution of the Interplanetary Dust," *Monthly Not. Roy. Astronom. Soc.* 122(2):157-176, 1961 (See also the three preceding papers by D. E. Blackwell and M. F. Ingham, pp. 113-155)

EVIDENCE FROM THE MOON'S SURFACE FEATURES
FOR THE PRODUCTION OF LUNAR GRANITES*

by

John A. O'Keefe and Winifred Sawtell Cameron
Goddard Space Flight Center

SUMMARY

If tektites come from the moon, they indicate a granitic constitution for a considerable portion of its outer crust, especially if allowance is made for the chemical effects of volatilization (loss of alkalies). The evidence for granitic rocks from the morphology of the moon's surface is considered in this paper. The displacement of the center of the moon's visible surface with respect to the center of mass is considered evidence of isostasy on the moon. It is shown here that this displacement is not merely a limb phenomenon, and is probably not explicable in terms of the kind of lumpy interior proposed by Urey to explain the differences of the moments of inertia. Evidence for characteristic granite topographic features, including tholoids and laccoliths, is summarized. The possibility that the maria were produced by the fluidization of volcanic ash is considered. The transporting fluid is considered to be the contained gases as in a terrestrial ash flow. Ash flows on the earth are responsible for the emplacement of a large fraction of all volcanic ash. From a study of the physics of ash flows, it is determined that the fluidization should be even more effective on the moon. It is concluded that the morphology of the moon's surface does not contradict the notion that large amounts of acid rock are present on its surface.

INTRODUCTION

Evidence has been adduced from the writing of Nininger, Dietz, O'Keefe, Varsavsky, Gold, and Chapman (References 1-6) in support of the hypothesis, originally enunciated by Verbeek (Reference 7), that tektites come from the moon. Chapman's work in particular has shown that the external features of the australites indicate a velocity of entry into the earth's atmosphere between 10 and 13 km per second. Taken in conjunction with the observed surface distribution, this figure excludes direct origin from the earth, and it likewise excludes normal meteoric orbits. It is, on the other hand, entirely consistent with the theory of origin from the moon. Since particles coming from the

---

*This paper will also be published in *Icarus*, Vol. I, No. 3.

moon as a result of meteorite impacts are to be expected a priori, and since these ought to be different from meteorites, it is highly likely that at least some of these particles are tektites.

Is the hypothesis of a lunar origin for tektites consistent with what is known about the structure of the moon's surface?

In the present paper we will attempt to relate the observable features of the moon's surface with the kind of rocks which would be expected to yield tektites. First an effort will be made to deduce the type of rock which formed the parent of the tektites; then the common surface features of the earth associated with rock of this kind will be noted; and finally we shall attempt to identify these features on the moon.

THE ROCK WHICH YIELDS TEKTITES

In the first place, it is clear that, if they are lunar, the tektites are related to the igneous rocks since sedimentary processes in the ordinary sense do not occur on the moon — unless Gilvarry's radical hypothesis of lunar oceans is correct (Reference 8). In the second place, tektites belong with the acid igneous rocks of the earth (those with a silica content of 65 percent or more) rather than with the intermediate rocks (55 to 65 percent silica) or the basic rocks (55 percent or less silica). No known tektite has less than 65 percent silica; nearly all have more than 68 percent (Reference 9).

Tuttle and Bowen showed that the majority of the acid igneous rocks can be thought of as consisting principally of three minerals — quartz, orthoclase, and albite — in roughly equal proportions (Reference 10).
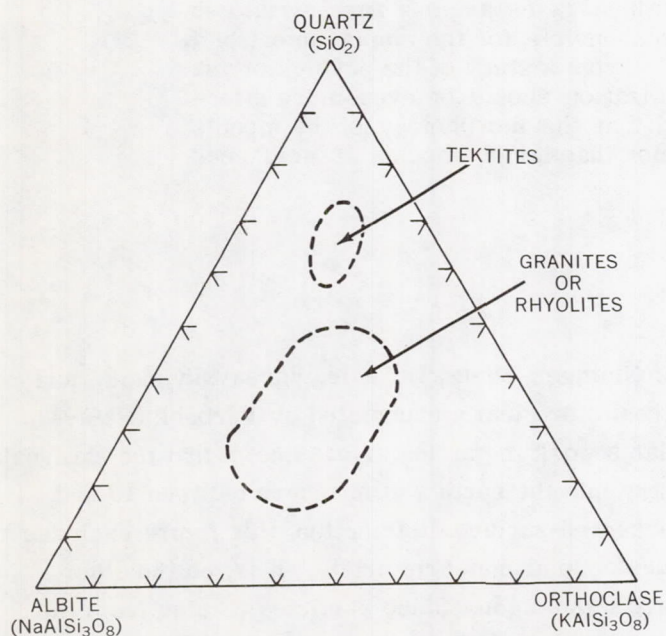

Figure 1—Normative compositions of granites and tektites, weight percentage (modified from Reference 10; tektite norms from Reference 11)

Petrologists express such a relation with a triangular diagram, such as that in Figure 1, in which each corner is labeled with the name of one of the three constituents. The relative proportions of the three constituents are expressed by the position of a point on the diagram; its distance from any side of the triangle is proportional to the abundance of the mineral marked on the opposite vertex. The normative composition is the theoretical equilibrium mineral composition as computed from chemical analysis of the rock.

It can be seen that granites and their volcanic equivalents, rhyolites, cluster around the center of the triangular diagram (Figure 1). There is experimental evidence for this behavior and it can be

explained theoretically. If the composition of the first fraction of liquid produced by melting in this system — in the first instance, at atmospheric pressure — is projected onto this diagram, it is found that the granites occupy the locus of lowest melting point, near the center of the diagram. At higher water pressures there is some migration of the low-melting-point trough, but it remains near the center. The granites therefore are believed to be formed either as the last portion of a magma to solidify (magmatic differentiation) or the first portion of a solid rock to liquefy. In the first case, they might represent the last remaining liquid in a large underground reservoir of magma; in the latter case they might represent a liquid sweated out of a solid mass at high temperature. These possibilities are further discussed elsewhere by Lowman (Reference 12).

The important point to see here is that tektites as they are found do not fit the picture. As is shown in Figure 1, tektites are on the quartz side of the granite field (and the low-melting-point trough), in a region where very few igneous rocks are located. If the tektites fell below the central region (i.e., on the orthoclase-albite side), it would be possible to explain their composition as due to incompleteness of one of the igneous processes mentioned. There are sound reasons for thinking that, either on the earth or on the moon, many acid igneous rocks have been derived from basaltic magma or from some rock of lower silica content. Terrestrial rocks that would be above the trough in Figure 1 can be explained as remelted sandstones, since sand is mostly silica; but this explanation is not available for lunar materials. The problem is so serious that many students of tektites, including Urey, reject the theory of a lunar origin of tektites, for just this reason, emphasizing that the chemistry of silicates ought to be the same on the moon as on the earth.

A possible solution of the problem has been provided by Cohen (Reference 13) and Taylor (Reference 14), who have pointed out the significance of volatilization in altering the composition of tektites. Taylor showed that the flanges of australites, which have been exposed to two meltings, are about 20 percent poorer in soda and potash than the cores, which have been exposed to only one melting. Cohen showed that the ratio of the volatile element germanium to the less volatile gallium was lower in the flanges than in the cores. Taylor applied his work only to the australite problem, but Cohen made the interesting suggestion that the same process had been at work in the formation of the tektites in general.

Cohen's hypothesis is in good accord with many other physical and chemical properties of tektites, namely:

1. The remarkable lack of water and other volatiles (Reference 15);

2. The presence of FeO rather than Fe_2O_3;

3. The almost total lack of magnetization (Reference 16);

4. The glassy nature of the tektites themselves.

These characteristics by themselves suggest a thorough heating at a temperature above that of ordinary lavas. At high temperatures, the escape of alkalies is commonly observed in the laboratory (Reference 10, p. 6).

It is therefore plausible to suppose that the tektites are derived from a material much like a granite or other acid igneous rock, provided that we accept the idea of a period of heating at very

high temperatures, lasting several minutes, during some part of the history of the tektites. Perhaps the heating occurred during a hypothetical formation of the tektites as ablation drops in the atmosphere. The mechanism of ablation heating is known, from the example of the australite flanges, to be competent to account for the volatilization. An alternative possibility, that the heating resulted from impact on a surface such as that of the moon, encounters the difficulty that the time duration of impact heating appears to be short, as judged from the lack of homogeneity of terrestrial impact glasses.

Thus the first part of this discussion is completed; we find that the tektites belong with the granitic kindred. It should be mentioned that the term "granite" is used here primarily in a chemical sense; strictly speaking, granite is a coarse-grained rock, usually formed at a great depth and exposed later by erosion. Although there may be some granite in the moon which has been exposed in craters, it should be uncommon; the granitic magmas will typically have formed fine-grained volcanic rocks such as rhyolite and tuff.

SURFACE FEATURES ASSOCIATED WITH GRANITIC ROCKS

The second part of this discussion is the listing of land forms that are associated with granitic rocks, especially those which might be visible on the moon. They are:

1. Isostasy — continental blocks of crust supported in a more or less hydrostatic fashion by flotation above a heavier substratum. The continents of the earth are made essentially of granite or its derivatives. The ocean basins, however, are apparently underlain by basaltic rock with a density about 10 percent higher.

2. Batholiths — large masses of granitic rock typically found in the cores of large folded mountain belts such as the Appalachians. Since there are no folded mountains of this type (consisting of thick accumulations of sedimentary rock) on the moon, we do not expect evidence that typical batholiths exist there.

3. Laccoliths — mushroom-shaped bodies, usually composed of acid igneous rock, intruded between the layers of a stratified country rock and causing the overlying strata to become dome-shaped.

4. Peleean volcanism, characterized by:

    a. Extrusion of lava in the form of spines and ridges, owing to high viscosity.

    b. Production of ash, both as ordinary ash falls and especially as ash flows, in which the solid material is fluidized and transported by the contained gases.

EVIDENCE FOR THE EXISTENCE OF ISOSTASY, LACCOLITHS, AND PELEEAN VOLCANISM ON THE MOON

Isostasy

The fundamental evidence for isostasy on the moon is the difference of position between the moon's center of gravity and its center of figure. The difference is well established; for example, it has been

regularly employed for the calculation of the eclipses of the sun (see the *American Ephemeris and Nautical Almanac for 1962*, p. 291). It amounts to approximately 1 km, in the sense that the center of figure is south of the center of gravity. The basic principle is that observations of the moon give the position of the center of the moon's visible face, whereas theory refers to the center of gravity. A discrepancy appears between theory and observation, by which the observed position is persistently south of the calculated one. The discrepancy cannot be removed by amending the lunar theory, since this does not contain constant terms in the celestial latitude. It is therefore attributed to a difference between the centers. Similar differences might in principle exist in the east-west direction or in the radial direction; but there is no easy observational way to find them.

The reality of the effect has been questioned on the ground that the moon's southern limb is conspicuously rougher than the northern limb (private communication with H. C. Urey). Hence the effect might be due merely to the fact that at the limb we are looking at the ridge lines. In rough country their average height is higher than the ground as a whole.

It is possible, however, to verify that the same displacement exists to an even greater extent for points well away from the limb. The reader may examine the maps of Baldwin (Reference 17) or the recent U.S. Army Map Service Topographic Map of the Moon, produced under the supervision of A. L. Nowicki. Both give elevations referred to a center which fits the limb observations, and hence lies south of the center of gravity. Nevertheless, it can be seen at once that the average height of the ground in the southern portion is greater, on these charts, than in the northern part. This means that the center of figure as derived from the maps falls even further south of the center of gravity than the center as derived from limb observations.

For obtaining a quantitative estimate, use was made of the catalog of 150 points, on the surface of the moon, established by G. Schrutka-Rechtenstamm (Reference 18). His catalog gives rectangular coordinates in the usual system, the unit being the radius of the moon, referred to the following coordinates for the center of the crater Mösting A:

$\xi = -0.08992$ (ξ positive to west),

$\eta = -0.05551$ (η positive to north),

$\zeta = +0.99521$ (ζ positive toward the earth).

These coordinates refer to a center derived from limb observations which is, as usual, about one km south of the center of gravity.

A least squares solution was made for the center of that sphere which most nearly fits the coordinates given by Schrutka-Rechtenstamm. Since the solution is almost independent of the correction in the radial (ζ) direction, the ζ correction was arbitrarily fixed at zero. The derived corrections to the ξ and η coordinates are $\Delta\xi = -0.4 \pm 0.4$ (m.e.) and $\Delta\eta = +1.4 \pm 0.4$ (m.e.), from which it follows that the center of figure should be a kilometer or so farther south. The correction in the east-west direction is small and uncertain. This result tends to confirm what is seen on the maps, as would be expected, since the maps are based on the coordinates of Schrutka-Rechtenstamm and his predecessors. The result is not, of itself, as decisive as it might appear, since the coordinates

available omit the outer rim of the moon's disk. Owing to foreshortening, the outer rim forms only a small fraction of the visible *disk*, although it makes up nearly half of the visible *hemisphere*. A significant point is that the rough continental areas are found to be, in fact, higher than the smooth maria, both in the coordinate calculations and on the maps.

On the whole, however, it appears impossible to doubt the reality of the displacement of the centers. Urey's contrary statement (Reference 19, pp. 22-25) is due to the fact that the occultation data which he used were calculated from the center of the moon's face rather than from the center of gravity.

Two explanations might exist for the displacement of the center of figure.

1. It might be due to isostasy. On the earth the center of mass is at the center of figure of the *geoid* (sea level surface) according to a theorem in potential theory. Since the Pacific hemisphere, which is centered near 180° longitude and 30°S latitude, is nearly all water, whereas the other hemisphere is nearly all land, it is clear that for the earth there is also a displacement of the center of figure with respect to the center of mass. It is well known that this displacement exists because the continents are essentially granite, whereas the ocean bottoms are essentially basalt, so that there is an excess of density in the ocean hemisphere. The displacement of the moon's center of figure may be due to a similar structure. A division of the moon into roughly two physiographic parts is apparent to the eye and telescope from coloration and comparative elevation; the lower elevation is associated usually with darker colored material than the higher elevation. This suggests an excess of density in the maria.

2. A second possibility, to which Urey, Elsasser, and Rochester (Reference 20) have drawn attention, is that the moon is inhomogeneous in a more or less random way, and consists of a finite number of lumps of unequal density.

To distinguish between these two hypotheses, we make use of the evidence from the second harmonics of the moon's gravitational field which indicates density inhomogeneities. If the irregularities in density are at the surface, and are supported in a more or less hydrostatic way, then the net effect on the external gravitational field will be small, since, by Archimedes' principle, the floating continental blocks will displace their own weight of basic rock, leaving the gravitational field approximately the same, at least at great distances. If, on the other hand, the inhomogeneities are irregularly distributed through the mass of the moon, then much larger gravitational effects are to be expected.

The external gravitational potential U of any planet can be expressed as a series of spherical harmonics, of the form

$$U = \sum_{n=0}^{\infty} \frac{A_n}{r^{n+1}} S_n(b, l) \, , \tag{1}$$

where r is the radius, b the latitude, l the longitude; the values of $S_n(b, l)$ are surface spherical harmonics, and the A_n's are coefficients of the harmonics. In this expression, the harmonic of zero order represents the field which the body would have if the mass were concentrated at one point. If the

origin of coordinates is taken at the center of mass, then by a theorem in potential theory, the three first harmonics in the potential vanish; this is equivalent to the above remark about the center of figure of the geoid coinciding with the center of mass of the earth.

Since the effect of irregularities in the moon's gravitational field must be measured from the action of the irregularities on the earth or the sun (together with the reaction on the moon), it follows that the effects will die out rapidly as we use higher and higher harmonics. The second harmonics are the lowest harmonics whose effects can be expected to reflect the irregularities of the moon; they are also the highest harmonics which can now be detected.

We wish to compare the observed variations in the second harmonics over the moon's surface with the variations to be expected from a theory of lumps. We shall first obtain an expression for the moment of inertia, I, in an arbitrary direction, in terms of quantities determined in libration theory. Next we shall find the deviation of I from its average value I_0, square the deviation, and integrate it over the sphere, to find the mean squared value. This we shall compare with the mean squared deviation to be expected from a statistical analysis like that of Urey, Elsasser, and Rochester (Reference 20), but more rigorous. Finally, we shall compare the lumpiness needed to produce these effects in the second harmonic with those required to produce the observed effect in the displacement of the centers, and thus see whether the gravitational field is notably smoothed, as would be expected in the case of isostasy.

It is also a general result of potential theory that the coefficients of the spherical harmonics of order n are proportional to linear combinations of the nth moments of the mass distribution. Second harmonics in particular are functions of the moments of inertia. The theory is given in standard texts — in Reference 21, for example. If the moments of inertia around the ξ, η, and ζ axes are respectively denoted by B', C', and A', then the theory of the moon's figure gives the quantities

$$\left. \begin{aligned} L' &= \frac{3}{2} \frac{C' - A'}{M'a'^2} = + 0.0003734, \\[2ex] K' &= \frac{3}{2} \frac{B' - A'}{M'a'^2} = + 0.000070, \end{aligned} \right\} \tag{2}$$

where, as in Reference 21, primes refer to the moon. Also,

$$J' = \frac{3}{2} \frac{C' - \frac{1}{2} A' - \frac{1}{2} B'}{M'a'^2}$$

$$= L' - \frac{1}{2} K' = + 0.0003384. \tag{3}$$

The general expression for the moment of inertia I around an axis with direction cosines λ, μ, and v, referred to the axes of A', B', and C', respectively, is

$$I = A'\lambda^2 + B'\mu^2 + C'v^2 . \tag{4}$$

Setting

$$\lambda = \cos b \cos l ,$$

$$\mu = \cos b \sin l ,$$

$$\nu = \sin b ,$$

where b is the selenographic latitude, and l the selenographic longitude, we have

$$I = A' \cos^2 b \cos^2 l + B' \cos^2 b \sin^2 l + C' \sin^2 b . \tag{5}$$

Following Jeffreys' treatment of a similar problem (Reference 21, p. 133), we look for a linear expression for I in terms of both the mean value

$$I_0 = \frac{A' + B' + C'}{3} , \tag{6}$$

and the spherical harmonics (in Jeffreys' notation)

$$p_2^0 = \frac{3}{2} \sin^2 b - \frac{1}{2} , \tag{7}$$

and

$$p_2^2 \cos 2l = \frac{3}{2} \cos^2 b \cos 2l , \tag{8}$$

with J' and K' in the coefficients of the spherical harmonics. We find

$$I = I_0 + M'a'^2 \left(\frac{4}{9} J'p_2^0 - \frac{2}{9} K'p_2^2 \cos 2l \right) , \tag{9}$$

as may be verified by evaluation at the moon's poles (b = ±90°, I = C'), at the center of its visible face (b = 0, l = 0, I = A'), and at the east and west limbs (b = 0, l = ±90°, I = B'). These three conditions suffice to fix the three coefficients of the linear form.

The mean squared value of $(I - I_0)$ over the sphere Ω is then

$$\overline{\Delta I^2} = \overline{(I - I_0)^2} = \frac{1}{4\pi} \iint_\Omega (\Delta I)^2 d\omega , \tag{10}$$

where $d\omega$ is the surface element of the sphere.

In the integration, the surface integral of the cross products of the spherical harmonics vanishes, since spherical harmonics are orthogonal; hence

$$\overline{(\Delta I)^2} = \frac{1}{4\pi} \iint\limits_{\Omega} \left[\frac{16}{81} J'^2 (p_2^0)^2 - \frac{4}{81} K'^2 (p_2^2 \cos 2l)^2 \right] d\omega .$$ (11)

The surface integral of any zonal harmonic is

$$\frac{4\pi}{2n + 1} ,$$

and for a tesseral harmonic it is

$$\frac{2\pi}{2n + 1} \frac{(n - s)! \ (n + s)!}{(n!)^2} ,$$

where n is the degree of the harmonic, and s is the order (Reference 21).

Substituting these values into Equation 11 and integrating, we find

$$\overline{(\Delta I)^2} = \frac{16}{405} \left[J'^2 - \frac{3}{4} K'^2 \right] ,$$

$$= 0.000\ 000\ 004\ 38 .$$ (12)

This estimate was made with only two degrees of freedom; it depends on J' and K'. In effect, we forced the mean value of ΔA, ΔB, and ΔC to be zero. The expected random variations if we do not make this requirement, i.e., with three degrees of freedom, are greater by the ratio 3/2; hence, the standard deviation of I, as judged from J' and K', is given by

$$\sigma_I^2 = \frac{3}{2} (0.000\ 000\ 004\ 38) ,$$

$$\sigma_I = 0.000081 .$$

To compare this with the theory, we imagine the body of the moon constituted of n lumps of equal volume v (Reference 20). If the lumps were of equal mass m, the moment of inertia I would be given by

$$I = \sum_{i=1}^{n} m \rho_i^2 ,$$ (13)

where ρ_1 is the distance of the ith lump from the axis around which the moment is taken.

Assume, however, that there is a variation Δm in the mass of any individual volume. If the standard deviation of m is σ_m, then it can be shown, by dividing the mass into cylindrical shells of constant ρ_i, that the expected standard deviation of I will be given by

$$\sigma_I^2 = \sum_{i=1}^{n} \left(\sigma_m \rho_i^2 \right)^2$$

$$\approx \sigma_m^2 \sum_{i=1}^{n} \rho_i^4 \, , \tag{14}$$

where we neglect a factor of $n/(n-1)$ which arises from the fact that the deviations of m are referred to the mean.

To evaluate the sum, which we denote by S, we convert it to a triple integral, noting that

$$v = \frac{V}{n} \, , \tag{15}$$

where V is the total volume. Then

$$S = \sum \rho_i^4 = \frac{n}{V} \sum_{i=1}^{n} \rho_i^4 v$$

$$\approx \frac{n}{V} \iiint_V p^4 dv \, , \tag{16}$$

over the moon. The triple integral may be obtained from elementary methods by using trigonometric functions (Peirce's Tables, Integral No. 273); it is found that

$$S = \frac{8}{35} \, na^4 \, . \tag{17}$$

Therefore

$$\sigma_I^2 = \sigma_m^2 \left(\frac{8}{35} \, na^4 \right) \, .$$

The moment of inertia I of a homogeneous sphere around an axis is

$$I = \frac{2}{5} M a^2 = \frac{2}{5} \, nma^2 \, ;$$

therefore

$$\frac{\sigma_I^2}{I^2} = \frac{10}{7}\left(\frac{1}{n}\frac{\sigma_m^2}{m^2}\right) .$$ (18)

The comparable equation

$$a = \pm A \sqrt{n} ,$$ (19)

in Urey's notation (Reference 20) then requires a correction factor of $\sqrt{10/7}$. We now apply the same method to the calculation of the x-coordinate of the center of mass, defined as

$$\bar{x} = \frac{m_1 x_1 + m_2 x_2 + m_3 x_3 \cdots}{M} ,$$ (20)

where M is the total mass of the moon. Since the square of the standard deviation of $\bar{x}$ is the sum of the squares of the standard deviations of the terms which make it up,

$$\sigma_{\bar{x}}^2 = \left(\frac{\sigma_m x_1}{M}\right)^2 + \left(\frac{\sigma_m x_2}{M}\right)^2 + \left(\frac{\sigma_m x_3}{M}\right)^2 + \cdots ,$$

or

$$\sigma_{\bar{x}}^2 = \frac{\sigma_m^2}{m^2 m^2} \sum_{i=1}^{n} x_i^2 .$$ (21)

As before we convert the summation to an integral over the volume, setting

$$x = a \cos \phi ,$$ (22)

where ϕ is colatitude, and using the Peirce Tables, Integral Number 273, we obtain

$$\frac{\sigma_{\bar{x}}^2}{a^2} = \frac{1}{5}\left(\frac{1}{n}\frac{\sigma_m^2}{m^2}\right) .$$ (23)

Dividing this equation by Equation 18, we find the ratio

$$\frac{\dfrac{\sigma_{\bar{x}}^2}{a^2}}{\dfrac{\sigma_I^2}{I^2}} = \frac{7}{50} ;$$ (24)

therefore

$$\frac{\dfrac{\sigma_{\bar{x}}}{a}}{\dfrac{\sigma_I}{I}} = 0.374 .$$ (25)

The actual numerical values are:

$$\left.\begin{array}{r} \sigma_{\bar{x}} = 1 \text{ km} \\[2em] a = 1735 \end{array}\right\} \quad \frac{\sigma_{\bar{x}}}{a} = 0.00058 \; ,$$

$$\left.\begin{array}{r} \dfrac{\sigma_I}{Ma^2} = 0.000081 \\[2em] \dfrac{I}{Ma^2} = 0.40 \end{array}\right\} \quad \frac{\sigma_I}{I} = 0.00020 \; ,$$

$$\frac{\dfrac{\sigma_{\bar{x}}}{a}}{\dfrac{\sigma_I}{I}} = 2.9 \; .$$

The value of the last ratio is 7.8 times larger than the theoretical one (Equation 25). It indicates that the gravitational field is smoother than would have been expected on the basis of the displacement of the centers. Whether the difference is significant will be examined below; for the moment, the important point is that the expected ratio is a pure number, dependent neither on the number of lumps assumed nor on their dispersion in mass.

Urey, Elsasser, and Rochester (Reference 20) estimate the value of n, the number of separate lumps, from their equivalent of Equation 18, in which

$$\frac{\sigma_I}{I} = 0.00020 \; ;$$

and they have assumed

$$\frac{\sigma_m}{m} = 0.042 \; .$$

They find $n = 29{,}000$. Substituting in our equation, we find 63,000 separate lumps. With either Urey's or our estimate of the effect of Urey's hypothesis the probability is of the order of 10^{-5} that the same set of lumps could give a displacement of the centers which is over seven times the theoretical value.

If we calculate n from Equation 23, we get about 1100 lumps, corresponding to a sevenfold larger value of σ_I/I. The probability of getting an observed value of σ_I/I which is 1/7 of the expected one is about 0.1; it is thus far greater than that of getting a deviation 7 times the expected one. On the

other hand, there are *two* determinations of the deviation of the moments of inertia from regularity, so that the overall probability is about 0.01.

Obviously the most probable situation is that the true number n is between 1100 and 63,000, but it must be nearer to 1100 than to 63,000. A situation of this kind is conveniently handled by the F-ratio test. To apply this F-ratio test, the ratio F of the two variances (i.e., the squares of the dispersions) is formed; and the probability that these two variances are significantly different is taken from a triple entry table, whose entries are F, n_1 (the number of degrees of freedom in the numerator), and n_2 (the number of degrees of freedom in the denominator).

The term "number of degrees of freedom" is a measure of the number of difference measurements which have been made on the quantity whose dispersion is to be determined. The number of degrees of freedom is one less than the number of measurements made; clearly, if we have only one measurement of a given quantity to work with, we have no idea of the dispersion; if we have two measurements, we have only one difference to work with, and so on. Here we are estimating the quantity

$$\frac{1}{n} \frac{\sigma_m^2}{m^2} \, ,$$

in the first place, on the basis of the difference in position between the center of figure and the center of gravity. This amounts to two measurements or one difference, and hence one degree of freedom. We have

$$\frac{1}{n} \frac{\sigma_m^2}{m^2} \;=\; \frac{7}{10} \left(\frac{\sigma_I}{I}\right)^2 \;=\; 0.000\ 000\ 028 \; .$$

In the second place, we are estimating the same quantity on the basis of two differences, J' and K', among three quantities, A', B', and C'; hence we are estimating with two degrees of freedom. We find

$$\frac{1}{n} \left(\frac{\sigma_m}{m}\right)^2 \;=\; 5 \left(\frac{\sigma_{\bar{x}}}{a}\right)^2 \;=\; 0.000\ 001\ 68 \; .$$

The ratio F of the two determinations of σ_m^2 is therefore 58.0. Considering the F test table, with one degree of freedom for the greater variance, and two degrees of freedom for the smaller, we find that the probability of such an occurrence by chance is between 1 and 5 percent.

It is thus clear that the displacement between the center of the moon's figure and its center of gravity does actually suggest the existence of isostasy.

The differences of the moments of inertia imply stress differences deep in the moon which are of the same order of magnitude (about 2×10^7 dynes/cm^2) as those implied by the nonhydrostatic components of the earth's gravitational field. These were worked out by Jeffreys (Reference 21) who started with gravimetric determinations of the harmonics; but his estimates of the general size of

the harmonics are so close to those found from satellite observations that his conclusions can be applied without change.

Some minor features of the moon's surface likewise suggest isostatic readjustment. In particular, many maria are surrounded by evidence of tectonic readjustment along their shores; specifically:

1. More or less circular systems of rilles surround Mare Crisium, Mare Imbrium, Mare Serenitatis, and Mare Tranquillitatis;

2. Fault scarps are visible on the shores of Mare Humorum and Mare Nubium, the downthrow sides being toward the maria;

3. Most of the maria have craters along their shores which dip downward toward them. In the case of Mare Humorum, two of these craters have actually been sliced in two by a fault; the same is suspected of the Straight Wall.

The evidence of tectonic instability and, especially, of sinking, means that the maria are more than just holes blasted by impacts in an essentially homogeneous moon. For in the latter case, hydrostatic forces would be pushing the maria upwards to seek the same level as the continents. The fact that, although lower than the continents, they tend to sink, suggests that they are underlain by heavier material than are the continents.

A possible alternative reason for sinking might be that the maria are enormous calderas of collapse; if the dark material of the maria has been withdrawn from the interior in any manner, certainly collapse would be expected over large areas. This cannot, however, be the whole story of the origin of the maria, since in this case the material withdrawn would be sufficient to fill them up. Moreover, the liquefaction, or the rendering plastic, of so large a body of rock probably implies a degree of weakness, in the crust as a whole, which is hard to reconcile with the mechanical strength necessary to support the difference of level between the continents and maria.

Laccoliths

The second manifestation of granitic rock which ought to produce observable effects on the moon is the production of laccoliths. Laccoliths are moderate-sized intrusions; on the earth they are usually found in sedimentary rocks, where a weaker layer permits the magma to spread laterally more easily than by forcing its way vertically upward. Laccoliths tend to produce surface bulges which are generally round in plan, with a diameter of the order of 10 km, and gentle external slopes. Basaltic magmas do not ordinarily produce laccoliths because of their low viscosity; instead of accumulating around the pipe through which they came, the basaltic magmas usually spread laterally forming the sills. Thus the presence of laccoliths indicates viscous, and hence silicic, magmas.

On the moon the structures called domes by Spurr (Reference 22) and others correspond in many respects to terrestrial laccoliths. They are normally found in the maria, though observational selection may play a part here, since it is hard to detect a gentle gradation in a rough area; their sizes, up to a diameter of 10 km, are similar to those of terrestrial laccoliths; the slopes are also similar.

About 2/3 of the domes have summit craters, as do certain terrestrial laccoliths described by Daly (Reference 23).

Many authorities, including Salisbury, Spurr, Kuiper, Shoemaker and Hackman, and Gold, do not consider the domes to be laccoliths (References 22, 24-27). A principal objection is the requirement for a layered rock, which on earth usually means a sedimentary rock. If the maria consist of basaltic flows, then weak strata are not to be expected. If they are composed, as Gold has suggested (Reference 27), of dust derived from high ground, then they ought not to contain especially strong layers. If, however, they consist of ash flows laid down episodically, then strata of varying strength may be expected because of the welding of the central portions of ash flows. This point will be considered further in the discussion of ash flows. It may be concluded that lunar evidence is consistent with the presence of laccoliths, but does not unambiguously indicate that they are present.

Surface flows of acid rocks tend to have irregular upper surfaces because of their higher viscosity (Reference 28). A possible example of a rough surface on a recent flow is west of Copernicus (about 8°E, 4°N). This dark area seems to interrupt some of the rays from Copernicus; it may therefore be one of the very latest events in the moon's evolution.

Peleean Volcanism

At the surface the principal effects of the extrusion of granitic rock may be classified under the head of Peleean volcanism, named after Mont Pelée in Martinique. (The Hawaiian fire goddess Pele has also had at least one phenomenon, Pele's hair, named after her; this is confusing because the Hawaiian volcanoes are typical of the basaltic group.) Peleean volcanism (Reference 29) is characterized by at least three phenomena which might be distinguished on the surface of the moon. These are:

1. The extrusion of lava in the form of ridges, spines, and tholoids (small, steep-sided domes). These appear to consist of very viscous lavas extruded under pressure, through cracks and holes in the crust. The most remarkable case is that of a spine extruded to a height of 300 meters from the crater of Mont Pelée within a period of a few months.

2. The production of ash: this is divided into:

    a. Ash falls, like the famous eruption of A.D. 79 which covered Pompeii.

    b. The remarkable — but by no means uncommon — phenomenon of ash flows.

These effects will be considered in order. Under the extrusion of lava would be included some small swellings very common on the moon, a kilometer or two in diameter, which may be compared with the terrestrial spines and tholoids. On the moon, such swellings are common in the area surrounding Mare Imbrium; Urey considers them rubble thrown out of the crater at the time of its formation by collision (Reference 19). If they are rubble, however, it is difficult to see why this material failed to produce the characteristic elongated craters which are found in such numbers associated with Tycho and Copernicus. In these latter, relatively certain cases, the relief produced is negative; it is

hard to see why the Imbrian ejecta should produce positive relief, especially when the pieces had farther to go and hence possessed more energy per gram.

Shaler compared the ridges which are a common feature of the central belt of the moon, south of Mare Imbrium, with the ridges formed on the earth by the extrusion of viscous (he mentioned trachytic) lavas (Reference 30). These structures are most clearly seen on the moon near Boscovich and Julius Caesar, and in the Haemus mountains. They run parallel to a system of narrow valleys found in the same areas, which diverge from the center of Mare Imbrium. These features have been attributed, by Gilbert (Reference 31) and Urey (Reference 19), to scoring by masses fired from Mare Imbrium. Once again the parallel with large craters is missing. The long groove-like valleys are entirely unlike the short elliptical craters, for example, those associated with Copernicus.

The central peaks of certain craters constitute a special group of hills associated with the aforementioned ridges. These peaks were regarded as extrusions by Shaler (Reference 30) and Kuiper (Reference 25). This view does not necessarily conflict with impact theories of the origin of the craters; on the earth such tholoids are common along cracks of an entirely independent origin (Reference 29). It is interesting to note that the central peak of Alphonsus, like several other peaks, is aligned toward the center of Mare Imbrium, although it is mechanically impossible that it could have been shaped by fragments from the Imbrian center. The tectonic significance of the direction toward the center of Mare Imbrium is further emphasized by the Straight Wall, which is a clearly defined fault not far from Alphonsus. It is, in fact, clear that such ridges are manifestations of one of the lunar tectonic grids on which Fielder has laid emphasis (Reference 32). This grid is clearly related to Mare Imbrium in a subtler way than by mechanical scoring.

With reference to the ejection of volcanic ash, there is a little evidence for ash *falls* on the moon. A few craters, notably several inside Alphonsus, are surrounded by darkened areas which may represent ash falls. One small crater, approximately 2 diameters of the crater Mairan east of it, appears to be a typical ash cone, with slopes of about 38 degrees (E. A. Whitaker, verbal communication).

Terrestrial ash *flows* (which are quite different from ash *falls*) consist of avalanches of volcanic ash which are fluidized by contained gases (Reference 33). Several features of an ash flow are of especial importance:

1. The total emplacement, which may be comprised of one or more individual ash flows, is very extensive, so that on the earth the area covered by ash flows may be fully as great as that covered by basaltic flows.* Individual units cover tens of thousands of square miles (Reference 34);

2. The surface is level and remarkably smooth (Reference 35);

3. The edges, unlike the edges of basaltic flows, feather out against the surrounding topography;

4. The top surface is composed of loose ash (Reference 35);

---

*It is only rather recently that geologists in general have recognized the extent and importance on earth of ash flows that produce welded tuffs (ignimbrite). According to Ross and Smith (Reference 33), "Many ash flow tuffs have not been mapped as such in the past because they were not recognized and many areas previously mapped as lava flows are now known to be ash flow tuffs. Other areas will doubtless be found after more detailed laboratory study and areal mapping."

5. The ash bed is welded into a solid obsidian in the middle, where the heat has stayed longest in the ash — not at the bottom where it escapes into the ground, nor at the top where it escapes into the air. The welding is such that it converts loose ash into a rock of unusual strength and toughness;

6. The collapse of the porous structure is greatest where the ash is deepest. Hence the surface of an ash flow tends to show the same features as the underlying original surface, although much diminished in height and depth (Reference 28);

7. The chemical behavior of the interior depends in part on the gases which pass up through it; hence the chemistry at any point depends on the depth (verbal communication from Michael Bickerman, student at Arizona State University).

These features strengthen the suggestion tentatively put forward by Shoemaker and Hackman (Reference 26) that the maria might possibly be regarded as ash flows (ignimbrite). This idea is very close to Gold's hypothesis that the maria are fluidized dust (Reference 27). In support of his idea, Gold pointed out radar evidence that the surface is quite level on the scale of the radar wavelength, i.e., around 10 cm. This evidence has been further supported by the studies of Senior and Siegel on the significance of polarization in radar returns (Reference 36). It disagrees entirely with the expected surface of a basaltic flow, which is likely to be blocky on a scale of a meter or so. Where comparatively smooth surfaces are found on lava flows, they are the result of aqueous erosion which has either removed the blocky crust or filled the cracks with silt.

Gold further pointed out the significance of the absence of scarps at the edges of the maria, and of the thermal indications of a loosely compacted surface.

On the other hand, the welding of the ash flows in horizontal strata is not predicted by Gold's mechanism of dust fluidization; and an effect such as this is necessary if we are to understand the domes as laccoliths. The alternation of loose ash and welded tuff which would be expected from the ash flow hypothesis does provide the necessary stratification; but if the dust moves continuously into the maria, then it is hard to see why there should be the pronounced stratification which is required.

The tendency of ash flows to reproduce the underlying topography on their surfaces recalls the phenomenon of ghost craters. On certain maria, it is possible to trace the outlines of craters that apparently are mostly below the surface. Sometimes a crater can be traced from the mare border inward, so that we can be sure that what we see on the mare is really the outline of a crater. The crater is revealed both by its effect on the surface elevations and by its effect on the coloration of the surface. The latter is apparently due to the effect pointed out by Bickerman—the dependence of the chemical state of the tuff on its depth.

Since ash flows are supported by gas, it is necessary to ask whether such eruptions could travel very far in the near-vacuum at the moon's surface. It might seem at first that the flow would collapse rapidly because of the escape of gas into space. This possibility is strongly implied by McTaggart (Reference 37), who suggested that the mobility of ash flows is due primarily to air entrapped by the advancing front. If McTaggart is correct, we cannot appeal to ash flows as a means of covering large areas of the moon's surface; we shall therefore discuss his treatment in some detail.

McTaggart's analysis considers a large block supported by gases flowing from beneath; it is based on Torricelli's formula for the laminar flow of an inviscid fluid through an orifice. The inertial terms in the flow equations are taken into account. This analysis is believed to rest on a misapprehension of the problem. The fundamental differential equation for flow in the x direction, at the velocity u, is

$$\frac{\partial p}{\partial x} = \rho \frac{du}{dt} + \rho X + \mu \nabla^2 u, \tag{26}$$

where p is the pressure, ρ the density, du/dt the time rate of change of velocity (since we are following the flow, i.e., for a chosen element moving with the fluid), X the body force in the x direction per unit mass, and μ the viscosity. McTaggart has neglected the second and third terms on the right-hand side, and has, by his use of Torricelli's equation, in effect equated the left-hand side to the first term on the right. Physically, this means that he assumed the particles are suspended by the inertial reaction of the gases as they speed up in passing through the passages around the particles. McTaggart correctly shows that this force is entirely inadequate to support the materials.

If, however, the materials are finely divided, then a different and more effective mechanism comes into play, namely the viscous resistance of the air. Since the passages between the particles are narrow and the layer next to the particles is at rest with respect to them, there are steep velocity gradients and the viscosity effects are large. Numerical estimates show that in this case it is correct to regard the first two terms on the right-hand side of this equation as negligible, by comparison with the third, and write

$$\frac{\partial p}{\partial x} = \mu^2 u . \tag{27}$$

From this equation, Lamb derived the Poiseuille law for the flux ϕ through a capillary tube (Reference 38, p. 585, Equation 4):

$$\phi = \frac{\pi a^4}{8\mu} \frac{\Delta p}{L} , \tag{28}$$

where a is the radius and L the length. If we consider instead the average velocity u_0, so that

$$\phi = \pi a^2 u_0 , \tag{29}$$

then

$$\Delta p = \frac{32 \mu u_0 L}{D_t^2} , \tag{30}$$

where D_t is the tube diameter. It is in this form that Leva quotes the Poiseuille equation (Reference 39, p. 44).

The weight of the column of material which the pressure must support is

$$L\left(\rho_s - \rho_f\right)(1 - \epsilon)g = \Delta p , \qquad (31)$$

where g is the acceleration due to gravity. Here the quantity $\left(\rho_s - \rho_f\right)$ represents the density of the solid particles minus the buoyancy effect (negligible for gases); and ϵ represents the fraction of a given volume of the aggregate which is occupied by voids, so that $\rho_s(1 - \epsilon)$ is the average density of the aggregate. Equating the two expressions for Δp and replacing $\rho_f u_0$ by the rate of flow G in grams per second per cm^2, we have

$$G = \frac{1 - \epsilon}{32} \frac{D_t^2 \rho_f \left(\rho_s - \rho_f\right)g}{\mu} . \qquad (32)$$

In practice we can only hope to find a law of the above *form*. We are not given the tube diameter D_t, but only the related particle diameter D_p. The passages are crooked, and thus the length L in Equation 30 is not really the same as in Equation 28. The effect of particle roughness will be felt both directly and through its effect on the voidage ϵ.

Leva has demonstrated the remarkable and fortunate fact that over a wide range of densities, flow rates, particle sizes, and fluid viscosities of both gases and liquids, the minimum flow G_{mf} required to fluidize an aggregate is

$$G_{mf} = C \frac{D_p^2 \rho_f \left(\rho_s - \rho_f\right)g}{\mu} , \qquad (33)$$

where C is not quite constant, but a slowly varying function of the Reynolds number R:

$$C \propto R^{-0.063} ,$$

where

$$R = \frac{GD_p}{\mu} \qquad (34)$$

as usual. The resulting empirical equation in cgs units, if we neglect buoyancy, is

$$G_{mf} = 1.09 \times 10^{-3} \frac{D_p^{1.82} \left(\rho_f \rho_s g\right)^{0.94}}{\mu^{0.88}} . \qquad (35)$$

We will now apply this equation to two cases, a terrestrial and a lunar case. The results are summarized in Table 1. The assumed bed thickness is 100 meters, in agreement with typical terrestrial ash flows. The temperature of 850°C is that determined by Boyd (Reference 28). The percentage of water in the rock (0.1 percent) is near the minimum for terrestrial granites. Most granites have values nearer 1 percent; tektites, however, probably owing to the heating to which they have

Table 1

Values of Parameters for Application of Equation 35.

Parameter	Terrestrial Case	Lunar Case
Bed thickness	100 m	100 m
Temperature	850°C	850°C
Percentage water in rock	0.1 percent	0.1 percent
Particle diameter	0.01 cm	0.01 cm
Gravity	980 gal	162 gal
Gas (steam) density	1.7×10^{-2} gm/cm^3	2.5×10^{-3} gm/cm^3
Viscosity	4.2×10^{-4} po	4.2×10^{-4} po
Solid density	2.5 gm/cm^3	2.5 gm/cm^3
Minimum gas flow	7.6×10^{-3} gm/cm^2-sec	2.3×10^{-4} gm/cm^2-sec
Duration of flow	0.8 hr	27 hr
Extent of flow	80 km	2700 km

been subjected, often have as little as 0.002 percent, though Friedman (Reference 15) has measured values as high as 0.014 percent in philippinites.

The particle diameter is toward the lower end of the size distribution observed. The reason is that the size of the passages between the particles is controlled, not by the large particles, but by the small ones. The pressure, not listed in Table 1, is calculated for the midpoint of the bed from Equation 31, by assuming 1 atmosphere pressure at the surface in the terrestrial case, and 0 atmosphere in the lunar case. From the pressure and temperature, the density and viscosity are found with the usual tables. The solid density corresponds to an acid rock.

The minimum gas flow required for fluidization can be calculated from Leva's equation. The duration of flow is estimated by comparing the rate of flow for minimum fluidization with the available amount of water. The extent of flow is calculated on the assumption that it moves at the rate observed on earth, about 100 km/hr.

The greater duration and extent of the lunar flows are the result of the lower gravity, which acts in two ways: (1) Directly, by reducing the weight of the layers to be supported; (2) Indirectly, by reducing the pressure at every depth, and hence the density, and thus the mass of fluid required. (The supporting power of a gas flow depends on its volume and its viscosity; since the viscosity is independent of the density, a flow of low density gives the same support as one of high density and is more economical in regard to material.) The combination of these two effects produces a factor of about 32 in favor of the greater duration and extent of lunar ash flows.

The absence of an atmosphere on the moon is almost irrelevant, since all the equations for the support of the layer involve only a pressure difference. However, in calculating density at a given temperature, the absolute value of the pressure must be used; and here it is clear that the lunar flows will require less gas than terrestrial flows, since they will have lower pressures and densities

near the surface. Surprisingly, lunar conditions are actually more favorable to deposition of extensive tuffs from ash flows than are terrestrial conditions.

CONCLUSION

It appears that it is quite possible to furnish explanations of the observed lunar land forms on the assumption that the moon's surface has a high proportion of granitic rocks. The explanations are not always the accepted ones; but they are well within the boundaries of physical plausibility. They do not appear to conflict with Dollfus' polarization observations of the moon, or with his conclusions as to the volcanic nature of the lunar surface (Reference 40).

ACKNOWLEDGMENTS

REFERENCES

1. Nininger, H. H., "The Moon as a Source of Tektites, Pt. 1," *Sky and Tel.* 2(4):12-15, February 1943; "The Moon as a Source of Tektites, Pt. 2," ibid. 2(5):8-9, March 1943

2. Dietz, R. S., "The Meteoritic Impact Origin of the Moon's Surface Features," *J. Geol.* 54(6):359-375, November 1946

3. O'Keefe, J. A., "Origin of Tektites," *Nature* 181(4603):172-173, January 18, 1958; see also "The Origin of Tektites," NASA Technical Note D-490, November, 1960

4. Varsavsky, C. M., "Dynamical Limits on a Lunar Origin for Tektites," *Geochim. et Cosmochim. Acta* 14(4):291-303, 1958

5. Gold, T., "Origin of Tektites," *Nature* 181(4603):173-174, January 18, 1958

6. Chapman, D. R., "Recent Re-Entry Research and the Cosmic Origin of Tektites," *Nature* 188(4748): 353-355, October 29, 1960

7. Verbeek, R. D. M., "Over Glaskogels van Billiton," *Verslagen van de Gewone Vergaderingen der Wis- en Natuurkundige Afdeeling, Koninklijke Akademie van Wetenschappen te Amsterdam* 5:421-425, 1897

8. Gilvarry, J. J., "Origin and Nature of Lunar Surface Features," *Nature* 188(4754):886-891, December 10, 1960

9. Lowman, P. D., Jr., "Tektites vs. Terrestrial Rocks: A Comparison of Variance in Compositions," *Geochim. et Cosmochim. Acta* 26:561-579, May 1962

10. Tuttle, O. F., and Bowen, N. L., "Origin of Granite in the Light of Experimental Studies in the System NaAlSi$_3$O$_8$-KAlSi$_3$O$_8$-SiO$_2$-H$_2$O," New York: Geological Society of America, 1958 (Geological Society of America, Memoir 74)

11. Barnes, V. E., "North American Tektites," in: *Contributions to Geology, 1939*, Part 2, The University of Texas Press, 3945:477-582, 1939

12. Lowman, P. D., Jr., "The Relation of Tektites to Lunar Igneous Activity," *J. Geophys. Res.* 67(4):1646, April 1962 (Abstract)

13. Cohen, A. J., "Trace Element Relationships and Terrestrial Origin of Tektites," *Nature* 188(4751):653-654, November 19, 1960

14. Taylor, S. R., "Distillation of Alkali Elements During Formation of Australite Flanges," *Nature* 189(4765):630-633, February 25, 1961

15. Friedman, I., "The Water, Deuterium, Gas and Uranium Content of Tektites," *Geochim. et Cosmochim. Acta* 14(4):316-322, 1958

16. Senftle, F. E., and Thorpe, A., "Magnetic Susceptibility of Tektites and Some Other Glasses," *Geochim. et Cosmochim. Acta* 17(3/4):234-247, 1959

17. Baldwin, R. B., "A Lunar Contour Map," *Sky and Tel.* 21(2):84-85, February 1961

18. Schrutka-Rechtenstamm, G., "Neureduktion der 150 Mondpunkte der Breslauer Messungen von J. Franz," *Sitzungsberichten der Österreichischen Akademie der Wissenschaften, Mathematisch-Naturwissenschaftliche Klasse, Abteilung II*, 167(1-4):71-123, 1958

19. Urey, H. C., "The Planets; Their Origin and Development," New Haven: Yale University Press, 1952

20. Urey, H. C., Elsasser, W. M., and Rochester, M. G., "Note on the Internal Structure of the Moon," *Astrophys. J.* 129(3):842-848, May 1959

21. Jeffreys, H., "The Earth: Its Origin, History, and Physical Constitution," 4th Ed., Cambridge University Press, 1959, Chapter IV

22. Spurr, J. E., "Geology Applied to Selenology," Lancaster, Pennsylvania: Science Press Printing Co., 1944, p. 83

23. Daly, R. A., "Igneous Rocks and the Depths of the Earth," New York: McGraw-Hill, 1933, p. 153

24. Salisbury, J., "Origin of Lunar Domes," *Proc. Lunar and Planet. Exploration Colloq.* 2(2):22-26, March 17, 1960

25. Kuiper, G. P., "The Exploration of the Moon," in: *Vistas in Astronautics*, ed. by M. Alperin and H. F. Gregory, New York: Pergamon Press, 1959, Vol. 2, pp. 273-313

26. Shoemaker, E. M., and Hackman, R. J., "Stratigraphic Basis for a Lunar Time Scale," in: *Astrogeologic Studies, Semiannual Progress Rept., August 25, 1960 to February 25, 1961*, U. S. Geological Survey, March 1961, p. 21

27. Gold, T., "The Lunar Surface," *Monthly Not. Roy. Astronom. Soc.* 115(6):585-604, 1955

28. Boyd, F. R., "Welded Tuffs and Flows in the Rhyolite Plateau of Yellowstone Park, Wyoming," *Bull. Geol. Soc. Amer.* 72(3):387-426, March 1961

29. Cotton, C. A., "Volcanoes as Landscape Forms," 2nd Ed., Christchurch: Whitcombe and Tombs, 1952

30. Shaler, N. S., "A Comparison of the Features of the Earth and the Moon," Washington: Smithsonian Institution, 1903 *(Smithsonian Contributions to Knowledge, Part I, Vol. 34)*

31. Gilbert, G. K., "The Moon's Face; A Study of the Origin of Its Features," *Bull. Phil. Soc. Washington* 12:241-292, 1892-1894

32. Fielder, G., "Structure of the Moon's Surface," New York: Pergamon Press, 1961

33. Ross, C. S., and Smith, R. L., "Ash-Flow Tuffs: Their Origin, Geologic Relations, and Identification," Washington: U.S. Government Printing Office, 1961 (U.S. Geological Survey, Professional Paper 366)

34. Smith, R. L., "Ash Flows," *Bull. Geol. Soc. Amer.* 71(6):795-841, June 1960

35. Griggs, R. F., "Our Greatest National Monument," *Nat. Geog. Mag.* 40(3):219-292, September 1921

36. Senior, T. B. A., and Siegel, K. M., "Radar Reflection Characteristics of the Moon," in: *Paris Symposium on Radio Astronomy*, ed. by R. N. Bracewell, Stanford: Stanford University Press, 1959, pp. 29-46

37. McTaggart, K. C., "The Mobility of Nuées Ardentes," *Amer. J. Sci.* 258(5):369-382, May 1960

38. Lamb, H., "Hydrodynamics," 6th Ed., Cambridge University Press, 1932; New York: Dover, 1945, p. 585, Equation 4

39. Leva, M., "Fluidization," New York: McGraw-Hill, 1959

40. Dollfus, A., "La Courbe de Polarisation de la Terre et la Nature du Sol Lunaire," *Comptes Rendus, Académie des Sciences* (Paris) 235(18):1013-1016, November 3, 1952

OBSERVATIONAL ASTROPHYSICS FROM
ROCKETS; STELLAR SPECTRA

by
Theodore P. Stecher and James E. Milligan
Goddard Space Flight Center

SUMMARY

Instrumentation was flown in an Aerobee rocket to obtain stellar spectra in the ultraviolet and it encountered a bright ultraviolet aurora with no visible counterpart. The radiation, which occurred in the 1300-1800A region, had a strong north-south asymmetry but was geometrically quiescent. Although this background radiation limited the number of stellar spectra to a fraction of what had been expected, satisfactory spectra were obtained between 1800A and 4000A for 10 stars. The spectral types ranged from FoIa to 0_5f and WC_7. Satisfactory agreement between theoretical model atmospheres and the observations was obtained only for the FoIa star. For the hotter stars, a fundamental disagreement occurs at wavelengths below 2400A, resulting in a discrepancy of a factor of 10 or more at 2000A. It appears that the source of this disagreement is in the atmosphere of the star, and the authors suggest that it is due to quasi-molecular and molecular absorption by various combinations of hydrogen and helium atoms and ions. The reduced stellar fluxes considerably change the ultraviolet interstellar radiation field.

The earth's atmosphere is completely opaque to optical radiation that has a wavelength shorter than 3000A. For many problems in astrophysics, observations at shorter wavelengths are necessary in order to make theoretical progress. This is brought out by the fact the maximum in the Planck curve for a blackbody at 10,000°K occurs below the atmospheric cutoff. Since most of the naked-eye stars have an effective temperature greater than this, it has been impossible to adequately check the theoretically predicted structure of their atmospheres from the ground. The resonance lines of most of the more abundant elements occur at these short wavelengths. Similarly, the electronic transitions of most molecules of astrophysical interest also are in the ultraviolet which is unobservable from the ground. Because of the importance of these problems to physics and astrophysics, our first efforts in the use of space vehicles for astronomical purposes have been made in the ultraviolet. The effort being made in this direction ranges from the use of simple photometers in unguided sounding rockets to the implementing of a 36-inch spectrophotometric telescope in an orbiting spacecraft. This paper describes our first attempt to obtain ultraviolet stellar spectra and discusses the results.

On November 22, 1960, at 0842 UT we launched an Aerobee rocket containing four objective grating stellar spectrophotometers from the Wallops Island, Virginia, launch site. The detailed description of the experiment will be found in Reference 1. For the sake of completeness, a brief description will be given here.

The design of the experiment was an extension of the method used by Kupperian, Boggess, and Milligan (Reference 2) in an Aerobee rocket to obtain nebular isophotes in the ultraviolet; i.e., the instrumentation looks out the side of the rocket and scans the sky as the rocket spins and precesses during free fall. The determination of the rocket's aspect then enables us to identify the objects viewed. The extension of the technique was to let the spin of the rocket accomplish the spectral scan as well as the scan for objects of interest; this is simply done by using an objective dispersive system — motion of the instrument will cause the displacement of the spectral image. If this displacement is across a slit, spectral scanning occurs. In this experiment two gratings were used in a mosaic as the dispersive element.

The spin rate of the rocket was preselected to give a scan rate of 5000 angstroms per second. The frequency response of the associated electronics was chosen to match this scan rate. The spectral resolution was 50A on one pair of spectrophotometers and 100A on the other. The short wavelength cutoff was at 1300A for one and 1700A for the other in each pair. The wavelengths in the stellar spectra were determined from the zero-order image and the spin rate. Ideal dynamic behavior was attained by the rocket.

Figure 1 is a portion of a compressed FM-FM telemetry record showing the scanning through two rotations of the rocket. It shows the northern horizon, stars, the southern airglow horizon, and the earth including some cities. Of particular interest to the geophysicist is the asymmetry between the northern and southern horizons. The higher intensity in the north extended to an angular distance of 60 degrees above the rocket horizon. The two shorter wavelength spectrophotometers were saturated throughout the flight although they had lower sensitivity than the longer wavelength ones. We interpret this high surface brightness as being an ultraviolet aurora associated with the November, 1960, solar event. This phenomenon was completely unexpected on the basis of previous experience.

NORTH   ZENITH   SOUTH   NADIR   NORTH
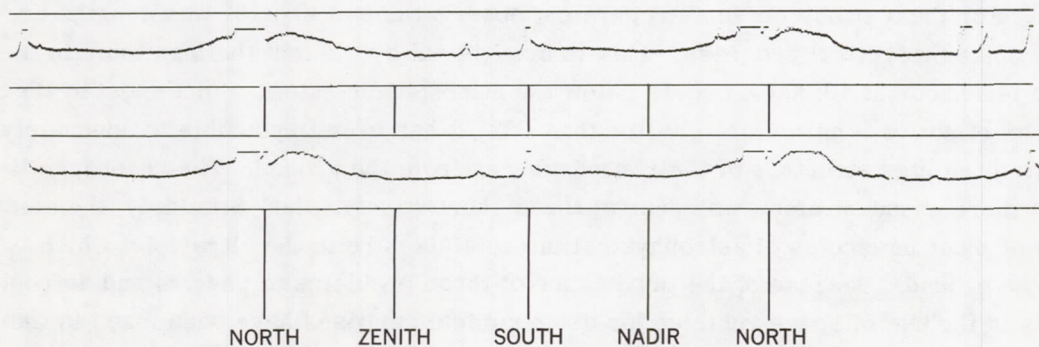
Figure 1—Compressed FM-FM telemetry record showing the scan of a spectrophotometer as the rocket spins. The difference between the northern and southern horizon is to be noted. Star signals also appear

The sensitivity of each instrument with respect to the others was known, and therefore a minimum surface brightness can be given. For the short wavelength spectrometers looking straight up at the peak of the flight (180 km) the minimum surface brightness was more than a factor of 10 brighter than that of night Lyman-α.

The minimum value of the sky brightness observed by the long wavelength instruments was 10^{-3} erg/cm²-sec-ster if it is assumed that the radiation occurs at 2500A where the instruments have maximum sensitivity. While an objective dispersive instrument does not give spectra for extended objects, the wavelength interval may be guessed from the known behavior of the instruments. It appears that the UV radiation was confined to the region below 1800A. If this is the case, the actual specific intensity was closer to 10^{-2} erg/cm²-sec-ster for the long wavelength instruments and more than 10^{-1} erg/cm²-sec-ster looking straight up at 180 km.

It appears as if the rocket flew into and never got out of an atmospheric emission which has not been previously reported. The Lyman-Berge-Hopfield bands of N_2 and the Schumann-Runge bands of 0_2 both appear in the 1300-1800A region of the spectrum along with the electronic transitions of several other molecules. Observations of the ultraviolet airglow and aurora with instruments designed specifically for this purpose will be necessary to decide the issue.

It should be pointed out that the geometrically quiescent behavior of this ultraviolet aurora, along with simultaneous occurrence of a magnetic bay and a disturbed ionosphere, presents an interesting problem in respect to the energy source.

Good stellar spectra were obtained for seven stars at 50A resolution between 1600 and 4000A. For eight other stars, usable spectra were obtained over part of the range of interest. The relative energy distribution was good to 10 or 20 percent and the absolute energy to 30 percent.

The spectrum of each star was compared with a theoretical model atmosphere computed to represent the same spectral class. One star, α Carinae, FoIa, the lowest temperature star observed, was in very good agreement with the appropriate model atmosphere. For the rest from AoV to 0_5f and Wc7, a deficiency in flux started at 2400A; this discrepancy increased to more than a factor of 10 at 1800A. A sample spectrum is shown in Figure 2, with a theoretical model atmosphere computed by Underhill (Reference 3).

Arguments may be given to show that this is an intrinsic property of the stellar atmosphere (Reference 1) and not due to absorption between the instrument and the star. This presents the problem of the source of opacity in stars.

A theoretical model stellar atmosphere is calculated from a temperature distribution through the atmosphere obtained by solving the radiative transfer problem under conditions of local thermodynamic equilibrium and then numerically solving the equation of hydrostatic equilibrium. It is tested by requiring the flux to remain constant at each point in the atmosphere.

Since the structure of the atmosphere is dependent upon the opacity as a function of depth, a detailed knowledge of the chemical composition and the absorption coefficient for each atom and ion is necessary. It is at this point that the compromise is usually made. For the early type stars it

OBSERVED:
ϵ Canis Majoris, B_1 II —o—

THEORETICAL:
$T_e = 28407$, Log $g = 3.80$ —x—

FREQUENCY X 10^{-15} (cps)
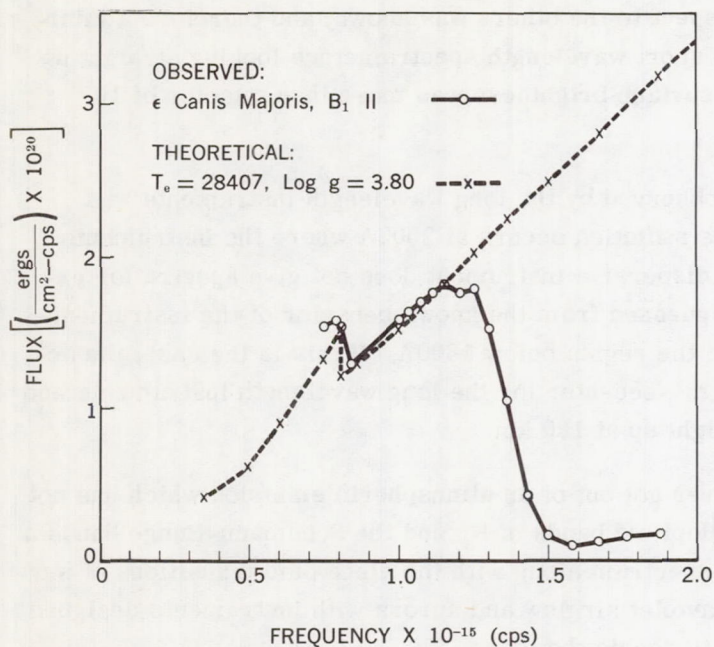
Figure 2—Observed absolute flux of ϵ Canis Majoris, B_1 II. The theoretical flux curve (Reference 3) has been arbitrarily normalized to the observed one at $\nu = 10^{15}$ cps.

is generally assumed that absorption is due to hydrogen and helium, since these are by far the most abundant constituents. Electron scattering is also taken into account. The atomic absorption by heavier elements is generally considered unimportant. A number of B star models have been computed for a pure hydrogen atmosphere since helium only contributes 10 percent of the opacity in this temperature range. The frequency dependence of the hydrogen continuous absorption coefficient is such that the gas becomes quite transparent on the low frequency side of a series limit. This results in a large increase in flux over that of a blackbody on the low frequency side of the Lyman limit. It is in this region that we now have observations which disagree with the models.

The problem of the observed absorption is complicated by the wide range of temperature over which it is present. The form of the absorption is suggestive of molecules. While certain molecules are important in cool stars, in the hot stars these same molecules would be dissociated and the constituent atoms ionized. It would appear that only hydrogen and helium are abundant enough for consideration as constituents of a molecule. A number of molecules and quasi-molecules may be formed out of various combinations of hydrogen and helium atoms and ions. The quasi-molecule of H_2 will absorb in this region while H_2 itself will not (Reference 4). Since it has a much larger binding energy (Reference 5), H_3^+ should be considered for those stars where H_2^+ and H^- are important. HeH^+ has a stable ground state (Reference 6). It could be important in either its quasi or molecular form, but at this time its optical transitions are unknown.

The exact wave functions for HeH^{++} have been computed for a number of states (Reference 7). Oscillator strengths have also been computed and are high (Reference 8). The $2p\sigma$ state is a partially attractive one with a rate coefficient for formation that is very high and almost independent of temperature (Reference 9); absorptions from it fall in the proper region of the spectrum to be of interest.

The basic difficulty with a molecular source of opacity in a stellar atmosphere is that the number of molecules per unit volume is proportional to the product of the number densities of the component constituents. The emergent flux for an atmosphere in local thermodynamical equilibrium is given by

$$F_\nu(\tau = 0) = 2 \int_0^\infty S_\nu(\tau_\nu) \, E_2(\tau_\nu) \, d\tau_\nu \,, \tag{1}$$

where $S_\nu(\tau)$ is the source function, E_2 is the exponential-integral function, and the optical depth τ_ν at frequency ν is obtained from the mass absorption coefficient κ_ν by

$$d\tau_\nu = -\kappa_\nu \rho dx . \tag{2}$$

From this it is immediately obvious that the frequency dependence of the absorption coefficient will cause the emergent flux for different frequencies to originate from physically separate layers.

The boundary conditions require that the temperature increase with physical depth. This requires a high optical depth near the physical boundary of the star in order to obtain agreement with the observations which require $S_\nu \tau_\nu$ to be small and the density to be low. Thus high absorption at low density and temperature is necessary.

Model stellar atmospheres are further complicated at this point by several other difficulties. It has been shown that the luminosity for a star in radiative equilibrium is completely determined by the mass (Reference 10). Under the assumption that the masses for B stars are well known, we are unable from the observations to account for half of the star's luminosity. One possible solution to this would be in the reradiation of a molecular absorber. For instance, HeH^{++} can absorb radiation in the $2p\sigma$ state by the $2p\sigma - 3d\sigma$ transition and reradiate by the $3d\sigma - 1s\sigma$ transition, giving a continuum below 304A. Such a mechanism would have interesting consequences on the ionization of the interstellar medium. Another mechanism to account for the needed flux is through particle radiation (Reference 11) which can also explain (Reference 12) the nebular radiation observed at 1300A (Reference 2).

The observed high opacity will steepen the temperature gradient, probably to the point where it will exceed the adiabatic gradient and convective energy transport will result. Convection must be present to provide energy for the magnetic field necessary for corpuscular radiation if it is to be invoked as the energy loss mechanism. Convection would also be expected to produce a large high-temperature corona. It may be mentioned that the hydrodynamic problem for this type of convective equilibrium is yet to be solved by the theoretician. The computation of model stellar atmospheres appears to be a very difficult problem.

An important consequence of the observation is the necessary revision of the interstellar radiation field. Dunham (Reference 13) made the classical calculation of the interstellar radiation field by assuming that each star radiated as a blackbody. Lambrecht and Zimmerman (Reference 14) have recalculated the field using model atmospheres and comprehensive counts of the number of stars in each spectral class at each magnitude. The large discrepancy in flux observed in the ultraviolet makes a considerable difference in these and other calculated radiation fields.

Strömgren (Reference 15) has written the classic paper on the ionic concentration of the elements in the interstellar medium. The state of ionization of those atoms and ions whose ionization potential is more than 5 ev is determined by the flux in the radiation field, which must be changed. The recalculation of abundance ratios, temperature, and densities, now in progress, may considerably change the detailed picture of the interstellar medium.

REFERENCES

1. Stecher, T. P., and Milligan, J. E., "Stellar Spectrophotometry from above the Atmosphere," *Astrophys. J.* 136(1), 1-13, July 1962

2. Kupperian, J. E., Jr., Boggess, A., III, and Milligan, J. E., "Observational Astrophysics from Rockets. 1. Nebular Photometry at 1300A," *Astrophys. J.* 128(3):453-464, November 1958

3. Underhill, A. B., "Four B-Type Model Atmospheres," *Publ. Dominion Astrophys. Observ. Victoria, B. C.* 10(19):357-391, 1957

4. Erkovich, S. P., "Coefficient of the Absorption of Radiation by Quasi Molecules of Hydrogen," *Optika i Spektroskopiia* 8(3):307-311, March 1960 (In Russian): Translation in *Optics and Spectroscopy* 8(3):162-164, March 1960

5. Varney, R. N., "Mobility of Hydrogen Ions," *Phys. Rev.* Letters 5(12):559-560, December 15, 1960

6. Coulson, C. A., and Duncanson, W. E., "Comparison of Wave-Function for HeH^{++} and HeH^{+}," *Proc. Roy. Soc. London* 165A(920):90-115, March 18, 1938

7. Bates, D. R., and Carson, T. R., "Exact Wave Function of HeH^{2+}," *Proc. Roy. Soc. London* 234A(1197):207-217, February 7, 1956

8. Arthurs, A. M., Bond, R. A. B., and Hyslop, J., "The Oscillator Strengths of the $1s\sigma\text{-}2p\sigma$, $2p\sigma\text{-}2s\sigma$, $2p\sigma\text{-}3d\sigma$ and $2p\sigma\text{-}2p$-Transition of HeH^{2+}," *Proc. Phys. Soc.* (London) 70A(8):617-619, August 1957

9. Arthurs, A. M., and Hyslop, J., "Radiative Charge Transfer from H Atoms to He^{2+} Ions," *Proc. Phys. Soc.* (London) 70A(12):849-856, December 1957

10. Huang, S-S., "A Stellar Model of Mixed Opacity and its Variations with the Mass, Chemical Compositions, Opacity Coefficients, and Energy-Generation Coefficient," *Astrophys. J.* 136(1):193-201, July 1962

11. Huang, S-S., Milligan, J. E., and Stecher, T. P., "Suggestion Concerning the Boundary Conditions of B Stars," *Publ. Astronom. Soc. Pacific* 74(439): August 1962 (In Press)

12. Shklovskii, I. S., "Corpuscular Emission from Early-Type Stars as a Possible Cause of Emission from Nebulae in the Region 1225-1250A," *Astronomicheskii Zhurnal* 36(4):579-584, July-August 1959 (In Russian): Translation in *Soviet Astronomy-AJ* 3(4):569-574, January-February 1960

13. Dunham, T., Jr., "The Material of Interstellar Space," *Proc. Amer. Philos. Soc.* 81(2):277-293, June 1939

14. Lambrecht, H., and Zimmermann, H., "Neuberechnung des Interstellaren Strahlungsfeldes. II," *Wissenschaftliche Zeitschrift der Friedrich-Schiller-Universität, Jena, Mathematisch-Naturwissenschaftliche Reihe* 5:217-220, 1956; also *Mitteilungen der Universität-Sternwarte zu Jena* No. 14, 1956

15. Strömgren, B., "On the Density Distribution and Chemical Composition of the Interstellar Gas," *Astrophys. J.* 108(2):242-275, September 1948

THE UTILIZATION OF IONOSPHERE
BEACON SATELLITES

by

G. W. Swenson, Jr.
University of Illinois

SUMMARY

This paper discusses the application of beacon transmitters in earth satellites to ionospheric research, and the need for world-wide cooperation in beacon satellite observation. The theories of Faraday rotation and Doppler methods of determining atmospheric electron content are reviewed briefly and the working formulas are listed. Desirable characteristics of beacon satellites are outlined. Methods of observation and equipment are discussed in some detail, as are the minimum standards for the production of high-quality data. An extensive bibliography is also presented.

INTRODUCTION

With the launching of the first artificial satellite Sputnik I (1957 α), an opportunity was presented to the scientific community to investigate the ionosphere by observing the changes in character of a radio signal, produced by its passage through this region. The early Russian satellites transmitted signals at frequencies of approximately 20 and 40 Mc, low enough to be influenced substantially by existing electron densities and magnetic fields in the ionosphere. Sputnik III (1958 $\delta 2$) was particularly useful for ionospheric studies because its rather eccentric orbit carried it, at times, well above the most heavily ionized regions, and because it transmitted for well over a year.

Three United States satellites have transmitted radio signals in the vicinity of 20 Mc: Explorer VII (1957 $\iota 1$), and Discoverers XXXII (1961 $\alpha \gamma 1$) and XXXVI (1961 $\alpha \kappa 1$). The former, unfortunately, had an elliptically polarized antenna and was spin stabilized. Therefore it was of limited usefulness for ionospheric research. The latter two were specifically designed to study scintillation, had short lifetimes, and orbited at rather low heights. Therefore they too had limited utility.

With the exception of the two Discoverers mentioned above (the Nora-Alice experiment), no satellites specifically designed for ionosphere research by means of their radio transmissions have been available. Two efforts by the National Aeronautics and Space Administration to launch "ionosphere beacon" satellites were unsuccessful.

A new NASA program is being implemented which aims at providing such a satellite with characteristics optimized for investigations of the ionosphere-beacon variety. It is the purpose of this paper to encourage wide utilization of this beacon satellite for ionospheric research and to suggest some ways in which this can be done.

At present a number of satellite tracking stations are actively engaged in ionospheric research by means of satellite beacon transmitters. The stations known to have been active at some time since 1957 are shown on the map in Figure 1. This map is undoubtedly incomplete, but it is quite apparent that the geographic coverage is grossly nonuniform. Of the stations charted, few have reported the results of long series of observations and many apparently have been operated only on an ad hoc basis.

This method of ionospheric research is relatively simple and inexpensive, and it seems highly desirable that a more widespread geographic coverage be obtained and that observations be made by more-or-less standard techniques over long periods of time.

This report is intended as a type of handbook for persons contemplating field programs. It is hoped that it will help promote participation on a widespread geographical basis. To this end, attention will be concentrated upon the simplest feasible methods and equipment, with particular emphasis upon operation at remote sites. The basic requirements are an antenna, a receiver, a recorder, and a timing system. These requirements are essentially the same whether one considers a station operated at a laboratory with elaborate equipment and highly-trained personnel or at a remote field site having only absolutely necessary facilities. Principal requirements for this sort of operation are a high degree of reliability, adequate technical performance, and the nearest practicable approach to automatic operation. Only if these criteria are met can records of good quality be obtained over long periods by relatively inexperienced personnel. It is also important to a synoptic program that data taken at different locations and times have comparable characteristics. Therefore, standards for data collection will be discussed in a later section of this report.

SCIENTIFIC OBJECTIVES OF THE BEACON TRANSMITTER PROGRAM

An orbiting beacon provides the means for a synoptic study of the ionosphere as it varies in time and space. One of the principal features of this research technique is the simplicity of the equipment and of the methods of data reduction. Another is the ease with which observations can be made over a very long period.

The collected data can be used to determine the columnar electron content (or integrated electron density) and the distribution of irregularities in the ionosphere. Although the columnar electron content is not generally regarded as a parameter directly applicable to engineering problems, it is useful in interpreting other data, such as ionograms; it serves as a check on determinations of the electron density profile; and it is readily correlated with other geophysical phenomena such as magnetic activity. The general method of determining columnar electron content has been demonstrated by several investigators and may be regarded as well established. It is therefore appropriate to undertake a long term program of determining temporal changes in the columnar electron content.
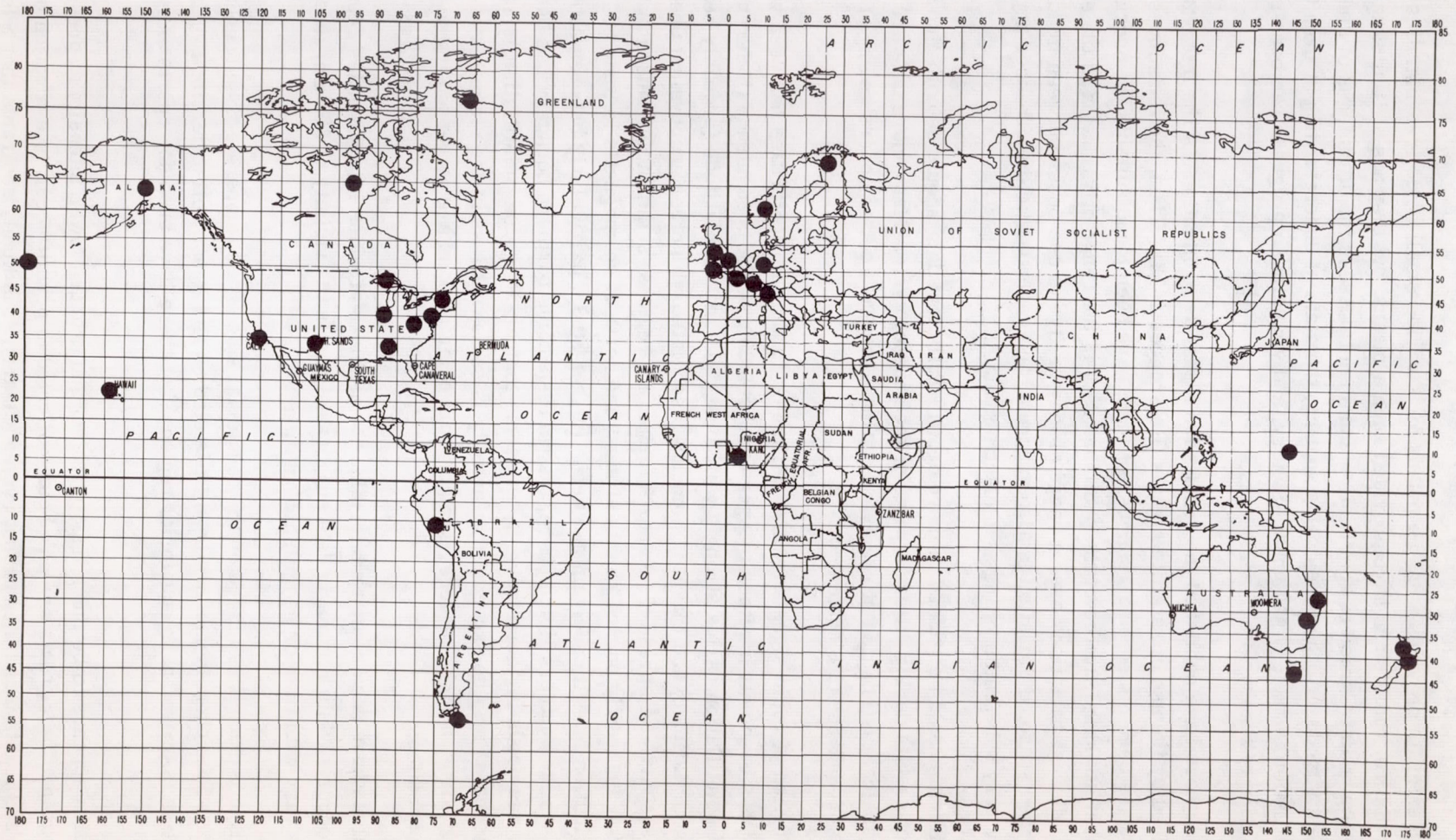
Figure 1 – World-wide distribution of known ionosphere-beacon satellite monitoring stations

A beacon satellite provides a unique means for studying small scale irregularities in the ionosphere. Heretofore, radio stars have provided such a means, but they are of limited utility in determining the latitude distribution of scintillation and do not possess the advantages of single-frequency phase-coherent signals. At the time of this writing, the state of understanding of even the "morphology" of scintillation is sketchy and unsatisfactory, and virtually no progress has been made toward the reconciliation of theory with observations.

Several authors have published the results from past determinations of the integrated electron content obtained by the use of satellite signals (References 1-13). Thus, the techniques of observation and analysis have been tested, and a number of them have been found suitable for operational use. One of the most striking features of the published data is the range of variation in the electron content. Typical diurnal variations over a range of four or five to one occur between midday and midnight. A marked seasonal variation is also apparent, and geomagnetic disturbances appear to be accompanied by very substantial changes in electron content.

These effects should be studied in more detail. Sufficient data should be collected to permit the comparison of results during different parts of the sunspot cycle. Many more data are needed, from a wide geographical distribution of receiving stations, to give a better understanding of the latitude and longitude dependence of electron content.

The distortion of radio signals from satellites by random irregularities has been widely studied, but the result has been only a rather meager understanding of the phenomenon (References 14-27). It is known that scintillation varies strongly with local time and with latitude (probably being associated with geomagnetic latitude) and that it is somehow associated with other geophysical phenomena such as magnetic activity and spread F. In north temperate regions, scintillation caused by irregularities in the F region apparently occurs mostly at night and north of geomagnetic latitude 50° north. This latitude distribution is still uncertain and needs further study, particularly between about 120° west and 50° east. In the Southern Hemisphere, the corresponding northern boundary has been observed only recently and needs further study. If, as seems logical, F region scintillation is associated with the auroral zones, it may be expected that activity is somewhat less in the vicinities of the magnetic poles. Observations of high frequency signals from polar regions are as yet too few to permit resolution of this question.

Some efforts have been made to determine the altitudes at which irregularities responsible for scintillation occur. While results to date suggest heights in the vicinity of 300 km, it is not known how these heights vary with time or geographic position.

Scintillation is sometimes noted on the equatorial side of the temperate zone boundaries, usually in the daytime. This phenomenon has been little studied and is not well understood. Also, it is known that scintillation is prevalent in equatorial regions, but there have been no reports of systematic studies.

Scintillation appears to be much less prevalent and of much lower intensity at present than it was in 1958-59, but insufficient data are now being collected to permit accurate evaluation of the relationship between scintillation and the sunspot cycle. Clearly, it is highly desirable that a long-term effort

be instituted to gather scintillation data, involving many observing stations with a wide geographical distribution.

Irregularities in electron density of the order of hundreds of kilometers in extent have been reported by various researchers (References 9 and 11). Satellites in low orbits are very useful for studying such phenomena, since they cover large regions in short periods of time.

Many reports of unusual radio propagation phenomena observed by means of satellites have been published (References 18 and 28-35). Most of these observations were from low satellites which were within the F region; however, it is of scientific interest to determine whether the antipodal propagation effect, for example, also occurs for satellites in higher orbits.

DESIRABLE CHARACTERISTICS OF A BEACON TRANSMITTER

To give the widest geographical coverage and permit studies of the polar ionospheres, the satellite orbit should be inclined approximately 90 degrees from the earth's equatorial plane. In order to minimize certain difficulties in data analysis and to keep the satellite well above the regions producing scintillation and above most of the electrons in the ionosphere, the height should be at least 1000 km. A circular orbit also simplifies analysis. An orbit meeting these criteria will be relatively free from atmosphere drag, permitting accurate prediction of observation times and simplifying the computation of accurate post-factum ephemerides.

In the past considerable difficulty has been experienced as a result of spinning or tumbling of satellites. It is desirable either that the antennas have electromagnetic symmetry about the spin axis or that the satellite be stabilized in such a way that the antenna aspect presented to a ground observer changes only very slowly, say at one revolution in several minutes, or less.

For reasons that will be apparent later, it is very useful to have several transmitting frequencies and it is important that they be locked together in phase. Obviously, enough power should be radiated to permit reception with good signal-to-noise ratios by simple equipment on the ground. For the orbits under consideration, a few hundred milliwatts is sufficient for high frequency radiation whereas 50 mw or more is needed in the VHF band.

The emissions should be purely continuous-wave in nature, with no modulation which would confuse a phase-locked receiver. A sequence of frequencies which has been chosen as appropriate for such an experiment is 20.005, 40.010, 41.010, and 360.080 Mc, all harmonics of 1.00025 Mc. It is expected that future ionosphere beacon satellites of the U.S. will utilize these frequencies.

Beacon experiments have been performed often enough so that in the future they should be considered "monitor" rather than "definitive" experiments. Thus, the satellite should transmit for the longest possible period. If the desired orbital characteristics are attained, the satellite will have an orbital lifetime of many years; and through use of solar power supplies it is also feasible to plan for a comparable transmitter lifetime. To guard against the nuisance of a transmitting satellite whose usefulness has ceased, a reliable means of turning off the transmitter must be provided; but it should

also be possible to turn it on again if the occasion demands. It is desirable that the actual experiment be conducted during at least half of a sunspot cycle, and preferably longer.

THE FARADAY ROTATION METHOD OF MEASURING INTEGRATED ELECTRON DENSITY

Basis of the Measurements

In traversing a magnetoionic medium a plane wave undergoes a rotation of its plane of polarization, the total angle of rotation depending approximately on the average magnetic field component in the direction of propagation and on the total number of electrons in a column one square meter in cross section and equal in length to the length of the propagation path. As a satellite moves continuously with respect to the magnetic field, there occurs a time-variation of the total angle of rotation that the electric vector experiences along the propagation path. The result is a continuous rotation of the electric vector at the receiving point. The magnetic field of the earth is known to the desired accuracy; therefore, the total angle of rotation along the transmission path determines, approximately, the columnar electron content along the path. In practice it generally is not possible to measure the total angle of rotation; instead, the *rate* of rotation and the number of complete rotations between two points on the orbit are determined. Methods have been developed to determine the total electron content from these data.

The principal advantage of the Faraday rotation method of determining electron content is its simplicity, both in data collection and in analysis. Other methods may yield more detailed and accurate data, but at the cost of far greater effort and expense. The Faraday rotation method seems well suited for long-term monitoring experiments.

"Single Frequency" Methods

Measurement of the rate of change of polarization angle at a given instant yields an approximate determination of the electron content. Theoretically, a determination can be made for a given instant of time (that is, for a given ray path). In practice it is necessary to measure the number of revolutions of the electric vector in a finite time in order to determine the rate accurately enough. This *rate of rotation method* probably constitutes the simplest means of obtaining an approximation of the electron content of the ionosphere.

The basic equation, as derived by Bowhill (Reference 36), is

$$\int N\,dh = \frac{z f^2}{K_1 H_x v_x} \dot{\Omega} ,$$

(1)

where

$\int N\,dh$ = number of electrons in a column 1 meter square extending from the satellite to the receiver;

$$K_1 = \frac{e^3 \mu_0}{8\pi^2 m^2 C \epsilon_0} = 0.0297 \quad \text{(mks rationalized units)};$$

z = altitude of the satellite (m);

f = radio frequency (cps);

H_x = component of the earth's magnetic field in the direction of v_x (amp/m);

v_x = horizontal component of the satellite velocity with respect to the observer (m/sec);

$\dot{\Omega}$ = rate of change of the Faraday rotation angle (rad/sec).

This formula was derived under the assumptions of a horizontally moving satellite, a plane earth, and a horizontally stratified ionosphere. Garriott (Reference 7) has discussed the errors involved in neglecting the vertical component of velocity and has developed a method of correction. In addition, it is assumed that the frequency is high compared with the maximum critical frequency of the ionosphere, and that the ray path is a straight line. All these assumptions lead us to expect limited accuracy from the method, and most observers have preferred to resort to more accurate formulas requiring more elaborate observational techniques. However, the regular and sporadic variations in electron densities observed with the more accurate methods are large compared with the errors expected to arise from the aforementioned assumptions. In fact, detailed comparison of data (Reference 8) reduced by Equation 1 with data reduced by more accurate methods (Reference 12) shows that the major features are the same. Thus Equation 1, whose application does not require the use of an electronic computer, is useful for the quick evaluation of large amounts of data.

The total angle of Faraday rotation is given approximately (Reference 37) by

$$\Omega \approx \frac{K_1}{f^2} \, \overline{M} \int N \, dh, \tag{2}$$

where

Ω is the total angle of rotation of the electric vector in traversing the ionosphere,

H is the magnetic field (amp/m),

ϕ is the angle between H and the ray,

i is the vertical angle of the ray, and

$\overline{M}$ is a suitable average value of $H \cos \phi \sec i$.

Unfortunately, under typical conditions Ω amounts to many complete revolutions so that the integral in Equation 2 can be determined only ambiguously. However, if the ionosphere is assumed to have no horizontal gradients and if the satellite is above most of the electrons in the ionosphere, then $\int N \, dh$ will be the same for any path. Consider the satellite to move from point 1 to point 2. The difference $\Omega_1 - \Omega_2$ is the differential rotation of the electric vector seen by the observer during this interval. The integrated electron density can then be determined unambiguously as

$$\int N\, dh \;=\; \frac{\Omega_1 - \Omega_2}{\overline{M}_1 - \overline{M}_2}\; \frac{f^2}{K_1}\;\;, \tag{3}$$

in what is therefore called the *differential rotation method*. Here $\overline{M}$ must be computed carefully from measured values at ground level. A computer program has been prepared for this purpose (References 12 and 38) which can be used to compute the necessary values of $\overline{M}$ for any satellite position as viewed from any geographical location.

Second-Order Faraday Rotation Methods

The differential rotation method involves essentially the same assumptions and approximations as the rate of rotation method. It is hoped that future ionosphere beacon satellites will be in high, circular orbits so that the effects of neglecting the vertical component of velocity are minimized. Corrections can be made for the high-frequency approximation and for refraction by using two widely separated frequencies and reducing the data by means of second-order formulas given by Yeh (Reference 39). It is convenient (but not necessary) for this purpose to use two harmonically related frequencies, say 20 and 40 Mc. The use of these methods indicates that the errors caused by refraction and the high-frequency approximation are in the neighborhood of 5 percent for close passages and up to 30 percent for distant passages.

In the *second-order rate of rotation method* the integrated electron density is given (Reference 39) by

$$\int N\, dh \;=\; \frac{2 f^2}{K_1\, H_x\, v_x}\; \frac{1}{m^2 - 1} \left[m^4 \dot{\Omega}(mf) - \dot{\Omega}(f) \right]\;\;, \tag{4}$$

in which m is the ratio of the higher to the lower frequency and the other symbols are as defined before, $\dot{\Omega}(mf)$ and $\dot{\Omega}(f)$ being the rates of Faraday rotation of the two frequencies.

A similar second-order extension may be made of the *differential rotation method*. The integrated electron density is given by

$$\int N\, dh \;=\; \frac{f^2}{K_1\, (m^2 - 1)}\; \frac{m^4 \Delta\Omega(mf) - \Delta\Omega(f)}{\overline{M}_1 - \overline{M}_2}\;\;, \tag{5}$$

in which $\Delta\Omega(mf)$ and $\Delta\Omega(f)$ are the rotations (in radians) of the frequencies mf and f observed as the satellite moves from point 1 to point 2, and $\overline{M}_1$ and $\overline{M}_2$ are the magnetic field geometric factors for the two points.

"Closely Spaced Frequencies" Method

The use of two closely spaced frequencies permits an unambiguous determination of the total angle Ω through which the electric vector is rotated in traversing the ionosphere. By using

plane-polarized antennas and receivers with logarithmic amplitude response, records such as those shown in Figure 2 will be obtained. It is most convenient to reckon in terms of complete revolutions, as indicated by the nulls in the pattern; a null occurs every half revolution. The working formulas (referred to Figure 2) are:

$$\delta\Omega = \frac{2\pi(T_2 - T_1)}{T_1} + n\pi \text{ radians}, \quad n = 0, 1, 2, \ldots ; \tag{6}$$

$$\int N\,dh = \frac{f^2}{K_1}\frac{\Omega}{\overline{M}} ; \tag{7}$$

$$\frac{\partial\Omega}{\partial f} = \frac{-2\Omega}{f} \approx \frac{\delta\Omega}{\delta f} ; \tag{8}$$

$$\Omega = -\frac{f}{2}\frac{\delta\Omega}{\delta f} . \tag{9}$$

The electron content is determined by substituting from Equations 6 and 9 into Equation 7. This is a first-order determination; however, it is anticipated that it will be used at about 40 Mc, at which frequency the refraction and high-frequency approximation errors should be quite small.

The principal advantages of this method are simplicity in the data reduction, and the ability to make an unambiguous measurement of integrated electron content in a relatively short interval of time. The latter feature is important in evaluating horizontal variations of electron distribution.
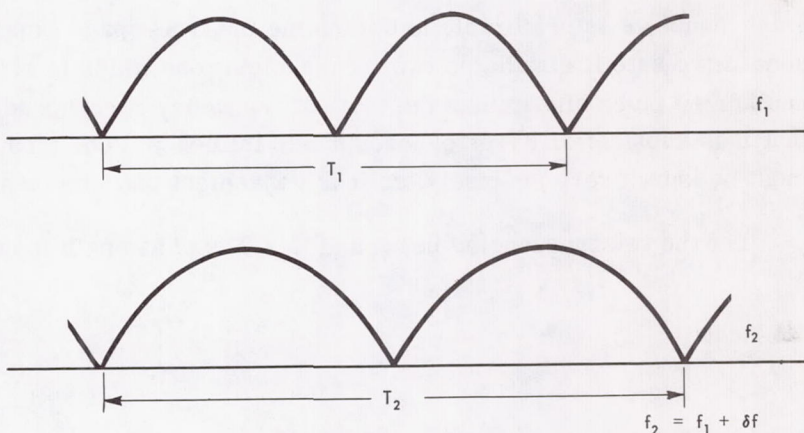
Figure 2—Typical received signal obtained in the "Closely Spaced Frequencies" method, employing plane-polarized antennas and receivers with logarithmic amplitude response

THE DOPPLER METHOD OF MEASURING INTEGRATED ELECTRON DENSITY

The high velocity of a satellite relative to a ground-based observer results in a substantial Doppler shift in the observed frequency. In the ionosphere, the phase velocity depends upon the electron density; thus, the observed frequency also depends upon this parameter. Observation of the exact frequency as a function of time can be used to determine the electron content of the ionosphere.

Many authors have discussed the Doppler method of electron content measurement and several series of actual measurements have been reported (References 4, 10, 11, 15, and 40-48). Most of the

actual measurements have involved elaborate receiving and frequency-measuring equipment — for example, phase-locked receivers capable of determining the phase difference between a satellite signal and one of its harmonics. It is possible to obtain excellent measurements in this way, but at the cost of expensive installations and constant attention by highly skilled technicians. In particular, a phase-locked receiver must be attended continually during a satellite passage lest momentary reductions of signal strength cause the tracking loop to unlock, resulting in loss of the data. Phase-locked receivers are capable of very great sensitivity by virtue of the narrow bandwidths that can be achieved; however, ionosphere beacon satellites to be available in the near future are expected to have adequate power to permit the use of simpler receiving equipment.

It is concluded that the more elaborate techniques of Doppler determination of electron content are more suitable for use at well staffed and well equipped laboratories, and that simpler equipment should be relied upon for field station use. It may well happen that Faraday rotation methods prove to be best for field use; however, for the sake of completeness a method of Doppler analysis with relatively simple equipment, suggested by the work of Ross (Reference 10), will be described here.

In order to determine the ionospheric effect on the Doppler shift, it is necessary to know the Doppler shift that would occur in the absence of the ionosphere. This, in turn, implies an accurate knowledge of the orbit and of the radiated frequency of the satellite. In many cases such knowledge does not exist; hence, it is preferable to determine the free-space Doppler shift by observation. This can be done if the satellite radiates two frequencies: one which is strongly affected by the ionosphere, and another so much higher than the critical frequency corresponding to the maximum electron density that it is substantially free of ionospheric influence. The frequency ratio between the two signals must be known very precisely, so it is convenient that one be a harmonic of the other.

Let the two frequencies be f_1 and f_2. The phase path length corresponding to either is

$$P = \int_r^s n \, ds \ , \tag{10}$$

where n is the index of refraction for the frequency in question and ds is an element of path length. The number of wave cycles between the satellite at s and the receiver at r is

$$\int_r^s \frac{ds}{\lambda} = \frac{P}{\lambda_0} \ , \tag{11}$$

in which λ and λ_0 are the wavelengths in the medium and in free space, respectively. The observed frequency is the emitted frequency minus the rate of change of the number of cycles along the path, $f - \dot{P}/\lambda_0$, and the "Doppler shift" is the difference between the observed and emitted frequencies $-\dot{P}/\lambda_0$.

In the ionosphere the index of refraction is given by

$$n^2 = 1 - \frac{80.6 \, N}{f^2} \ , \tag{12}$$

or, if the frequency is well above the critical frequency, by

$$n \approx 1 - \frac{40.3\, N}{f^2} \; . \tag{13}$$

The phase path length in the ionosphere is thus

$$P_i = \int_r^s \left(1 - \frac{40.3N}{f^2}\right) ds \; , \tag{14}$$

and in the absence of the ionosphere it is simply

$$P_{fs} = \int_r^s ds \; . \tag{15}$$

The difference between these quantities, sometimes called the "phase path defect" (Reference 47), is

$$\Delta P = P_{fs} - P_i = \int_r^s (1-n)\, ds \;\; \approx \;\; \frac{40.3}{f^2} \int_r^s N\, ds \; . \tag{16}$$

At any point along the ray path

$$ds = \sec i\, dh \; , \tag{17}$$

where dh is an element of length in the vertical direction and i is the local zenith angle of the ray path. If attention is restricted to those parts of the orbit rather near the zenith and if i_F is the value of i near the maximum of density of the F region, then

$$ds \approx \sec i_F\, dh \; , \tag{18}$$

and

$$\Delta P \approx \frac{40.3 \sec i_F}{f^2} \int_r^s N\, dh \; . \tag{19}$$

It happens that the ratio $\Delta P/P_{fs}$ is nearly constant if the orbit is nearly circular and the ionosphere is spherically stratified. Thus

$$\frac{\Delta P}{P_{fs}} = \frac{\Delta \dot{P}}{\dot{P}_{fs}} = \frac{\Delta \ddot{P}}{\ddot{P}_{fs}} \; , \tag{20}$$

where $\dot{P}$ is the rate of change of frequency and, in particular, $\ddot{P}_{fs}$ is the maximum slope of the free-space Doppler shift curve when plotted as a function of time. In practice, $\ddot{P}_{fs}$ and $\Delta \ddot{P}$ can be evaluated

directly from observation, provided that the two frequencies are appropriately chosen from Equations 19 and 20:

$$\int_r^s N\,dh = \frac{f^2 P_{f_s} \cos i_F}{40.3} \frac{\Delta \ddot{P}}{\ddot{P}_{f_s}} \,,\tag{21}$$

where P_{f_s} is simply the geometrical distance from satellite to receiver and can be determined from the known orbital elements, as can i_F; the symbol f refers to the lower of the two radiated frequencies; and $\Delta\ddot{P}$ is determined by comparing the Doppler shifts on the two frequencies.

To illustrate the determination of $\Delta\ddot{P}$ and $\ddot{P}_{f_s}$ consider, for example, a satellite radiating phase-locked signals on 40 and 360 Mc. Since ΔP varies inversely as the square of the frequency, the phase path defect will be about 81 times as large on 40 as on 360 Mc. Consider, then, that the 360 Mc wave is not influenced by the ionosphere. A separate superheterodyne radio receiver is used for each frequency (Figure 3). An additional "beating oscillator" is provided which has phase-locked outputs near 40 and 360 Mc, and these outputs are injected into the RF input terminals of the respective receivers. Thus, an AF beat is produced in each receiver, the 360 Mc receiver's beat frequency being *approximately* nine times that of the 40 Mc receiver. Next, the beat note of the 40 Mc receiver is multiplied in frequency by a factor of nine and mixed with the beat note from the 360 Mc receiver, and the "difference frequency" is selected by means of an appropriate filter. This difference frequency is $\Delta\dot{P}/\lambda_0$ and its rate of change is $\Delta\ddot{P}/\lambda_0$. The difference frequency is low enough to be recorded directly on a graphic record. At the same time, the beat frequency from the 360 Mc receiver is recorded separately to permit determination of $\ddot{P}_{f_s}$ or $\dot{P}_{f_s}$.
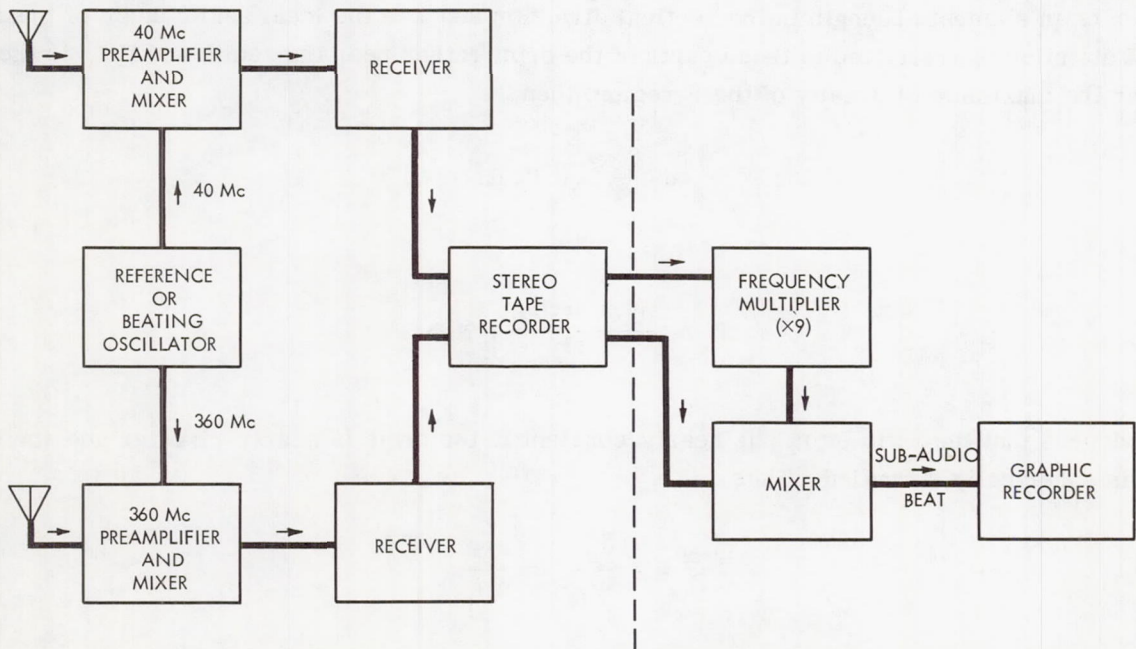
Figure 3—Simplified two-frequency Doppler system

The records will appear approximately as shown in Figure 4, in which the upper curve is the 360 Mc Doppler shift, approximately equal to $\dot{P}_{fs}$, and the lower curve is the difference frequency or "dispersive Doppler frequency," $\Delta\dot{P}/\lambda_0$. The slope of the upper curve at the inflection point is P_{fs}/λ_0.

Only the two receivers, the beating oscillator, and the tape recorder need be installed at the field station. All equipment to the right of the dashed line in Figure 3 may be installed at the central laboratory, and one setup of this kind can be used to transcribe the tape records from several field stations.

The foregoing analysis is the simplest one possible and involves the following assumptions: The satellite is near the zenith and the ionosphere is spherically stratified. The orbit is circular. The high-frequency approximation is satisfied for the lower of the two frequencies, and the higher frequency is so high that its phase velocity is almost that of free space. The effect of the magnetic field is neglected.
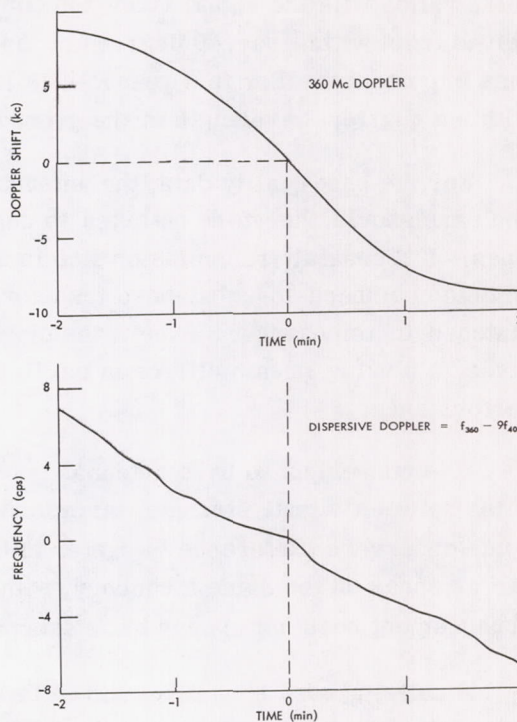
Figure 4—Doppler records

THE FARADAY ROTATION OBSERVATION STATION

The Site

It is essential that a quiet site be chosen, as noisy records are apt to be useless. Although the contemplated signal strengths will be more than adequate in most cases, proximity to heavily travelled highways or streets, industrial or commercial activity, or densely settled residential areas will inevitably cause trouble. Automobile ignition systems, farm machinery, neon signs, fluorescent lighting, defective power transformers, and high-voltage power lines are frequent causes of interference at the frequencies in question. Fortunately, noise of these types attenuates rapidly with distance and it has been found that locating the receiving equipment a mile or so from the offending source usually provides sufficient isolation. Thus, a well-isolated site should be chosen.

Terrain does not appear to be particularly important, though reasonably flat ground is desirable. Only if it is desired to erect a radio-interferometer for position measuring purposes is a flat area required, and even then it may be possible to use level metal ground planes erected on sloping terrain.

Antennas

For Faraday rotation measurements the antennas must be plane polarized. Simple half-wavelength dipoles have been used almost universally for this purpose. As the frequencies used are in the HF or

the lower VHF bands, a half-wavelength dipole has adequate effective area to yield good signal-to-noise ratios with the signal strengths contemplated. The most valuable Faraday rotation data are received from within, say, 40 degrees of the zenith, whereas data from low-altitude angles are of much less importance. For this reason it is logical that the dipoles be horizontally polarized and situated within a quarter-wavelength of the ground.

For the best quality data, the antenna should have a negligible circular component of polarization, and care should therefore be taken to suppress the effects of antenna currents on the transmission lines. If a coaxial transmission line is used, the antenna should be connected through a carefully adjusted balanced-to-unbalanced transformer. Open-wire lines should be symmetrical and properly matched in impedance. If the transmission lines are of substantial length, consideration should be given to placing preamplifiers in the field near the antennas in order to improve the system noise performance.

It is convenient to have antennas on different frequencies oriented similarly, in order to distinguish between signal strength variations due to Faraday rotation and those due to satellite motion. Some observers (Reference 7) prefer to keep track of the sense of the Faraday rotation; this requires two antennas on the same frequency, with different directional orientation. In general, however, this arrangement does not appear to be essential.

Finally, a word should be said in favor of substantial construction. Experience has shown that a surprisingly large proportion of the technical difficulties experienced by field stations are due to broken antenna or transmission-line wires or to poor connections. The use of sturdy wooden structures and heavy gauge copper-clad steel wires, and proper securing of transmission lines to prevent repeated flexing at connections, are worthwhile precautions. Outdoor splices in coaxial cables should be avoided.

Receivers

Receivers for Faraday-rotation recording are invariably of the superheterodyne type as illustrated in Figure 5. As the radio frequencies are above about 20 Mc and the required bandwidths quite narrow, a double-conversion system is usually used. In the past, many high grade communications receivers have been so employed with very good results, including the Hammarlund SP-600, the Collins 51-J, and the military R-390. For best results some modifications are usually required, as will be discussed below. When contemplating a long-term program of routine data gathering, however, it is appropriate to consider receivers specially designed and built for the task. The general purpose receivers usually are very heavy and intricate and thus difficult to maintain, usually have features not required for the task, and often have some undesirable characteristics.

In order to achieve optimum signal-to-noise ratios it is desirable that the overall bandwidth be as narrow as possible. The limit is set by the Doppler shift of the signal. At 20 Mc this amounts to about 500 cps for a close orbit, requiring a total bandwidth of 1 kc. At 40 Mc the effect is doubled, requiring a bandwidth of 2 kc. The highest frequency likely to be used for Faraday rotation studies is 54 Mc, so that a standard 3-db bandwidth of slightly over 2.5 kc should accomodate all cases. This bandwidth is established in the second IF stage. Ceramic IF filters at 455 kc are now available which require no

FIRST RF AMPLIFIER 20, 40, OR 54 Mc → **SECOND RF AMPLIFIER** → **FIRST MIXER** → 1.5 Mc → **SECOND MIXER** → 455 kc

FIRST LOCAL CRYSTAL OSCILLATOR

SECOND LOCAL CRYSTAL OSCILLATOR

AGC Bus

AGC AMPLIFIER ← **AGC DETECTOR** ← **IF AMPLIFIER STRIP (CERAMIC FILTERS): TWO STAGES**

TO RECORDER

THIRD IF: ONE STAGE → **AUDIO DETECTOR** → **AUDIO AMPLIFIER: ONE STAGE**

AUDIO OUTPUT
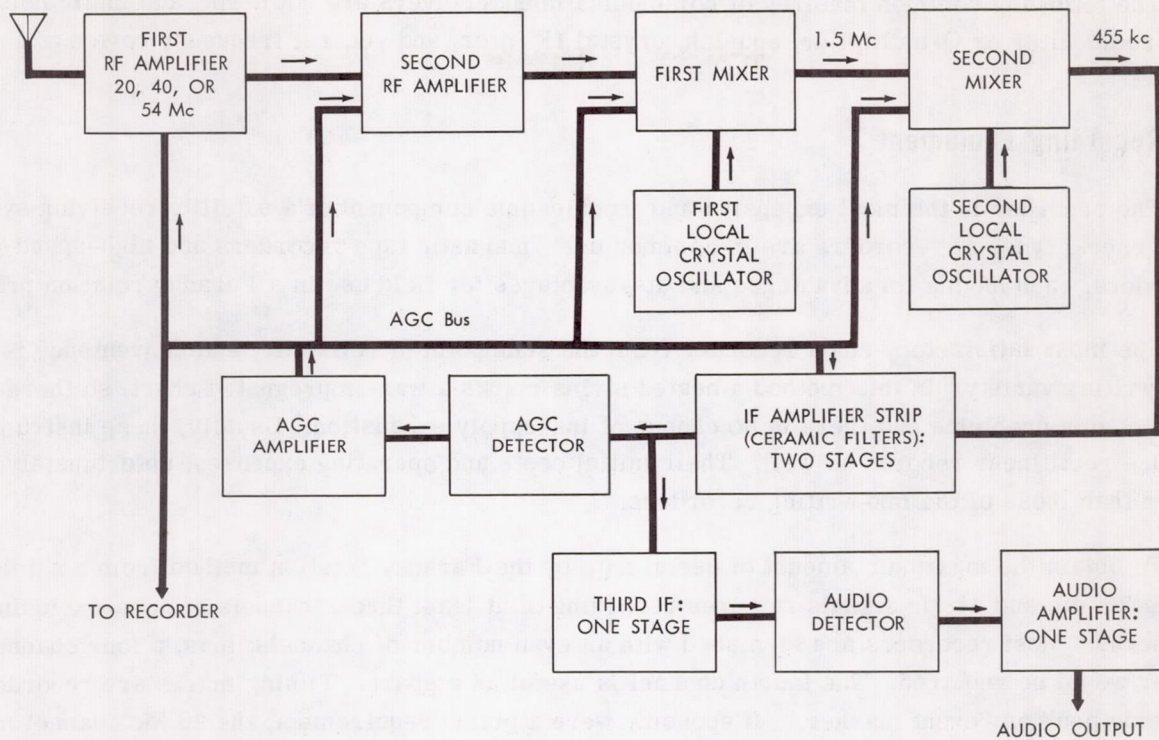
Figure 5—Superheterodyne receiver for Faraday rotation observations

adjustment and which apparently are drift-free over long periods of time. Combined with transistor amplifiers, these should permit the construction of a virtually maintenance-free IF strip. These can be made very economically in the form of standard modules for ease of replacement.

A low-noise RF amplifier is needed to insure that the sky noise, rather than receiver noise, limits the performance of the system. Two crystal-controlled local oscillators are needed. The first crystal is changed to accommodate satellites of different frequencies. In this way there is little chance that the receiver will be mistuned.

Particular attention should be paid to the automatic gain control circuits. It is desirable to have a logarithmic amplitude response, both to prevent saturation of the receiver or recorder and to sharpen the nulls of the Faraday rotation records. Satellite signals are usually faint, so the AGC circuits should develop appreciable voltage at receiver inputs of the order of 0.2 microvolt. If a commercially built receiver is used it is usually necessary to modify the AGC circuits to remove the "delay bias" in order to accomplish logarithmic response down to these low input levels. The AGC time constant must be small, not higher than 0.1 second for Faraday rotation and 0.02 second for scintillation.

Although not strictly necessary, it is very convenient to have a beat-frequency oscillator in order to permit qualitative checks of the presence of the satellite signal, signal strength, nature and identity of interfering signals, and so on. It is essential, however, that the BFO should not contribute to the AGC voltage. It is also convenient to have an "s-meter" to permit visual monitoring of the signal strengths, and an audio detector, amplifier, and loudspeaker for use with the BFO.

The following common features of communications receivers are not used: automatic noise limiter, audio filter or Q-multiplier, squelch, crystal IF filter, and general frequency coverage.

Recording Equipment

The recorder is the most expensive and troublesome component of a satellite receiving system. Two general types of recorders are in common use: magnetic tape recorders and high-speed graphic recorders, each having its advantages and disadvantages for field use in a Faraday rotation program.

The most satisfactory chart recorder from the standpoint of reliability and convenience is the heat-writing variety. In this method a heated stylus marks a wax-impregnated chart, so there are no pen-clogging problems and there is no chance of ink-supply exhaustion. Usually, these instruments produce rectilinear records as well. Their initial costs and operating expenses, unfortunately, are higher than those of the ink-writing recorders.

To obtain the maximum amount of useful data by the Faraday rotation method from a satellite having 20, 40, and 41 Mc signals requires recording of at least three channels of data, excluding timing marks. Most recorders are furnished with an even number of channels; thus, a four channel recorder would be required. The fourth channel is useful as a spare. Timing marks are recorded on the "side pen" or "event marker." If economy were a prime requirement, the 20 Mc channel might be eliminated and a two channel recorder used, at the sacrifice of the greater scintillation sensitivity and the corrections for refraction and the high-frequency approximation that are obtainable with the 20 Mc signal.

Acceptable specifications for a chart recorder for Faraday rotation work are as follows:

Number of channels: minimum 2, 3 preferred; event marker.
Frequency response: 0 to 50 cps or better.
Chart speed: 5 or 10 mm/sec, preferably both.
Type of recording: Ink-writing or heat-writing.
Transistorized amplifiers desirable for reliability.

Magnetic tape recording can also be used. It has the disadvantages that no visual record is available for immediate inspection, and that it is ultimately necessary to re-record the signals on a graphic recorder. Usually the magnetic tapes from several field stations are sent to a central laboratory where they can be transcribed; thus only one graphic recorder is needed. Probably the best practice is to transform the variable AGC voltages from the receivers into variable-frequency audio tones by means of voltage-controlled oscillators. Several of these audio tones of different frequencies can be recorded on the same tape channel and separated later by means of appropriate filters. Frequency discriminators are used to convert the tones back to varying dc signals for graphic recording.

For Faraday rotation work the tape recorders need not be of extremely high quality, but should be very reliable in operation. The principal typical deficiency of an inexpensive tape recorder of the consumer market variety is inconstant tape speed (jitter, wow, flutter) which results in frequency modulation of the record. If not too severe, this should not be a serious defect for purposes of Fara-

day rotation recording. In any event, it is possible to overcome this problem by recording a constant, standard tone along with the signals, and later electronically subtracting the dc output of the discriminator associated with this tone from the outputs associated with all the other channels. Thus, the graphic recordings should be free from jitter. By proper spacing of the tones in frequency, it should be possible to record five channels of data, including time signals and a speed-calibration tone, on one tape. If a "stereo" recorder is used, one channel can be reserved for voice announcements, time signals, and the speed-calibration tone; and the other channel for the three satellite signals.

By comparison with the graphic recorder the magnetic tape recorder has the following advantages: It is less expensive. A record on tape can be transcribed to a graphic record at any desired speed and any desired number of copies can be made. Frequently, especially when studying scintillation, it is desirable to have graphic records at more than one speed. If economy is a principal requirement, the magnetic tapes can be re-used after they have been transcribed. Magnetic tape recorders are generally more adaptable to unattended operation, though the heat-writing graphic recorders are quite usable in this way. The main disadvantage of the magnetic recorder is the lack of a visual record to assist the operator in making adjustments and corrections while a pass is in progress. As the receiving equipment described in this report is designed for a minimum of operator attention and adjustment, it may well be that this consideration is not applicable.

For an organization planning to operate several field stations the choice of magnetic tape recorders seems a good one, with one graphic recorder and associated filters and discriminators at the central data-handling facility. If only one station is to be operated, however, recording directly on a graphic recorder eliminates the need for the magnetic recorder and associated equipment.

Time Signals

To be of any scientific value, all satellite recordings must contain precise, unambiguous time marks. An error of, say, 1/4 second will generally be quite acceptable, but errors of several seconds will not.

Time marks can be derived from many of the radio time services, and, if the station is so situated that regular time signals can be received reliably, these can be recorded directly from the radio receiver onto the time channel of the magnetic tape. For a graphic recorder, the time ticks can be filtered, rectified, and transformed into low impedance pulses to operate the event-marker pen. These radio time signals are often received by means of ionospheric propagation, however, and are not always reliable. Many of the stations use the same frequencies, and they sometimes interfere. For example, at Adak, Alaska, signals from stations WWVH and JJY interfere so badly that they are useless for automatic registration.

Recently a number of stations have begun transmitting time signals on VLF wavelengths, for example, NBA on 18 kc in the Panama Canal Zone. This station is powerful enough to be heard anywhere on earth. A pocket-sized battery-powered transistorized receiver with a ferrite "loopstick" antenna has been constructed which is capable of receiving these signals sufficiently well for satellite recording, and it has been found that there is essentially no variation of signal strengths with time. Apparently, however, no standard time-signal format has been adopted by this station; and its usefulness is somewhat limited until this is done.

A relatively inexpensive local time-standard can be built by using a tuning fork oscillator and power amplifier to drive a clock motor. Such a device, utilizing a cam-operated switch to provide time ticks every ten seconds with a different identifying tick every minute, demonstrated a precision equivalent to about one second of error per week. Radio time signals can usually be heard with adequate quality to calibrate a local time-standard, even though not good enough for direct recording.

The ideal timing system would be a quartz-crystal oscillator driving a chain of frequency dividers to give hour, minute, and second ticks. This system is the most expensive, but is capable of very high accuracy and can also provide a program function for unattended automatic operation of the satellite recording equipment.

In addition to time marks for the satellite records it is very useful to have a "program clock" to permit scheduling of unattended satellite recording. As was mentioned above, a quartz-crystal oscillator and frequency divider chain can provide for this function, but at relatively high cost. The tuning-fork frequency standard can be used to drive any of a variety of low-cost commercially available program timers that are satisfactory for the purpose. When a program clock is used, it is necessary that unambiguous time marks be placed on the chart in addition to the regular second or minute ticks.

STANDARDS

In order that the results from different stations be comparable, some degree of standardization of observing practice must be achieved. It is always tempting to the observer to experiment with different methods, but it is important to a long-range monitoring program that the records be taken in a consistent manner throughout the program. Experiments with different methods should be performed independently of the routine data-gathering effort.

Suggested standards for recording satellite data are listed below.

Faraday Rotation and Scintillation

Amplitude scintillation can be studied directly from the records of amplitude variation due to Faraday rotation. The following standards have been found suitable:

Time Marks — Accurate to 0.5 second. A reference should be made at least every minute, preferably every few seconds, and unambiguous time marks should be made at least every five minutes. At least one, and preferably more, of the unambiguous time marks must be available on each record.

Chart Speed — For Faraday rotation studies, chart speeds of 5 to 10 mm per second are generally satisfactory. For passages in the vicinity of noon and at tropical latitudes the higher speed is almost mandatory. In studying scintillation it may sometimes be advantageous to increase the chart speed to 25 or 50 mm per second; however, it is recommended that this be done on an auxiliary recorder so as not to disturb the routine arrangements. For this purpose a magnetic tape recorder is very useful; the tape can be recorded at any convenient speed and can then be transcribed any number of times to paper charts running at a variety of speeds.

Receiving System Time-Constants — As was mentioned earlier, the AGC time constant should be not greater than 0.1 second for Faraday rotation recording and not greater than 0.02 second for scintillation. The same limitations apply to other parts of the system, including recorders.

Signal-to-Noise Ratio — It is difficult to place a numerical specification on the necessary signal-to-noise ratio for good results. Suffice it to say that the better the quality of the record, the easier is the analysis of the data. With reasonable care it has been found possible to produce records that are essentially noise-free; that is, on which the Faraday rotation and scintillation amplitude variations are very well defined, but on which the noise variations are barely discernible. Satellites specifically designed for beacon use will generally have adequate power to produce such records with dipole antennas and receivers such as those described herein.

Amplitude Calibration — No amplitude calibration is necessary for Faraday rotation analysis. For investigation of the geographical and temporal distributions of scintillations, infrequent calibrations may be useful. However, for studies of the detailed structure of the signals and of the irregularities producing scintillation, it is important that frequency calibration of the amplitude-response characteristics be made with a standard signal generator.

Record Annotation and Logging — One of the most persistent difficulties in the collection of high-quality satellite records is the failure of operators properly to annotate the records. Each record should bear the following information:

Date
Time of beginning and ending of pass
Unambiguous and precise identification of one or more of the periodic time marks on the chart
Time system used (GMT or zone time)
Antenna identification for each trace
Satellite identification
Frequencies for each trace
Identification of noise bursts or interfering signals
Station name and/or location
Operator's name

In addition, a logbook should be kept, containing the above information for each pass and also notations concerning equipment maintenance or modification, spurious signals or noise on the records, and any unusual events or phenomena observed.

Doppler Method

Most of the foregoing comments also apply to the Doppler method. As the dispersive Doppler records made in the field will almost certainly be recorded on magnetic tape, no definite standard need be adopted for tape speed. In the laboratory, when the records are transcribed to paper charts, the chart speed can be adjusted to allow easy counting of the dispersive Doppler cycles.

Cost of Equipping a Field Station

It is estimated that the ground-based instrumentation required to perform the geophysical mission described herein would cost approximately $3,200.

ACKNOWLEDGMENTS

REFERENCES

1. Al'pert, Ya. L., "Results of Investigations of the Outer Region of the Ionosphere According to Observations of Radio Signals of the First Artificial Earth Satellite," New York: U.S. Joint Publications Research Service, 1958 (JPRS/NY Rept. No. 724); Translation from *Preliminary Results of Scientific Research by Means of the First Soviet Earth Satellites and Rockets* No. 1, Part II, pp. 40-108 (in Russian)

2. Al'pert, Ya. L., Dobryakova, F. F., et al., "Electron Concentration in the Upper Ionosphere as Determined from Radio Signals of the First Earth Satellite," *Soviet Physics-Doklady* 3(3):584-587, January 1959; Translation from *Doklady Akademii Nauk SSSR* 120(4):743-746, 1958

3. Blackband, W. T., Burgess, B., et al., "Deduction of Ionospheric Electron Content from the Faraday Fading of Signals from Artificial Earth Satellites," *Nature* 183(4669):1172-1174, April 25, 1959

4. Hibberd, F. H., and Thomas, J. A., "The Determination of the Electron Distribution in the Upper Ionosphere from Satellite Doppler Observations," *J. Atmos. Terrest. Phys.* 17(1/2):71-81, December 1959

5. Vassy, E. J., "Densité Électronique au-dessus de F-Maximum, Déduite de l'Émission des Satellites," in: *The Upper Atmosphere above F2-Maximum*, ed. by H. Poeverlein, North Atlantic Treaty Organization, Advisory Group for Aeronautical Research and Development, AGARDograph 42, May 1959, pp. 263-270

6. Blackband, W. T., "The Determination of Ionospheric Electron Content by Observation of Faraday Fading," *J. Geophys. Res.* 65(7):1987-1992, July 1960

7. Garriott, O. K., "The Determination of Ionospheric Electron Content and Distribution from Satellite Observations, I and II," *J. Geophys. Res.* 65(4):1139-1157, April 1960

8. Hame, T. G., and Stuart, W. D., "The Electron Content and Distribution in the Ionosphere," *Proc. IRE* 48(10):1786-1787, October 1960

9. Little, C. G., and Lawrence, R. S., "The Use of Polarization Fading of Satellite Signals to Study the Electron Content and Irregularities in the Ionosphere," in: *Space Research, Proc. 1st Internat. Space Sci. Sympos. Nice, January 1960,* ed. by H. K. Bijl, Amsterdam: North-Holland Pub. Co., 1960, pp. 340-365

10. Ross, W. J., "The Determination of Ionospheric Electron Content from Satellite Doppler Measurements, 1 and 2," *J. Geophys. Res.* 65(9):2601-2615, September 1960

11. de Mendonca, F., "Ionospheric Electron Content and Variations Measured by Doppler Shifts in Satellite Transmissions", Stanford Univ., Radioscience Lab. (Preprint submitted with Semiannual Status Report for the Period July 20, 1961, to January 20, 1962, NASA Grant NsG-30-60), January 1962

12. Yeh, K. C., and Swenson, G. W., Jr., "Ionospheric Electron Content and Its Variations Deduced from Satellite Observations," *J. Geophys. Res.* 66(4):1061-1067, April 1961

13. Munro, G. H., "Diurnal Variations in the Ionosphere Deduced from Satellite Radio Signals," *J. Geophys. Res.,* 67(1):147-156, January 1962

14. Slee, O. B., "Radio Scintillations of Satellite 1958 α," *Nature* 181(4623):1610-1612, June 7, 1958

15. Aitchison, G. J., Thomson, J. H., and Weekes, K., "Some Deductions of Ionospheric Information from the Observations of Emissions from Satellite 1957 $\alpha2$," *J. Atmos. Terrest. Phys.* 14(3/4):236-248, 1959

16. Kent, G. S., "High Frequency Fading Observed on the 40 Mc/s Wave Radiated from Artificial Satellite 1957α," *J. Atmos. Terrest. Phys.* 16(1/2):10-20, October 1959

17. Parthasarathy, R., and Reid, G. C., "Signal Strength Recordings of the Satellite 1958 $\delta2$ (Sputnik III) at College, Alaska," *Proc. IRE* 49(1):78-79, January 1959

18. Yeh, K. C., and Swenson, G. W., Jr., "The Scintillation of Radio Signals from Satellites," *J. Geophys. Res.* 64(12):2281-2286, December 1959

19. de Mendonca, F., Villard, O. G., Jr., and Garriott, O. K., "Some Characteristics of the Signal Received from 1958 δ^2," *Proc. IRE* 48(12):2028-2030, December 1960

20. Frihagen, J., and Tröim, J., "Scintillations of the 20 Mc/s Signals from the Earth Satellite 1958 δ II," *J. Atmos. Terrest. Phys.* 18(1):75-78, April 1960

21. Mawdsley, J., "Fading of Satellite Transmissions and Ionospheric Irregularities," *J. Atmos. Terrest. Phys.* 18(4):344, August 1960

22. Bain, W. C., "Irregular Fading of Satellite Transmissions," *Nature* 189(4759):129, January 14, 1961

23. Frihagen, J., and Tröim, J., "On the Large Scale Regions of Irregularities Producing Scintillation of Signals Transmitted from Earth Satellites," *J. Atmos. Terrest. Phys.* 20(2/3):215-216, March 1961

24. Kent, G. S., "High Frequency Fading of the 108 Mc/s Wave Radiated from an Artificial Earth Satellite as Observed at an Equatorial Station," *J. Atmos. Terrest. Phys.* 22(4):255-269, December 1961

25. Mawdsley, J., and Richards, I. R., "Ionospheric Scattering of Satellite Transmissions," *Nature* 189(4768):906-907, March 18, 1961

26. Singleton, D. G., Lynch, G. J. E., and Thomas, J. A., "Field-Aligned Ionospheric Irregularities and the Scintillation of Satellite Radio Transmissions," *Nature* 189(4758):30-31, January 7, 1961

27. Swenson, G. W., Jr., and Yeh, K. C., "Summary of Satellite Scintillation Observations at the University of Illinois," Univ. of Illinois, Engng. Exp. Sta., Elect. Engng. Res. Lab., Report on NASA Grant NsG-24-59, August 4, 1961

28. Dewan, E., "An Interesting Propagation Effect of Sputnik I," U.S. Air Force Cambridge Res. Ctr., Electromagnetic Radiation Lab. AFCRC-TR-58-354, December 1958

29. Garriott, O. K., and Villard, O. G., Jr., "Antipodal Reception of Sputnik III," *Proc. IRE* 46(12):1950, December 1958

30. Wells, H. W., "Unusual Propagation at 40 Mc from the USSR Satellite," *Proc. IRE* 46(3):610, March 1958

31. Dewan, E. M., "Unusual Propagation of Satellite Signals," *Proc. IRE* 47(11):2020, November 1959

32. Woyk, E. (E. Chvojková), "The Antipodal Reception of Sputnik III," *Proc. IRE* 47(6):1144, June 1959

33. Whitney, H., Strick, H., et al., "Sudden Amplitude Variations of Sputnik III Signals," *J. Geophys. Res.* 65(12):4210-4212, December 1960

34. Chvojkova, E. (E. Woyk), "Antipodal Reception of Satellite Signals and Telecommunication on Small Planets," *Bull. Astronom. Institute Czechoslovak Acad. Sci.* 12(1):1-7, 1961

35. Yeh, K. C., and Swenson, G. W., Jr., "Observed Field Strength in the Neighborhood of the Skip Distance," *J. Geophys. Res.* 66(2):654-656, February 1961

36. Bowhill, S. A., "The Faraday-Rotation Rate of a Satellite Radio Signal," *J. Atmos. Terrest. Phys.* 13(1/2):175-176, 1958

37. Browne, I. C., Evans, J. V., et al., "Radio Echoes from the Moon," *Proc. Phys. Soc. (London)* 69B(9):901-920, September 1956

112

38. Yeh, K. C., and Gonzalez, V. H., "Note on the Geometry of the Earth Magnetic Field Useful to Faraday Effect Experiments," *J. Geophys. Res.* 65(10):3209-3214, October 1960

39. Yeh, K. C., "Second-Order Faraday Rotation Formulas," *J. Geophys. Res.* 65(8):2548-2550, August 1960

40. Hibberd, F. H., "The Effect of the Ionosphere on the Doppler Shift of Radio Signals from an Artificial Satellite," *J. Atmos. Terrest. Phys.* 12(4):338-340, 1958

41. Weekes, K., "On the Interpretation of the Doppler Effect from Senders in an Artificial Satellite," *J. Atmos. Terrest. Phys.* 12(4):335-338, 1958

42. Berning, W. W., "Earth Satellite Observations of the Ionosphere," *Proc. IRE* 47(2):280-288, February 1959

43. Hutchinson, H. P., "Application of Satellite Doppler Shift Measurements. Part II. Slant Range at Nearest Approach," in: *IRE National Convention Record*, New York: Institute of Radio Engineers, 1959, Vol. 7, Part 5, pp. 61-66

44. Kelso, J. M., "Doppler Shifts and Faraday Rotation of Radio Signals in a Time-Varying, Inhomogeneous Ionosphere. Part I. Single Signal Case," *J. Geophys. Res.* 65(12):3909-3914, December 1960

45. de Mendonca, F., and Garriott, O. K., "The Effect of the Earth's Magnetic Field on Measurements of the Doppler Shift of Satellite Radio Transmissions," Stanford Univ., Radioscience Lab. (Preprint submitted with Semiannual Status Report for the Period July 20, 1961, to January 20, 1962, NASA Grant NsG-30-60), December 1961

46. Garriott, O. K., and Nichol, A. W., "Ionospheric Information Deduced from the Doppler Shifts of Harmonic Frequencies from Earth Satellites," *J. Atmos. Terrest. Phys.* 22(1):50-63, September 1961

47. Garriott, O. K., and Bracewell, R. N., "Satellite Studies of the Ionization in Space by Radio," in: *Advances in Geophysics*, New York: Academic Press, 1961, Vol. 8, pp. 85-135

48. Henderson, R. E., "Measuring the Doppler Frequency Shift on Satellite Transmissions," *Brit. Commun. and Electronics* 8(7):506-512, July 1961

ADDITIONAL BIBLIOGRAPHY

1956

Daniels, F. B., "Electromagnetic Propagation Studies with a Satellite Vehicle," in: *Scientific Uses of Earth Satellites*, ed. by J. A. Van Allen, Ann Arbor: University of Michigan Press, 1956, pp. 276-282

Hagen, J. P., "The Exploration of Outer Space with an Earth Satellite," *Proc. IRE* 44(6):744-747, June 1956

Mengel, J. T., "Tracking the Earth Satellite, and Data Transmission, by Radio," *Proc. IRE* 44(6): 755-760, June 1956

Van Allen, J. A., "The Scientific Value of the Earth Satellite Program," *Proc. IRE* 44(6):764-767, June 1956

1957

Brown, R. R., Green, P. E., Jr., et al., "Radio Observations of the Russian Earth Satellite," *Proc. IRE* 45(11):1552-1553, November 1957

Peterson, A. M., and Staff, "Radio and Radar Tracking of the Russian Earth Satellite," *Proc. IRE* 45(11):1553-1555, November 1957

Staff of the Royal Aircraft Establishment, Farnborough, "Observation on the Orbit of the First Russian Earth Satellite," *Nature* 180(4593):937-941, November 9, 1957

1958

Bracewell, R. N., and Garriott, O. K., "Rotation of Artificial Earth Satellites," *Nature* 182(4638): 760-762, September 20, 1958

Briggs, B. H., "A Study of the Ionospheric Irregularities which Cause Spread-F Echoes and Scintillations of Radio Stars," *J. Atmos. Terrest. Phys.* 12(1):34-45, 1958

Kraus, J. D., and Albus, J. S., "A Note on Some Signal Characteristics of Sputnik I," *Proc. IRE* 46(3):610-611, March 1958

Kraus, J. D., and Dreese, E. E., "Sputnik I's Last Days in Orbit," *Proc IRE* 46(9):1580-1587, September 1958

Kraus, L., and Watson, K. M., "Plasma Motions Induced by Satellites in the Ionosphere," *Phys. of Fluids*, 1(6):480-488, November-December, 1958

Munro, G. H., and White, R. B., "Observations in Australia of Radio Transmissions from the First Artificial Earth Satellite," *Nature* 181(4602):104, January 11, 1958

Warwick, J. W., "Radio Observations of Soviet Satellites 1957 Alpha 2 and 1957 Beta 1," *IGY Satellite Rept. Series* No. 5, June 30, 1958

Woyk, E. (E. Chvojková), "Investigation of the Ionosphere Using Signals from Earth Satellites," *Nature* 182(4646):1362-1363, November 15, 1958

1959

Arendt, P. R., "On the Existence of a Strong Magneto-Ionic Effect Topside of the F Maximum of the Kenelly-Heaviside Layer," *J. Appl. Phys.* 30(5):793-795, May 1959

Brito, J. M., "A Correction Necessary for the Application of the Doppler Effect to the Measurements of Distances to Satellites," *Proc. IRE* 47(11):2023, November 1959

Daniels, F. B., and Bauer, S. J., "The Ionospheric Faraday Effect and Its Applications," *J. Franklin Inst.* 267(3):187-200, March 1959

Hame, T. G., and Kennaugh, E. M., "Recordings of Transmissions from the Satellite 1958 Δ_2 at the Antenna Laboratory, The Ohio State University," *Proc. IRE* 47(5):991-992, May 1959

Hibberd, F. H., "The Faraday Fading of Radio Waves from an Artificial Satellite," *J. Geophys. Res.* 64(8):945-948, August 1959

Kallmann, H. K., "A Preliminary Model Atmosphere Based on Rocket and Satellite Data," *J. Geophys. Res.* 64(6):615-623, June 1959

Kazantsev, A. N., "Absorption and Electron Distribution in the F_2 Layer Determined from Measurements of Transmitted Radio Signals from Earth Satellites," *Planet. Space Sci.* 1(2):130-135, April 1959

Krassovsky, V. I., "Exploration of the Upper Atmosphere with the Help of the Third Soviet Sputnik," *Proc. IRE* 47(2):289-296, February 1959

Munro, G. H., and Heisler, L. H., "Recording Radio Signals from Earth Satellites," *Nature* 183(4664):809-810, March 21, 1959

Paetzold, H. K., "Observations of the Russian Satellites and the Structure of the Outer Terrestrial Atmosphere," *Planet. Space Sci.* 1(2):115-124, April 1959

Parthasarathy, R., Basler, R. P., and DeWitt, R. N., "A New Method for Studying the Auroral Ionosphere Using Earth Satellites," *Proc. IRE* 47(9):1660, September 1959

Schilling, G. F., and Sterne, T. E., "Densities and Temperatures of the Upper Atmosphere Inferred from Satellite Observations," *J. Geophys. Res.* 64(1):1-4, January 1959

Storey, L. R. O., "A Method for Measuring Local Electron Density from an Artificial Satellite," *J. Res. Nat. Bur. Standards* 63D(3):325-340, November-December 1959

Warwick, J. W., "Decay of Spin in Sputnik I," *Planet. Space Sci.* 1(1):43-49, January 1959

1960

Aarons, J., Whitney, H. E., et al., "Atmospheric Phenomena Noted in Simultaneous Observations of 1958 δ II (Sputnik III)," U.S. Air Force, Electronics Research Directorate ERD-TR-60-174, August 1960; Also in *Planetary and Space Sci.* 5(3):169-184, July 1961

Bijl, H. K.(ed.),"Space Research: Proc. 1st Internat. Space Sci. Sympos., Nice, January 1960," Amsterdam: North-Holland Pub. Co., 1960

Garriott, O. K., and Little, C. G., "The Use of Geostationary Satellites for the Study of Ionospheric Electron Content and Ionospheric Radio-Wave Propagation," *J. Geophys. Res.* 65(7):2025-2027, July 1960

Graves, C. D., "Radio Propagation Measurements Using the Explorer VI Satellite," *J. Geophys. Res.* 65(9):2585-2587, September 1960

Klinker, L., Schmelovsky, K. H., and Knuth, R., "Jahreszeitliche Variationen der Mittleren Elektronenkonzentration Zwischen 400 und 1200 Km Höhe," *Naturwissenschaften* 47(9):197-198, May 1960

Kraus, J. D., Higgy, R. C., and Crone, W. R., "The Satellite Ionization Phenomenon," *Proc. IRE* 48(4):672-678, April 1960

Lockwood, G. E. K., "Spin Rate of the Satellite Echo I as Determined by a Tracking Radar," *Canadian J. Phys.* 38(12):1713, December 1960

Macrakis, M. S., "A Possible Long-Range Communications Link Between Ground and Low-Orbiting Satellites," *J. Atmos. Terrest. Phys.* 19(3/4):260-271, December 1960

Munro, G. H., "Ionospheric Information from Satellite Signals," *Nature* 187(4742):1017-1018, September 17, 1960

Rand, S., "Wake of a Satellite Traversing the Ionosphere," *Phys. of Fluids* 3(2):265-273, March-April 1960

1961

Al'pert, Ya. L., "Investigation of the Ionosphere and of the Interplanetary Gas with the Aid of Artificial Satellites and Space Rockets," *Soviet Physics-Uspekhi* 3(4):479-503, January-February 1961; Translated from *Uspekhi Fizicheskikh Nauk* 71(3):369-409, July 1960

Anderson, L. J., "108-216 Mc./s. Radio Signals from Satellites below the Horizon," *Nature* 190(4777):708, May 20, 1961

Anderson, R. E., "Sideband Correlation of Lunar and Echo Satellite Reflection Signals in the 900-Mc Range," *Proc. IRE* 49(6):1081-1082, June 1961

Cain, J. C., Shapiro, I. R., et al., "A Note on Whistlers Observed above the Ionosphere," *J. Geophys. Res.* 66(9):2677-2680, September 1961

116

Capon, I. N., "The Application of Ray Tracing Methods to Radio Signals from Satellites," *Proc. Phys. Soc. (London)* 77(2):337-345, February 1, 1961

Croft, T. A., and Villard, O. G., Jr., "An HF Radar Search for Possible Effects of Earth Satellites upon the Upper Atmosphere," *J. Geophys. Res.* 66(10):3109-3118, October 1961

Croft, T. A., "An HF-Radar Search for the Effects of Earth Satellites Upon the Ionosphere," Stanford Univ., Radioscience Lab. Technical Rept. No. 24, March 10, 1961

Holland, A. C., "The Effects of Atmospheric Refraction on Angles Measured from a Satellite," *J. Geophys. Res.* 66(12):4171-4175, December 1961

Jakes, W. C., "A Transatlantic Communication Experiment via Echo I Satellite," *Nature* 190(4777): 709, May 20, 1961

Kallmann-Bijl, H. K., "Daytime and Nighttime Atmospheric Properties Derived from Rocket and Satellite Observations," *J. Geophys. Res.* 66(3):787-795, March 1961

Medved, D. B., "Secondary Electron Emission and the Satellite Ionization Phenomenon," *Proc. IRE* 49(6):1077-1078, June 1961

Sørensen, E. V., "Magneto-Ionic Faraday Rotation of the Radio Signals on 40 Mc from Satellite 1957 α (Sputnik 1)," *IRE Trans. on Antennas and Propagation* AP-9(3):241-247, May 1961

Titheridge, J. E., "The Calculation of the Electron Density in the Ionosphere from Elevation-Angle Measurements on Artificial Satellites," *J. Geophys. Res.* 66(10):3103-3107, October 1961

Toman, K., "Minimum Range to Artificial Earth Satellites," *Nature* 190(4773):333-334, April 22, 1961

Yeh, K. C., "Propagation of Spherical Waves in a Weak Random Medium," Univ. of Illinois, Engng. Exp. Sta., Elect. Engng. Res. Lab., Report on NASA Grant NsG-24-59, December 1961

Yeh, K. C., and Chow, H., "Variations of Ionospheric Electron Content During Disturbances," Univ. of Illinois, Engng. Exp. Sta., Elect. Engng. Res. Lab., Report on NASA Grant NsG-24-59, August 1, 1961

THE COMPARISON AND COMBINATION OF SATELLITE WITH OTHER DETERMINATIONS OF GEODETIC PARAMETERS

by

William M. Kaula
Goddard Space Flight Center

SUMMARY

Three areas of geodetic interest can be defined in which it is desirable to compare satellite results with those obtained by terrestrial and lunar methods:

1. Variations in the gravity field. Determinations from satellite orbits of tesseral harmonics need an independent check. Terrestrial gravimetry at present is of dubious adequacy, except to confirm the order of magnitude of the variations determined by use of autocovariance analysis. An excellent partial check on the phase as well as the amplitude of the variations is the astro-geodetic geoid. For comparison satellite data must be transformed from a harmonic to a spatial representation.

2. Station positions. Satellite data so far have yielded only the rather negative conclusion that the position determinations of the major continental geodetic systems are probably correct to within 100 meters.

3. The scale relationship between laboratory and satellite systems, most conveniently expressed in terms of GM. An appreciable discrepancy already exists between the GM value obtained from lunar observations and that obtained from terrestrial geodesy. Thus far, satellite results in this area are inconclusive.

INTRODUCTION

The fullest utilization of satellite geodesy requires the development of methods to compare its results with those obtained by other means. Satellites, after all, are rather limited as measuring devices. Therefore, their results are subject to distortion and independent confirmation is desirable.

Such confirmation is difficult; in fact, our interest in satellite geodesy is largely generated by the incompleteness and distortions of other methods.

This paper is a brief commentary on satellite geodesy in relation to conventional methods. We shall discuss this subject from three standpoints: the geoid (or gravitational field); station positions; and the scale relationship between satellite and laboratory measuring systems.

THE GEOID

The results of satellite orbit studies to obtain details of variations in the earth's gravity field are presently somewhat static, because orbital variations which must be used to determine the tesseral harmonics accurately are orders of magnitude smaller than variations used to determine the zonal harmonics. To enable analysis of such variations, significant improvement is needed in at least one of the following respects:

1. Better orbits—perigees above 800 km, eccentricities on the order of 0.01-0.12, and a variety of inclinations.

2. Frequent accurate tracking of all parts of the orbit, both day and night sides.

3. Better physical models of the upper atmosphere.

4. Better data analysis techniques.

Items 1 and 2 are already forthcoming, so it is timely to consider what sort of independent checks might be available.

The first and most evident of such checks is the latitude variation observations indicating that the harmonic U_2^1, which would exist only if rotation of the earth was not about a principal axis, is negligibly small. It is thus hoped that satellite orbit analyses incorporate a sufficient variety of conditions that U_2^1 can be included in the solution; its difference from zero in the results will then be some measure of reliability of the determinations for other harmonics.

Further checks from terrestrial geodesy are the gravimetric and astro-geodetic data. Both are very incomplete. It is doubtful that any existing treatment of gravimetry is adequate: Those of Heiskanen (Reference 1) and Kaula (Reference 2) depend too much on step-by-step extrapolation and correlation with topography; those of Jeffreys (Reference 3) and Zhongolovitch (Reference 4) are distorted by approximations used to overcome the poor distribution of observations. The recent results of Uotila (Reference 5), based on much more data, may constitute an appreciable improvement.

The astro-geodetic geoid is good but is limited in coverage. Figure 1 shows the latest geoid published by Fischer (Reference 6). Heavy arrows have been inserted on it to mark all major slopes which might be indicated by satellite orbits — those longer than 1/4 wavelength (22-1/2 degrees) of a fourth degree harmonic and having a geoid height change of more than 40 meters. Figure 2 shows the geoid corresponding to Table 1, which consists of results derived solely from satellite data. The zonal harmonics in Table 1 are rounded-off averages of the results obtained by the principal
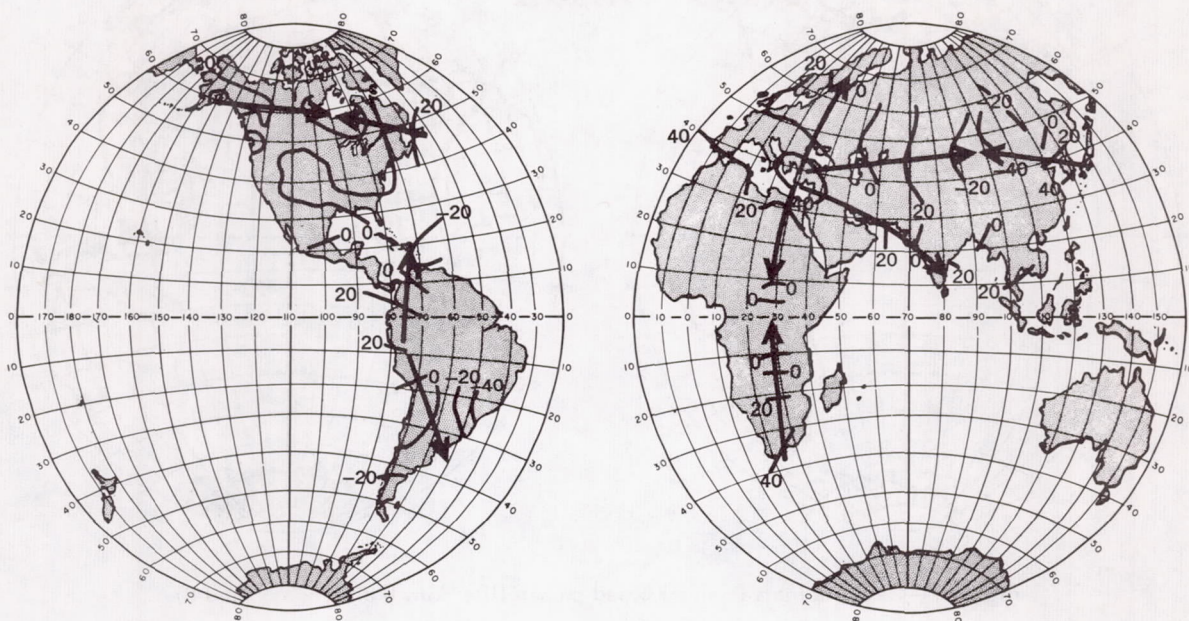
Figure 1—Geoid heights (meters) based on astro-geodetic data (Reference 6)

Table 1

Gravitational Harmonics Obtained from Satellite Orbits

(multiply by a scaling factor of 10^{-6})

n	m	Conventional $C_{n,m}$	$S_{n,m}$	Partly Normalized $A_{n,m}$	$B_{n,m}$	Fully Normalized $A_{n,m}$	$B_{n,m}$	RMS Geoid Height Contribution (meters)
2	2	2.1	-0.8	10.1	-3.7	3.2	-1.2	± 22
3	0			2.30		0.87		6
4	0	1.80		1.80		0.60		4
4	1	-1.2	-0.2	-5.5	-1.0	-1.3	-0.2	8
5	0	0.30		0.30		0.09		± 1

investigators, with greatest weight given to those of Kozai (Reference 7); the n,m = 2,2 and 4,1 harmonics are those given by Newton (Reference 8), at present the only published data at least partly satisfying items 1 and 2 on the list given above. $C_{n,m}$, $S_{n,m}$, $A_{n,m}$, and $B_{n,m}$ in Table 1 are as defined by the International Astronomical Union recommendation (Reference 9). $\overline{A}_{n,m}$ and $\overline{B}_{n,m}$ are the coefficients of

$$\frac{\mu}{r}\left(\frac{a_e}{r}\right)^n \sqrt{\frac{(n-m)!}{(n+m)!}(2n+1)\kappa_m} \frac{\cos^m\phi}{2^n \cdot n!} \sum_{t=0}^{\frac{n-m}{2}} \frac{(2n-2t)!}{(n-m-2t)!}\binom{n}{t}(-1)^t \sin^{n-m-2t}\phi \begin{Bmatrix} \cos \\ \sin \end{Bmatrix} m\lambda ,$$

$$(\kappa_0 = 1; \; \kappa_m = 2, \; m \neq 0);$$

121
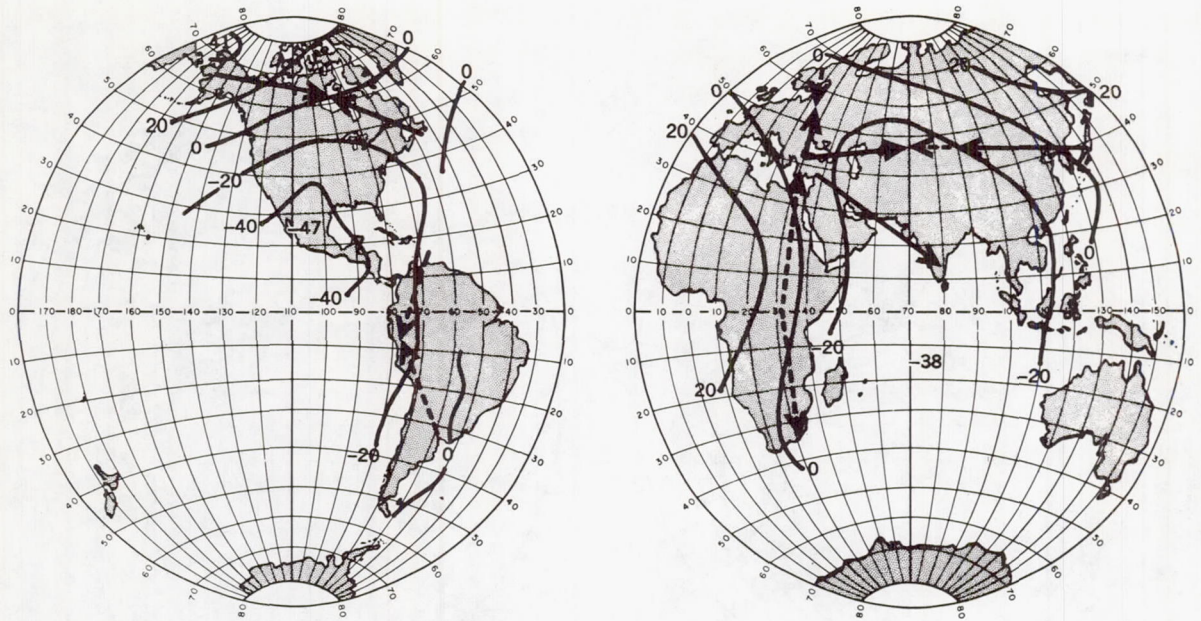
Figure 2—Geoid heights (meters) based on satellite data (References 7 and 8)

Table 2

Comparison of Spherical
Harmonics from Satellite Motions
with the Order of Magnitude
Predicted by Autocovariance
Analysis of Gravimetry

(multiply by a scaling factor of 10^{-6})

n	$\sigma\{\overline{A}_{n,m}, \overline{B}_{n,m}\}$	$\overline{A}_{n,m}, \overline{B}_{n,m}$
3	±1.27	0.87
4	±0.62	0.60, -1.3, -0.2
5	±0.25	0.09

and they have the advantage, for geophysical purposes, of being identical with the rms amplitudes.

On Figure 2 arrows have been drawn in locations corresponding to those on Figure 1. The solid arrows indicate agreement, and the dashed arrows disagreement, with the astro-geodetic geoid. The only major feature for which there is good agreement is the hollow in the center of Asia. Some of the discrepancies might be explained by the third degree harmonics which are absent from the satellite geoid, but it is disappointing that there is not better agreement in the north-south direction, in which the zonal harmonics would be expected to prevail. It is disturbing that the dominant term in the satellite geoid, $\overline{A}_{2,2}$, $\overline{B}_{2,2}$, is the most poorly determined: the partial derivative of the longitude of Transit IV-A (1961o_1) along its orbit with respect to $\overline{A}_{2,2}$, $\overline{B}_{2,2}$, is about half the derivative with respect to $\overline{A}_{4,1}$, $\overline{B}_{4,1}$.

The satellite geoid does not compare any better with any of the gravimetric geoids which have been published. An improvement might be obtained by applying to the gravimetry the generalization of linear autoregression for non-uniformly distributed data. But we do have one limited category of gravimetric data which agrees well—the degree variances from autocovariance analysis, which afford a check on the order of magnitude of the harmonic coefficients of the third and higher degrees. Table 2 compares the magnitude of coefficients predicted by the autocovariance analysis in Reference 2 with those from Table 1. Results are not yet sufficiently accurate to make a precise definition of the geoid a matter of concern

in any comparisons. An interesting study by Pellinen (Reference 10) gives effects on the order of $\pm 0.08 \times 10^{-6}$ on $\overline{A}_{3,m}, \overline{B}_{3,m}$ from the higher order term in Molodenskii's theory.

STATION POSITIONS

Since the errors in station positions connected to the major geodetic datums are believed to be smaller than the principal effects of the tesseral harmonics on satellite orbits, determinations for datum shifts so far are even more speculative than those for the gravitational field. Experience has borne out the estimates of station position accuracies fairly well: Usually position shifts of less than 100 meters are required to get a best fit to satellite observations for stations connected to the principal geodetic systems of America and of Eurasia-Africa, but shifts of more than 100 meters are ordinarily needed for a station on an isolated system such as Hawaii, Australia, or Argentina. The sets of observations have not been well-conditioned enough, however, to give results which could be called conclusive.

SCALE RELATIONSHIP

Despite drag and other complications, the semimajor axis giving a mean motion that fits observations of a satellite over more than a few days is rather accurately determined—usually with a proportionate error of less than 10^{-6}. Holding fixed station positions, or the differences between them, suggests a possibility for determining the scale relationship of the satellite system to the cgs system. This relationship is usually expressed in terms of GM, which ties together time and length through Kepler's law: $n^2 a^3 = GM$. There now exists a proportionate discrepancy of 3×10^{-5} between GM from terrestrial data and GM from the lunar mean motion and radar distance measurements. In the terrestrial determination the most likely defect is the equatorial radius as found by fitting the astrogeodetic to the gravimetric geoid; in the astronomic determination, the most likely defect is the lunar mass deduced from the lunar inequality found from observations of Eros (Reference 11). A determination of GM from satellite motions with the station positions held fixed depends on the accuracy of these absolute positions—at best the proportionate error is on the order of 5×10^{-6}, whereas a determination with the *differences* of positions held fixed depends on the accuracy of the triangulation connecting the stations—the proportionate error is on the order of 3×10^{-6} for transcontinental distances. However, neither way can be considered independent of the determination made entirely from terrestrial data.

Determinations from satellite orbits so far have indicated proportionate changes on the order of 10^{-5} in GM—without, however, any marked consistency.

REFERENCES

1. Heiskanen, W. A., "The Columbus Geoid," *Trans. Amer. Geophys. Union* 38(6):841-848, December 1957

2. Kaula, W. M., "Statistical and Harmonic Analysis of Gravity," *J. Geophys. Res.* 64(12):2401-2421, December 1959

3. Jeffreys, H., "The Determination of the Earth's Gravitational Field (Second Paper)," *Monthly Not. Royal Astronom. Soc. Geophys. Suppl.* 5(3):55-66, 1943

4. Zhongolovich, I., "The External Gravity Field of the Earth and the Fundamental Constants Connected with it," *Trudy Instituta Teoreticheskoy Astronomii* (Akademiya Nauk SSSR) No. 3, 1952

5. Uotila, U. H., "Theoretical Gravity Formula Corresponding to Current Gravity Holdings," Paper presented to the 43rd Annual Meeting of the American Geophysical Union, Washington, April 1962

6. Fischer, I., "An Astrogeodetic World Datum from Geoidal Heights Based on the Flattening f = 1/298.3," *J. Geophys. Res.* 65(7):2067-2076, July 1960

7. Kozai, Y., "The Gravitational Field of the Earth Derived from Motions of Three Satellites," *Astronom. J.* 66(1):8-10, February 1961

8. Newton, R. R., Presentation to the Internat. Sympos. on the Use of Artificial Satellites for Geodesy (Sponsored by the Committee on Space Research and the International Association of Geodesy), Washington, April 1962

9. Hagihara, Y., "Recommendations on Notation of the Earth Potential," *Astronom. J.* 67(1):108, February 1962

10. Pellinen, L. P., "Accounting for Topography in the Calculation of Quasigeoidal Heights and Plumb-Line Deflections from Gravity Anomalies," *Bull. Geod.* 63, 57-65, March 1962

11. Rabe, E., "Derivation of Fundamental Astronomical Constants from the Observations of Eros During 1926-1945," *Astronom. J.* 55(4):112-126, June 1950

MIDDLE ULTRAVIOLET PHOTOELECTRIC
DETECTION TECHNIQUES

by
Lawrence Dunkelman, John P. Hennes
and Walter B. Fowler
Goddard Space Flight Center

SUMMARY

Astronomical and geophysical observations from rockets in the ultraviolet region of the spectrum have been either spectral studies with dispersive optical systems or broad-band photometric measurements at particular wavelength regions of interest. In this paper nondispersive optical techniques are described for the middle (3000-2000A) ultraviolet. Bandpass (200-300A) and cutoff filters which may be used with conventional cesium-antimony photodetectors are described. When near ultraviolet and longer wavelength radiation must be rejected to a greater degree, "solar blind" photocathodes, with higher work functions, such as the alkali tellurides, can be used. These photodetectors, their calibration, and their applications are discussed.

INTRODUCTION

Optical measurements from rockets by Goddard Space Flight Center have placed new emphasis on regions of the ultraviolet spectrum that cannot be observed from the ground because of absorption by the ozone layer at about 25 km altitude. This and other absorbing layers block geophysical and astrophysical measurements at wavelengths shorter than 3000A. Measurements from rockets in the region below 3000A have been restricted to certain spectral passbands by the limited development of filters and detectors. These ultraviolet wavelengths of interest may be divided into two regions: the middle and vacuum ultraviolet. In round numbers, the middle ultraviolet is from 3000 to 2000A, while the vacuum ultraviolet extends below 2000A. This paper is primarily concerned with techniques of nondispersive optics in the middle ultraviolet.

FILTERS

The variety of optical materials used in the visible part of the spectrum is not available in the middle ultraviolet. Those materials which are useful can be put into three classes: long-wave pass

filters which transmit all wavelengths longer than a short wavelength absorption edge; bandpass filters which transmit moderately well over broad regions of the middle ultraviolet; and absorption edge filters which have strong absorption over small wavelength intervals and are useful for producing sharp transmission cutoffs.

The first category of filter is used in photodetector envelopes, windows, or trimmers to produce the short wavelength cutoff in spectral response; Figure 1 shows the transmittance curves for various materials which are available for such use. Corning 9700 glass, with a transmittance of less than 0.05 percent at 2537A, is useful for subtractive filter photometry, for example, with a low pressure mercury arc source. Corning 7910 (9-54), which is 96 percent silica, is also useful for subtractive photometry techniques and can be compared with pure fused silica. The nickel sulfate hexahydrate, $NiSO_4(H_2O)_6$, crystal* is not strictly a cutoff filter, since it has an absorption region from 3500 to 4500A. However, its absorption edge at 1900 makes it a very useful solid for separating the middle from the vacuum ultraviolet, and it is included here for comparison.

In Figure 1, the two curves marked "5" show different samples of commercial sapphire. The wide variation in ultraviolet transmittance shows the problem that faces users of this material. The similar variations in transmittance found in the vacuum ultraviolet materials such as LiF, CaF_2, NaF, BaF_2, etc.—are not found in the fused silica and other materials whose transmittances are shown in curves 6 to 9. In choosing between fused silica (or cultured quartz) and sapphire as a phototube window, the advantages in transmission properties must be weighed against those of sealing properties. For example, with fused silica a long-graded seal is required while sapphire is readily sealed to glass without a graded seal.

Some of the curves in Figure 2 illustrate the second category of filter materials, those which transmit within a limited band of wavelengths. The $NiSO_4(H_2O)_6$ curve mentioned above is seen here to have two large transmission regions: one covering the middle ultraviolet, the other in the blue-green.

The dashed curve representing the optical density of a crystal of KCl:KBr doped with 0.05 percent lead is an example of an absorption edge filter and is shown in more detail in Figure 3. The very sharp absorption edges of these alkali halide crystals can be used to produce

Figure 1—Window transmittance cutoffs in the ultraviolet region. Curve 1 is LiF (1 mm); curve 2 is CaF_2 (1 mm); curve 3 is NaF (1 mm); curve 4 is BaF_2 (1 mm); curve 5 is sapphire (1 mm); curve 6 is fused silica (1 mm); curve 7 is $NiSO_4(H_2O)_6$ (3 mm); curve 8 is Corning 7910 glass (9-54); curve 9 is Corning 9700 glass (2 mm). The two curves numbered "5" indicate the variation in ultraviolet transmission qualities of commercial sapphire.
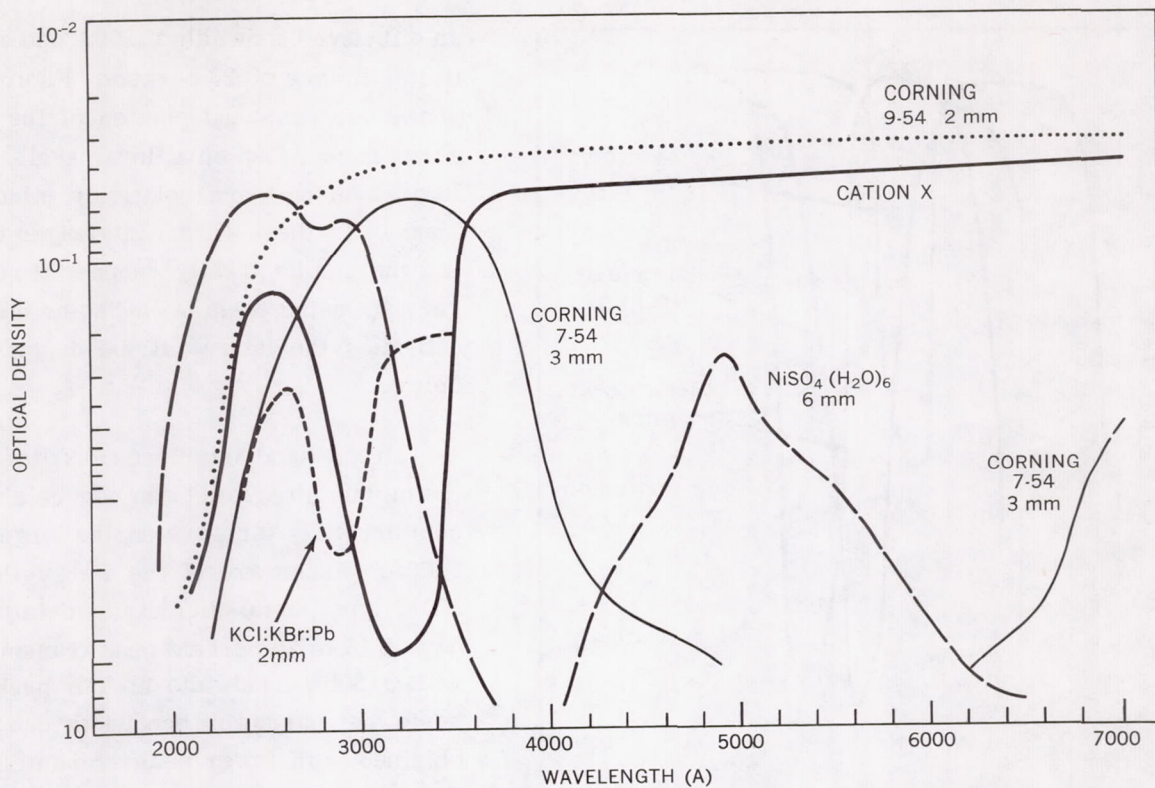
Figure 2—Optical densities of typical samples of NiSO$_4$(H$_2$O)$_6$ crystal, KCl:KBr:Pb crystal, cation-X, and Corning filters 9–54 and 7–54.

equally sharp edges in transmission filter responses when they are combined with other materials. A useful variation in the wavelength of this edge can be achieved by varying the amounts of KBr and KCl in the crystal.

The narrow-band multilayer dielectric interference filters widely used for the visible and infrared regions have not been generally available in the ultraviolet. In the last five years, however, rocket measurements have been made with several broad-band ultraviolet filters. One of these is the chemical filter described by Dunkelman and Field in 1955 (Reference 1). The transmission of this filter, which was developed to replace the liquid "chemical" filters described by Kasha (Reference 2), can be inferred from a comparison of curves 13 and 5 in Figure 6. The quantum efficiencies of a variety of photosurfaces discussed in the next section are also shown in this Figure. This chemical filter, however, is unstable in direct sunlight and its use has been restricted to measurements of the night airglow and stellar fluxes.

In 1960, several filters were assembled at Goddard Space Flight Center which were quite stable and that have been used for measurements of both solar and stellar fluxes. These filters, described in a recent paper by Childs (Reference 3), are made up of the solid glasses and crystals whose characteristics are shown in Figures 1 through 3. The transmittance characteristics of a typical filter are shown in Figures 4 and 5.

Figure 4 shows the transmittance of a 2600A filter made up of lead-doped KCl:KBr, a sheet of cation-X, a 3 mm crystal of NiSO$_4$(H$_2$O)$_6$, a Corning 7-54 filter, and a Corning 9-54 filter. This filter has
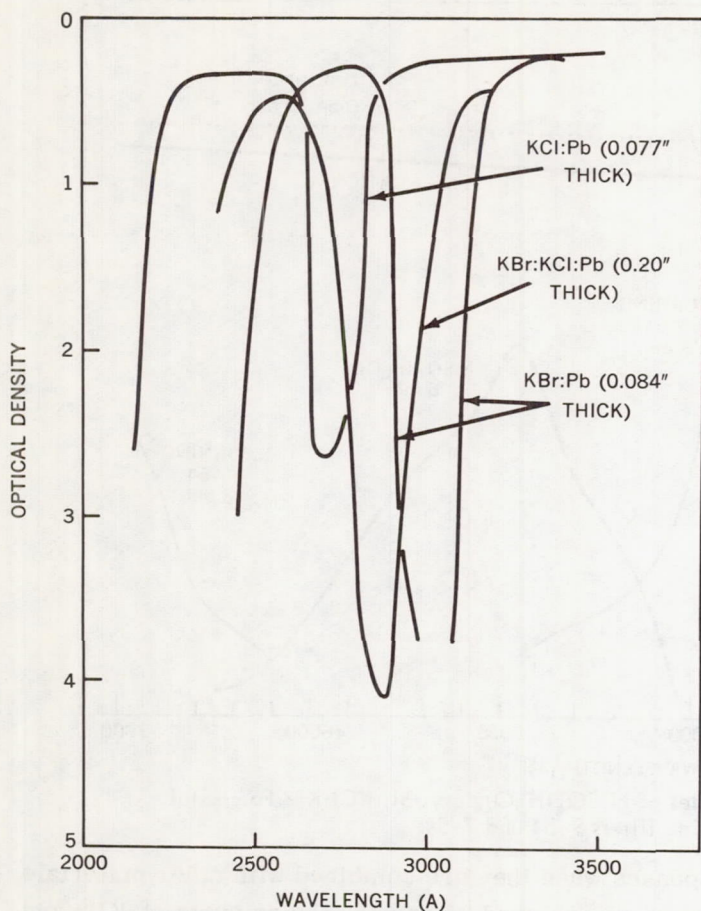
Figure 3—Ultraviolet absorption curves of several lead-doped alkali halide crystals. The absorption edge may be shifted between 2650 and 2900A by varying the amounts of KBr or KCl in the crystal.

an effective bandwidth of 200A and a peak transmittance of 23 percent. Figure 5 shows the passband portion of the same curve normalized on a linear scale. The long wavelength and relatively minor "leaks" in these filters at longer wavelengths can be greatly reduced if necessary by using them with "solar blind" cathodes; the latter will be described below.

Broad-band interference filters for the middle ultraviolet can now be obtained commercially for wavelengths longer than 2100A. These are of the Fabry-Perot MDM type (metal-dielectric-metal). They have a 15 to 20 percent peak transmittance with a 300A bandwidth at half peak. A somewhat narrower bandwidth can be obtained with lower peak transmission. For solar flux measurements, selected optical materials described above have been added to these interference filters for further trimming. Research on improved Fabry-Perot filters of the MDMDM type—where M represents aluminum and D a low-index dielectric such as MgF or chiolite ($2 NaF \cdot AlF_3$)—is being carried out by A. F. Turner (private communication) at Bausch and Lomb and by D. J. Schroeder (private communication) at the University of Wisconsin.

Notable advances in multilayer interference filters have been reported abroad. Sokolova and Krylova (Reference 4) report an excellent transmission filter of ThO_2 and SiO_2 at wavelengths as short as 2200A. Sebire, Cojan, and Giacome (Reference 5) report a 2595A multilayer dielectric filter with 28 percent peak transmission and a 12A passband at half peak. The multilayers are of PbF_2, and cryolite ($Na_3 Al F_6$).

CATHODES

Photocathodes can be divided into three spectral types: those sensitive to both visible and ultraviolet wavelengths, those sensitive only to ultraviolet wavelengths below 3500A, and those sensitive only to vacuum ultraviolet wavelengths.

Typical of the first category is the 1P28 photomultiplier which contains a cesium-antimony (Cs-Sb) cathode and a Corning 9741 glass envelope. The long wavelength response, which extends into the red (Figure 6, curve 5), is a property of the Cs-Sb photoemitter. The short wavelength response is limited by the glass envelope to 1800A. With a quartz envelope, as described by Dunkelman and Lock (Reference 6) in 1950, the short wavelength response is extended to below 1600A. Recently the spectral range has been further extended by means of a CaF_2, window. Such tubes have been studied at Goddard Space Flight Center (Reference 7), and the response was found to be comparatively flat down to 1225A, the window cutoff.

A spectral response with a more constant quantum efficiency can be obtained by coating the front face of a glass-enveloped multiplier, for example, the 1P21, with a layer of sodium salicylate
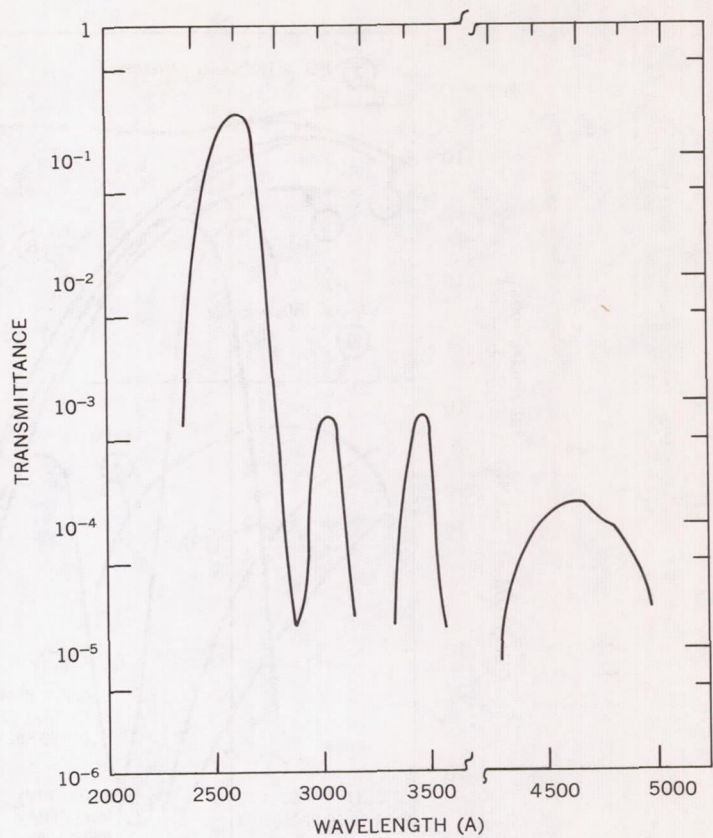
Figure 4—Transmittance curve of a 2600A filter made up of lead-doped KCl:KBr, cation-X, $NiSO_4(H_2O)_6$, a Corning 7-54 filter, and a Corning 9-54 filter.
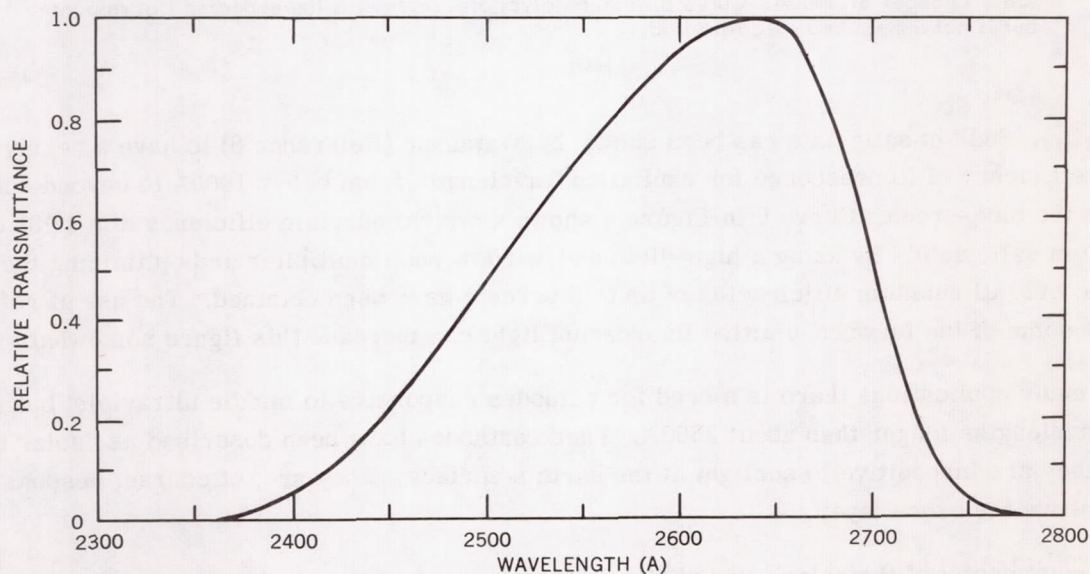
Figure 5—Passband portion of the 2600A filter transmittance curve shown in Figure 4, here normalized and put on a linear scale.
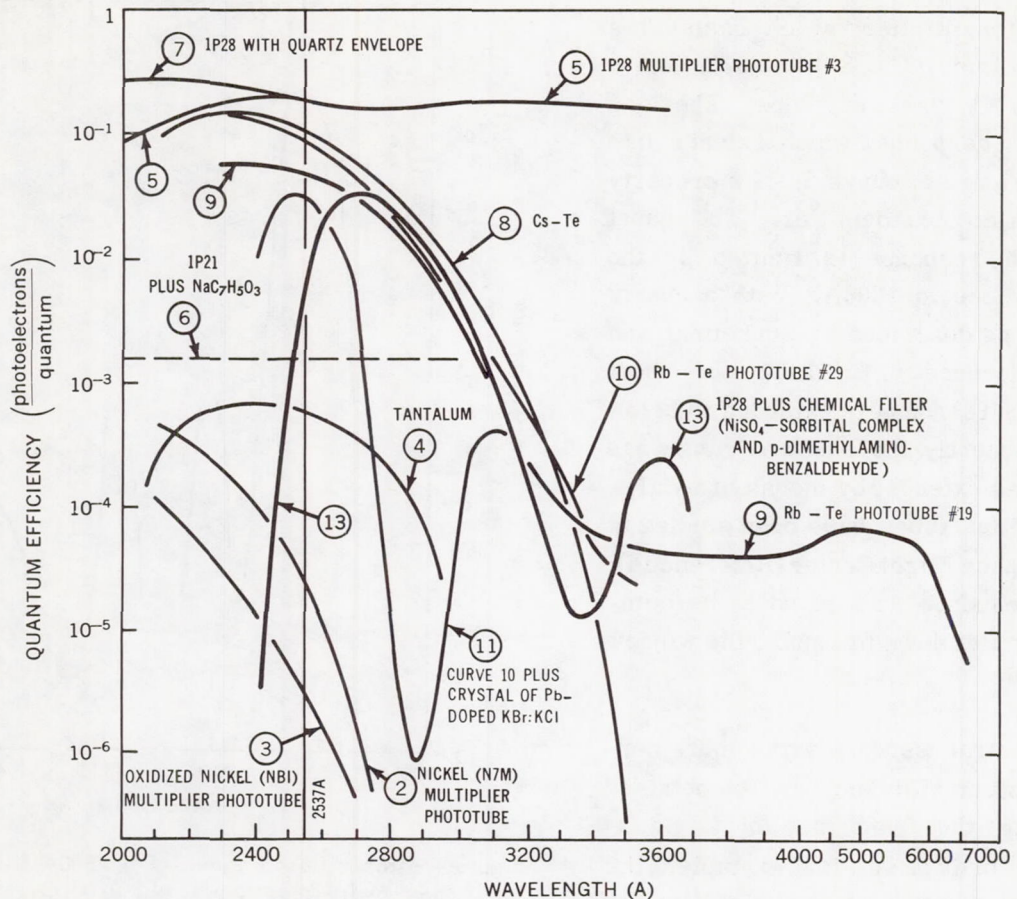
Figure 6—Quantum efficiency of various photocathodes. Curves 11 and 13 represent responses which include optical filters to improve selectivity. Note that the wavelength scale changes at 4000A. Curve 6, sodium salycilate, represents the expected flat response but is not a measured spectral yield.

($NaC_7H_5O_3$). Sodium salicylate has been shown by Watanabe (Reference 8) to have a nearly constant quantum efficiency of fluorescence for excitation wavelengths from below 1000A to beyond 3000A; emission is in the blue-green. Curve 6 in Figure 6 shows a typical quantum efficiency of a 1P21 coated with sodium salicylate. By using a high-yield end-window photomultiplier and optimizing the coating thickness, overall quantum efficiencies of up to 5 percent have been obtained. The use of reflectors to collect some of the forward-emitted fluorescent light can increase this figure somewhat.

For many applications there is a need for cathodes responsive to middle ultraviolet but insensitive to wavelengths longer than about 3500A. These cathodes have been described as "solar blind" because they are insensitive to sunlight at the earth's surface. They are, of course, responsive to sunlight above the ozone layer.

The most useful of the solar blind photosurfaces known to date are the alkali tellurides. Cesium-tellurium (Cs-Te) and rubidium-tellurium (Rb-Te) offer high quantum efficiencies with good solar blindness (curves 8, 9 and 10 in Figure 6). These responses were first reported by Taft and Apker

in 1953 (Reference 9). For the middle ultraviolet, Cs-Te and Rb-Te cathodes have shown no significant difference in response. The long wavelength tail of curve 9 is produced by an excess of rubidium above the stoichiometric ratio of two rubidium atoms to one tellurium atom. By varying the cesium or rubidium content of the cathode, the manufacturer has some control over both the shape of the response curve in the 3000A region and the peak quantum yield. Increased proportions of cesium generally cause both slightly higher quantum yield at short wavelengths and increased sensitivity at long wavelengths. With a LiF window the response of the Cs-Te continues approximately uniformly into the vacuum ultraviolet. Tubes using Cs-Te cathodes and quartz, sapphire, or LiF windows are now commercially available and make possible a number of interesting measurements that must be made in the presence of a strong long-wavelength background, such as that from the sun.

Even more solar blind but much less sensitive are the pure metal photocathodes (Reference 10). Figure 6 shows responses of cathodes of nickel, curve 2; tantalum, curve 4; and oxidized nickel, curve 3. In each case here, and with other metals not shown, the quantum yields are down by two or three decades from those of the alkali halide photosurfaces.

Applications using the second category of photocathodes described above often depend on selection of phototubes for solar blindness as well as quantum yield. One criterion for determining their merit is their sensitivity to wavelengths below 2900A as compared with this small but measurable response to sunlight. One such figure of merit, arbitrarily taken, is the irradiance at 2537A necessary to produce an anode current equal to that produced by full sunlight with skylight excluded. This "equivalent sunlight input" is admittedly not a precise measurement since the intensity of short wavelength sunlight, to which the phototube is relatively most sensitive, depends on the angular altitude of the sun, the clarity of the sky, and the amount of atmospheric ozone. Nevertheless, "equivalent sunlight input" has proved useful in comparing a wide variety of photodevices. Values for a number of cathodes are listed in Table 1. The measurements were taken with the sun above 30 degrees altitude in a cloudless sky. The quantum efficiency at 2537A is also listed. Both the quantum efficiency and solar blindness should be considered, particularly when available flux in the middle ultraviolet is low and considerable long-wavelength background is present.

The curves of Figure 7 include the third category—vacuum ultraviolet photodetectors. Phototubes made by Sommer at RCA with cathodes of copper iodine (Cu-I), curve 3, and cesium iodine (Cs-I), curve 2, have a very strong rejection of all middle and near ultraviolet wavelengths but a large response at the short wavelengths around 1200A.[‡] Also shown for comparison are two metal cathode responses (nickel and tungsten), and the flat response of Cs-Sb in the phototube with the CaF_2 window mentioned above.

Figure 8 shows some of the photomultipliers examined at GSFC. The ASCOP* tube (third from the left) with the LiF window, and the CBS** tube (at the far right) with the sapphire window, are both commercially available solar blind photomultipliers using Cs-Te photocathodes.

---

*ASCOP Division of Electro-Mechanical Research Inc.
**CBS Laboratories, a Division of Columbia Broadcasting System, Inc.
‡The large quantum yields shown for these tubes represent an early and preliminary measurement. Subsequent measurements of Cs-I and Cu-I cathodes show that in general a peak quantum efficiency of 10 to 20 percent is more typical with Cs-I being 3 to 5 times more sensitive than Cu-I at the Lyman Alpha wavelength (1216A).

Table 1

Solar Blindness of Various Cathodes.

Photocathode	Equivalent Sunlight Input* at 2537A $\left(\dfrac{\text{watts}}{\text{cm}^2}\right)$	Quantum Efficiency at 2537A $\left(\dfrac{\text{photoelectrons}}{\text{quantum}}\right)$	Remarks
Cesium-Tellurium	1.7×10^{-5}	5×10^{-2}	Semitransparent cathode in a photodiode.
Cesium-Tellurium	1.2×10^{-5}	2.7×10^{-2}	Semitransparent cathode in a 14-stage photomultiplier
Cesium-Tellurium	8.5×10^{-6}	13×10^{-2}	Opaque cathode in a photodiode
Cesium-Tellurium	6.7×10^{-6}	1.4×10^{-2}	Semitransparent cathode in a 14-stage photomultiplier
Tantalium	8×10^{-9}	6.5×10^{-4}	Opaque cathode in a photodiode
Oxidized Nickel	6×10^{-9}	3.5×10^{-4}	Opaque cathode in a 9-stage photomultiplier
Silver	3×10^{-9}	1.5×10^{-5}	Opaque cathode in a 9-stage photomultiplier
Nickel	1×10^{-9}	5×10^{-6}	Opaque cathode in a 9-stage photomultiplier
Copper Gauze	2×10^{-11}	2.8×10^{-7}	Photon counter

*Watts/cm^2 of 2537A radiation required to produce a detector signal equal to that produced by full sunlight (less sky background).
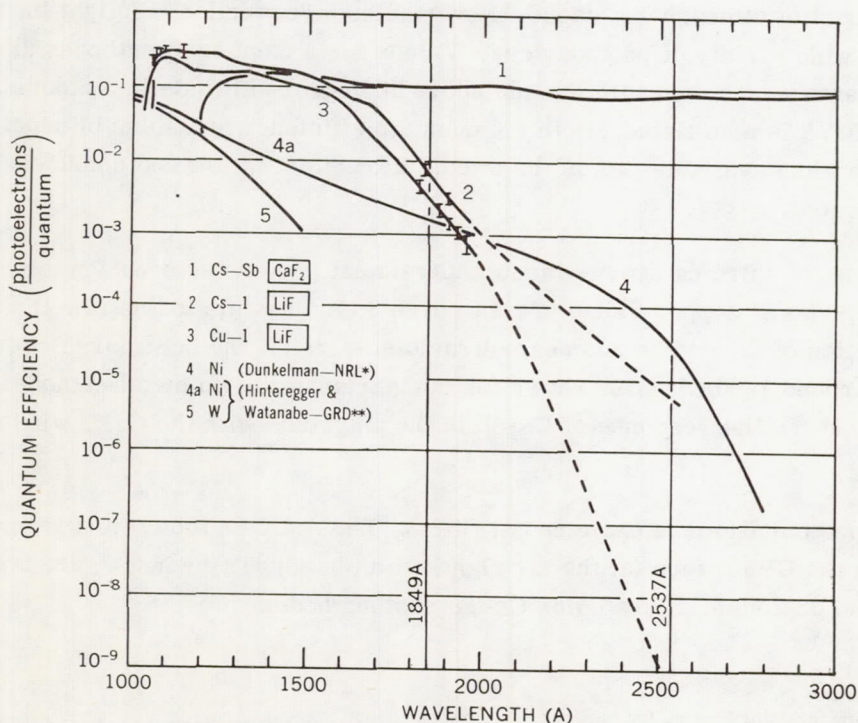
Figure 7—Spectral response curves of a variety of photocathodes showing the high rejection of some of the iodide compounds at longer wavelengths. The advantage of the relatively high yield composite photosurface over the lower yield pure metal is also evident. The dashed portions represent estimated yields interpolated between the measured values at 2000A and 2537A.

*Naval Research Laboratory
**Geophysics Research Directorate, Air Force Cambridge Research Center
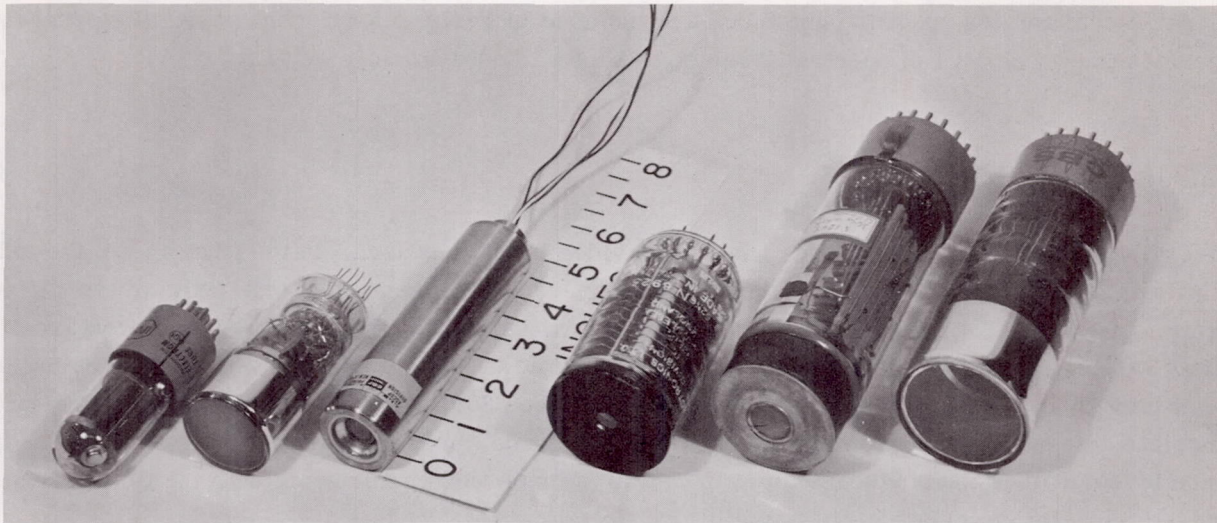
Figure 8—Some of the photomultipliers examined at the Goddard laboratory. Left to right: RCA 1P28, Cs–Sb cathode, 9741 glass envelope; RCA 7151c (ruggedized version of 6199 tube); ASCOP 541F, semitransparent Cs–Te cathode, LiF window (potted with resistor chain in place); EMI 6256B, semitransparent Cs–Sb cathode, fused silica window; RCA (A.H. Sommer experimental tube), Cs–Te cathode, LiF window; CBS CL 1067, semitransparent Cs–Te cathode, sapphire window.

Table 2

Commercial Photomultipliers and Photodiodes Examined
at Goddard Space Flight Center.

Tube	Cathode	Window	Cathode Diameter (mm)	Tube Diameter (cm)	Tube Length (cm)	Quoted Dark Currents[††] at Gains of 10^6 (amperes)
Photomultipliers						
EMI*						
6256B	CsSbO	Quartz	10	5.1	10.7	10^{-9}
6255S	"S"	Quartz	42	5.1	12.0	6×10^{-9}
CBS†						
CL1050	Cesium–Antimony	Sapphire	19	5.1	16.8	3×10^{-9}
CL1067	Cesium–Tellurium	Sapphire	42	5.1	15	not available
RCA‡						
1P28	Cesium–Antimony	9741	8 x 23[‡‡]	3.3	8.0	5×10^{-8}
C70128	Cesium–Tellurium	LiF	12	1.9	8.9	not available
ASCOP§***						
541FO8	Cesium–Tellurium	LiF	10	3.2	12.7	2×10^{-11}
541FO5M	Cesium–Tellurium	Sapphire	25	3.2	11.4	1×10^{-10}
Photodiodes						
CBS CL1051	Cesium–Antimony	Sapphire	12[‡‡]	2.5	7.0	
RCA c70126‖	Cesium–Tellurium	LiF	11	1.9	4.4	
ITT FW 156**	Cesium–Tellurium	LiF	11[‡‡]	1.9	3.8	
ASCOP 540F	Cesium–Tellurium	LiF	8	1.9	6.3	
Westinghouse	Cesium–Iodine	LiF	12	1.9	6.3	

*Electrical Musical Instruments/United States
†CBS Laboratories, a Division of Columbia Broadcasting System, Inc.
‡Radio Corporation of America Laboratories.
§ASCOP Division of Electro-Mechanical Research, Inc.
‖Radio Corporation of America Electron Tube Division.
**International Telephone and Telegraph Laboratories.

††Much lower dark currents have been measured at GSFC for all of these tubes. A dark current of 2.5×10^{-12} ampere at a gain of 10^6 has been observed for a Cs-Te photomultiplier.
‡‡Opaque cathode deposited on a metal substrate.
***Tubes potted with resistor chain in place.

Additional data on specific phototubes are included in Table 2. A recent paper (Reference 11) describes the properties of spectrally selective photocathodes in more detail.

CALIBRATION

Calibration of the photocathodes has been divided into two phases. In the first phase, the relative cathode spectral response is determined from measurements taken at the exit beam of the Cary 14 double monochromator and the 1 meter McPherson vacuum monochromator. A hydrogen arc light source is used with both instruments. The quantum yield of sodium salicylate fluorescence is taken to be constant throughout the wavelength region from above 3300A down to below 1000A. For this reason the relative spectral response of the unknown photocathode, in terms of quantum yield, can be obtained by comparing the photocathode response to the monochromator beam with the fluorescent response of sodium salicylate to the same beam.

In the second phase, the relative quantum yield is put on an absolute basis by optical bench measurements. In general, use is made of a calibrated 2537A line of the mercury arc. On some occasions, the 2138A line of a zinc arc and the 1849A line of the mercury arc are also employed.

The mercury arc used is a small pencil-like septum lamp described by Childs (Reference 12). This lamp has a flux at one meter of about 2 μw/cm^2 for a specified axial position and is relatively insensitive to ordinary changes in line voltage or room temperature. The mercury arc 2537A line calibration is based on the use of three calibrated ultraviolet intensity meters, each consisting of a cadmium photocell and simple electrometer amplifier. These intensity meters were manufactured by the Lamp Development Laboratory of the General Electric Company. They were calibrated by the GE Company and are frequently compared against each other at GSFC. Their accuracy is estimated to be within 5 percent. These meters are used as a laboratory calibration reference and are employed each time a photosurface yield is measured against a mercury arc lamp. Thus, reliance is placed on photosurfaces rather than on discharge sources. The calibration of these meters has been checked by comparison with National Bureau of Standards (NBS) sources: first with an NBS mercury source by means of an NBS tantalum cell; then at GSFC with an NBS standard carbon filament lamp by means of a gold-black Golay cell.

GEOPHYSICAL AND ASTRONOMICAL APPLICATIONS

To date, middle ultraviolet astronomy (Reference 13) has been limited to preliminary surveys of the sky from unguided rockets. Most of these sky-survey type measurements have been made from White Sands, New Mexico (Reference 14), and Wallops Island, Virginia, with American Aerobee vehicles. More recently, southern sky measurements have been made from Woomera, Australia, with United Kingdom Skylark rockets. Although filter limitations have allowed only broadband photometry in certain spectral regions, these surveys are nevertheless of considerable value for comparison with predicted ultraviolet intensities and for intelligent planning of more sophisticated experiments.

A typical photometer is shown in Figure 9. These photometers may be mounted in pairs, triplets, etc., with parallel optical axes. With each photometer sensitive to a different band, multicolor observations can be taken. The orientation is such that during observation the combined precession and rotation of the rocket causes the photometers to scan a large portion of the sky. To increase the sky area coverage, sets of photometers may be pointed at several angles with respect to the rocket axis. On recent flights instruments have been mounted 105, 90, and 75 degrees from the longitudinal axis of the rocket.

Figure 10 shows, as an example, selected portions of a telemeter record for one photometer and demonstrates the heretofore unavailable data which may be obtained from simple middle ultraviolet techniques. In this case, the photometer optical axis was inclined 75 degrees from the rocket axis. During the portion of the flight represented by the upper trace the rocket was rising out of the airglow layer, and the stars may be seen superimposed on a decreasing airglow signal. In the lower traces the rocket was above the emitting layer, and the strong saturated signal at the edges of the trace is due to the bright airglow "horizon."

The ultraviolet airglow is of interest in its own right. Broida and Gayden (Reference 15) found that the Herzberg bands of molecular oxygen were the dominant feature in laboratory-produced air afterglow between 2500 and 3000A. Rocket measurements have shown this layer to be between 85 and 120 km, with ozone absorption evident up to 50 km.

The solar blind photocathodes described earlier may be used in photomultipliers for many conventional applications. In addition, work has begun on image converter tubes which will be selective to the middle and vacuum ultraviolet. Using such devices in a monocular or binocular system, an astronaut might survey for astrophysical or geophysical effects.
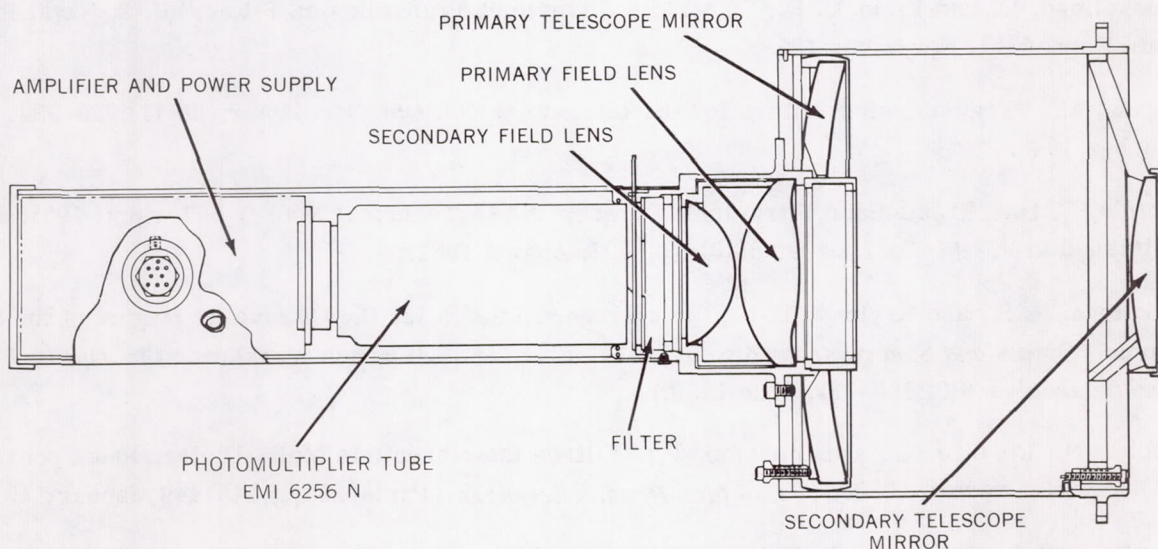
Figure 9—Photometer used for recent stellar measurements at Woomera, Australia. The objective mirrors are a modified Cassegrainian arrangement with a concave parabolic primary and a spherical secondary. The field lenses are quartz. In the filter cavity, filter pieces with diameters from 2.8 to 4.2 mm are centered over the entrance aperture.
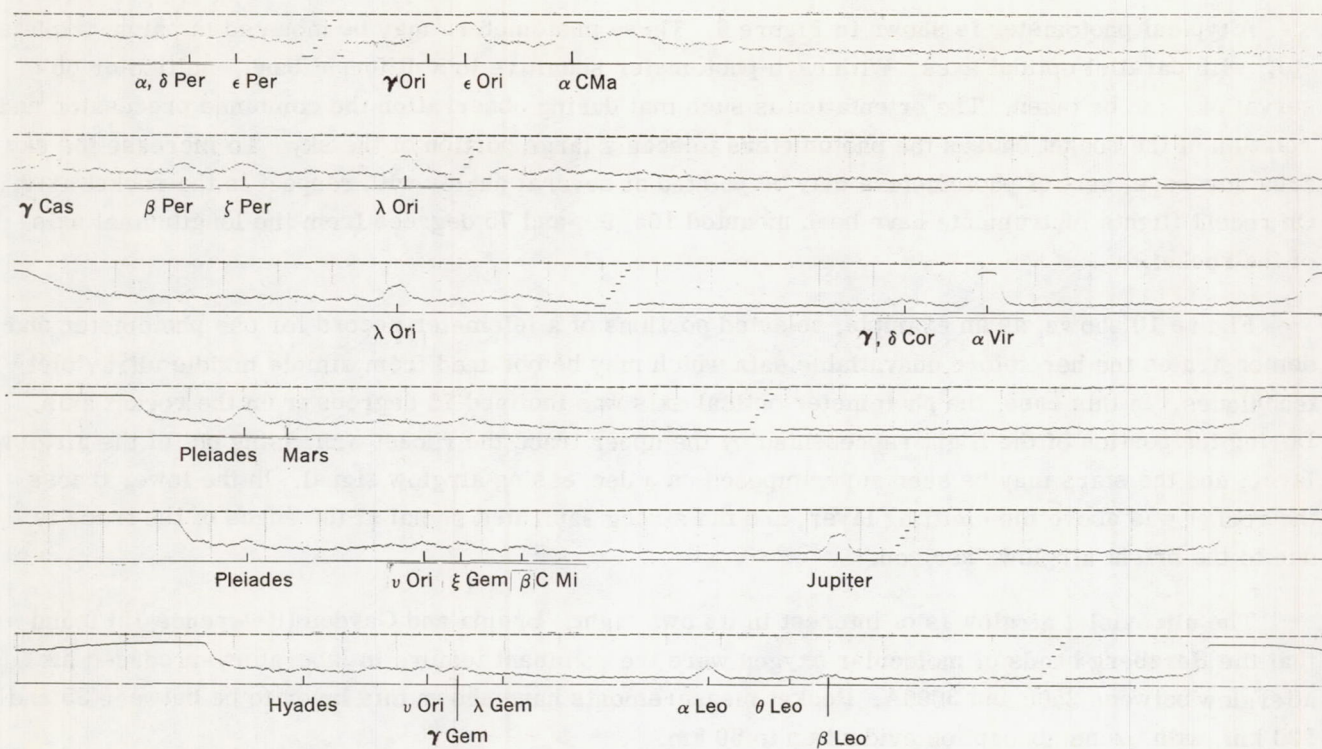
Figure 10—Telemeter record of 2700A rocket borne photometer. Saturated signals at the ends of the trace are due to the airglow horizon. Each trace is 12 seconds in duration. Telemeter calibrations indicate 1 volt steps.

REFERENCES

1. Dunkelman, L., and Field, D. E., "A Middle Ultraviolet Transmission Filter," U. S. Naval Res. Lab. Rept. 4647, November 1955.

2. Kasha, M., "Transmission Filters for the Ultraviolet," *J. Opt. Soc. Amer*. 38(11):929-934, November 1948.

3. Childs, C. B., "Broad-Band Ultraviolet Filters," NASA Technical Note D-697, April 1961; also published in *J. Opt. Soc. Amer*. 51(8):895-897, August 1961.

4. Sokolova, R. S., and Krylova, T. N., "Interference Filters for the Ultraviolet Region of the Spectrum," *Optics and Spectroscopy* 6(6):513-515, June 1959. (English translation of: *Optika i Spektroskopiya* 6(6):788-791, June 1959.)

5. Sebire, N., Cojan, J. L., and Giacomo, P., "Filtres Interferentiels Multi-Dielectriques pour l'Ultraviolet vers λ ≡ 2500A," *Comptes Rendus Sciences* (Paris) 254(3):448-449, January 15, 1962.

6. Dunkelman, L., and Lock, C., "Ultraviolet Spectral Sensitivity Characteristics of Photomultipliers having Quartz and Glass Envelopes," *J. Opt. Soc. Amer*. 41(11):802-804, November 1951.

7. Causse, J. P., "Status Report on the Development of the ASCOP Multipliers," *IRE Trans. on Nuclear Science* NS-9(3):90-96, June 1962.

8. Watanabe, K., and Inn, E. C. Y., "Intensity Measurements in the Vacuum Ultraviolet," *J. Opt. Soc. Amer.* 43(1):32-35, January 1953.

9. Taft, E., and Apker, L., "Photoemission from Cesium and Rubidium Tellurides," *J. Opt. Soc. Amer.* 43(2):81-83, February 1953.

10. Dunkelman, L., "Solar-Blind Ultraviolet Multiplier Phototubes," *J. Opt. Soc. Amer.* 45(2):134-135, February 1955.

11. Dunkelman, L., Fowler, W. B., and Hennes, J. P., "Spectrally Selective Photodetectors for the Middle and Vacuum Ultraviolet," *J. Opt. Soc. Amer.* 51(12):1461, December 1961 (Abstract); also to be published in *Appl. Optics*, November 1962.

12. Childs, C. B., "Low Pressure Mercury Arc for Ultraviolet Calibration," to be published in *Appl. Optics* November 1962.

13. Boggess, A., III., "Ultraviolet Astronomical Photometry from Rockets," NASA Technical Note D-673, June 1962. Also included *Space Astrophysics* ed. by W. Liller, New York: McGraw-Hill Book Co., 1961, pp. 121-132.

14. Boggess, A., III., and Dunkelman, L., "Stellar Flux Measurements at 2700Å," *Astronom. J.* 63(1262):303, September 1958 (Abstract).

15. Broida, H. P., and Gaydon, A. G., "The Herzberg Bands of O_2 in an Oxygen Afterglow and in the Night-Sky Spectrum," *Proc. Royal Soc.* London 222A(1149):181-195, March 9, 1954.

LOW-ENERGY TRAPPED PROTONS

by

Leo R. Davis

and

James M. Williamson

Goddard Space Flight Center

SUMMARY

A scintillation detector designed to measure the directional intensity and spectrum of 100 kev to 4.5 Mev protons and the directional energy flux and spectrum of 10 to 100 kev electrons has been flown on the Explorer XII satellite (1961 v). Analysis of a portion of the data recorded during the last half of August 1961 has shown that (1) the radial distance to the outer boundary of the geomagnetically trapped radiation is variable, ranging from 8.5 to 11.0 R_e; (2) electrons are trapped more or less uniformly from 2 R_e to the outer boundary; and (3) protons are trapped throughout the same region.

The proton intensity peaks on the dipole field line having an equational radius (R_o value) of about 3.5 R_e, where the maximum intensity is 6×10^7 protons/cm^2-sec-ster. The proton spectra may be approximated by exp $(-E/E_o)$ with, for example, E_o values of 400, 120, and 64 kev at R_o values of 2.8, 5.0, and 6.1 R_e, respectively.

During the magnetic storm which began on September 30, 1961, the proton intensity measured at high latitudes was enhanced by a factor of 3. The possibility that the main phase decrease of the storm was produced by the protons is discussed.

INTRODUCTION

The directional intensity and spectrum of 100 kev to 4.5 Mev protons and the directional energy flux and spectrum of 10 to 100 kev electrons trapped in the geomagnetic field have recently been measured on the Explorer XII satellite (1961 v). Explorer XII was launched at 0321 UT, August 16, 1961, into an elliptical orbit inclined 33 degrees to the equatorial plane, with a perigee altitude of 300 km, an apogee altitude of 77,300 km, and an orbital period of 26-1/2 hours. Initially, apogee was near local noon. The satellite instrumentation functioned properly up to December 6, 1961, when it abruptly ceased transmitting. Data were recorded nearly continuously throughout the life of the satellite, and when processed will be available for about 80 percent of that time. When the satellite ceased transmitting, apogee was near six hours local time.

The analysis, to date, has been in the nature of an initial survey to establish the proper operation and calibration of the instrumentation and to determine the gross features of the electron and proton radiation. The results have shown that (1) the trapped radiation exhibits a well marked outer boundary whose position is variable, ranging from 8.5 to 11.0 R_e; (2) electrons are trapped more or less uniformly from 2 R_e to the outer boundary; and (3) protons are trapped throughout the same region.

The present paper reports the initial results on the low energy trapped protons.

INSTRUMENTATION

The ion-electron detector flown on Explorer XII is similar to detectors flown previously on sounding rockets to measure auroral particles (Reference 1) and solar flare protons (Reference 2). It employed a 4.4 mg/cm² thickness of powder phosphor, ZnS(Ag), settled on the face of a photo-multiplier tube which was located behind a stepping absorber wheel. This is illustrated in Figure 1, which also shows a block diagram of the electronics. Both the dc output and the pulse counting rate of the phototube are telemetered. The ambient radiation can be admitted through either of the two apertures shown in Figure 1, depending on the wheel position. When radiation entering through the lower aperture is allowed to pass through the wheel, it reaches the phosphor directly. Radiation entering through the upper aperture can only reach the phosphor after having scattered off the gold surface shown positioned in front of the apertures in Figure 1.
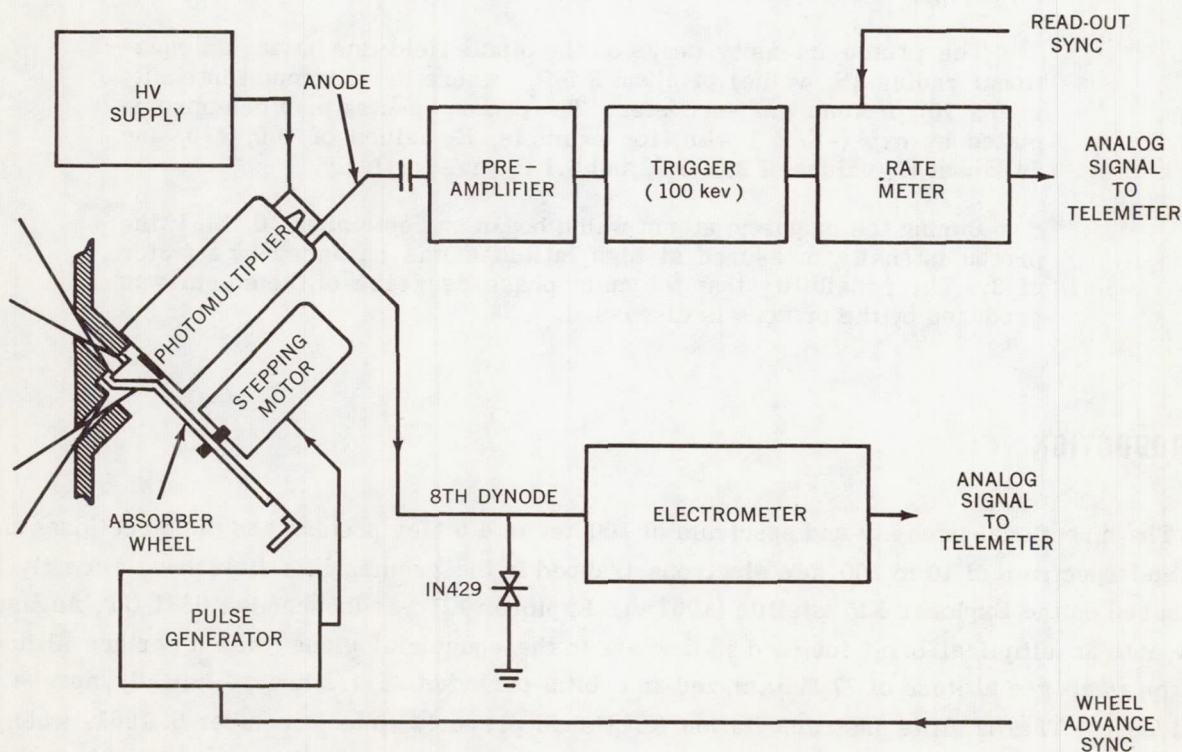
Figure 1—Simplified drawing of ion-electron detector geometry and block diagram of electronics

When the detector is operated in the scatter mode, the dc current of the phototube is essentially a measure of the energy flux of electrons since few protons or other heavy particles will be scattered. In the direct geometry, the current is a measure of the total energy flux of particles stopping in the phosphor. The measured sensitivities as a function of particle energy are shown in Figure 2 for electrons and protons incident in the direct geometry and for electrons in the scatter geometry. Sensitivity is defined here as the phototube output current per unit power of the mono-energetic particle beam passing through the aperture.

The trigger level of the pulse channel is set to count ions losing 80 kev or more energy in the phosphor. The measured proton counting efficiency as a function of proton energy is shown in Figure 2. From the figure it can be seen that the proton counting efficiency exceeds 50 percent between 100 kev and 4.5 Mev and falls off rapidly outside this energy range. The detector also counts heavier ions with high efficiency, i.e., alpha particles having energies between 120 kev and 130 Mev. Electrons are discriminated against by the phosphor thinness (the maximum average energy loss of an electron which will just traverse the phosphor is 60 kev) and by the particular light-pulse-decay characteristic of the ZnS(Ag) phosphor which allows electron-produced pulses to be partially differentiated out in the pulse amplifier. As a result, single electrons will not be counted.

The low energy cutoff of the response curves shown in Figure 2 results from the particles having to penetrate a 1000A thick aluminum coating on the phosphor (and, in addition, for ions to lose 80 kev in the phosphor to count). The wheel is used to interpose additional absorber which moves the low energy cutoff to successively higher values. The ratio of outputs with the different absorbers gives a rough measure of the energy spectra and a quite sensitive measure of any change in the spectra of electrons or ions. A thick plug position is provided on the wheel to determine the background produced by any penetrating radiation reaching the phosphor through the sides of the detector. There are also three wheel positions with radioactive sources for inflight calibration.

This paper presents proton intensities and spectra derived from the counting rate and absorption data on the assumption that all of the particles counted were protons. In this regard it should be noted that a second count rate channel was included to determine the ratio of protons to heavier ions. The trigger level of this channel was set greater than the energy loss of a proton which would just traverse the phosphor, i.e., at 900 kev compared to 800 kev. The results of a preliminary analysis show that a significant portion of the particles were heavier than
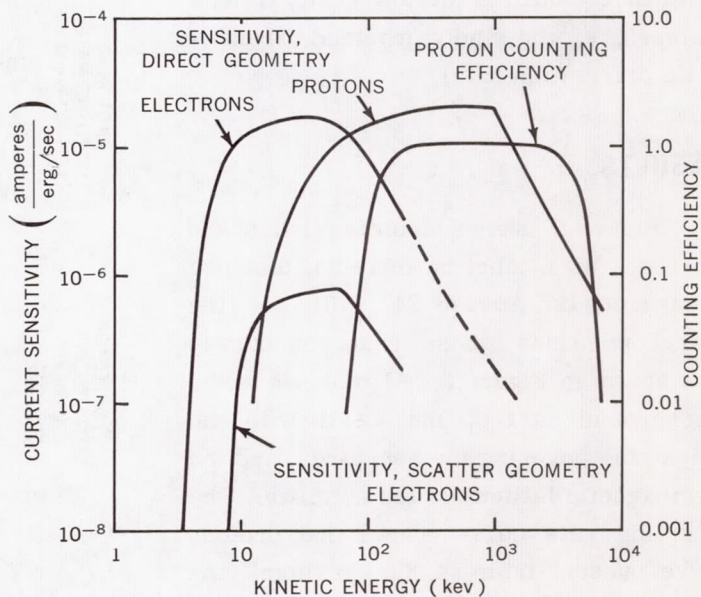
Figure 2—Current sensitivities to electrons and protons and proton count efficiency of ion-electron detector with no absorber

protons. These results are dependent on the trigger level remaining stable, and an analysis which will test this stability is now being made. Should the results be confirmed, the present proton intensities will need to be corrected downward. The correction will be 30 percent or less, and the shape of spectra will be little affected.

The count-rate meter has a 0 to 5 volt analog output which is proportional to the logarithm of the number of counts stored since the last readout. The output was sampled three times per second. Telescope factors of 5.8×10^{-4} and 5.4×10^{-3} cm^2-ster were employed and proton intensities up to $10^7/cm^2$-sec-ster could be measured.

The electrometer has a 0 to 5 volt analog output proportional to the logarithm of the input current for currents of 10^{-10} to 10^{-4} amp. Thus, electron and proton energy fluxes from about 10^{-2} to 10^{+4} erg/cm^2-sec-ster could be measured.

The detector was positioned to look out at 45 degrees to the satellite spin axis. Full opening angles of 15 degrees and 22 degrees were used. The satellite spun about an axis which was fixed in inertial coordinates with about a 2-second spin period. Thus, it is possible to measure directly the angular dependence of the particle fluxes. Over the satellite orbit, the angle between the spin axis and geomagnetic field varied from 25 degrees to 90 degrees; therefore, the scanned range of particle pitch angles varied from as much as 0 to 90 degrees to as little as 20 to 70 degrees. The detector orientation in inertial coordinates and with respect to the local magnetic field was measured by a solar aspect indicator, and a three component magnetometer (the magnetic field measurements on Explorer XII were performed by Dr. Lawrence Cahill, of the University of New Hampshire, who kindly provided the magnetic orientation data).

RESULTS

Figure 3 shows counting rates and currents as a function of radial distance measured on August 24, 1961, for the wheel positions whose response curves are shown in Figure 2. Also shown is the background current measured with the thick plug covering the apertures, and the geomagnetic latitude of the satellite. The counting rate curve shows that protons were present from 54,000 km radial distance down to 10,000 km. The peak proton intensity measured on this pass is $7 \times 10^6/cm^2$-sec-ster at three R_e. The
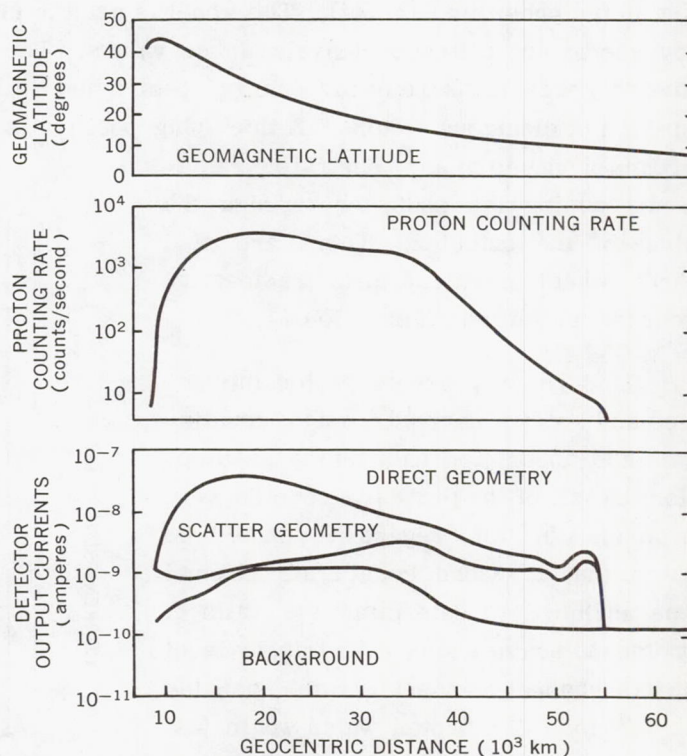
Figure 3—Ion-electron detector output currents and count rate as a function of geocentric distance on Explorer XII pass 7b August 24, 1961. The geomagnetic latitude of the satellite is also shown

142

difference between the current measured in the scatter geometry and the background current is a measure of the electron energy flux. As may be seen, the electron flux rises to a maximum at 35,000 km and slowly decreases with increasing distance out to 54,000 km, where an abrupt discontinuity is observed and the electron flux drops below a detectable value. The difference between the current measured in the direct geometry and scatter geometry could only be produced by protons and thus confirms the count rate data. The peak in the background current apparently is due to the penetrating radiation which forms the "outer belt" as defined by Geiger-Müller counter measurements (Reference 3).

The pitch angle distributions of the protons on the dipole field line having an equatorial radius (R_o value) of 3.5 R_e are shown in Figure 4. In Figure 4a are plotted the eight dynode currents measured at various local pitch angles on three crossings of the field line, each at a different geomagnetic latitude. The smooth lines drawn through the data points have been transformed from local pitch angle to equatorial pitch angle, assuming a dipole field and a constant $(\sin^2 a)/B$, and are shown in Figure 4b. The three segments of pitch angle distribution so obtained are in reasonable agreement and together trace out the equatorial pitch angle distribution from 10 to 72 degrees. The resulting distribution is well approximated by a $\sin^3 a_o$ curve, where a_o is the equatorial pitch angle.

Proton spectra measured on three field lines on August 26 are shown in Figure 5. The data are plotted as integral spectra; however, it should be noted that the detector does not measure protons having energies greater than 4.5 Mev and we are thus assuming there is no significant number of the
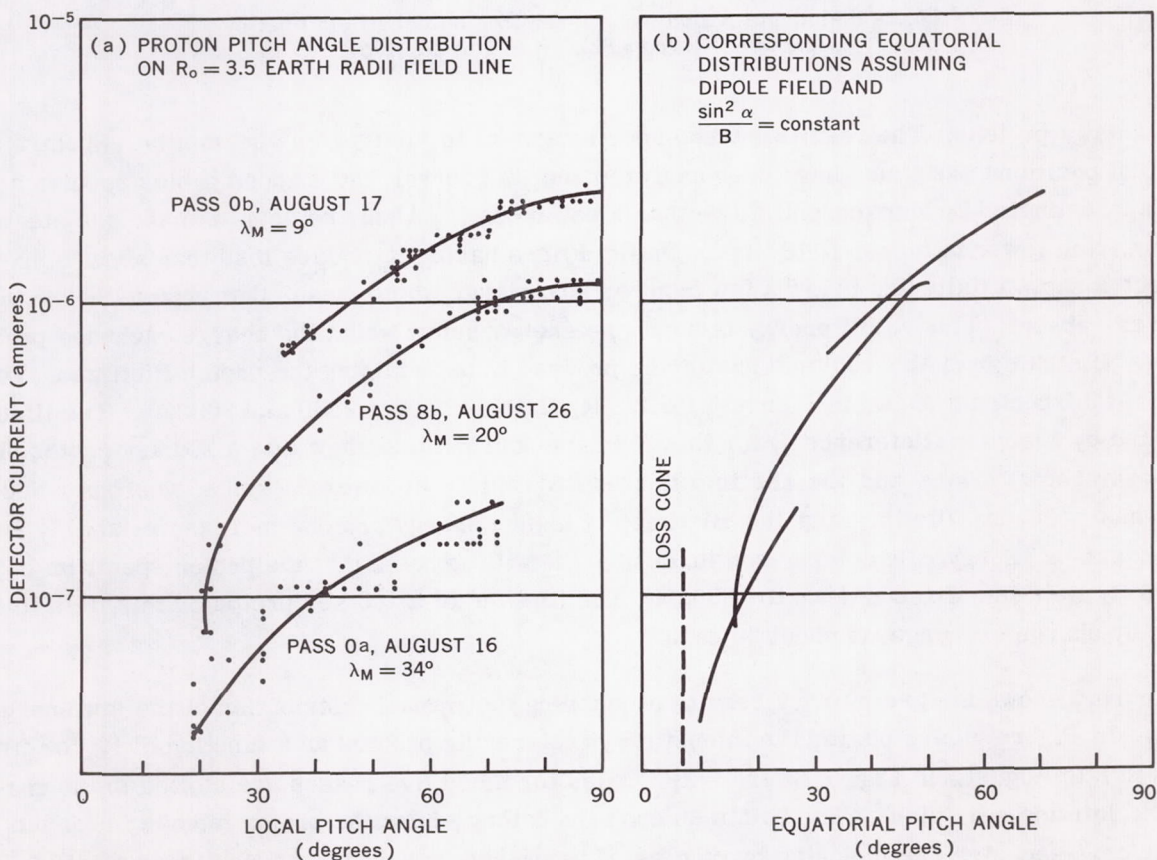
Figure 4—(a) Measured local pitch angle distributions of low energy protons on three crossings of the 3.5 R_e field line   (b) The corresponding equatorial pitch angle distributions
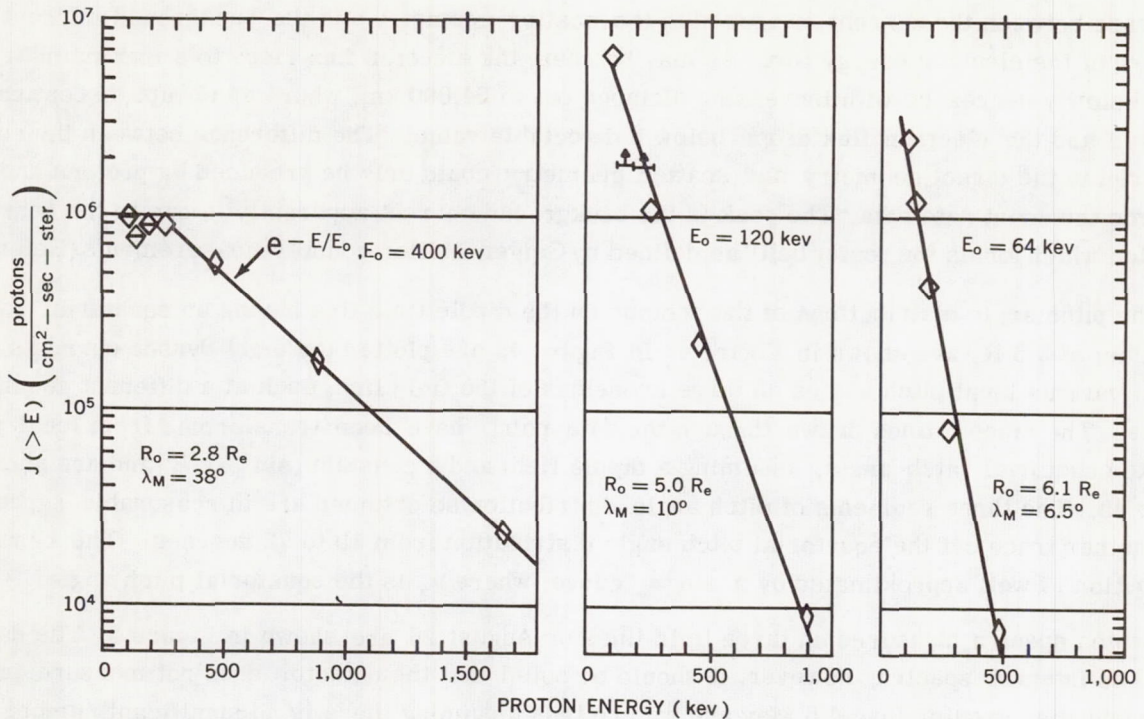
Figure 5—Integral proton spectra measured on three field lines by
Explorer XII (pass 8b), on August 26, 1961

higher energy protons. The resulting steep spectra appear to justify this assumption. Spectra at a number of positions and times have been analyzed and, in general, the trapped proton spectra are better approximated by an exponential law than a power law. As may be seen, the spectra steepen as we move from lower to higher field lines. On field lines having R_o values less than about 3 or 4 R_e, the spectra show a flattening below a few hundred kev energy which means that protons below this energy are absent. This cutoff energy is about the energy below which the charge exchange process becomes dominate over the coulomb scattering process in determining the proton lifetimes. For example, the spectrum shown in Figure 5 for 2.8 R_e flattens between 200 and 300 kev. The lifetimes calculated by Liemohn (Reference 4) for this field line and latitude show that a 200 kev proton has a lifetime of about 5 days and the lifetime decreases rapidly at lower energies, whereas a 300 kev proton has a 30-day lifetime and the lifetimes of higher energy protons increase relatively slowly with increasing energy. By comparison in Figure 5 it will be noted that the proton spectrum obtained on the 5 R_e field line extends down to 100 kev. The lifetime of a 100 kev proton on this field line, limited by charge exchange, is about 50 days.

Figure 6 shows the preliminary results of mapping the spatial distribution of the low energy protons. In Figure 6b are plotted the intensities of mirroring protons as a function of R_o for five passes in late August. In Figure 6a the trajectories for these five passes are plotted in the geomagnetic latitude — R_o plane. The points on each trajectory where the proton intensity reached 10^7 protons/cm^2-sec-ster are indicated by circles. The dashed line drawn through these points is, therefore, the corresponding proton intensity contour. The contour for an intensity value of 10^6 is

144

similarly shown. As may be seen the resulting contours show that the low energy proton intensity is a maximum at about 3.5 R_e.

The pulse channel of the detector is in saturation at intensities above $10^7/cm^2$-sec-ster. This effect can be seen on pass 8b in Figure 6b. The dc channel at this time is still some three decades below saturation and thus may be used to measure the proton intensity at the higher values. This has been done for passes 0b and 1b in Figure 6b. As may be seen, the maximum proton intensity is about $6 \times 10^7/cm^2$-sec-ster measured some 7 degrees off the geomagnetic equator. This measurement should be accurate to ± 50 percent. A more accurate value will be obtained when the spectrum in this region is derived. Using the measured pitch angle distribution and assuming an average proton energy of 400 kev, we calculate the proton density to be one-half proton per cubic centimeter. The corresponding proton kinetic energy density of 2×10^5 ev/cm^3 is about one-tenth the energy density of the geomagnetic field at this point.

Figure 6—(a) Six Explorer XII trajectories mapped in the geomagnetic latitude – R_o plane, and proton intensity contours for $J = 10^6$ and 10^7 protons/cm²-sec-ster (b) Directional intensities of locally mirroring protons (120 kev $\leq$ E $\leq$ 4.5 Mev) as functions of R_o measured on six passes through the proton belt

The proton energy density in the region from 4 to 8 R_e shows a remarkable tendency to track the field energy density. This is illustrated in Figure 6b where the curve labeled "J_H (200 kev)" shows the directional intensity of 200 kev protons which, if isotropic, would have a kinetic energy density equal to the dipole field energy density. As may be seen, the proton intensity measured at low latitudes is about one-third of J_H (200 kev). When the proton pitch angle distribution is taken into consideration this means that the ratio of field energy density to proton energy density in the equatorial plane is approximately 6 in the region 4 to 8 R_e.

Nineteen more or less complete passes through the proton belt are presently available for studies of temporal variations. The data obtained on 15 of these passes, scattered through the period August 16 to September 30, 1961, show no temporal change in the proton intensities measured on field lines which have $R_o < 7 R_e$; i.e., the data are constant to within ± 30 percent.

At 2108 UT on September 30, a sudden commencement (SC) occurred which was followed by a magnetic storm lasting several days. At the time of the SC, Explorer XII was nearing apogee. The

next pass through the proton belt occurred some 17 hours later. On this pass and three succeeding passes on October 1 and 2, the proton intensities measured in the region from 3 to 4.5 R_e were greater by a factor of 3 than the pre-storm values. However, the satellite crossings of this region were at geomagnetic latitudes greater than 30 degrees so that only protons having equatorial pitch angles of 34 degrees and less were sampled. From the pre-storm pitch angle distribution, it is known that only 4 percent of the protons trapped in these field lines have equatorial pitch angles of 34 degrees or less. Thus, with these data we cannot determine whether the total proton population was increased or whether there was simply a redistribution in pitch angles of the pre-storm population.

The total kinetic energy of the trapped low energy protons exceeds that of any other known population of trapped particles, and thus their disturbance of the geomagnetic field is greatest. It is of obvious interest to determine the magnitude of the disturbances. Akasofu, Cain, and Chapman (Reference 5), using a computer code developed for a previous theoretical study, have calculated the disturbance for a model proton belt which closely approximates our pre-storm belt. The results predict a decrease in the surface equatorial field of 40 γ. They have further calculated (private communication) the additional disturbance which would result if the storm time increase existed at all values of pitch angle. The results predict an 80 γ additional decrease which is to be compared with D_{st} values of 60 to 30 γ on October 1 and 2. Thus, we may hypothesize that the main phase decrease was produced by these low energy protons. A second large magnetic storm and several small storms occurred during the life of Explorer XII. When these data become available, further tests of this hypothesis will be made.

There are no previous measurements of trapped protons below 1 Mev in the region of the outer belt. However, the rocket measurements of Bame, Conner, et al. (Reference 6) have clearly shown that protons having energies down to 1 Mev are trapped on field lines having R_o values around 2.5 to 3 R_e. A preliminary comparison with their data, using, however, only dipole coordinates, shows agreement in both intensity and spectral slope for proton energies of around 1 Mev. Our results may be related to the results of Naugle and Kniffen (Reference 7) and of Freeman (Reference 8); however, to date no comparison has been made.

REFERENCES

1. Davis, L. R., Berg, O. E., and Meredith, L. H., "Direct Measurements of Particle Fluxes In and Near Auroras," in: *Space Research: Proc. 1st Internat. Space Sci. Sympos., Nice, January 1960,* ed. by H. K. Bijl, Amsterdam: North-Holland Publ. Co., 1960, pp. 721-735

2. Ogilvie, K. W., Bryant, D. A., and Davis, L. R., "Rocket Observations of Solar Protons during the November 1960 Events, 1," *J. Geophys. Res.* 67(3):929-937, March 1962

3. O'Brien, B. J., Van Allen, J. A., et al., "Absolute Electron Intensities in the Heart of the Earth's Outer Radiation Zone," *J. Geophys. Res.* 67(1):397-403, January 1962

4. Liemohn, H., "The Lifetime of Radiation Belt Protons with Energies between 1 Kev and 1 Mev," *J. Geophys. Res.* 66(10):3593-3595, October 1961

5. Akasofu, S. R., Cain, J. C., and Chapman, S., "The Magnetic Field of the Quiet-Time Proton Belt," *J. Geophys. Res.* 67(7):2645-2647, July 1962

6. Bame, S. J., Conner, J. P., et al., "Protons in the Outer Van Allen Belt," *J. Geophys. Res.* 67(4): 1628, April 1962 (Abstract)

7. Naugle, J. E. and Kniffen, D. A., "Flux and Energy Spectra of the Protons in the Inner Van Allen Belt," *Phys. Rev. Letters* 7(1):3-6, July 1, 1961; also NASA Technical Note D-412, August 1961

8. Freeman, J. W., "Detection of an Intense Flux of Low-Energy Protons or Ions Trapped in the Inner Radiation Zone," *J. Geophys. Res.* 67(3):921-928, March 1962

COSMIC RAY OBSERVATIONS IN SPACE

by

D. A. Bryant*, T. L. Cline, U. D. Desai* and F. B. McDonald

Goddard Space Flight Center

SUMMARY

The Explorer XII cosmic ray experiment is described and measure-
ments made during the solar event of September 28, 1961, are discussed.
Galactic cosmic ray measurements are also reported. A few hours before
the class 3 flare of September 28 two short counting rate increases were
observed and these have been interpreted as electron bursts. The ani-
sotropy of the solar protons is described. It is found that the history of
the intensity of the solar protons is consistent with their having diffused
through interplanetary space with an effective mean free path of 0.04 AU.
An estimate of the distance from the sun at which diffusion becomes un-
important and particles escape gives 2-3 AU. Simple diffusion, does not
account for the anisotropy observed early in the event. Two days after the
flare there was a large increase in the intensity of protons with energies
less than 15 Mev. As most of these particles, which have been called
"energetic storm particles", arrived after the sudden commencement, it
is suggested that they were solar protons trapped within the plasma cloud
which caused the magnetic storm. A possible trapping mechanism is out-
lined. Explorer XII measurements of the Forbush decrease of September
30, 1961, are compared with neutron monitor measurements at Deep
River. The decrease is larger at Explorer XII by a factor of 1.7 ± .3.

INTRODUCTION

Explorer XII (1961 v) was launched on August 16, 1961, into a highly elliptical orbit having an
initial perigee of 6700 km, an apogee of 83,600 km, and an orbital period of 26.5 hours. During its
active life the satellite, at apogee, was on the sunlit side of the earth. For more than half the time
in each orbit the satellite was beyond the magnetosphere so that it was possible to obtain cosmic ray
measurements free from the influence of the earth's magnetic field and the Van Allen radiation.

The cosmic ray experiment on Explorer XII was designed to measure the intensity and energy
spectra of the galactic cosmic ray protons between 100 and 600 Mev and the total proton intensity
above 600 Mev. The objectives of the experiment were to study the 11-year modulation, diurnal
variations, Forbush decreases, and other modulations that occur in the primary cosmic ray intensity
in addition to the dynamics of solar cosmic ray events.

---

*NAS-NASA Resident Research Associate

The lower limit of the detectable proton energy spectrum can be extended from 100 Mev, the quiet-time value, to 3 Mev during solar cosmic ray events. This extension, possible only when the intensity at low energies exceeds the background produced by the high energy particles, provides a sensitivity about 50 times greater than that which can be achieved by riometers.

This paper describes the detectors used and discusses the measurements made during the solar cosmic ray event initiated by a class 3+ flare on September 28, 1961. Fortunately, the satellite was at apogee both at the time of the arrival of the solar cosmic rays and when the magnetic storm began two days later.

The rise and recovery of the solar proton intensity were recorded as a function of energy from 3 to 600 Mev. A plasma cloud, apparently emitted at the time of the flare, produced a large magnetic storm and a moderate Forbush decrease about 46 hours later. At the time of the sudden commencement of the magnetic storm, an increase in the intensity of low-energy (E<30 Mev) protons was observed. The other four solar cosmic ray events observed during the 112-day active life of the satellite, and further details of the modulation of galactic cosmic rays, will be discussed in subsequent reports.

DETECTORS

Three cosmic ray detectors were used. The details of the electronics for this experiment have been described by Desai, Porreca, and Van Allen (Reference 1). A scintillation counter telescope (Figure 1) was used to detect medium energy (E>100 Mev) and high energy (E>1 Bev) protons. It is formed by two thin disks of plastic scintillator, and has a geometric factor of 13.6 cm^2-ster. When a coincidence occurs, the pulse height from one of the scintillators is measured by an on-board 32-channel differential pulse height analyzer which has a storage capacity of 65,535 counts per channel.
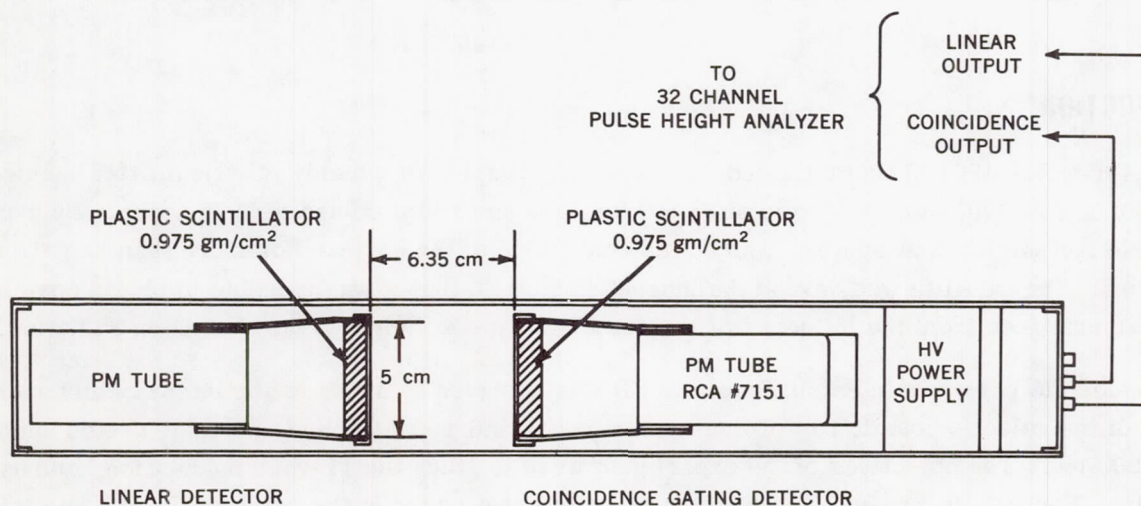
Figure 1—The scintillation counter telescope. A coincidence must occur to allow the pulse height from one scintillator to be recorded. This requirement and the bias levels of the 32 channel pulse height analyzer set the lower energy limit of detectable protons at 100 Mev

The analyzer stores information for 5 minutes and is read out for 2 minutes during each 7-minute interval.

The response of the analyzer to galactic cosmic rays on four days is shown in Figure 2 with the proton energy calibration. During these quiet times most of the particles are minimum ionizing and produce a well-defined peak between channels 7 and 8. The position of this peak serves as a calibration for all channels: a gain shift of about 4 percent between August 18 and September 6 is well marked. The distributions shown in Figure 2 are caused by the Landau spread of the minimum-ionizing particles and by the higher energy losses of the lower energy particles. An overflow channel records large energy losses and provides a composite measurement of alpha particles and of protons between 50 and 80 Mev. Statistical fluctuations in the energy loss of alpha particles result in some of their counts appearing in the last few channels of the analyzer. Since protons of energy less than 100 Mev are counted in these channels too, the lower limit for measuring protons with the detector is set at 100 Mev. The upper limit is set at 600 Mev because all protons above this energy suffer statistical fluctuations in energy loss comparable to the difference in their energy losses. High-energy electrons can register in the minimum ionization channels but cannot do so in the 100 to 600 Mev proton range.
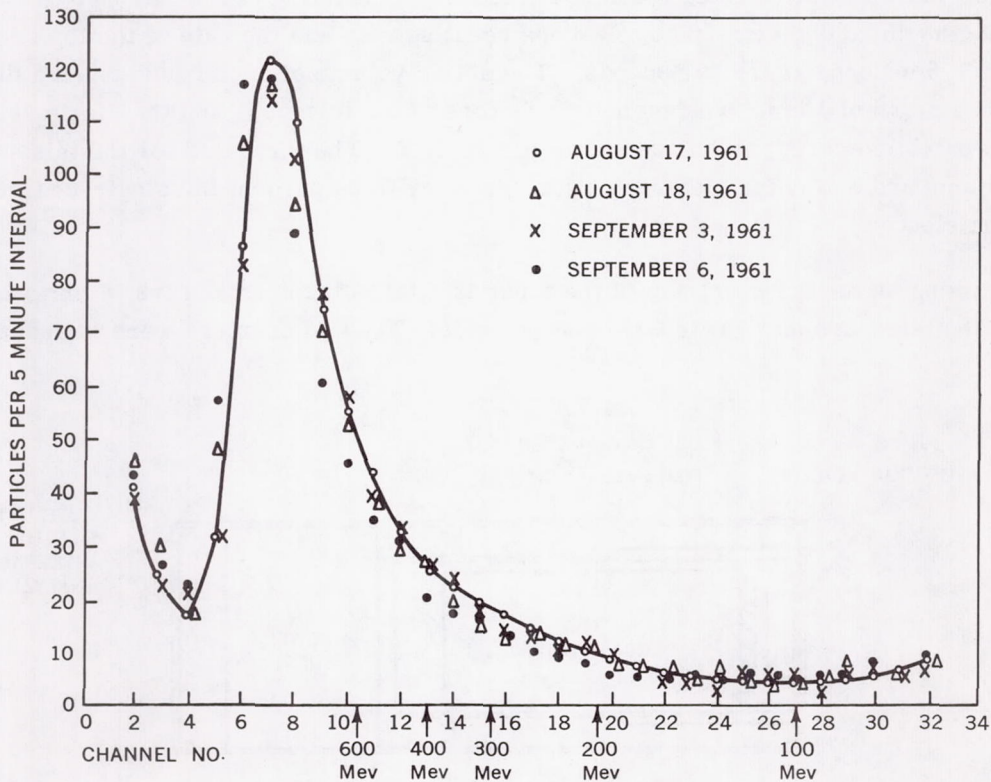
Figure 2—Scintillation counter telescope pulse height distributions taken on four days during solar quiet times. The peak is due to minimum ionizing cosmic rays

A thin *CsI (Tl)* crystal (Figure 3), 1.9 cm in diameter and 0.5 gm/cm^2 thick, covered only by a 6.5 mg/cm^2 aluminum foil, extended the measurements to lower energies. An aluminum collimator with an average thickness of 1.7 gm/cm^2 surrounds the crystal. The output of the photomultiplier viewing this crystal is fed to an 8-level integral pulse height analyzer. Counts are stored for 1.6 seconds once every 26 seconds at each level, with a 2.6 second interval between changing levels. Calibration is provided by a small Pu^{239} alpha particle source mounted on the front of the crystal. These alpha particles have an effective energy loss of 3.5 Mev in the *CsI* crystal.

The energy response for protons incident through the thin foil is shown in Figure 4. The response is double valued: Group A represents stopping protons and Group B represents those protons completely traversing the crystal. The single crystal data are corrected for particles in region B and for particles that are not directly incident on the foil but pass through the back and through the sides of the aluminum collimator. Assuming an isotropic distribution, data from the scintillation counter telescope and Geiger counter telescope are used to make these corrections. The 8th level, for example, then gives the differential proton intensity between 9 and 14 Mev, and levels 2 to 7 give differential intensities in the region 3 to 9 Mev. The first level is set at 120 kev and is sensitive to electrons above 130 kev and to protons above 2 Mev. The electron data will be discussed in a subsequent paper when bremsstrahlung, scattering, and nuclear-interaction background corrections have been evaluated.

A Geiger-Müller (GM) counter telescope (Figure 5) consisting of two halogen-filled disk-shaped counters, is the third detector. The telescope counting rate and the rate of the top counter are sampled for 1.6 seconds every 26 seconds. The active volume of each counter has a diameter of 4.45 cm and a depth of 1 cm. The geometric factors of the telescope and the single counter are functions of particle energy; these are shown in Figure 6. The threshold for the telescope is 70 Mev for protons and 8 Mev for electrons. Its efficiency is 88 percent for singly-charged minimum-ionizing particles.

By assuming an energy spectrum of the form $AE^{-\gamma}$ for solar cosmic rays, A and γ can be evaluated from the telescope and single GM counter rates. The GM counters were included primarily
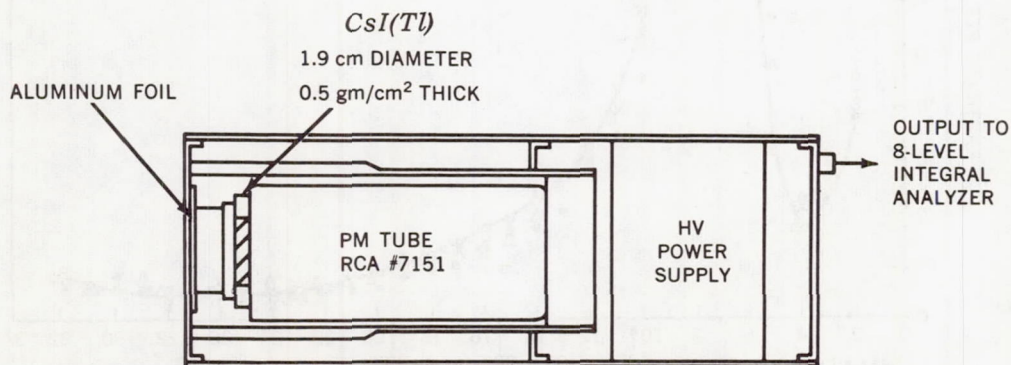
Figure 3—The scintillation counter assembly. The thin cesium iodide crystal, the aluminum collimator and foil, the photomultiplier and power supply are shown. The foil and the bias levels of the 8 channel pulse height analyzer set the lower limit of energy of detectable protons at 2 Mev
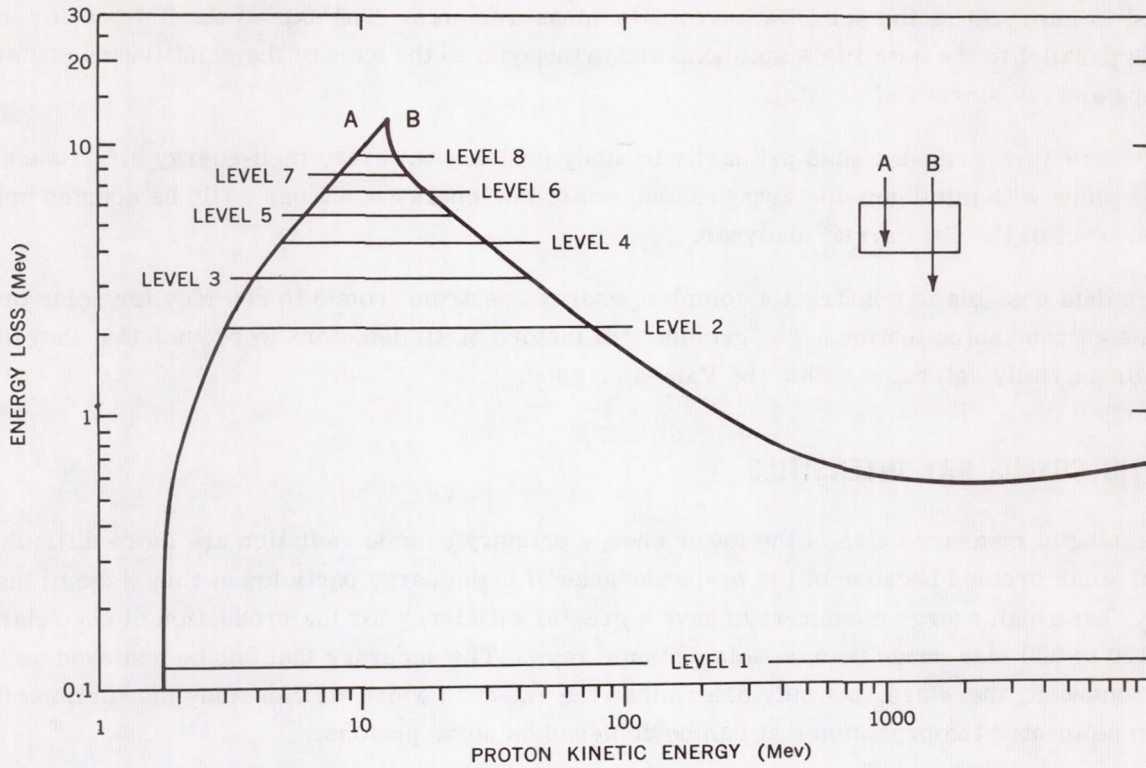
Figure 4—Energy loss in the *CsI* crystal versus proton energy. The response is double valued since protons traversing the crystal (B) can lose the same energy as those stopping (A). Information from the other detectors is used to resolve this ambiguity
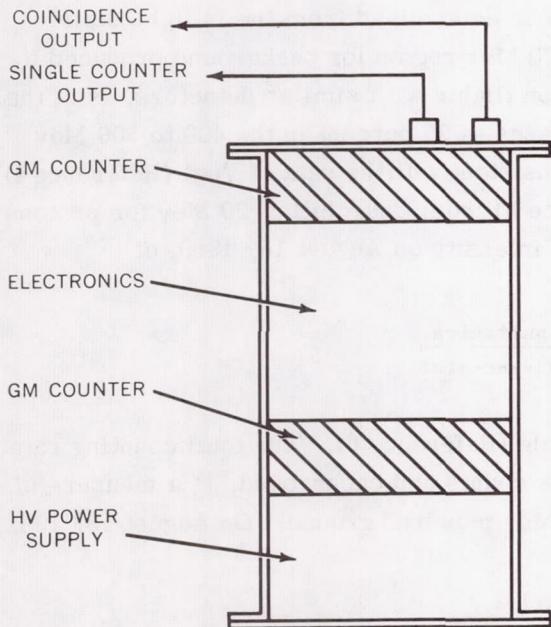

Figure 5—The Geiger-Müller counter telescope. The rate of coincident events and the rate of single events in the top counter are recorded
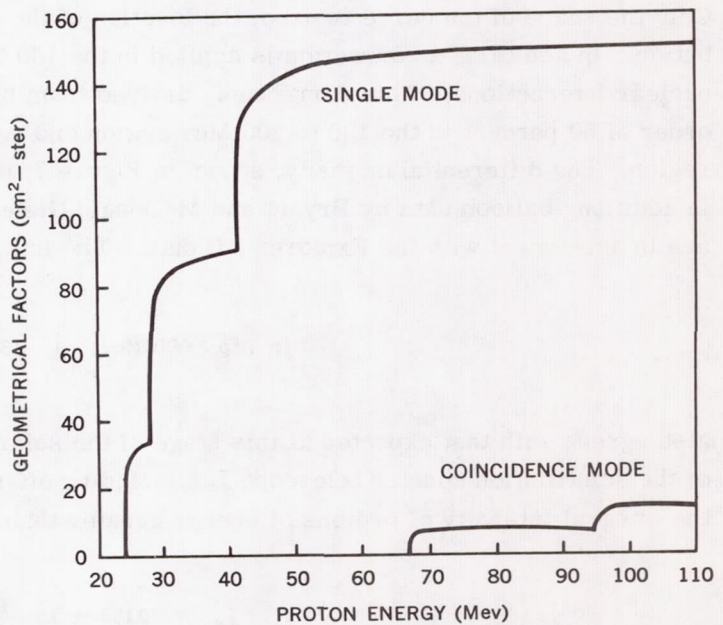

Figure 6—Geiger-Müller counter geometric factors, which are defined by the shielding, are shown as a function of energy for the single and coincidence modes

to assist in interpreting the scintillation counter measurements. The axis of the GM counter telescope is parallel to the satellite's spin axis and orthogonal to the axes of the scintillation counter telescope and the single *CsI* crystal.

The detectors were designed primarily to study protons; however, high-energy electrons could register along with minimum-ionizing protons, while low-energy electrons could be counted only on the first level of the *CsI* crystal analyzer.

It is thus possible to construct a complete energy spectrum from 3 to 600 Mev for solar protons without electron contamination. The geometrical factors of all detectors were such that they saturated or partially saturated within the Van Allen zone.

GALACTIC COSMIC RAY INTENSITIES

Meaningful measurements of the lower energy primary cosmic radiation are more difficult than those of solar protons because of the preponderance of high energy particles at this stage of the solar cycle. These high energy cosmic rays have a greater efficiency for the production of secondaries in the 100 to 600 Mev range than do solar cosmic rays. The accuracy that can be achieved on quiet-time intensities, therefore, not only determines the extent to which we can study modulation effects but also delineates the precision that can be achieved on solar protons.

Typical pulse height distributions from the scintillation counter telescope at apogee are shown in Figure 2. The primary alpha particle distribution is off-scale and cannot be resolved from very low energy protons and heavily ionizing background. A correction for the Landau distribution (References 2 and 3) is applied on the form of the curve obtained from μ mesons in a laboratory test. Only the shape of the curve is used; the location of the peak is determined from the inflight distribution. In addition, a correction is applied in the 100 to 600 Mev region for background produced by nuclear interactions. This correction, derived from balloon flights with similar detectors, is of the order of 50 percent in the 100 to 200 Mev region and decreases to 35 percent in the 400 to 500 Mev region. The differential intensity, shown in Figure 7, is consistent with the data of Vogt (Reference 4). In addition, balloon data by Bryant and McDonald (Reference 5) from Churchill at 90 Mev for protons are in agreement with the Explorer XII data. The integral intensity on August 18, 1960, of

$$J_P \ (E_P > 600 \ \text{Mev}) \ = \ 1380 \ \frac{\text{particles}}{\text{m}^2\text{-sec-ster}}$$

also agrees with that expected at this stage of the solar cycle (Reference 6). The total counting rate of the scintillation counter telescope J_T, including off-scale counts and background, is a measure of the integral intensity of protons of energy greater than 50 Mev plus background. On August 18, 1961,

$$J_T \ = \ 2100 \ \pm \ 70 \ \frac{\text{particles}}{\text{m}^2\text{-sec-ster}} \ .$$

For comparison, the total intensity measured by the GM counter telescope is

$$J_T = 1980 \pm 200 \frac{particles}{m^2\text{-sec-ster}}.$$

A detailed study of cosmic ray modulation is not made in this paper. The Forbush decrease of September 30, 1961, will be discussed in a later section.

THE SEPTEMBER 28, 1961 SOLAR COSMIC RAY EVENT

On September 28, 1961, a class 3+ solar flare occurred at 14°N and 30°E. Enhanced H_α emission began at 2202 UT, reached a maximum at

Figure 7—The low energy primary cosmic ray spectrum. The differential intensity between 0.5 and 1 Bv is consistent both with the results of Vogt and with a flat spectrum at these rigidities

2223, and ended at 0009 UT on September 29, and a type IV radio outburst occurred at 2212 UT (CRPL). At 2215 UT, a short x-ray burst reached maximum (K. A. Anderson, private communication).

Preflare Activity

A few hours before the flare (at 1803 UT and at 2105 UT), when the satellite was located outside the magnetosphere at 80,000 km, two short counting rate increases were recorded by the first level of the single crystal scintillator; these are shown in Figure 8. This level has a threshold of about 2 Mev for protons and about 130 kev for electrons and gamma rays, but also responds to pile-up of high-intensity low-energy electrons as observed in the outer radiation belt. The second level, having a threshold of 2 Mev for electrons and 3 Mev for protons, did not exhibit an increase. Thus, it is almost certain that these increases were caused not by protons but by either solar gamma rays or a cloud of high-energy electrons outside the radiation zone. On the basis of Explorer XII data alone we cannot decide between these two possibilities. However, Anderson, with a balloon-borne x-ray detector near the top of the atmosphere after 1800 UT on September 28, did not observe these increases (K. A. Anderson, private communication). We believe, therefore, that these bursts were due to electrons. The peak intensity observed in the first burst corresponds to about 120 electrons/cm²-sec-ster.

Figure 8—Preflare activity. Two counting rate increases which occurred several hours before the solar flare on September 28, 1961, are interpreted as electron bursts

Solar Cosmic Rays

The high-energy protons which arrived soon after the flare was observed were detected by the scintillation counter telescope and the GM counter telescope. Because of noisy reception from the satellite just at the time of the flare, reliable data were not available until after 2239 UT on September 28, about 24 minutes after the x-ray peak. The solar cosmic ray intensity had then reached only 50 percent of the intensity of galactic cosmic rays of energy greater than 100 Mev. Plots of the first few differential pulse height distributions recorded by the scintillation telescope after the flare are shown in Figure 9, illustrating the form in which the raw data are obtained. "Background" in the figure indicates the distribution of quiet-time galactic cosmic rays. Inspection of these curves reveals that, at first, the relative increase in the intensity of minimum-ionizing particles is greater than that of the more heavily ionizing particles.

Analysis of these distributions gives the differential energy spectra shown in Figure 10. The energy interval shown is between 120 and 620 Mev; the values of the integral intensities of the protons near minimum-ionization, or above 620 Mev, are not shown. It is evident that the differential intensity of the higher energy particles was greater at first but was gradually overtaken by the intensities of the successively lower energy particles. Each time-label indicates the start of the 5-minute interval during which the respective counts were stored in the analyzer. At the time corresponding to the last curve shown, the higher energy particles were reaching maximum intensity while the intensities of the particles below 100 Mev were still increasing.

Anisotropy of Medium Energy Solar Cosmic Rays

The scintillation counter telescope and the GM counter telescope were oriented on the satellite with orthogonal axes; the former was perpendicular and the latter parallel to the spin axis. Since

156
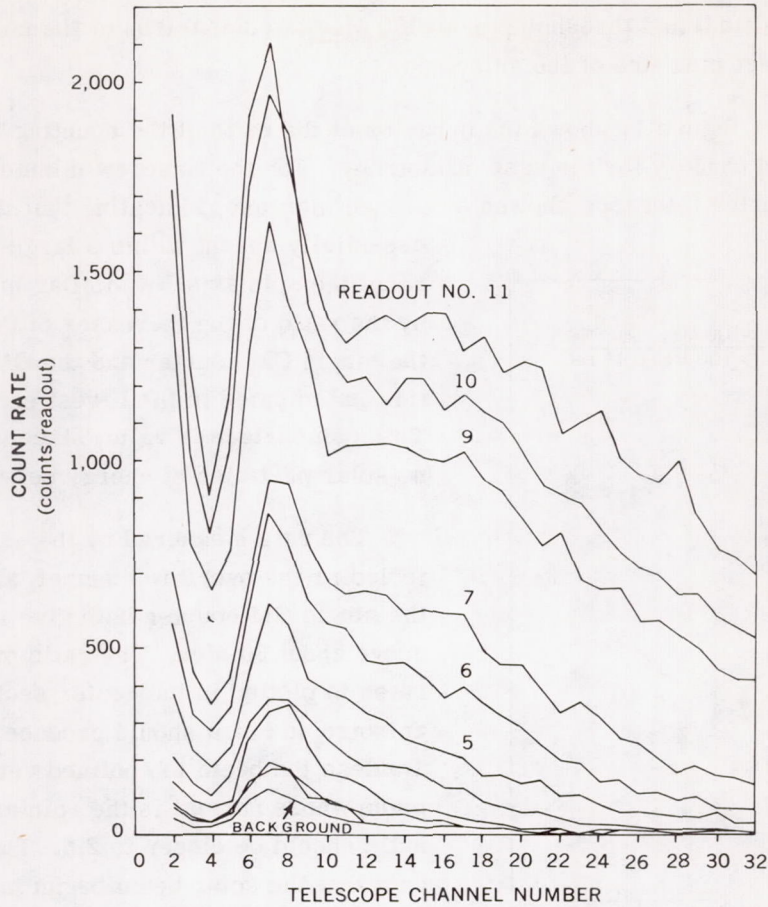
Figure 9—Differential pulse height spectrum from the 32-channel analyzer taken following the solar flare on September 28, 1961. (One spectrum is missing.) The background spectrum, taken a few hours before the flare, is indicated for comparison.
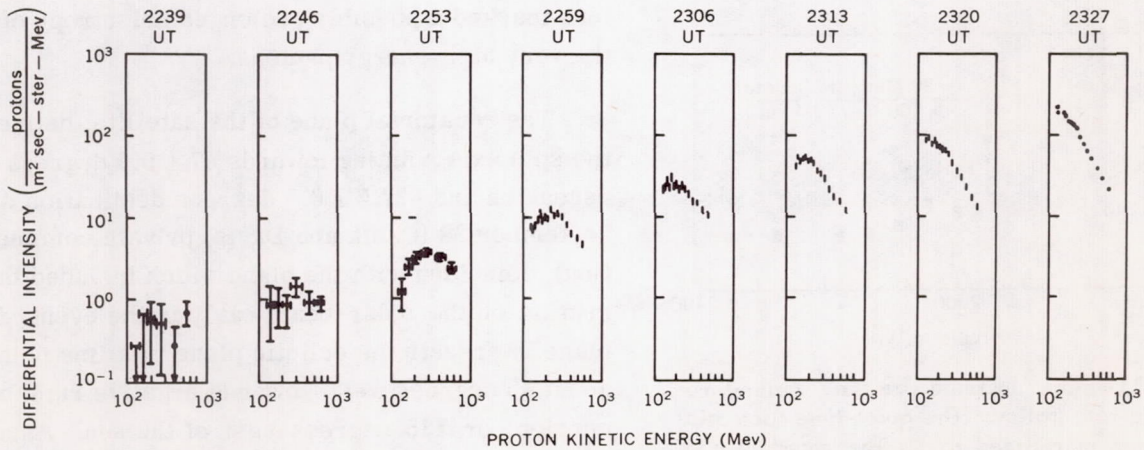

Figure 10—The rise of the September 28, solar proton event, showing differential energy spectra of the particle increases over galactic background. The "snapshots" of the solar proton spectrum were recorded about seven minutes apart and show that the spectral shape changed rapidly early in the event.

both the GM counter telescope and the scintillation telescope (used as an integral counter with the "overflow" counts omitted) had thresholds near 100 Mev, a comparison of the counting rates of these detectors gives a direct measure of the anisotropy.

The top section of Figure 11 shows the behavior of the ratio of the counting rate increases. The ratios are normalized to unity for the case of isotropy. For the first few minutes of reliable data recovery, the GM counter telescope showed almost no increase, indicating that the solar beam was essentially absent within a large-angle cone centered about the spin axis. A similar measure is provided by the ratio of the increases of the counting rates of the single GM counter and the GM counter telescope; this is indicated in the lowest section of Figure 11. This comparison is valid, since at that time there were no solar particles of energy between 30 and 100 Mev.

The rate measured by the scintillation counter, including the overflow channel, and that measured by the single GM counter both give integral intensities above about 30 Mev. The ratio of increases of these rates is plotted in the center section of Figure 11. An anisotropic beam should produce a ratio smaller than 1 unless the beam is confined very nearly within a plane whose normal is the spin axis, in which case the ratio should be closer to 2.5. The results, then, indicate that the solar beam began in this plane but smeared out towards isotropy within one hour following the flare. This trend towards isotropy of all solar protons of energy greater than 100 Mev must hold for all the energy intervals contained unless the increase in the intensity of completely isotropic medium-energy protons masked a possibly prolonged anisotropy of only the very high-energy protons.

The equatorial plane of the satellite, defined by the spin axis pointing towards 47 ± 0.5 degrees right ascension and -27.5 ± 0.5 degrees declination on September 28 (Caulk and Davis, private communication), coincided with the plane which included the direction of the solar beam early in the event. This plane intersects the ecliptic plane in a line pointing about 45 degrees west (towards negative right ascension) or 135 degrees east of the sun. Assuming that the solar protons traveled close to the plane of the ecliptic, one of these two directions is that of the


Figure 11—Flare increase versus quiet-time counting rate ratios. The quiet-time isotropic values are normalized to 1. The uncertainty in the isotropic ratio is indicated by the lower bars at "1" on the ordinate scale

apparent, or projected, proton source. The first location, 45 degrees west, agrees with earlier determinations by McCracken (Reference 7) which were calculated from data obtained with ground-based monitors.

Anisotropy of Low Energy Solar Cosmic Rays

The low energy solar protons also arrived anisotropically but the anisotropy was different from that observed at the medium energies. Periodic samplings of the intensity of protons at energies from 2 to 15 Mev are made by the single *CsI* crystal and the 8-level analyzer. Data are stored while the detector, mounted with its aperture perpendicular to the spin axis, sweeps through an angle of 290 degrees. Since the interval between samples is not equal to the spin period, the mean direction of observation changes from one sampling to the next. A complete scan is then obtained in a number of successive readouts.

A sinusoidal modulation of particle intensity with a period equal to the predicted period showed that an anisotropy existed for many hours at low energies. For early September 29, the low counting rates make a statistical analysis necessary to reveal the anisotropy but when the intensity increases the modulation is very clear and regular. The modulation lasted at least until after the low energy solar protons reached maximum intensity between 0300 and 0500 UT on September 29, but had disappeared by 24 hours later on September 30. Although further analysis is required to determine the degree and direction of the anisotropy, analysis to date has shown that the measurements are inconsistent with the existence of a beam highly collimated along the "garden hose" interplanetary field lines.

Dynamics of the Solar Cosmic Rays

Following the onset of isotropy of the solar protons of energy greater than 100 Mev, successively lower-energy groups increased in intensity until about 0300 UT on September 29. Sample differential spectra taken throughout September 29 and 30 are shown in Figure 12. The decrease in the intensity
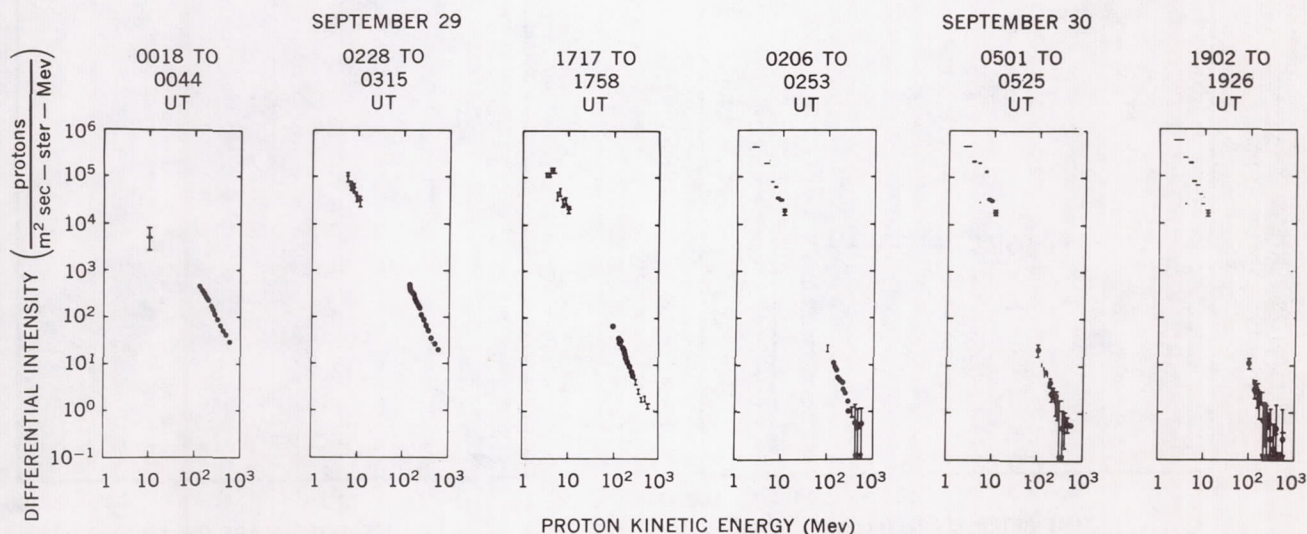

Figure 12—The intensity decay of the solar proton event. These differential energy spectra, taken over two days, show the gradual change in the medium and low energy proton intensities
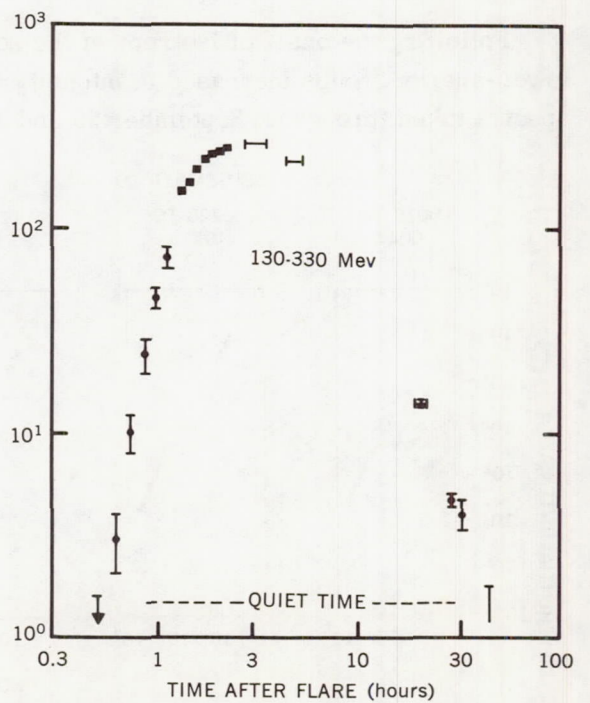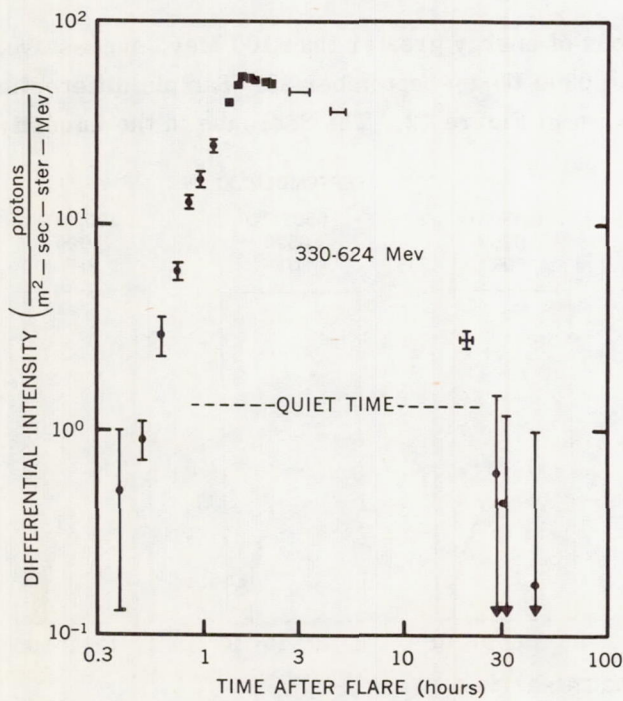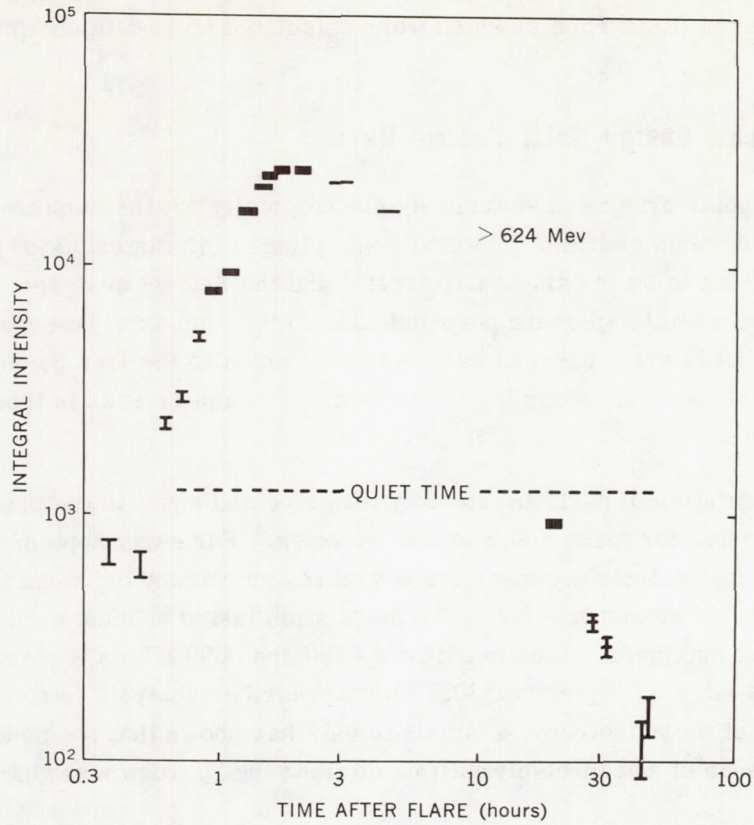
Figure 13—The intensities of representative energy components of the solar protons as a function of time. Onset times are later at lower energies

of the higher-energy components is evident; late on September 29 the slope of the proton energy spectrum from about 3 to 600 Mev was about -2, and later, on September 30, it was about -3. The maximum spectral intensity of solar cosmic rays in this event was between 1 and 1.5 decades below that of the November 12, 1960, event (References 8 and 9). Figure 13 shows the behaviour of the *integral* intensity of E > 600 Mev protons and the behavior of the *differential* intensities from two lower-energy groups. With decreasing energy, later onset times, steeper rises, and greater maximum intensities were observed. These features persist down to 3 Mev. The time taken for the intensity of each energy group to reach 90 percent of its maximum can be defined as the delay time of that spectral component. These delay times are shown in Figure 14 as functions of rigidity. The rectilinear travel time versus rigidity is indicated for comparison. The dashed line indicates the duration of the anisotropy of the medium energy particles. For a large energy interval, the delay time is proportional to $R^{-1/2}$. The delay time for the higher energy protons is 8 to 9 times as long as the rectilinear travel time; for the low energy protons, it is 3 to 4 times as long.
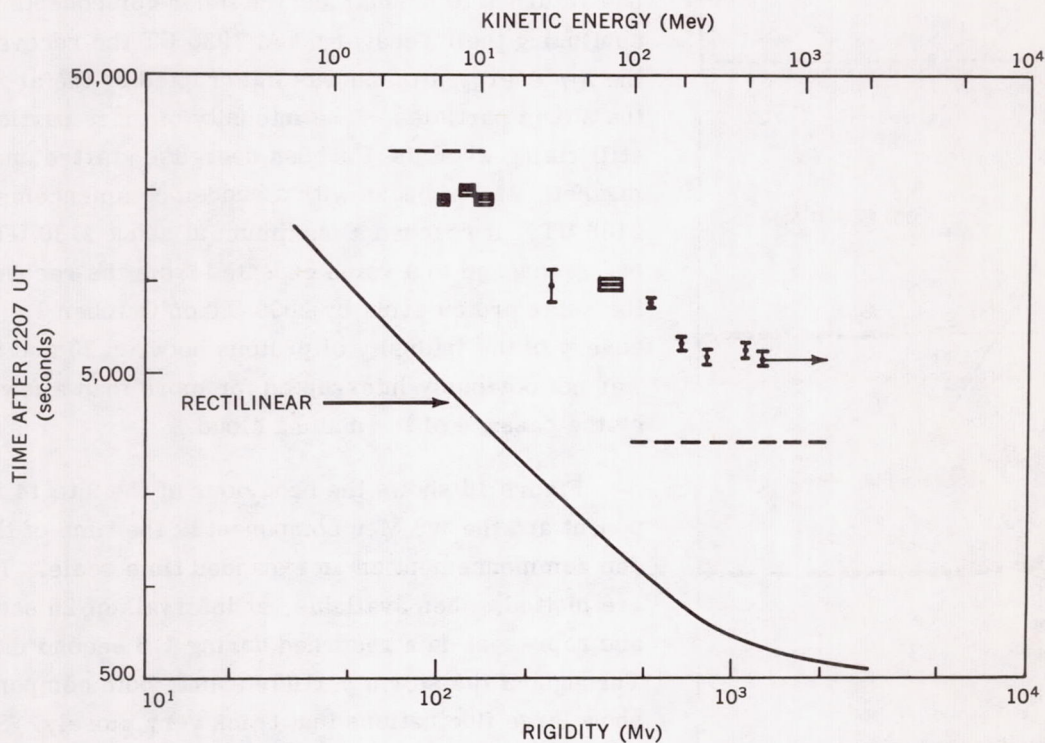
Figure 14—The time to 0.9 maximum intensity of the solar protons, versus rigidity. Rectilinear travel times are indicated for comparison. The dotted lines indicate the duration of the anisotropy of the greater than 100 Mev and of the 2 to 9 Mev components

THE ENERGETIC STORM PARTICLE EVENT OF SEPTEMBER 30, 1961

Associated with the geomagnetic storm and Forbush decrease that occurred on September 30, about 46 hours after the solar flare of September 28, was a great increase in the intensity of E > 15 Mev protons.
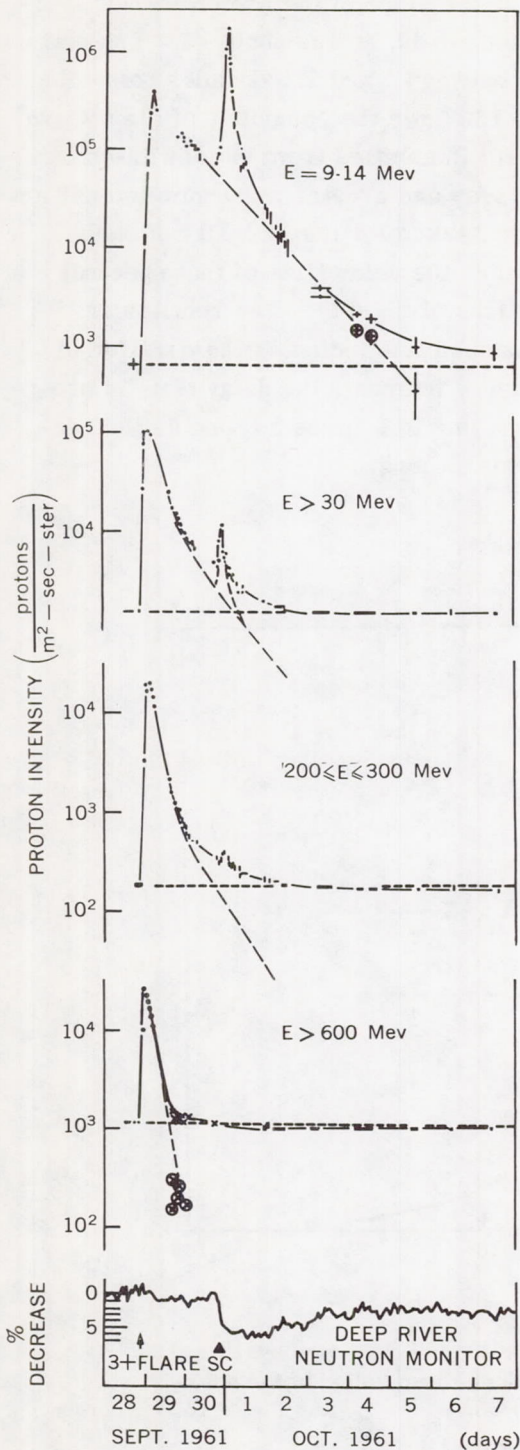
Figure 15—Representative proton intensities between September 28 and October 7, 1961, showing the decay of the solar proton event and the arrival of the energetic storm particles late on September 30. The Deep River neutron monitor record is shown for comparison

Figure 15 outlines the events taking place between September 28 and October 7, showing the intensities of representative components of the radiation. The Deep River neutron monitor rate is shown for comparison and the time of occurrence of the 3+ flare on September 28 and of the sudden commencement of the magnetic storm on September 30 are indicated. On September 29 and 30 the intensities of all components of the radiation observed at the satellite were recovering, after the solar proton event of September 28, towards the preflare levels shown in the figure. The departures from preflare levels are indicated by broken lines. At about 1900 UT on September 30, when the satellite emerged from the radiation zone, the intensity of the greater than 600 Mev component had returned to normal and the other components were continuing their recovery. At 1930 UT the recovery of the low energy protons was interrupted by the arrival of the storm particles. The intensity of these particles was still rising when the Forbush decrease started and the magnetic storm began with a sudden commencement at 2108 UT. It reached a maximum at about 2130 UT, and had recovered to a value expected from the recovery of the solar proton event by 2000 UT on October 1. The recovery of the intensity of protons between 30 and 600 Mev was not obviously interrupted for more than a few hours by the passage of the plasma cloud.

Figure 16 shows the behaviour of the 9 to 14 Mev component and the > 5 Mev component at the time of the sudden commencement on an expanded time scale. The points are plotted, when available, at intervals of 25 seconds and represent data recorded during 1.6 second intervals. Throughout the storm particle event, both components show large fluctuations that track very closely. Since these fluctuations are periodic and are closely connected with the spin of the satellite, they indicate a spatial anisotropy rather than a spatial or temporal variation.

Figure 17a shows energy spectra of the energetic storm particles at 2124 and 2131 UT on September 30. The event is essentially a low energy phenomenon and the intensities at lower energies are more than an order of magnitude greater than those reached in the solar proton event. Figure 17b shows that the low energy particles

162
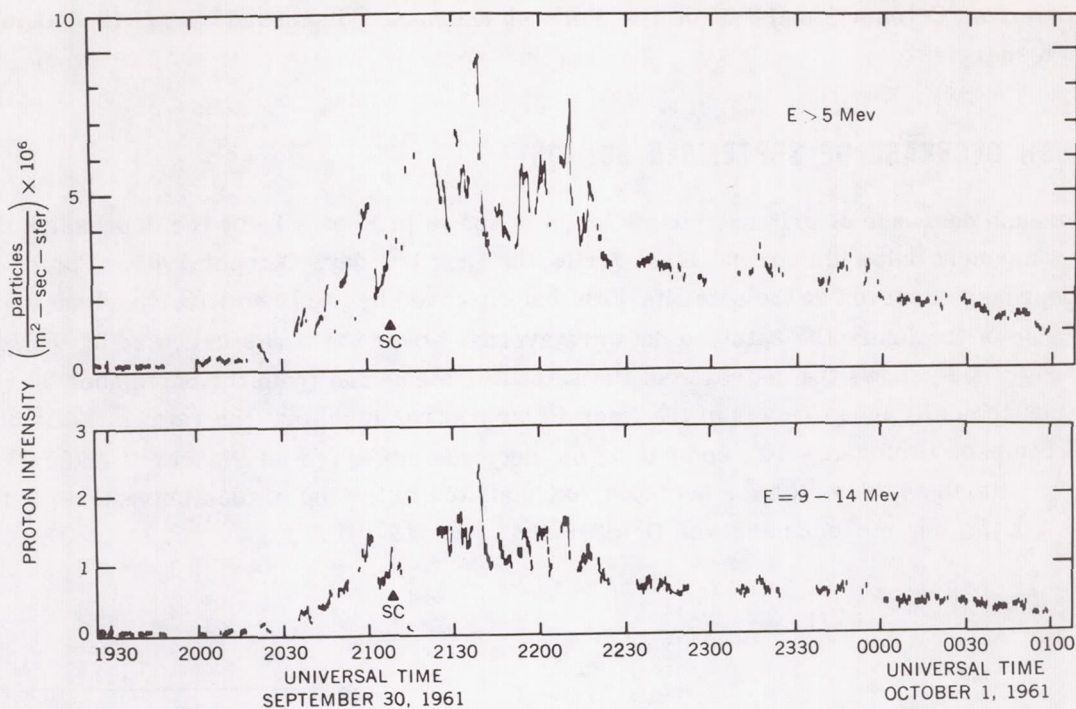
Figure 16—The energetic storm particles of September 30, 1961, showing that some of the particles arrived before the sudden commencement at 2108 UT. The intensity fluctuations are discussed in the text


a. September 30
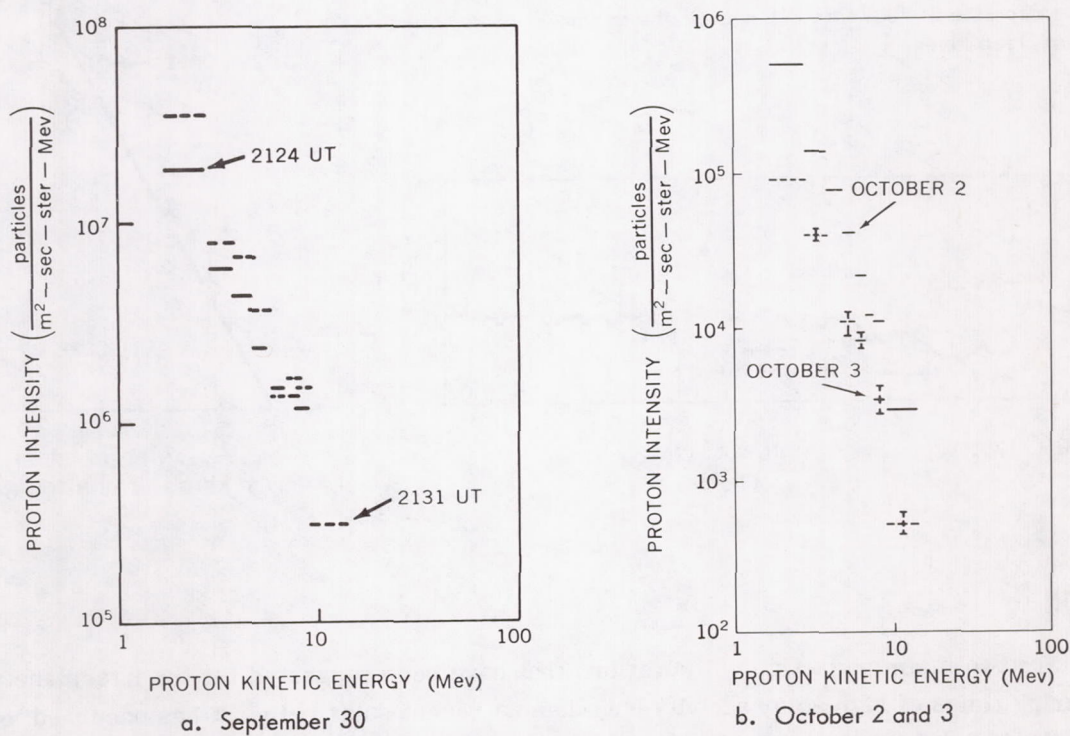
b. October 2 and 3

Figure 17—Differential energy spectra of the energetic storm particles at 2124 and 2131 UT on September 30, and those on October 2 and 3, 1961

163

are still present on October 2 and 3 while the Forbush decrease, discussed below, is still in evidence at high energies.

THE FORBUSH DECREASE OF SEPTEMBER 30, 1961

The Forbush decrease of primary cosmic rays is shown in Figure 15 by the depression of the > 600 Mev component below its normal level during the first few days October 1961. Figure 18 compares the decrease observed at the satellite with that observed by the Deep River neutron monitor. On the left side of the figure the satellite data are averaged over the times indicated by the horizontal bars. The right side shows the decrease at the satellite, measured from the September 27 value, plotted against the daily mean values of the Deep River neutron monitor: the ratio is 1.7 ± 0.3. Fan, Meyer, and Simpson (Reference 10), comparing the decrease observed on Pioneer V (1960 α) in April 1960 with the Climax neutron monitor decrease extrapolated to the top of the atmosphere, found a ratio of 1.3 ± 0.15: our measurements in October 1961 give 0.9 ± 0.2.

Figure 18—The Forbush Decrease of September 30, 1961. The left side shows the decrease measured by the Deep River neutron monitor and the behaviour of protons > 600 Mev observed on Explorer XII. The right side is a plot of the decrease at Explorer XII against the decrease observed at Deep River
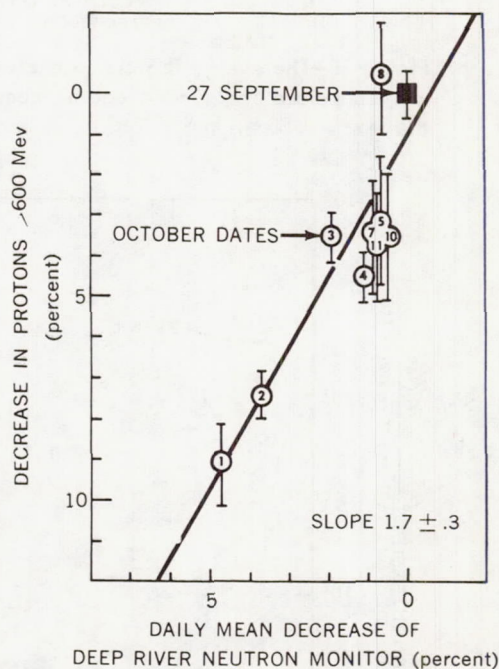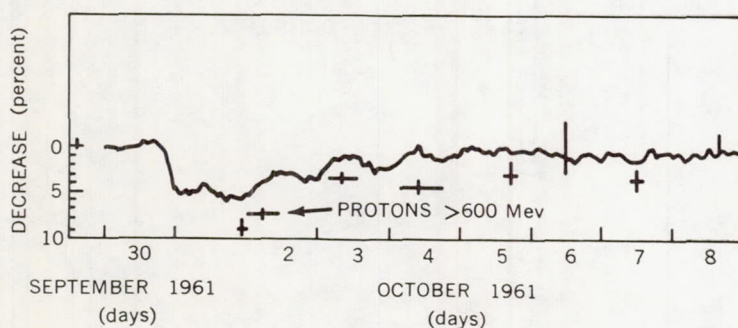
DISCUSSION

There are two main magnetic configurations that have been suggested for the interplanetary medium during times of high solar activity but when no recent solar outburst has occurred: one is an essentially radial field caused by continuous emission of the solar wind and curved due to the rotation of the sun; and the other is a dipole field which produces a field perpendicular to the ecliptic

at low solar latitudes (Reference 11). Both of these configurations contain magnetic irregularities which can act as scattering centers for solar protons.

Detailed calculations have been carried out for the diffusion of solar protons caused by scattering at the magnetic irregularities when the influence of the uniform magnetic field is negligible (Reference 11; and E. N. Parker, private communication). We shall confine our present discussion to this diffusion model because the quantitative calculations that have been carried out for diffusion under various boundary conditions permit the mechanism to be tested directly with Explorer XII data and the values of the parameters to be determined.

The application of classical diffusion theory yields the following expression for the time- and distance-dependence of the intensity (assumed isotropic) of particles diffusing from a point source into an infinitely extensive medium:

$$I(R,t) \ = \ \frac{NV}{32\pi \left(\frac{V\lambda\pi}{3} t\right)^{3/2}} \ \exp\left(-\frac{3}{4} \frac{R^2}{V\lambda t}\right) ,$$

where

I = Directional intensity,

N = Number of particles released at $t = 0$ and $R = 0$,

R = Distance from source,

t = Time after release,

V = Particle speed, and

λ = Mean free path.

It follows that

$$\ln\left[I(R_0,t) \ t^{3/2}\right] \ = \ \ln\left[\frac{NV}{32\pi\left(\frac{V\lambda\pi}{3}\right)^{3/2}}\right] - \frac{3}{4} \frac{R_0^2}{V\lambda} \frac{1}{t} ,$$

where R_0 is the astronomical unit. If the theory holds, a plot of $\ln\left[I(R_0,t) \ t^{3/2}\right]$ against $1/t$ is a straight line of slope $-3R_0^2/4V\lambda$, giving the value of λ on substitution for R_0 and V. Further, the intercept at $1/t = 0$ can then be used to determine N: this aspect will not be discussed here.

Figure 19 shows $\ln\left[I(R_0,t) \ t^{3/2}\right]$ plotted against $1/t$ for protons > 600 Mev and for protons between 200 and 300 Mev. Time is measured from the time of the x-ray burst at the sun on September 28 (K. A. Anderson, private communication). For the first 1.4 hours, when the intensity of both components was rising irregularly during the anisotropic phase of protons > 100 Mev mentioned earlier, the above solution of the diffusion equation is inapplicable. From 1.4 hours, when isotropy is established, to at least 7 hours the intensities of both components show very close agreement with diffusion theory. The times of maximum intensity of both components occurred during this phase.

TIME AFTER 2207 UT (hours)
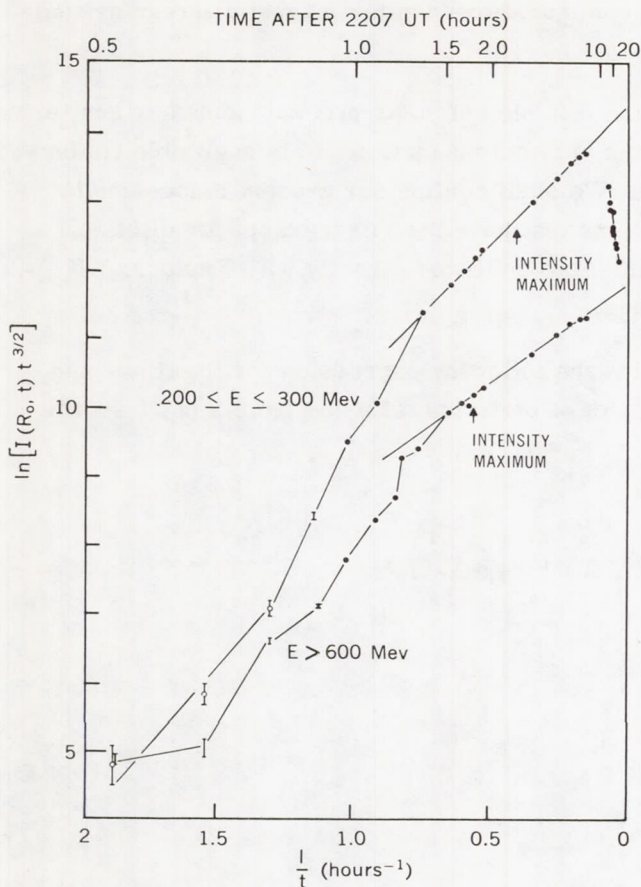
Figure 19—Plot of ln (Intensity x $t^{3/2}$) against 1/t for protons with energies between 200 and 300 Mev and energies above 600 Mev. From 1.4 hours after the x-ray burst when isotropy is established to at least 7 hours after the x-ray burst, both components show close agreement with diffusion theory

The slope of the straight line is -2.9 hours for protons > 600 Mev, and -4 hours for protons between 200 and 300 Mev. Taking V = 0.86 c as a typical velocity for the protons > 600 Mev, and V = 0.61 c for protons of 250 Mev,

$$\frac{\lambda}{R_0} = 0.042 \text{ at } 900 \text{ Mev}$$

and

$$\frac{\lambda}{R_0} = 0.043 \text{ at } 250 \text{ Mev}.$$

We see, then, that a simple diffusion model with a mean free path of 0.04 astronomical unit can explain the behavior of the solar protons near maximum intensity in this event. The fact that the mean free path is the same at values of rigidity that differ by a factor of 2 further supports the diffusion theory by indicating that large-angle scattering occurs at discrete scattering centers and that the diffusion is not strongly affected by continuous deflection in a regular magnetic field. It is clear, however, that simple diffusion in an infinite medium cannot account for the behavior late in the event, when the decay is closely exponential as is indicated in Figure 15. A modification of diffusion theory, by introducing a loss term produced by a finite boundary to the medium in which the particles are diffusing (E. N. Parker, private communication), shows that the intensity late in the event would decay exponentially. The introduction of general absorption, such as would be produced by the scattering into loss directions in the model proposed by Elliot (Reference 12), would also introduce an exponential multiplying term into the solution of the diffusion equation. Since no information could be obtained while the satellite was in the radiation zone between 7 hours and 20 hours after the start of the event, it may not be possible to distinguish between the case of general absorption, which would introduce an exponential multiplying term, and the case of loss from a finite boundary, which would show the gradual emergence of an exponential dependence. Parker (private communication) shows that, if the diffusion takes place only within a sphere of radius P, the time constant τ of the decay late in the event is given by

$$\tau = \frac{3P^2}{\pi^2 \lambda v} .$$

From Figure 15 we see that the time constants are about 4 hours for protons > 600 Mev, and about 16 hours for protons between 200 and 300 Mev. Substitution of the values of V and λ gives $P \approx 2$ AU for protons > 600 Mev and $P \approx 3$ AU for protons between 200 and 300. Mev.

In the September 28 event, then, the behavior of the solar protons can be accounted for, except during the first 1.4 hours, by diffusion within a sphere of radius 2 to 3 AU with a mean free path of 0.04 AU. This agreement with diffusion theory does not necessarily establish that the protons were diffusing within a finite medium, since no account has been taken of the influence of a general magnetic field or of the plasma cloud which was approaching the Earth on September 29 and 30.

Axford and Reid (Reference 13) have suggested a mechanism for the production of the particles responsible for the Polar Cap Absorption that occurred immediately before the magnetic storms of February 11, 1958, and September 30, 1961. They suggest that solar protons with energies of the order of 10 Mev were accelerated by repeated reflections from the magnetic field lines bent by the shock wave ahead of the advancing plasma. Since most of the energetic storm particles seen by Explorer XII arrived after the sudden commencement, and since the plasma cloud clearly contained solar protons (Figure 15), we suggest that the particles were solar protons that were trapped in the cloud during its passage through the interplanetary medium. Turbulent flow in the plasma cloud might cause regions of enhanced magnetic field to exist. Two such regions connected by a region of weaker field would form a trap for particles whose rigidities were less than a critical rigidity P_c determined by the strength of the field and its gradient. If particles with rigidity slightly greater than P_c entered such a region and were reflected by a region of strong magnetic field moving with the plasma and away from the particle, they would loose momentum and some would be trapped. Particles of higher rigidity would be scattered. Whether solar protons could be stored in such regions during the passage of the plasma cloud to the earth depends on the way in which the cloud expands and how the magnetic fields change with time. Detailed investigations of the intensity fluctuations and directional properties of the energetic storm particles should promote further understanding of their origin.

ACKNOWLEDGMENTS

REFERENCES

1. Desai, U. D., Van Allen, R. L., and Porreca, G., "Explorer XII Satellite Instrumentation for the Study of the Energy Spectrum of Cosmic Rays," in: *Proc. Nat. Telemetering Conf.,* Washington, May 1962, Vol. 1, Paper 7-5

2. Symon, K. R., "Fluctuations in Energy Lost by High Energy Charged Particles in Passing Through Matter," Ph.D. Thesis, Harvard University, 1948

3. Rossi, B. B., "High-Energy Particles," New York: Prentice-Hall, 1952

4. Vogt, R., "Primary Cosmic-Ray and Solar Protons," *Phys. Rev.* 125(1):366-377, January 1, 1962

5. Bryant, D. A., and McDonald, F. B., "dE/dx and E Experiment for Primary Cosmic-Ray Measurements," *Bull. Amer. Phys. Soc.* 7(4):311, April 23, 1962 (Abstract)

6. McDonald, F. B., and Webber, W. R., "A Study of the Rigidity and Charge Dependence of Primary Cosmic Ray Temporal Variations," in: *Proc. Internat. Conf. on Cosmic Rays and the Earth Storm, Kyoto, September 1961. II. Joint Sessions,* Tokyo: Physical Society of Japan, 1962, pp. 428-435

7. McCracken, K. G., "The Cosmic-Ray Flare Effect" *J. Geophys. Res.* 67(2):435-458, February, 1962

8. Biswas, S., Fichtel, C. E., and Guss, D. E., "A Study of the Hydrogen, Helium and Heavy Nuclei in the November 12, 1960 Solar Cosmic Ray Event," submitted to *Phys. Rev.,* April 1962

9. Ogilvie, K. W., Bryant, D. A., and Davis, L. R., "Rocket Observations of Solar Protons during the November 1960 Events, 1," *J. Geophys. Res.* 67(3):929-937, March 1962

10. Fan, C. Y., Meyer, P., and Simpson, J. A., "Rapid Reduction of Cosmic-Radiation Intensity Measured in Interplanetary Space," *Phys. Rev. Letters* 5(6):269-271, September 15, 1960

11. Meyer, P., Parker, E. N., and Simpson, J. A., "Solar Cosmic Rays of February, 1956 and Their Propagation through Interplanetary Space," *Phys. Rev.* 104(3):768-783, November 1, 1956

12. Elliot, H., "Cosmic-Ray Intensity Variations and the Interplanetary Magnetic Field," *Phil. Mag.* 5(54):601-619, June 1960

13. Axford, W. I., and Reid, G. C., "Polar-Cap Absorption and the Magnetic Storm of February 11, 1958," *J. Geophys. Res.* 67(4):1692-1696, April 1962

EXPLORER X MAGNETIC FIELD RESULTS

by

J. P. Heppner, N. F. Ness, T. L. Skillman, and C. S. Scearce
Goddard Space Flight Center

SUMMARY

Magnetic field measurements with the Explorer X satellite (1961 κ) over geocentric distances of 1.8 to 42.6 R_e during the period March 25-27, 1961, are presented. Analysis of the close-in data suggests the existence of a very weak ring current below 3 R_e along the trajectory, but alternative explanations for the field deviations are possible. Between 8 and 22 R_e, the existence of a large scale field directed away from the sun and earth within the geomagnetic cavity on the evening side of the earth is demonstrated. At distances greater than 22 R_e and prior to a sudden commencement of a magnetic storm late in the flight, the geomagnetic cavity boundary crossed the satellite trajectory on six principal occasions. Interpretations bearing on the form and boundary conditions of the cavity and solar-interplanetary fields external to the cavity are presented in the light of probable explanations and alternatives. Emphasis is placed on correlations with geomagnetic activity at the earth's surface.

INTRODUCTION

Explorer X (1961 κ), launched at 1517 UT, March 25, 1961, had the specific objective of obtaining vector magnetic field and plasma flux measurements along a trajectory traversing the geomagnetic field and extending into the interplanetary medium. Preliminary presentations of the magnetic field data (References 1 and 2) and the plasma data (Reference 3) were given at the International Confer-ence on Cosmic Rays and the Earth Storm in Kyoto, Japan, September, 1961. A variety of interpreta-tions have since been attempted with reference to various models of radiation belt currents, the geomagnetic cavity in the solar wind, the boundary properties of the cavity, and interplanetary field configurations. Direct interpretation in terms of existing models is not possible and their principal value is that of providing guidelines. In the case of model derivations of the surface geometry of the cavity, the data suggest that the model limitations stem in part from neglecting both the fields ex-ternal to the cavity and the variability of the solar wind and of the external field. The uniqueness of

interpretation is further limited by experimental factors such as the lack of continuous field and plasma data and of complete low energy particle spectra below 50 kev. Even more restrictive is the unavoidable fact that measurements are obtained locally along a single trajectory, whereas a satisfactory explanation of the cavity behavior necessarily involves unmeasured simultaneous behavior elsewhere. This paper summarizes major features of the magnetic field data and outlines the most plausible explanations for these features. Various alternatives are noted but are not treated in detail. Similarly, descriptions of instrumentation, calibrations, and data reduction techniques are omitted.

The magnetic field data presented at the Kyoto meeting are unchanged except for a few isolated points. The computed satellite trajectory has, however, changed considerably since the Kyoto presentation as the result of a more refined analysis of the tracking information. This demonstrated that primary use of Minitrack data led to standard deviations in position which have a relatively negligible effect on the field data. By use of the new trajectory, the large difference between computed and measured fields shown in the Kyoto paper between 1.8 and 4 earth radii (R_e) is greatly reduced. The other effect of the trajectory change is that all distances are increased at corresponding times.

SATELLITE AND PERFORMANCE

Explorer X was a 79-pound spin-stabilized satellite instrumented with: (1) a rubidium vapor magnetometer; (2) two redundant fluxgate saturable core magnetometers; (3) a plasma probe to measure the flux of low energy protons; and (4) an optical aspect system to determine the satellite's orientation relative to the earth, moon, and sun. Data were transmitted in the following sequence: Rb-magnetometer (126 sec), optical aspect (5 sec), temperature A (0.3 to 0.6 sec), fluxgate A (3 sec), temperature B (0.3 to 0.6 sec), fluxgate B (3 sec), temperature C (0.3 to 0.6 sec), and plasma probe (5 sec). The associated instrumentation included: (1) a bias field arrangement for converting the Rb-vapor magnetometer from a scalar to a vector instrument in weak fields; (2) a programmed sensitivity calibrator for the fluxgate magnetometers; (3) programming circuits for telemetry time sharing; (4) telemetry encoders for converting analog outputs to frequency; (5) a phase modulated 108-Mc transmitter; and (6) a 35-pound silver-zinc battery pack.

The active life of the satellite was estimated from battery limitations to be between 50 and 55 hours, which would provide measurements to approximately the expected apogee. In actual flight, 52 hours of calibrated data were collected and this was followed by a number of hours in which transmission continued but was unsatisfactory for data purposes. Performance was excellent except for one serious mishap: During the launching, there was excessive heating of the nose cone adjacent to the sphere containing the Rb-vapor magnetometer. The resultant outgassing caused deposition of a film on the sphere that increased the absorptivity of the surface. This raised the magnetometer temperature to 60°C after 2 hours in sunlight and caused the magnetometer to cease operating continuously. Intermittent operation continued for the next 6 hours, permitting inflight vector calibration of the fluxgates in weak fields.

ORBIT AND DATA COORDINATE SYSTEMS

The choice of orbit for Explorer X, relative to the earth-sun direction, was dictated by considerations of optimum geometry for plasma and optical measurements, thermal balance, radio noise background, and launch angle restrictions. The resulting orbit from launch to apogee is illustrated in Figure 1 in inertial coordinates chosen so that the X_i and Z_i axes coincide, respectively, with the vernal equinox and the north celestial pole. In geographical coordinates, the orbital plane was inclined 31 degrees and oriented so that the measurements at distances 22 to 42 R_e were located between the 2100 and 2200 local solar time meridians.

Figure 2 illustrates the orbit in solar-ecliptic coordinates chosen so that the X_{se} and Y_{se} axes lie in the plane of the ecliptic with the X_{se} axis pointing to the sun.

Figure 3 shows the payload coordinate system in which the data are initially reduced. The data from each fluxgate consist of the two field components (perpendicular and parallel to the spin axis) and the direction of the field in the $X_p Y_p$ plane (the angle ψ) relative to the sun. In the present paper,
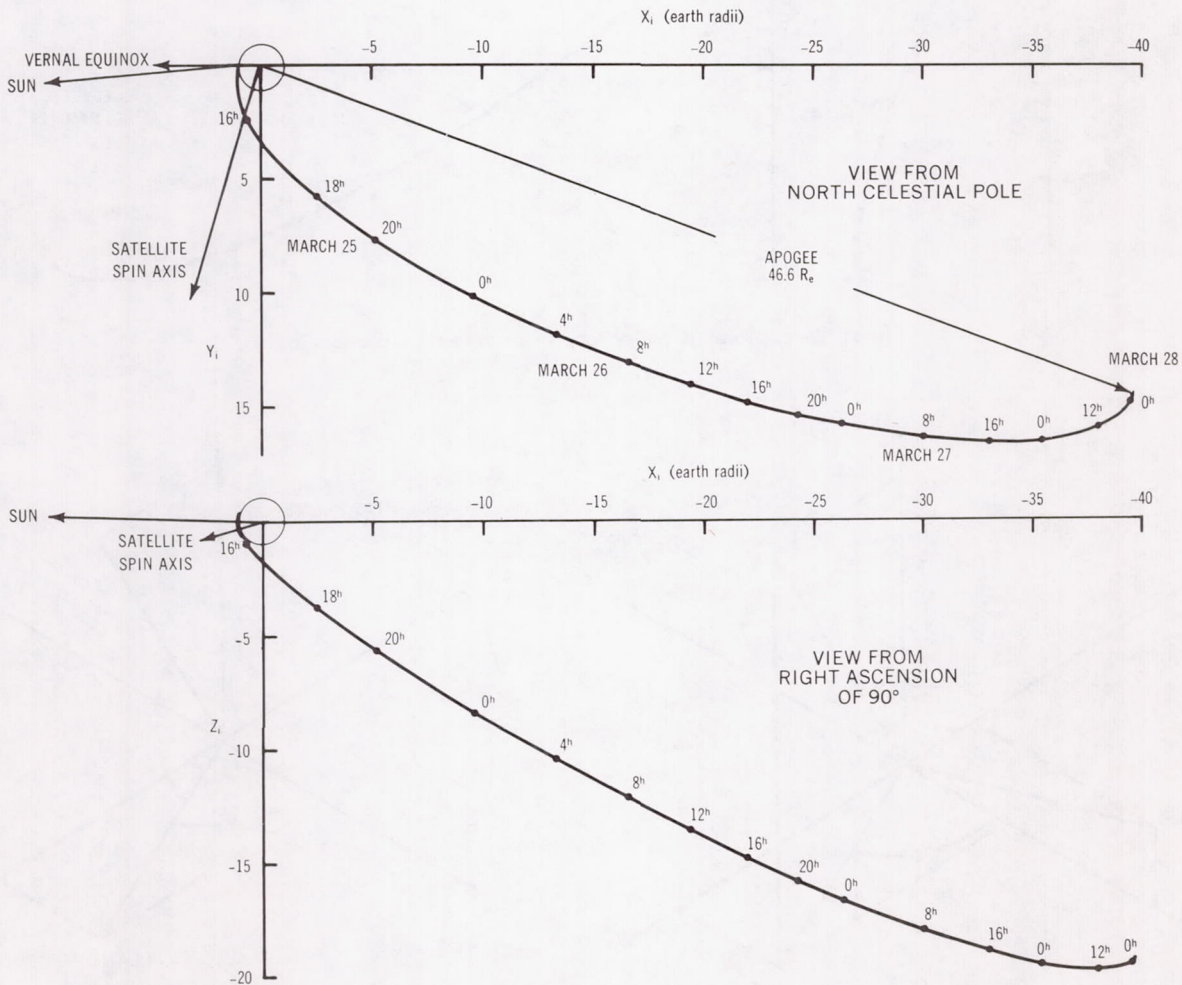

Figure 1—Explorer X trajectory and satellite orientation in inertial coordinates.
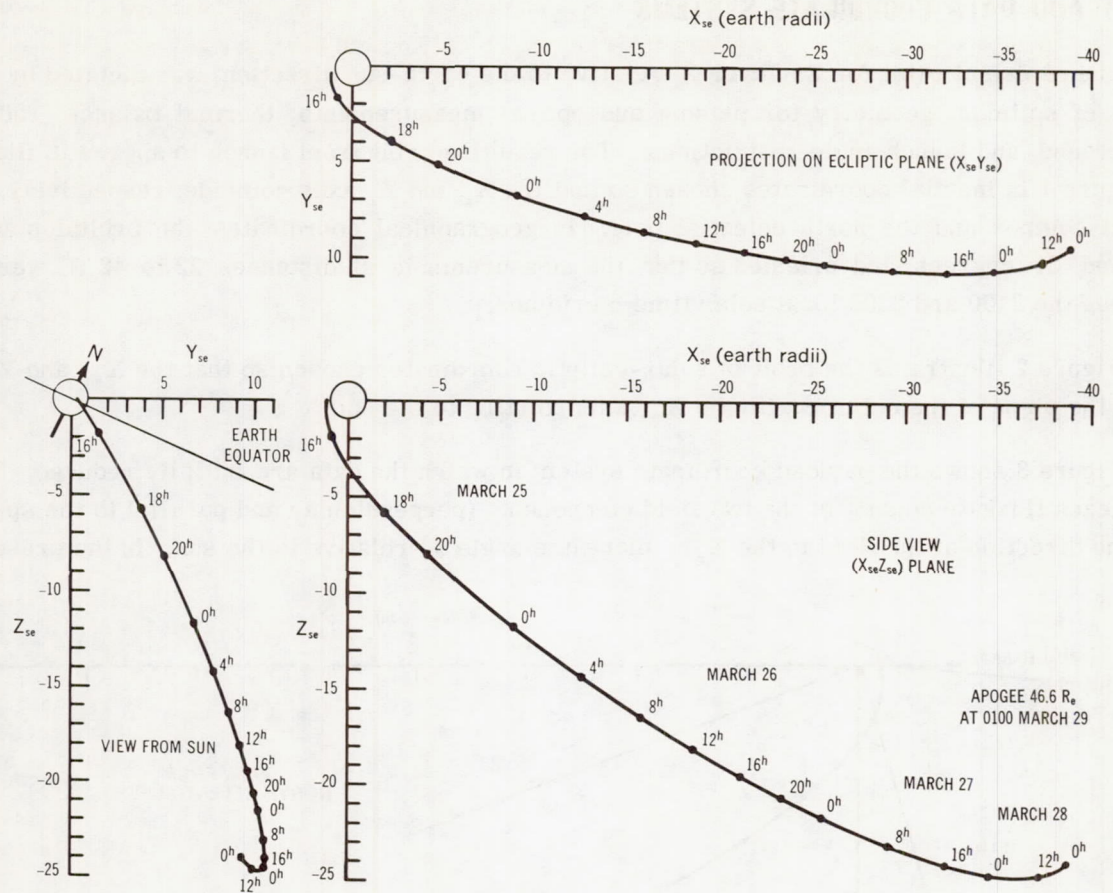
Figure 2—Explorer X trajectory in solar-ecliptic coordinates.
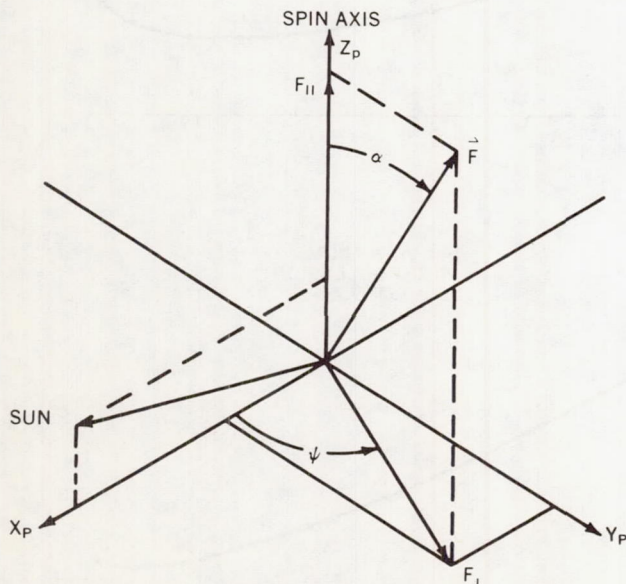
Figure 3—Payload coordinate system for F, α, and ψ measurement.
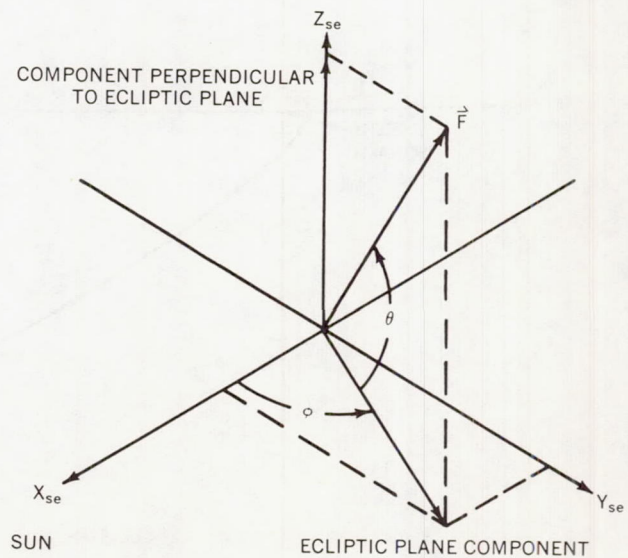
Figure 4—Solar-ecliptic coordinate system for F, θ, and φ measurement.

these coordinates are employed to 12 R_e so that the angle ψ can be presented at distances less than 7.3 R_e where the $F_\perp$ and F_{11} (the symbol F designates the total magnetic field vector) measurements are not separable and hence coordinate transformations are not possible. The spin axis Z_p is directed toward a right ascension of 71 degrees and declination of -15 degrees as is indicated in Figure 1.

Figure 4 illustrates the variables used for magnetic field data following transformation to solar-ecliptic coordinates. The symbols θ and ϕ designate, respectively, solar-ecliptic latitude and longitude. Field data at distances greater than 12 R_e are presented in these coordinates.

Figure 5 illustrates the path of the trajectory relative to a projection of geomagnetic field lines for the first nine hours of flight. Universal time is indicated at appropriate points along the trajectory.
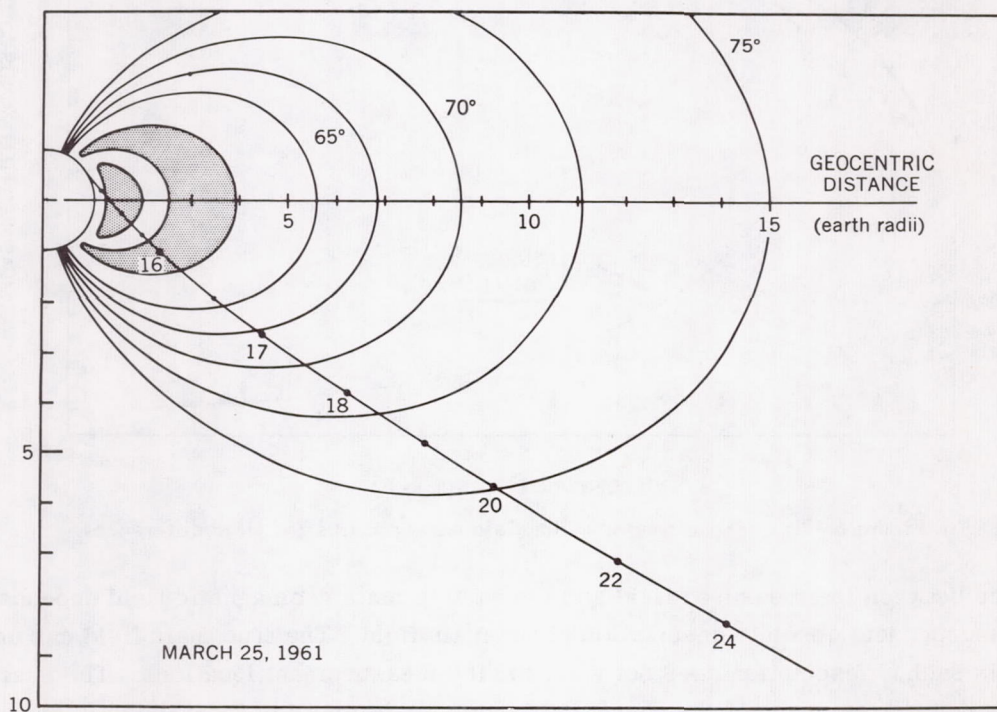

Figure 5—Explorer X path in geomagnetic projection.

MAGNETIC FIELD MEASUREMENTS

From 1.76 to 6.65 R_e

Measurements of the total scalar field intensity for the period of continuous operation of the rubidium magnetometer are shown in Figure 6. Points are plotted at one minute intervals except where the minute occurred during an encoder cycle. More detailed plotting on a scale of seconds yields a maximum fluctuation of several gammas.

To resolve spatial and/or time variation structure in the measurements, theoretical values of the field are computed by means of Finch and Leaton coefficients (Reference 4). These are subtracted from the measured values to give the "measured minus computed" curve of Figure 6. Finding the

173
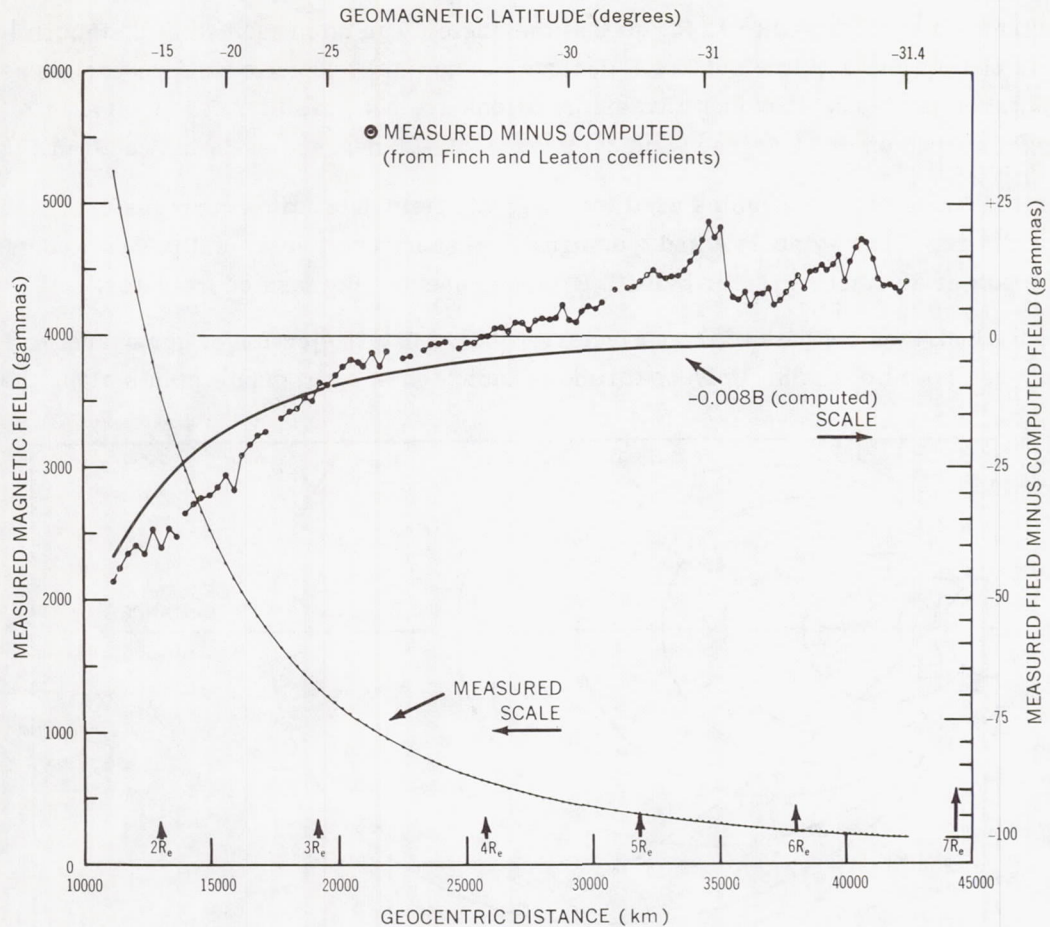
Figure 6—Rb - Magnetometer scalar field measurements and field differences.

true difference between the measured field and the earth's main geomagnetic field depends, however, on having an independent absolute description of the main field. The true main field can only be approximated, as such a description does not exist for the measurement locations. The nearest reference data in which the accuracy of the Finch and Leaton coefficients is independently known are the Vanguard III (1959 η) measurements (Reference 5) over South Africa at geocentric distances up to 10,000 km. Average errors in the Finch and Leaton values in this region are about -0.8 percent. The Explorer X measurements on Figure 6 are taken west of the Vanguard region, between Ascension Island and southwest South Africa. At the altitudes of interest, the percentage error in the computed field should not change greatly. Thus, for investigation of field differences, the computed values are multiplied by -0.8 percent and plotted on Figure 6. This represents an improved reference for the observed differences. A second order improvement in this reference curve might be obtained by taking into account the probable change in error with latitude, indicated by Vanguard III, and varying the correction from -0.5 to -0.8 percent with increasing south latitude.

As was noted previously, residuals in the most recent orbit analysis would alter the computed field an insignificant amount. However, this must be treated with some reservation as there is not

174

an absolute assurance on the accuracy of the orbital error estimate. Errors in orbit determination differentially shift the difference curves but do not alter its general shape or effect transition points (e.g., see Reference 1). Thus, changes in slope of the curve, sudden changes in the difference values, and maximum and minimum percentage difference points are not appreciably effected.

From 7 to 12 R_e

As the field intensity decreased to 100 gammas near 7.5 R_e, the fluxgate magnetometers were still saturated; but intensity measurements were obtained by matching sine curves to the slopes of the readings occurring during the alternating saturation caused by the satellite spin. The accuracy of this procedure increased as the field decreased in intensity to the unsaturated value of 30 gammas, and was verified by the intermittent readings of the Rb-magnetometer. In much stronger fields, it was possible to measure ψ, the direction of the field in the $X_p Y_p$ plane of the satellite, from the time differences between the sun pulse of the aspect system and the zero crossings of the fluxgates twice per satellite spin. The accuracy of the ψ angle readings is relatively independent of field intensity. In general, the errors are estimated to be ± 3 degrees but isolated points corresponding to poor signal-to-noise conditions may be in error by 5 to 10 degrees.

The fluxgate measurements from 7.3 to 12 R_e and the extension of the ψ angle values back to 4.2 R_e are shown in Figure 7. The total field values between 6 and 6.7 R_e are included for scale continuity.
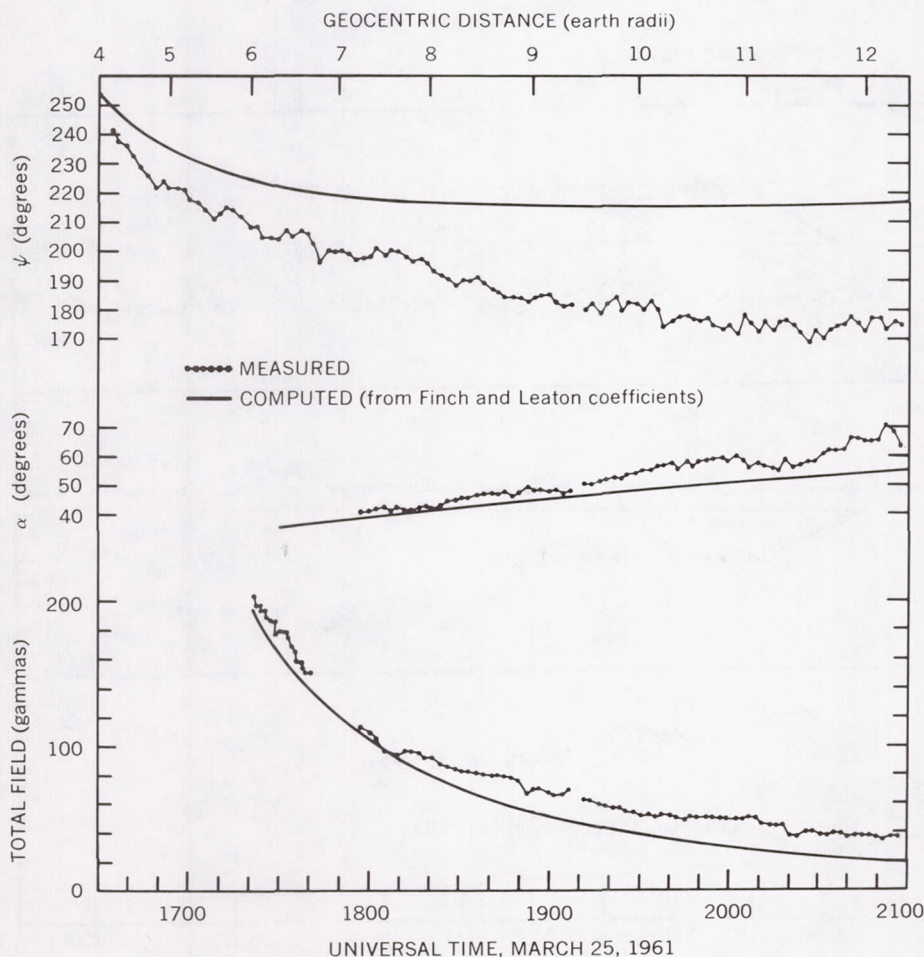
Figure 7—Field measurements in payload coordinates.

From 12 to 42 R$_e$

Measurements from the fluxgate magnetometers at distances greater than 12 R$_e$ are shown in Figures 8 through 13. Measurements between 2030 and 2100 UT near 12 R$_e$ are shown in both Figures 7 and 8 to illustrate the change in field coordinates from F, α, and ψ (Figure 3) to F, θ, and ϕ (Figure 4). At this distance, 12 R$_e$, the field direction reaches the nearly constant value that persists until solar plasma is first detected (References 3 and 6) near 22 R$_e$, 0530 UT (Figure 9). The computed, Finch and Leaton field is continued to 21 R$_e$ in θ, ϕ coordinates to illustrate the departure from the geomagnetic field.

Plotted points are averages over the fluxgate telemetry intervals. In general, after 1330 UT, March 26, deviations within these intervals are less than several gammas. In contrast, between 0530 and 1330 UT, variations within the sample intervals having amplitudes of several gammas or more occur frequently and in selected cases variations about the average are as much as 50 percent. Rapid variations are not observed when the field magnitude is large and plasma is not detected (References 3 and 6), e.g., between 1030 and 1200 UT, Figure 9.
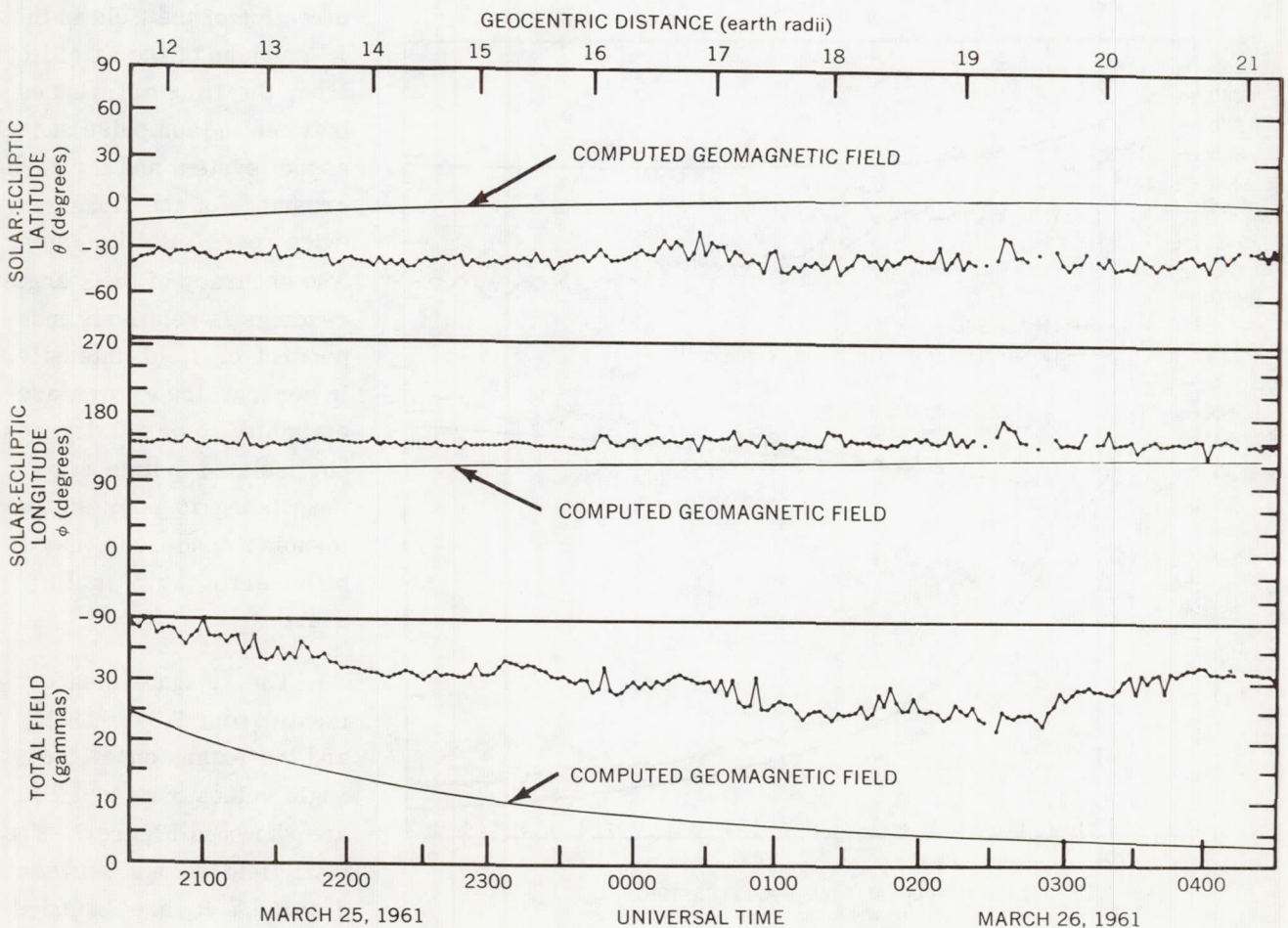


Figure 8—Field measurements in solar-ecliptic coordinates.
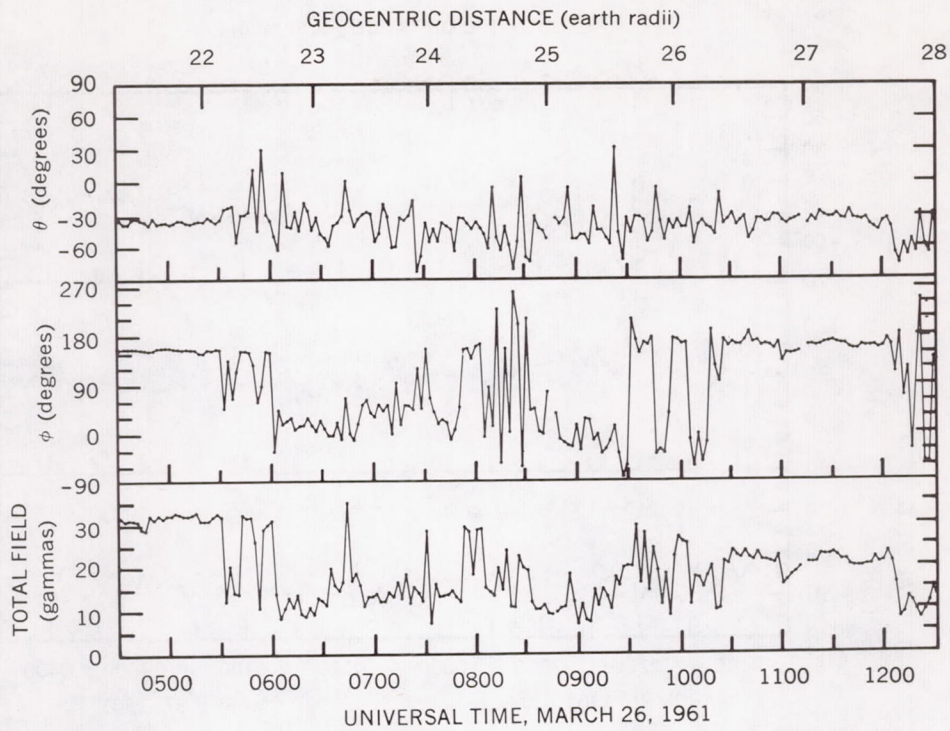
Figure 9—Field measurements in solar-ecliptic coordinates.
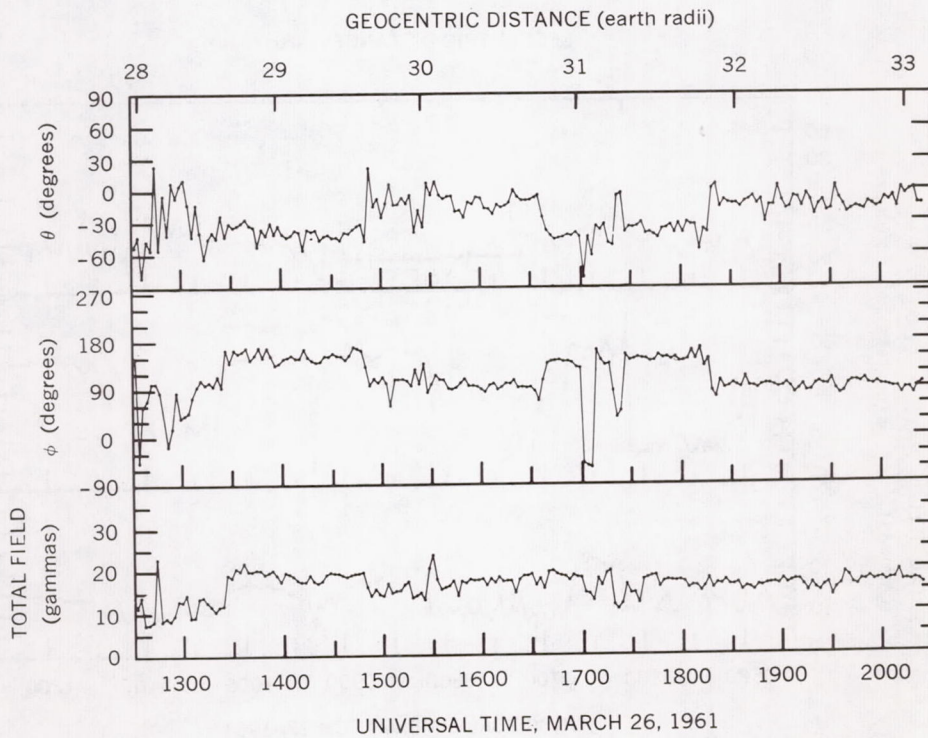
Figure 10—Field measurements in solar-ecliptic coordinates.

177

GEOCENTRIC DISTANCE (earth radii)
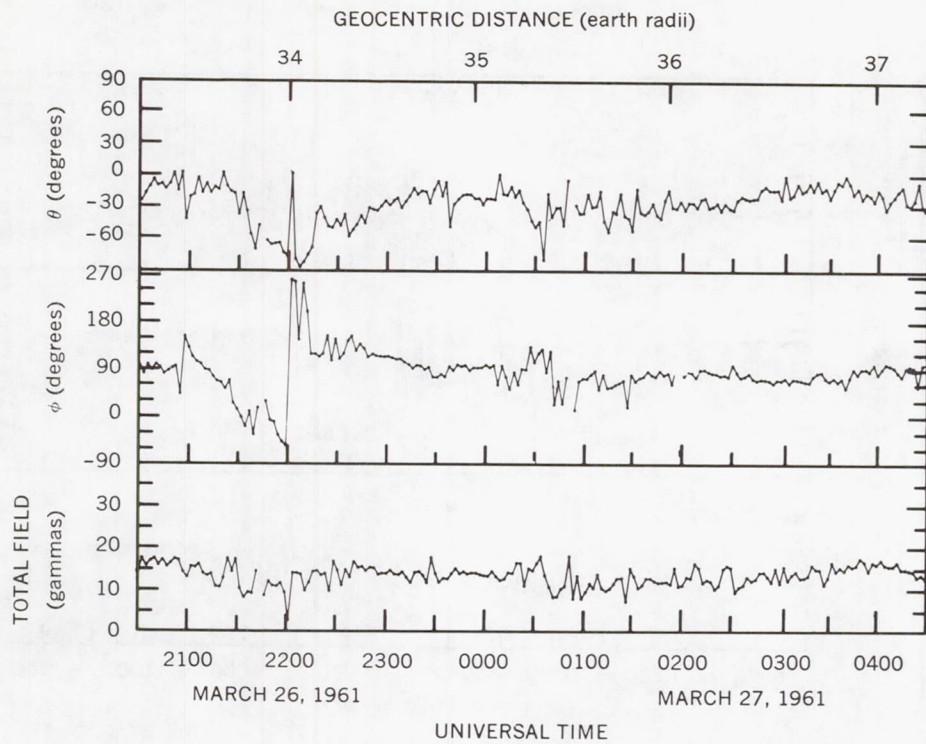
Figure 11—Field measurements in solar-ecliptic coordinates.

GEOCENTRIC DISTANCE (earth radii)
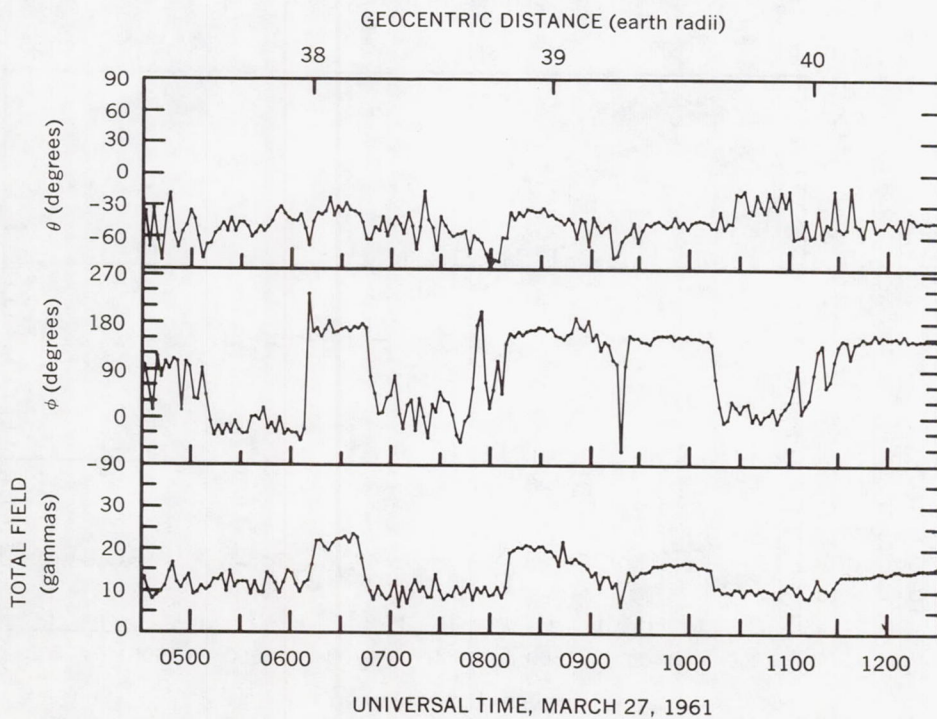
Figure 12—Field measurements in solar-ecliptic coordinates.
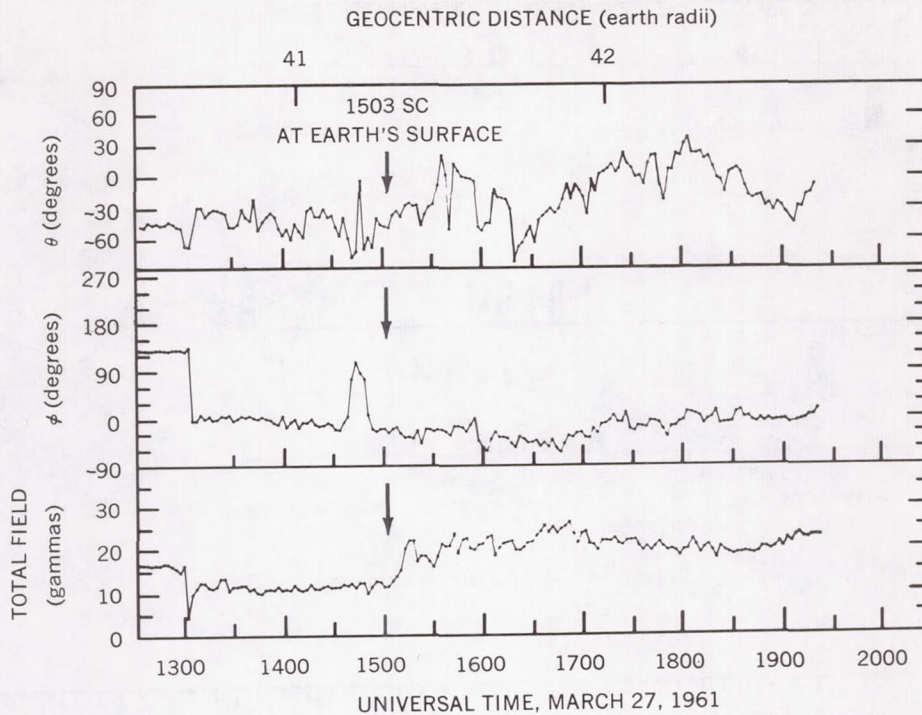
Figure 13—Field measurements in solar-ecliptic coordinates.

GENERAL SOLAR AND GEOMAGNETIC ACTIVITY

Solar observations for the period of interest were compiled by R. T. Hansen of the High Altitude Observatory, Boulder, Colorado. Figure 14, constructed from these tabulations, summarizes the activity observed optically for two days prior to the occurrence of a Class 3 flare, at 1009 UT, March 26, whose magnetic effects were registered near the end of Explorer X's active life. Prior to the large flare, the sun cannot properly be classified as either very quiet or disturbed, and the activity level can be considered as being average. Exception to this statement might be taken on grounds that the Zürich Provisional Sunspot Number of 76, on March 24, is larger than on any day between January 5 and the flight date. However, comparison with preceding months shows that this has little significance and 76 is only 25 percent greater than the average number for the first six months of 1961. A meaningful basis for summarizing solar radio noise data has not been deduced at this writing.

An attempt to summarize geomagnetic activity prior to the sudden commencement at 1503 UT, March 27, is illustrated in Figure 15. Records from 20 observatories providing fair coverage over the northern hemisphere were available for examination. In addition to the lack of south latitude stations, a possible gap in evaluation occurs in the auroral zone between Murmansk, USSR, and Alaska; however, observations at the Yakutsk Observatory, USSR, at a slightly lower latitude, serve as an indicator for this auroral region. The legend is relative within each of the three zones — polar cap, auroral, and low and middle latitudes. For example, the deviations classed as "small irregularities"
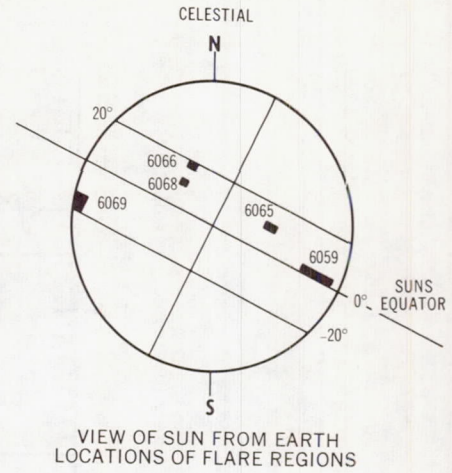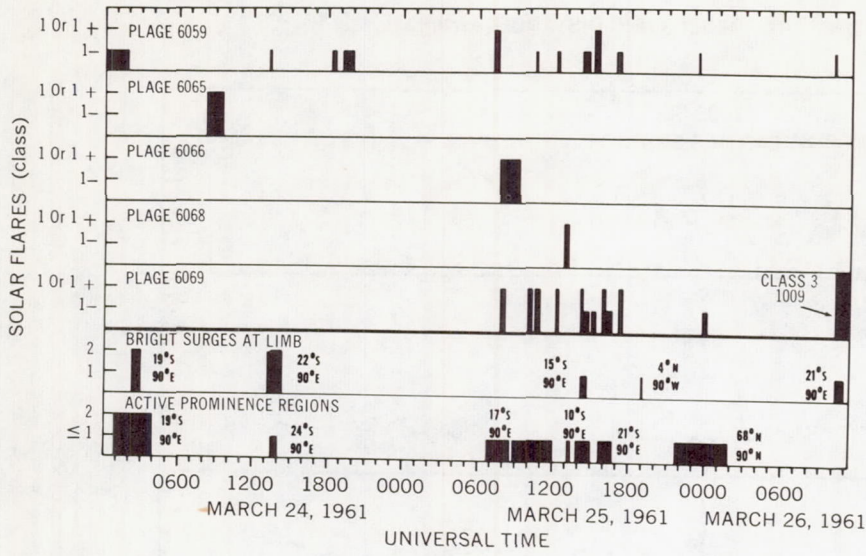
Figure 14—Solar activity prior to class 3 flare.
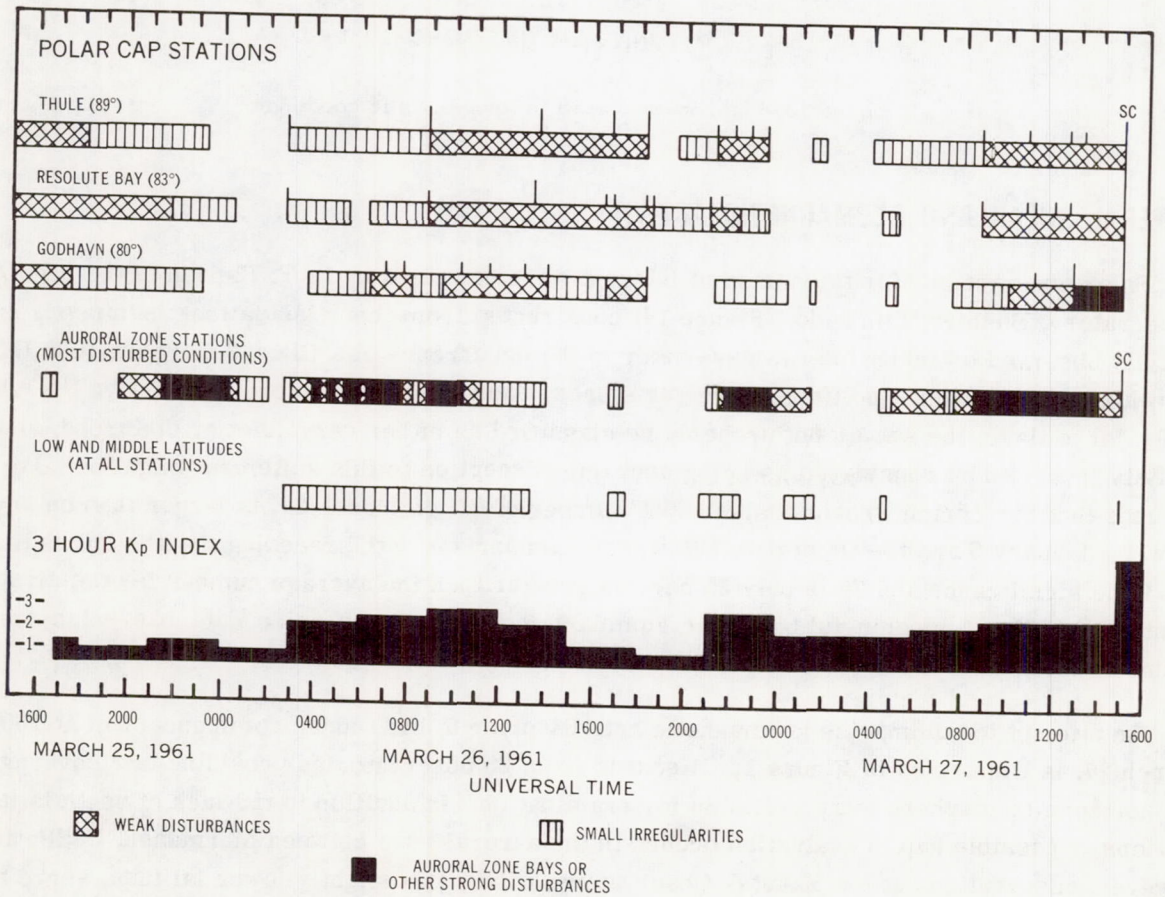
Figure 15—Summary of geomagnetic activity prior to sudden commencement.

at low latitudes are much smaller than at auroral or polar cap stations. Also, the classification of "small irregularities" at low and middle latitudes refers only to roughness or deviations on normal magnetograms that are seen by all observatories and does not include irregularities that are geographically isolated. Examples of this classification are apparent in later figures. The 3-hour K_p indices as well as the more zonal study demonstrate that conditions were neither very quiet nor disturbed on March 26 and 27 prior to the magnetic storm. The 25th, with a 24-hour K_p sum of 9, was fairly quiet. The days preceding the flight, March 21 to 24, were similar to March 26. Auroral zone magnetic activity prior to the storm was typical of average conditions. There are several intervals of 1 to 3 hours during the flight that can be classified as very quiet.

RADIATION BELT CURRENTS

Evidence for a Ring Current

By the use of preliminary trajectory analysis, it was previously concluded (Reference 1) that a field source located between the inner and outer radiation belts near the equator was necessary to explain the measurements. The more refined trajectory recently obtained has the effect of reducing the field differences from several hundred to 10 to 50 gammas, depending on the choice of reference baseline as discussed on pages 174 and 175 and illustrated in Figure 6. The difference curves, however, still show a maximum percentage difference near 2.5 R_e and a change in slope near 3 R_e. The existence of a quiet day diamagnetic ring current with maximum intensity located lower than the 3 R_e magnetic shell along the Explorer X trajectory (or roughly 3.8 R_e at the equator) is still possible. The magnitude of the effect is considerably less than reported for Soviet Space Probes I and II (References 7 and 8) which showed maximum effects of 800 and 140 gammas, respectively, several thousand kilometers closer to the earth than the location of the maximum intensity of the outer radiation belt. As the field shell is approximately the same as that of the Explorer X deviation, it remains to be seen if the magnitude difference can be explained on the basis that the Soviet space probes were launched during periods when the field was depressed following storm activity, as reported by Dolginov, et al. (Reference 8). Indirect evidence for a field source resembling a ring current in this region comes from the combination of Vanguard III and Explorer XII (1961 v) measurements. Under various degrees of disturbance Vanguard III (References 9 and 10) demonstrated that the source of main field depression at low latitudes must be at altitudes greater than that of maximum radiation intensity in the inner radiation belt; while, in turn, Explorer XII (Reference 11) has demonstrated that depressions in the field are not observed above the shell having an equatorial distance of approximately 4 R_e. This restricts the possible locations of a ring current maximum to roughly 1.5 to 4 R_e under disturbed conditions and to less than 4 R_e during quiet periods. Explorer XII (Reference 12) also revealed the existence of an intense proton flux in the outer belt, the peak intensity occurring near 3.5 R_e. The fact that the proton flux increased in the same region during a magnetic storm (Reference 13) suggests that the observed protons, which had energies E > 100 kev, may contribute significantly to ring current effects under both quiet and disturbed conditions. The possibility that an equal or greater contribution to ring current effects may come from lower energy protons in a greater number density cannot be ignored until energies below 100 kev are measured. At much lower energies, the Explorer X plasma measurements suggest that the energy spectra may be discontinuous with distance in this region. This indication comes from the disappearance above 3.0 R_e of a strong spin modulated signal that

persisted from 1.3 to 3.0 R_e (Reference 3). Rossi (Reference 14) and H. S. Bridge (personal communication) have interpreted this as velocity "scooping" of a stationary plasma which was terminated by positive charge accumulation on the satellite. An explanation has not been given for the double, rather than single, peak modulation which occurred on the last data sample, at 3.0 R_e, prior to the disappearance (Reference 14). The possible relationship between the disappearance of the plasma signal and the ring current, if not attributed to satellite charging, is only indirect in suggesting sharp changes in energy spectra with distance at low energies. The relationship to the field angle changes noted in the following section may be more direct.

At distances greater than 4.8 R_e, small total field deviations (Figure 6) are observed that do not have an apparent coincidence with time variations at the earth's surface. Instead, they may represent local variations in the field. The sign of the largest variations, about 15 gammas, is positive and thus does not suggest a ring current above 5 R_e such as do the strong, quiet day currents between 6 and 10 R_e derived from Explorer VI (1961 δ) observations (Reference 15).

Evidence for Meridional Currents

Between 1.5 and 3.2 R_e, the angle ψ was measurable by the technique described on page 175 for distances greater than 4.2 R_e. Between 3.2 and 4.2 R_e, however, the fluxgate saturation was in one direction and ψ could not be measured. Figure 16 shows the ψ angle measurements between 1.5 and 3.2 R_e along with a computed curve of the ψ angle expected on the basis of a Finch and Leaton field.
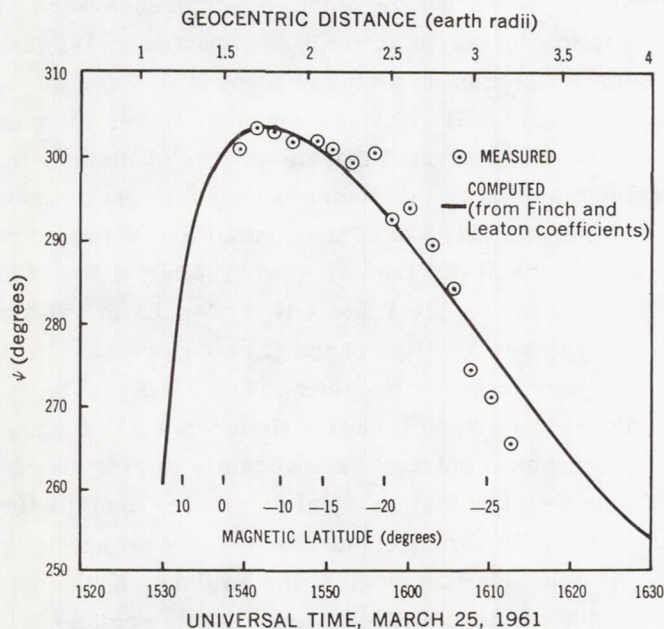

Figure 16—Angle ψ changes at low altitude (see text).

The interesting feature of these measurements is that angle deviations, thought to be greater than reading errors, occur near 2.5 R_e and 3 R_e in coincidence with other data features independently noted. For example: (1) the ψ angle point that falls on the curve (Figure 16, near 2.5 R_e) coincides in time with the small dip in the total field difference curve near 2.5 R_e in Figure 6; (2) the first point that falls below the computed curve at 2.99 R_e coincides with the occurrence of two peaks per satellite roll in the plasma observations prior to the disappearance of plasma signal (see above); and (3) the ψ angle shift near 3 R_e also coincides approximately with the change in slope of the total field difference curve in Figure 6. If it assumed that the ψ angle changes in strong fields are significant, an explanation

must be sought. In the 2.5 to 3 R_e region, a shift in the actual ψ angle relative to the computed ψ angle is equivalent to a change in declination; that is, a decrease in ψ corresponds to an increase in east declination of the magnetic field meridian plane. This follows from the consideration that a sizeable change in total field intensity does not accompany the angle change. Changing the ψ angle by 5 to 10 degrees is equivalent to adding an east-west vector of about 120 to 240 gammas at 3 R_e and 180 to 360 gammas at 2.5 R_e. The change must also be of local origin to explain the abruptness.

These changes, unless related to an unknown boundary condition, are not of the type expected from a ring current source and thus do not necessarily support the ring current arguments given earlier. Geometrically, the angle changes are most easily explained by postulating electric currents along field lines, a condition which violates the usual assumption that the field lines are also equipotential lines due to the extremely high electrical conductivity along the lines above the ionosphere. This condition may, however, be violated if: (1) the field lines intersect the ionosphere at points in opposite hemispheres which are not at the same potential; and (2) there is an ionospheric mechanism, equivalent to a generator in one or both hemispheres, that continuously maintains a small potential difference between the conjugate points. A difficulty in this explanation comes from the lack of observational evidence for the completion of the circuit in the ionosphere on a more localized scale than an ionospheric S_q system.

The above can only be treated as speculative; however, the ψ angle changes appear significant enough to merit future investigation.

Effects of the Geomagnetic Cavity at Several R_e

The total field deviations between 1.76 and 3 R_e were interpreted in a preceding section in terms of a current source within the same region. An alternative explanation for the deviations is suggested by the extension inward of a superimposed field presumably caused by the compression of the geomagnetic field by the solar wind. Thus, the magnetic field in the interior of the geomagnetic cavity can be considered as a superposition of the undisturbed geomagnetic field and the field due to sheath currents flowing on the cavity boundary. Fitting the observations by vector addition of an anomalous field to the geomagnetic field should thus reveal characteristics of the cavity field along the flight trajectory.

At distances above 7 R_e, where complete vector data are available, and below 22 R_e the superimposed field yielding an accurate fit to the observations is approximately constant with a magnitude 25 to 30 gammas and directed away from the sun and below the ecliptic plane. Indeed, for the interval between 4 and 12 R_e shown in Figure 17 a constant vector of 25.5 gammas directed so that $\phi = 182$ degrees and $\theta = -51$ degrees yields an excellent fit. At distances greater than 12 R_e (Figure 8) a fit to the data is obtained by gradually increasing the magnitude to 30 gammas and rotating the vector so that ϕ is decreased and θ is less negative.

The fit obtained with a nearly constant vector suggests continuing it back along the trajectory to investigate its effect on the close-in magnitude data. In Figure 18 this is illustrated for the range 1.76 to 6.7 R_e, where the vector used is the same as was used in Figure 17, and the measured field
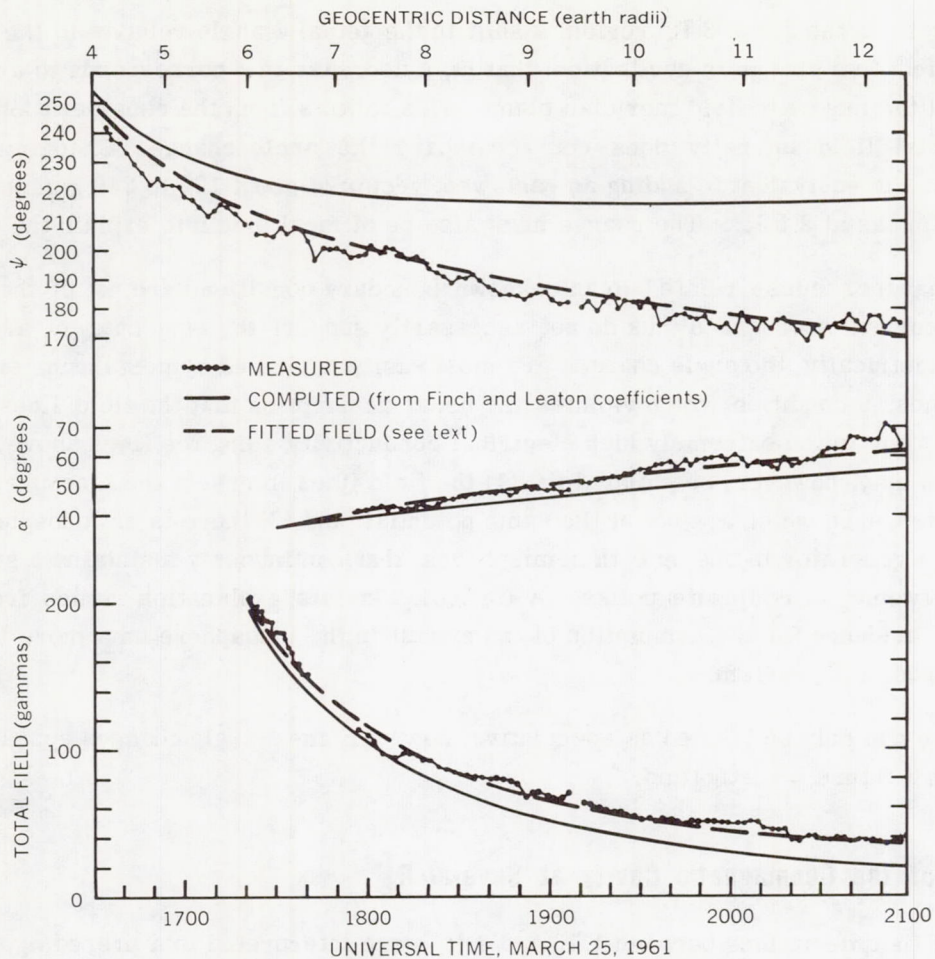
Figure 17—Field fit obtained by adding a constant vector (4–12 R_e)

is substracted from the resultant superposition field. The excellent fit above 3 R_e is apparent. Between 1.76 and 3 R_e, the fit becomes poorer but, nevertheless, shows the feature of a change from a positive to a negative anomaly. This suggests that it may be unnecessary to explain the deviations below 3 R_e in terms of a diamagnetic ring current. It suggests further that quiet day ring currents deduced from Explorer VI component data (Reference 15) should be re-examined with assumptions other than the preservation of magnetic meridian planes. Currently, this is difficult, as theoretical models of the cavity treat only the surface shape and do not predict the field interior to the cavity.

An uncertainty in the above arguments arises in that the same superposition vector when extrapolated to the surface of the earth would produce diurnal changes which are not entirely consistent with surface observations. This makes it apparent that the effects of a field due to cavity surface currents become more complicated near the earth. In turn, it raises a question as to how close to the earth the extrapolation discussed above is valid.
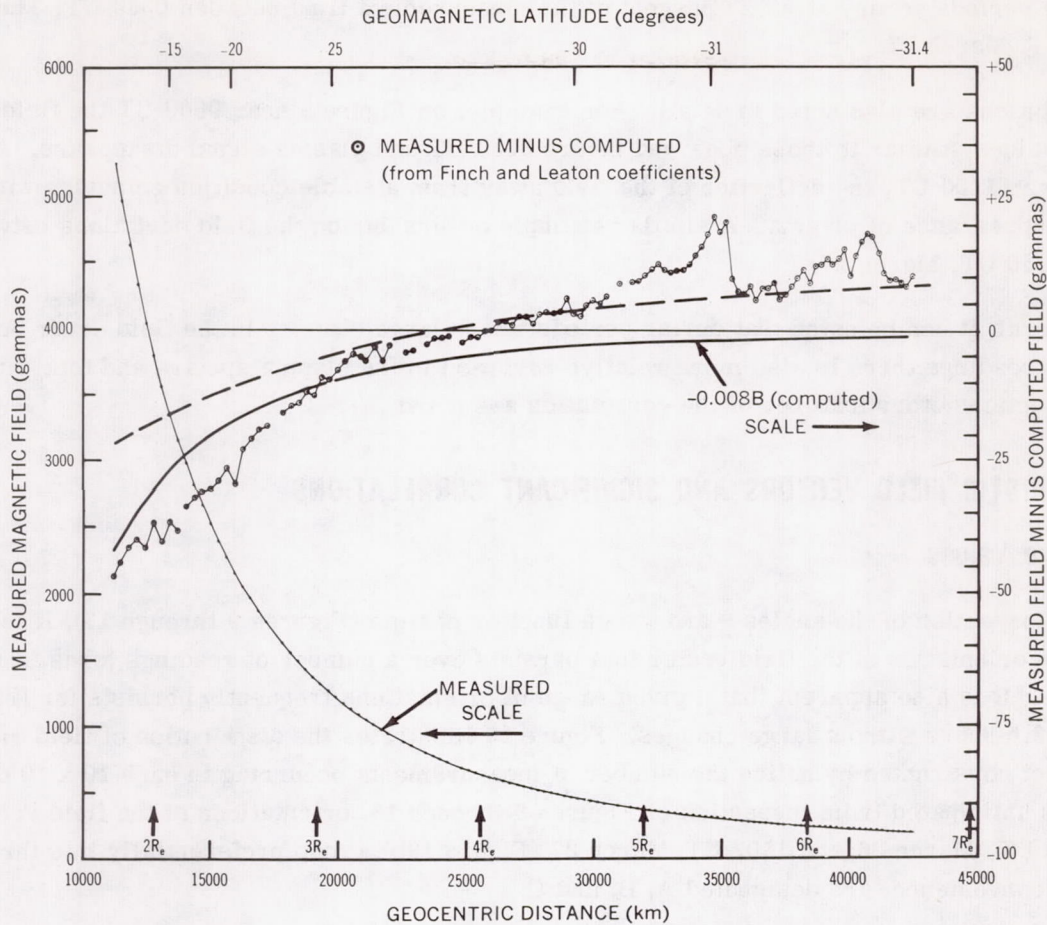
Figure 18—Field fit obtained by adding a constant vector (2-6 R_e).

MAGNETIC FIELD AND PLASMA CORRELATIONS

For a detailed account of the simultaneous plasma measurements conducted by the MIT group, the reader should consult the papers by Bridge, Dilworth, et al. (Reference 3) and Bonetti, Bridge, et al. (Reference 6). Principal features to note are the following:

1. Between approximately 3 and 22 R_e (or at 0530 UT, March 26), plasma was not observed, with the exception of a very weak signal near 0425 UT, March 26. The direction of the magnetic field at distances 12 and 22 R_e (Figures 8 and 9) correspondingly remained nearly constant.

2. At 0533 UT, March 26, the field angles and magnitude changed abruptly, and, on subsequent samples, plasma was observed whenever the 0 to 250, 0 to 800, and 0 to 2300 volt measurements were coincident with magnetic field angles substantially different than those observed between 12 and 22 R_e.

3. Between 0533 UT, March 26 (Figure 9), and the time of the sudden commencement at 1503 UT, March 27 (Figure 13), there were a number of periods in which plasma was not observed and the magnetic field direction returned approximately to the direction noted between 12 and 22 R_e. In

total, these periods occupy about 25 percent of the measurement time between 0533 UT, March 26 and 1503 UT, March 27.

Correlations are also noted in detail. For example, on Figure 9 near 0800 UT the field returns briefly to values similar to those observed before 0530 UT and plasma signal disappears. Also, on Figure 9 near 1100 UT, the deflection of the field away from a stable condition coincides with an isolated reappearance of plasma. A similar example occurs during the field deviations between 0900 and 0930 UT, March 27.

In general, it can be noted that during periods where large changes in the field occur between successive readings there is also more relative variation in the plasma spectra and total flux. In the following sections other features of the correlation are noted.

CHARACTERISTIC FIELD VECTORS AND SIGNIFICANT CORRELATIONS

Average Values

From inspection of the angles θ and ϕ as a function of time (Figures 9 through 13), it is apparent that a given orientation of the field vector that persists over a number of readings tends to reoccur at later times. It is also apparent that a given range of orientations frequently persists for fractions of an hour to 2.5 hours without large changes. Figure 19 illustrates the distribution of field orientations in a θ, ϕ plot constructed by noting the number of measurements occurring in each 10 x 10 degree sector. As anticipated from inspection of Figures 9 through 13, orientations of the field vector between 0530 UT, March 26, and 1502 UT, March 27 (Figure 19b), group preferentially into three regions which, for convenience, are designated A, B, and C.

Considering only those measurements that occur in a sequence of measurements in which the field orientation remains in one of the three regions A, B, and C, corresponding field intensities are obtained by averaging the values within each sequence. Figure 20 shows these averages. The length of the individual bars gives the time interval over which the intensities were averaged. From Figure 20, it is apparent that the level of field intensity is distinctly different in Regions B and C, and that field intensities in Region A appear to vary systematically with time.

Region A Characteristics

A large fraction of the measurements contributing to the density of Region A (Figure 19b) occurs during periods when solar plasma is not observed. The orientations of the field at these times closely resembles the orientation prior to the first appearance of solar plasma near 0530 UT, March 26, as illustrated in Figures 19a and 21. Thus, it is logical to postulate that the fields measured in the absence of plasma at distances greater than 22 R_e are extensions of the field observed between 12 and 22 R_e. If this field is in turn attributed to compression and draping of the geomagnetic field by the solar wind, it follows that the satellite was inside the geomagnetic cavity during the Region A periods (Figures 20 and 21). Acceptance of this argument depends, however, on also showing that the magnitude of the Region A field decreases with distance from the earth. As the next section shows, this condition can be satisfied on the basis of assumptions that can be at least subjectively supported.

186
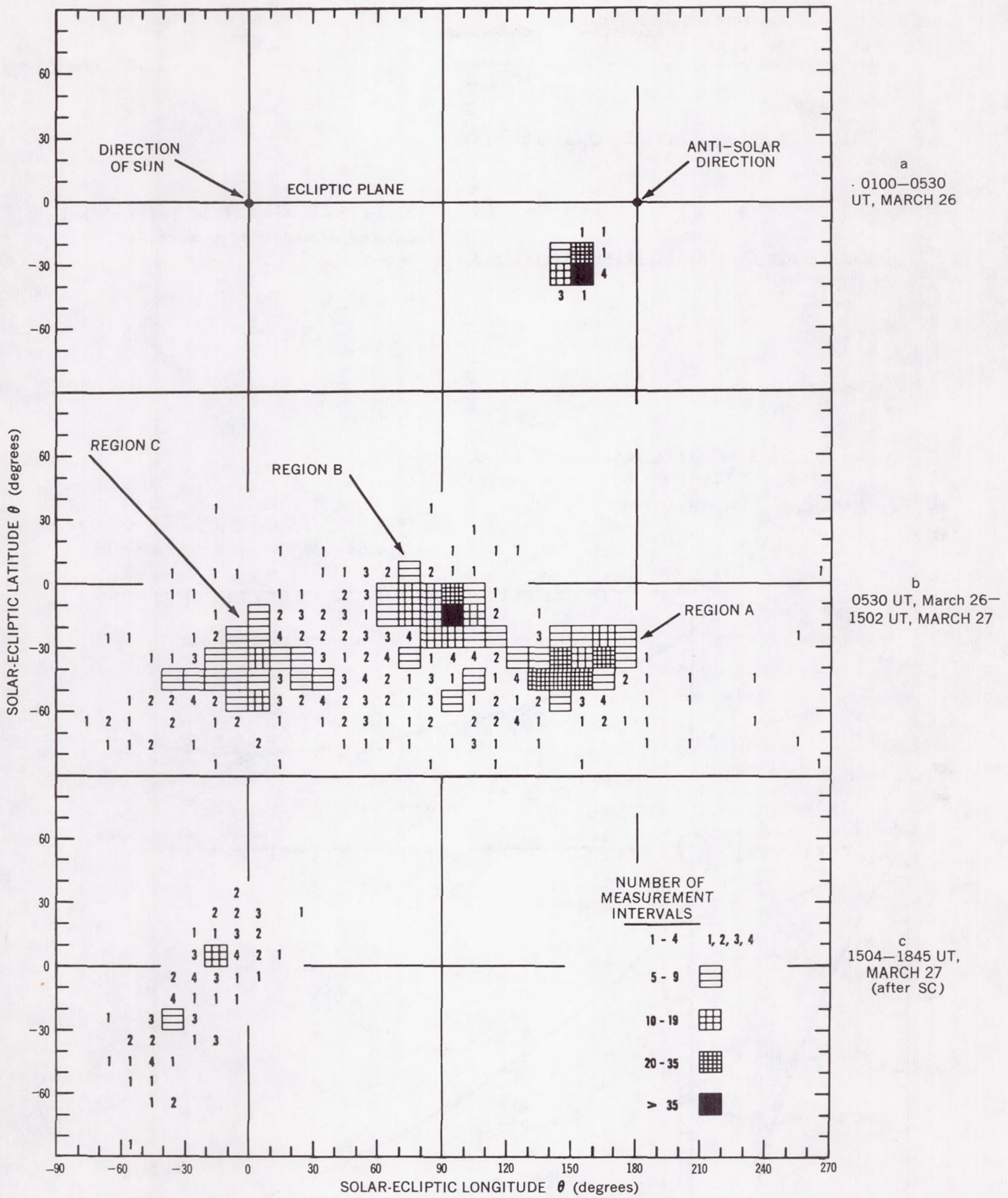
Figure 19—Statistical distribution of orientation of the field vector.

GEOCENTRIC DISTANCE (earth radii)

18 22   26 28 30 32   34   36   38   40 41

REGION C

REGION B

TOTAL FIELD (gammas)

REGION A

0   4   8   12   16   20 ` 0   4   8   12   16

MARCH 26   UNIVERSAL TIME   MARCH 27
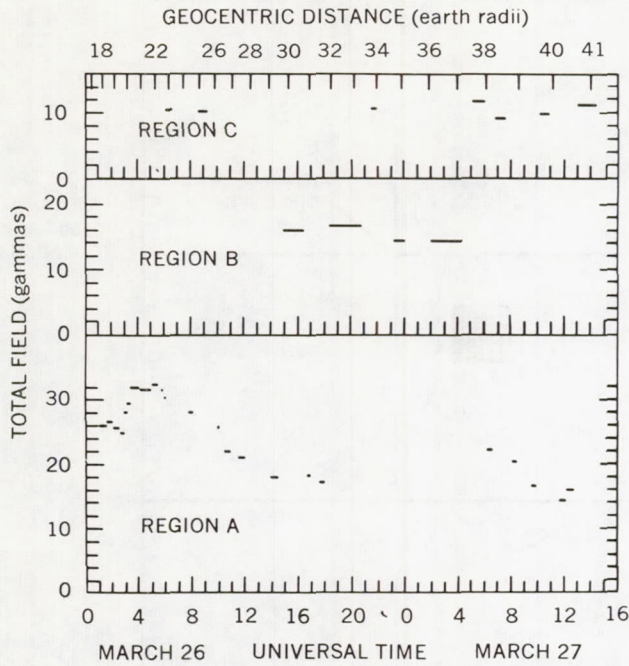
Figure 20—Average field intensities grouped according to characteristic field orientations.

X_{se} (earth radii)

-5   -10   -15   -20   -25   -30   -35   -40

16ʰ

18ʰ

Y_{se} 5   20ʰ   0ʰ   4ʰ 8ʰ 12ʰ 16ʰ   0ʰ   8ʰ   16ʰ 0ʰ 12ʰ 0ʰ

10   PROJECTION ON ECLIPTIC PLANE ($X_{se}Y_{se}$)

N

Y_{se} 5   10 X_{se} (earth radii)

-5   -10   -15   -20   -25   -30   -35   -40

EARTH EQUATOR   16ʰ   MARCH 25

16ʰ   18ʰ

-5   20ʰ

18ʰ   5

20ʰ   0ʰ

-10   10   SIDE VIEW ($X_{se}Z_{se}$) PLANE

0ʰ Z_{se} MARCH 26

-15   4ʰ   15   8ʰ

VIEW FROM SUN   20ʰ   MARCH 27   APOGEE 46.6 R_e AT 0100 MARCH 29

-20   20   0ʰ

MARCH 28

0ʰ   8ʰ   16ʰ 0ʰ 12ʰ 0ʰ

-25   12ʰ   -25
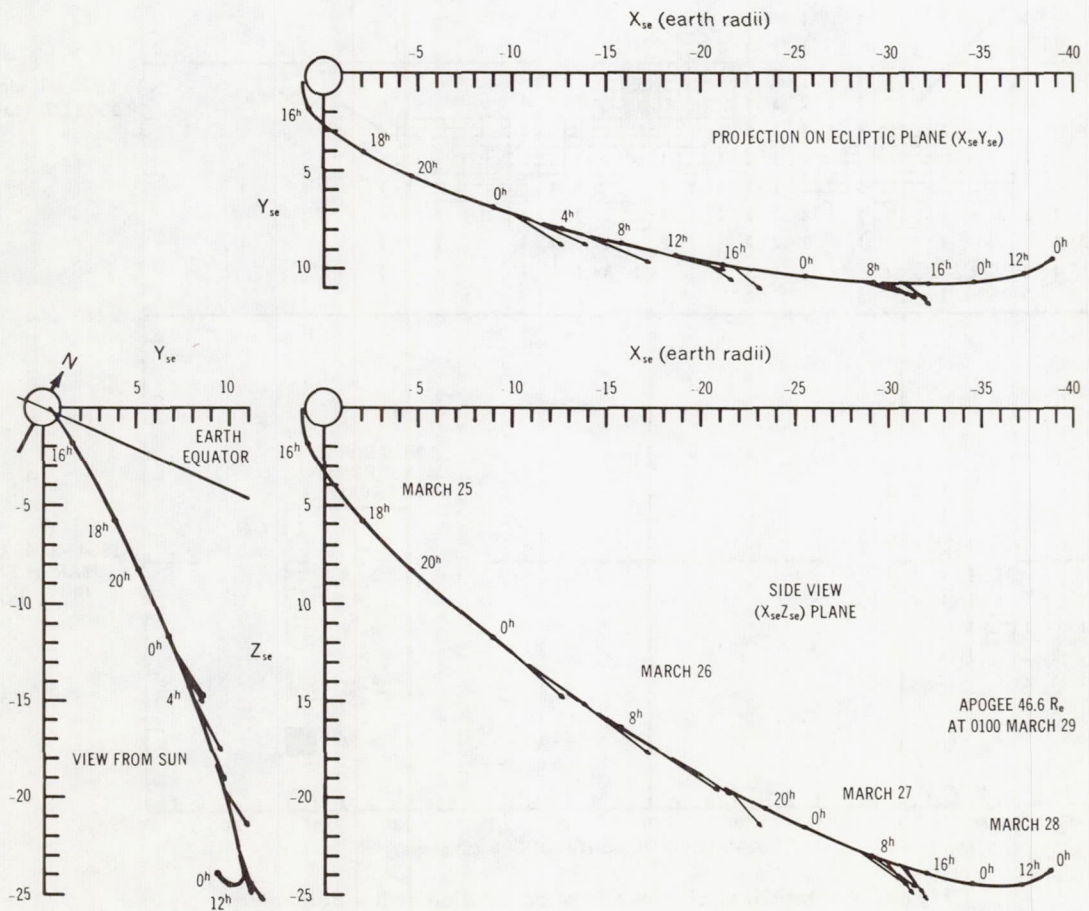
Figure 21—Average field vectors during Region A periods.

Region B Characteristics

The concentration of measurements in Region B of Figure 19b comes primarily from four periods occurring between 1500 UT, March 26, and 0430 UT, March 27 (Figures 20 and 22). A number of conditions appear to correlate with the Region B field direction:

1. Plasma is always observed.

2. The plasma flux and energy spectra appears to be less variable during these periods than at other times.

3. Magnetic activity on the surface of the earth during these periods was significantly lower than the average activity after 0300 UT, March 26. This is particularly obvious, from Figure 15, for the two periods of over two hours duration near 1900 UT, March 26, and 0400 UT, March 27.

4. Three of the four periods occur within the 12 hours, approximately 1800 UT, March 26, to 0600 UT, March 27, in which plasma is continually present and there is not a recurrence of an interval having Region A characteristics.
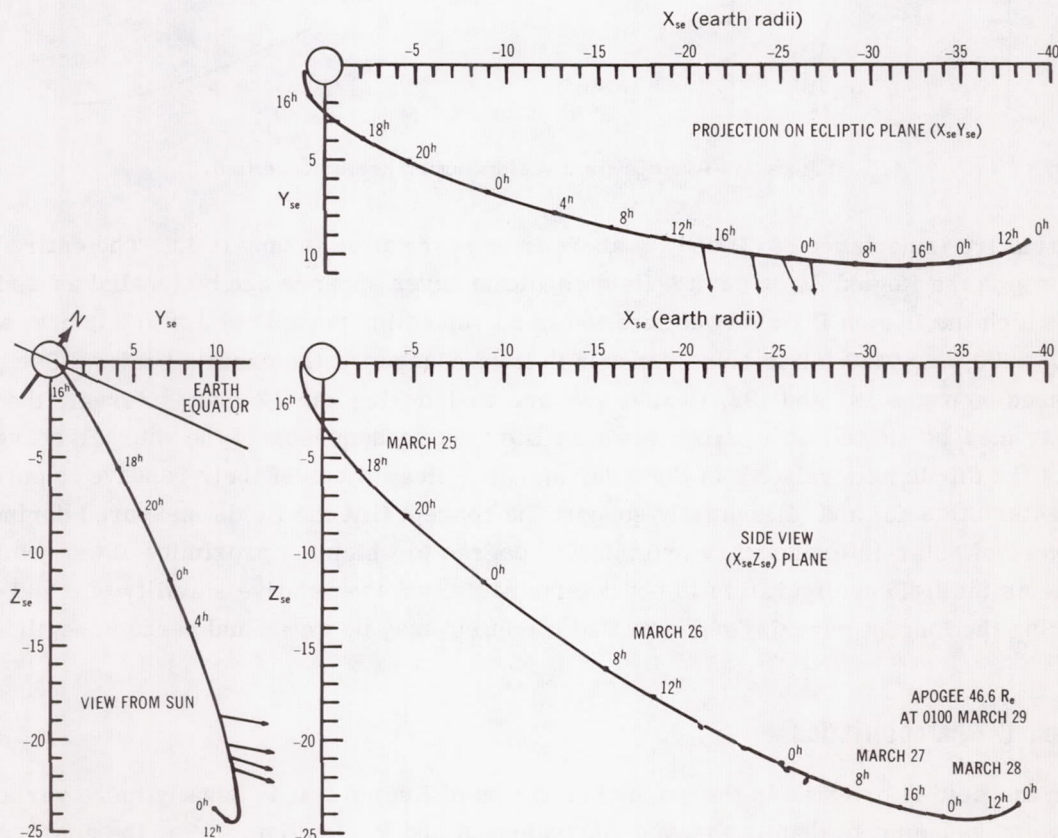

Figure 22—Average field vectors during Region B periods.
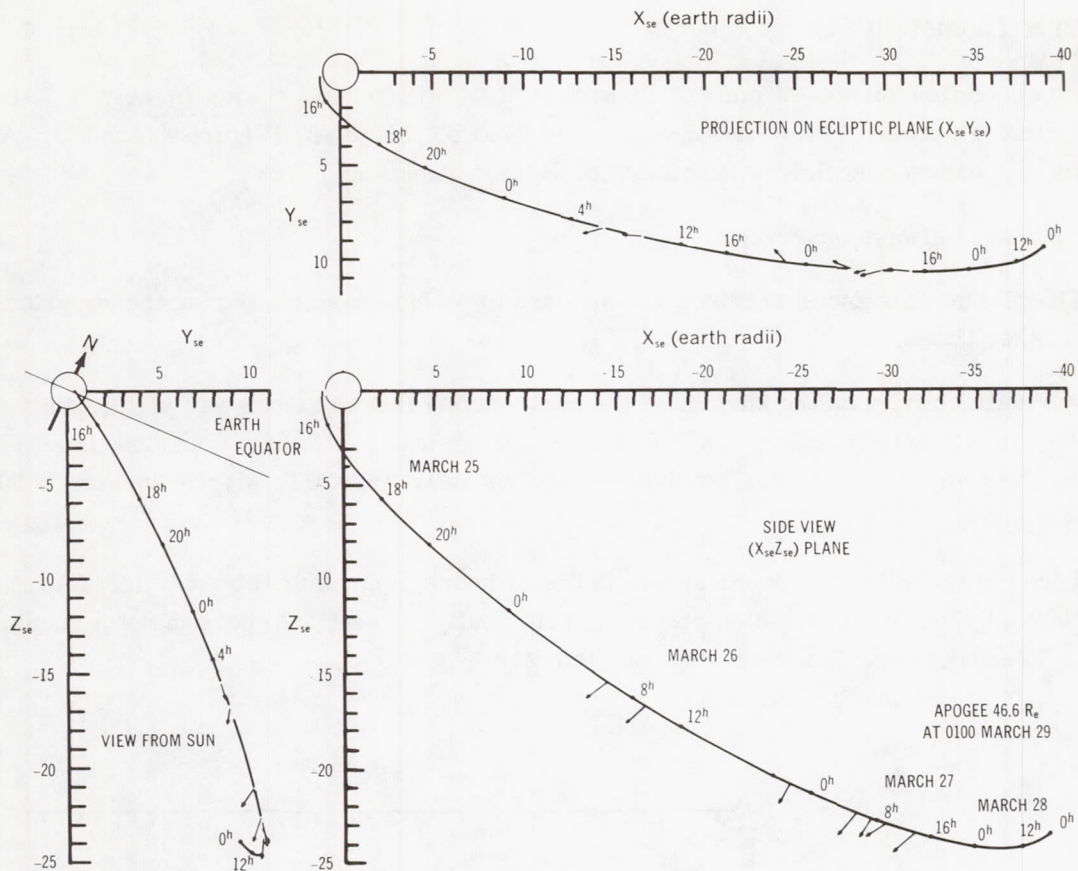
Figure 23—Average field vectors during Region C periods.

The relative importance of (3) and (4) above in interpretation is uncertain. The entire 12-hour period in which the Region A, or cavity, field condition never appears can be treated as a single interval in which the Region B field configuration is disrupted for periods of 1.5 to 2 hours, starting near 2100, 0000, and 0430 UT in coincidence with field changes at the earth's surface (See page 193). As discussed on pages 191 and 192, it also appears that during the 12-hour interval, the geomagnetic cavity may be shifted away from the satellite as a consequence of the diurnal change in the position of the dipole axis relative to the solar stream. Regardless of their relative importance the two characteristics (3) and (4) mutually support the concept that the fields measured during these periods were of solar-interplanetary origin. The degree to which the proximity of the geomagnetic cavity affects the field configuration is not determinable, but the relative stability of θ and φ, especially during the longest periods, suggests that the effect may be small and perhaps negligible.

Region C Characteristics

When the field is oriented in the general direction of Region C it is usually more variable between successive measurements than in the case of Regions A and B. In Figure 19b, the absence of a dense concentration of measurements in any 10 degree square and the general spread of angles makes this

apparent. Region C is nevertheless distinct and the fact that a statistical grouping exists comes largely from the recurrence of a number of periods in which the field has this general direction for 0.5 to 1.5 hours. The following conditions are characteristic for these periods:

1. The average field intensity is lower than during other periods (see Figure 20).

2. Plasma is always observed.

3. Magnetic activity on the earth's surface is greater than during periods of Region B field orientation.

4. The periods tend to alternate in occurrence with periods of Region A field orientation.

The exception to item 4, between 2100 and 2130 UT, March 26, gives added support to the significance of item 3, which will be discussed in more detail shortly. The field direction and the fact that field intensity during these periods is independent of distance from the earth (Figure 20) support the view that the field originates external to the geomagnetic cavity. It is possible, however, that the field configuration may be influenced considerably by the close proximity of the geomagnetic cavity.

FIELD INTENSITY VERSUS DISTANCE (REGION A)

As was noted in the last section, the argument that the fields measured when plasma is not observed are of geomagnetic origin, based primarily on the direction of the field, must also be supported by evidence that the field intensity decreases with distance from the earth. Considering first the range 11.5 to 22 R_e (Figures 7, 8, and 9) it is apparent that the field decreases much less rapidly than the computed field. It is also apparent that points can be chosen (e.g., at 16 and 21 R_e) so that $F(r) = F(r_1) (r_1/r)^\chi$ with $r > r_1$ gives a power $\chi = 0$ and a dependence is not found. Thus, the approach of looking for the maximum dependence (i.e., maximum χ) that can be partially justified is adopted. On this basis, the higher intensities following 0254 UT, March 26, are neglected on several possible grounds: (1) that these coincide with an increase in geomagnetic activity (Figure 15) having the character of greater compression of the earth's field (see page 193; (2) that the higher intensity may be a diurnal effect, explained later; and (3) that the higher intensity may be a cavity boundary effect. Using average values near 16.3 and 19.4 R_e relative to 11.7 R_e yields $\chi = 0.85$.

At distances above 22 R_e, it is again apparent that $\chi = 0$ and even a negative χ can be found from the 27 to 32 R_e periods relative to the 38 to 39 R_e periods (see Figure 20, Region A).

If, however, a more general view of the time sequence of occurrences of Region A fields is considered, there is reason to believe that the observed intensity has diurnal characteristics. The evidence comes from the decreasing level of intensity from 0600 to 1800 UT, March 26, and from 0600 to 1200 UT, March 27, as well as the absence of Region A fields from 1800 to 0600 UT. As a diurnal effect would most likely appear as a result of changes in the relative positions of the solar stream, the earth's dipole, and the satellite, these positions are illustrated in Figure 24. The geometry indicates that the field intensity at the satellite when it is inside the cavity may depend on the intensity of the field along the satellite-sun line on the side of the earth facing the sun. This suggests the

VIEW OF EARTH FROM ABOVE
NORTH GEOGRAPHIC POLE

S. MAG. POLE
WHEN
"CAVITY" FIELD
IS NOT OBSERVED

MERIDIAN OF
SOUTH MAGNETIC POLE
AT 1800 UT

SUN

MERIDIAN OF
SOUTH MAGNETIC POLE
AT 0600 UT

DECREASING
"CAVITY" FIELD
INTENSITY
AT SATELLITE

SATELLITE MERIDIAN

1300 UT, MARCH 27

0600 UT, MARCH 26

VIEW OF EARTH FROM 18ʰ
LOCAL TIME MERIDIAN

SUN

EQUATOR

SATELLITE LATITUDE

1300 UT, MARCH 27
0600 UT, MARCH 26

0600 UT   1800 UT
SOUTH MAGNETIC POLE

Figure 24—Relative positions of the sun, dipole axis, and satellite when
Region A, or cavity, field is observed.

calculation of χ on the basis of Region A intervals separated by approximately 24 hours. Using various combinations of intervals on March 26 and 27, separated by approximately 22 to 26 hours, gives the range $\chi = 0.2$ to 1.0 with most values between $\chi = 0.6$ and 1.0. Similarly, using minimum average intensities near 40.3 R_e relative to intensities at 11.7 R_e gives $\chi = 0.81$.

The above leads to a generalization that the average decrease in field intensity with distance inside the geomagnetic cavity along the Explorer X trajectory can be represented by $F(r) = F(r_1)\,(r_1/r)^{\chi}$ with $0.6 < \chi < 1.0$ for 11.5 $R_e < r < 40.5$ R_e and $r > r_1$. Different assumptions, or criticism of the assumptions used, can lead to a smaller χ (i.e., less dependence) but it seems unlikely that assumptions giving $\chi > 1.0$ can be justified.

CORRELATIONS WITH SURFACE GEOMAGNETIC VARIATIONS

Prestorm Correlations

The general level of geomagnetic activity during the flight was illustrated in Figure 15 and discussed on pages 179 through 181. A complete discussion of possible detailed correlations between satellite and surface measurements is beyond the scope of this paper; thus, the following discussion is limited to several examples involving primarily low latitude activity.

The period 0245 to 1345 UT, March 26, is of particular interest because of the simultaneous and similar behavior of all the low latitude magnetograms available for examination. Between 0245 and 0300 UT, March 26, the horizontal component increases from a previously quiet condition and remains positive with irregular but slow variations that are typically 5 or 10 gammas in amplitude for a number of hours. This activity disappears gradually between 1300 and 1345 UT, March 26. At much higher frequencies within this period the micropulsation energy spectra near 0.1 cps at Fredericksburg, Virginia, shifted to higher frequencies near 0600 UT (Reference 2), and micropulsations of "pearl" character were observed in California (L. R. Tepley, private communication) and in the USSR (V. H. Troitskaya, informal communication at Kyoto meeting September, 1961) for several hours after 0600 UT. Through this same time interval the field intensity at the satellite increased near 0300 UT, March 26, and remained at a high level until solar plasma was observed at 0530 UT. Between 0530 and 1330 UT (Figures 9 and 10), there was noticeably more variation between successive measurements by the satellite than at other times and much larger variations within the 6-second measuring period, as noted on page 176 and References 1 and 2. If the low latitude $+\Delta H$ irregularities are attributed to increased and more irregular compression of the geomagnetic field by the solar stream, it follows that the cavity dimensions and geometry should also vary. This may explain the short intervals of plasma disappearance and Region A fields between 0530 and 1030 UT, March 26. Similarly, change in the solar wind and/or any cavity influence on the configuration of external fields may explain the variability of the external field during this period. The average plasma flux (References 3 and 6) when present during this period appears to be higher than during most periods prior to the magnetic storm.

A sequence of three isolated cases of $+\Delta H$ roughness in surface magnetograms occurs during the 12-hour period in which plasma appears to be continually present and stable Region A field conditions do not appear. In Figure 25 an attempt is made to illustrate the simultaneous surface and satellite measurements. Details in the satellite measurements can be seen more clearly by inspection of Figures 10, 11, and 12. The low latitude times of interest are: (1) approximately 2045 to 2245 UT on March 26; (2) the change near 0030 UT on March 27; and (3) the change near 0445 UT on March 27. The first of these coincides with a 2-hour period at the satellite in which the field changes and rotates away from a relatively stable Region B configuration during the first hour, and rotates back during the second hours, as discussed in more detail below. The second and the irregularities that follow, coincide with a period of irregular variations at the satellite between two intervals in which the field has the Region B configuration. The third coincides approximately with an irregular slow transition from a Region B to Region C field configuration at the satellite. In both the second and third examples, the variations appear to begin at the satellite prior to the low latitude changes and in closer coincidence with small changes at high latitudes (e.g., the fluctuations starting near 0000 UT at Churchill and Pt. Barrow and near 0430 UT at most high latitude stations). The maximum variation at the satellite occurs, however, more in coincidence with, or following slightly, the low latitude changes. In case (1), the low latitude initial change appears to occur several minutes before the change at the satellite, depending on point selection, and an initial sharp change at high latitudes is not readily identified at a large number of stations.

The behavior of the field vector at the satellite during the case (1) interval is particularly interesting. In Figure 26, the successive positions of the end point of the vector is shown in solar-ecliptic
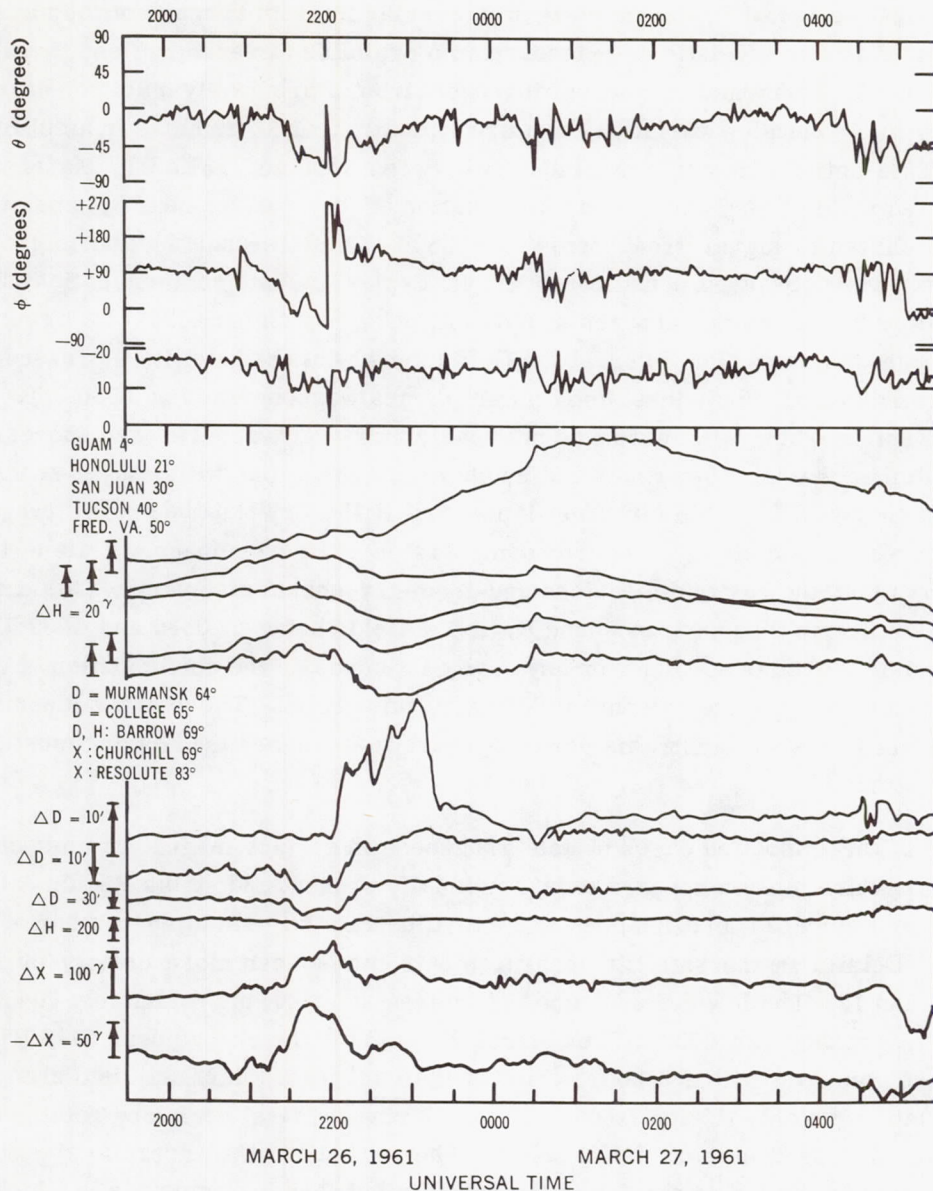
Figure 25—Simultaneous surface and satellite measurements.

coordinates for the center portion of this interval. After 2109 UT, the field rotated irregularly to the Region C field direction and at 2201 UT abruptly dropped in intensity to 2.5 gammas with a corresponding abrupt change in direction. Following the measurement at 2201 UT, the intensity and direction abruptly changed back to roughly the previous intensity level but to a different orientation from which it then rotated to a direction not characterized by Region A, B, or C. It then gradually returned to the Region B orientation. In addition to the total time interval correlation at low latitudes, the sharp change at 2201 UT may be significantly related to changes at high latitude. The sharp, simultaneous change at Murmansk on the night side of the earth is obvious in Figure 25. On the dayside of the earth, near local noon in Alaska, the declination changes considerably with only slight changes in field intensity. The most striking feature, however, is that the level of the D trace is shifted between the

194
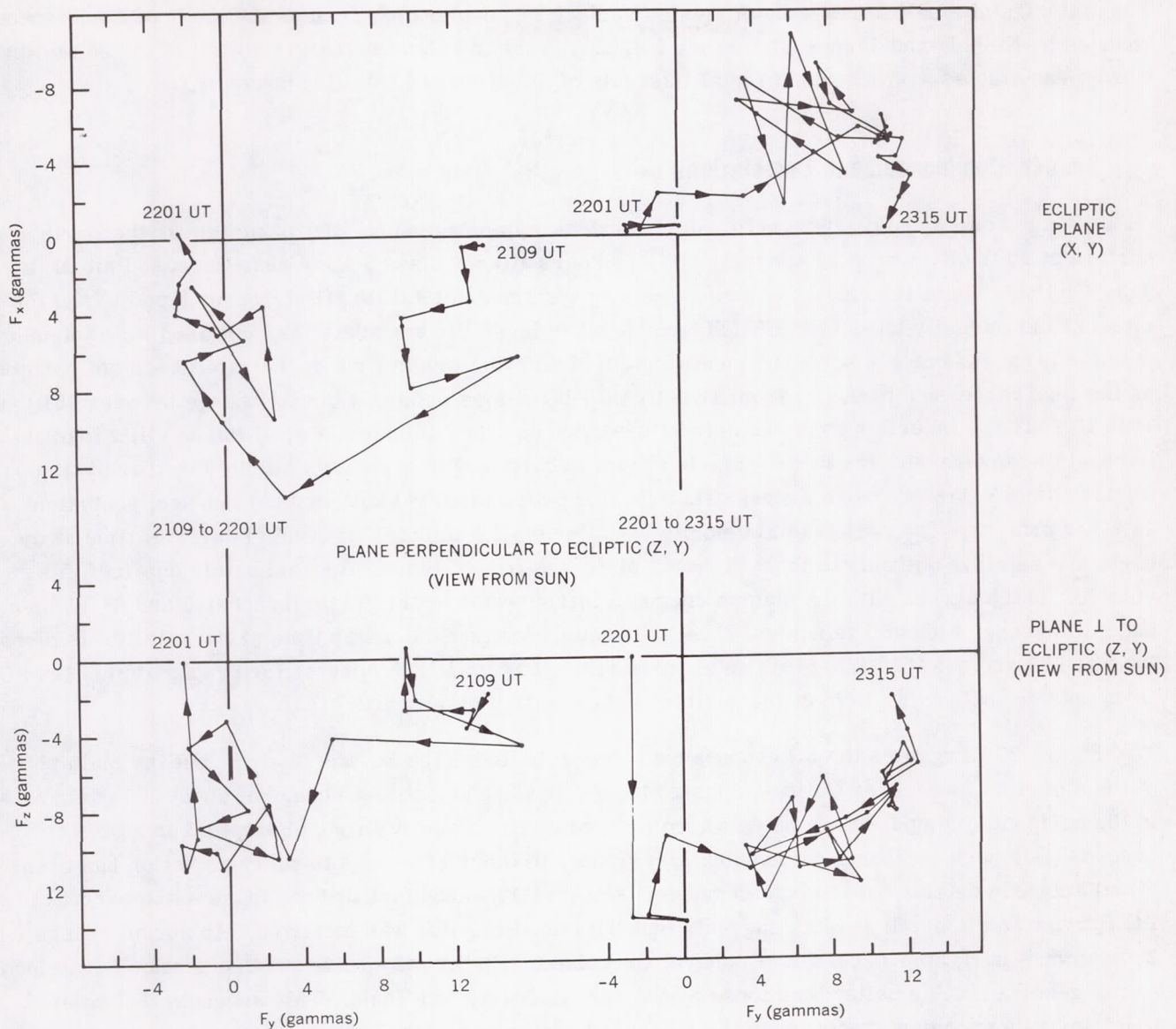
Figure 26—Rotation of the field vector in solar-ecliptic coordinates between 2109 and 2315 UT, March 26. Arrow marks indicate the time sequence of vector end points.

quiet hours preceding and following the change. In Figure 25, the level shift is apparent in the north component at Churchill as well as in D at College, Barrow, and Murmansk. In References 3 and 6, it is also obvious that the plasma spectra shifts to higher energies and greater flux over an interval centered on 2200 UT, March 26.

Although it is tempting to pursue explanations for the details of these correlations (e.g., treating the reading at 2201 UT in terms of a neutral sheet in a solar stream or cloud), the data is not sufficiently comprehensive. From a more general view, the correlations do suggest spatial structure in the solar wind and also that changes in this structure have a rather direct influence on magnetic activity at the surface of the earth, even during periods that will normally be called magnetically quiet.

Thus, studies of small world-wide effects on surface magnetograms, such as the study of simultaneous changes by Nishida and Jacobs (Reference 16), may yield an index for the variability of the solar wind when these studies are extended to total intervals of simultaneous, similar behavior.

Sudden Commencement Correlations

As noted on Page 179, a magnetic storm sudden commencement (SC) occurred at the earth's surface at 1503 UT, March 27 approximately 29 hours after a Class 3 flare near the east limb of the sun. On the basis of the change in plasma energy spectra and total flux (References 3 and 6) and the rise in field intensity after 1503 UT (Figure 13), it is logical to associate the increased field intensity with the SC at the earth's surface. Identification of an exact origin time at the satellite is not possible as the field increased gradually from 1503 to 1510 UT before making a larger change between 1510 and 1512 UT. Thus, the origin time can only be specified as 0 to 7 minutes later at the satellite than at the earth's surface with the largest single change occurring 7 to 9 minutes later. The transit time for the Class 3 flare gives an average straight line propagation velocity of 1460 km/sec, equivalent to 11.1 kev protons. The same radial velocity would give a 2.3 minute difference in arrival time at the earth and satellite due only to their different distances from the sun. Approximately one-half this velocity, which agrees with the plasma energies measured after the SC (References 3 and 6), gives a time difference of about 5 minutes. Thus, the assumption that the origin time at the satellite is close to 1503 UT, and not 1510 UT, gives an approximate *upper limit* of 5 minutes for propagation of the SC from outside the earth's field to the earth's surface.

Figure 27 illustrates the SC appearance. At low latitudes the SC was distinct, but the main phase of the storm was weak. At College, Alaska, the SC produced an abrupt change of about 300 gammas in the horizontal component which was accompanied by the onset of strong absorption on riometer records (Leinbach, personal communication) similar to other SC events in which radiation has been simultaneously detected at balloon altitudes (Reference 17). The fact that the SC is not apparent at Pt. Barrow and is small at Sitka suggests that the initial impulse was localized. An abrupt change, 280 gammas in H, also occurs at Godhavn, Greenland. The initial effects at other stations examined are in general much smaller than those at College, Godhavn, and Thule. This suggests that solar particles with energies greater than the measured proton energies (References 3 and 6) may accompany the plasma cloud (or stream) and that these reach particular high latitude regions by a rather direct path. This could also be suggested on grounds that the SC effect at the satellite represents an increase of only a factor of 2 in the observable plasma flux relative to a number of other periods during the flight.

It also presents the question as to whether or not the magnetic fields observed by Explorer X are not also affected by particles which have energies outside the range of detection of the plasma probe. This question arises when the data prior to the SC is examined. From Figure 13 it is apparent that the direction of the field vector was not significantly changed during the initial rise in field intensity following the SC time. Instead the field orientation up to half an hour after the SC appears to follow a slow shift (particularly apparent in the angle ϕ) that started two hours earlier. This shift was temporarily broken between 1435 and 1450 UT by a large change in field orientation that is not accompanied
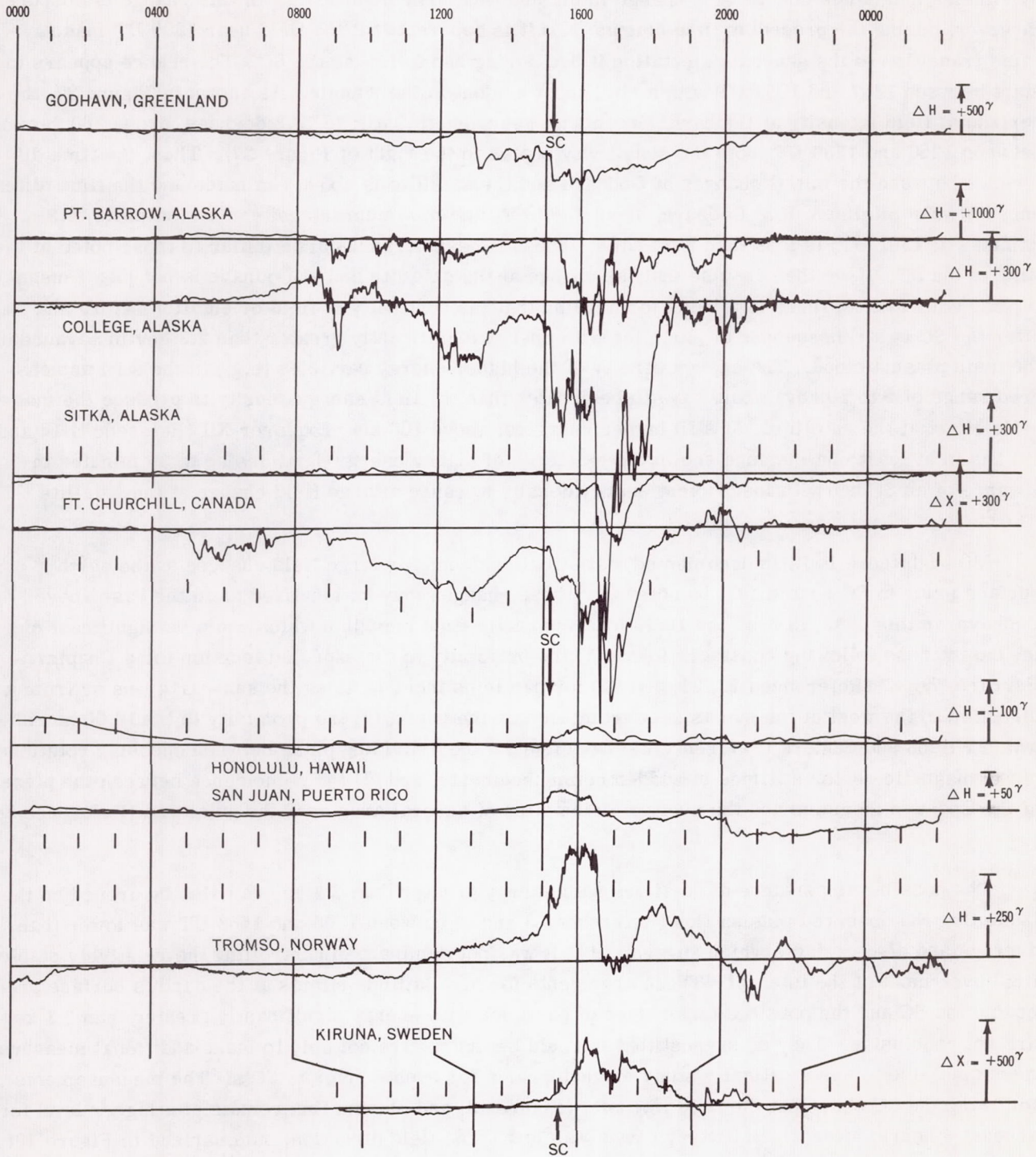
Figure 27—Magnetograms illustrating the sudden commencement at 1503 UT, March 27 (note scale differences).

by either a magnitude change or a change in plasma flux. The significance of this change is obscure. However, during the preceding time (Figure 13), it is apparent that the field near 1300 UT made a rapid transition to the general orientation it had during and following the SC. The change appears to start between 1257 and 1259 UT with a shift most evident in the θ angle. As shown in Figure 27, the horizontal field intensity at Godhavn, Greenland, geomagnetic latitude 79.8 degrees, drops 360 gammas between 1250 and 1300 UT (note the sensitivity scales to the right of Figure 27). Thus, the time difference between the initial changes at Godhavn and the satellite is about 7 minutes and the time difference between minimum H at Godhavn, about 1300 UT, and minimum intensity at the satellite, 4.2 gammas at 1301 UT, is less than 2 minutes. These time differences are similar to those noted at the time of the SC. If we then assume that the change at the satellite and at Godhavn is not just a meaningless coincidence, there is a basis for arguing that the continuity of field orientation before and after the SC is a consequence of particles with energy significantly greater than 2.3 kev in advance of the main plasma cloud. The energy density of the higher energy particles (e.g., in the still unmeasured range of 5 to 50 kev) would have to be greater than the field energy density to produce the magnetic effect at the satellite. At still higher energies, above 100 kev, Explorer XII (References 18 and 19) has in at least one instance shown the existence of higher energy particles up to 30 minutes in advance of an SC but with insufficient energy density to cause a large field change at the satellite.

Although there is little documented statistical evidence for large field changes at the earth's surface prior to SC's, it should be noted that these changes may be localized as in the case above. Godhavn, in this case, is near the 10:40 local magnetic time meridian which could be significant on the basis of the following considerations: (1) the proximity to the expected location for a Chapman-Ferraro "horn" (References 20, 21, and 22) for particles incident along the sun-earth line or from a direction to the west of the sun as seen from noon on the earth; (2) the promixity to the 10:00 meridian which Wilson and Sugiura (Reference 23) have found to be a dividing plane between opposing rotations of the magnetic vector at times of sudden commencements; and (3) the coincidence between the plane of the Godhavn meridian and the average orientation of auroral arcs over the polar cap (Reference 24).

The possible importance of particles with energy greater than 2.3 kev can also be argued on the basis that the observed plasma flux (References 3 and 6) between 1300 and 1503 UT was lower than average and also variable which suggests that it was not dominant in controlling the relatively stable field over most of the interval. These arguments for high latitude effects at the earth's surface preceding the SC and the possible importance of particles with energy significantly greater than 2.3 kev are not conclusive. They do suggest that it would be instructive not only to make additional measurements but also to systematically study magnetograms for events prior to SC's. The measurements following the SC show that the field intensity (Figure 13) and plasma flux remain at a higher level for at least 4 hours, after which battery power was lost. The field direction, summarized in Figure 19c, was, in general, such that the vector pointed to the west of the sun and varied irregularly, but somewhat systematically, above and below the ecliptic plane.

THE GEOMAGNETIC CAVITY

Cavity Models

The problem of interaction between the geomagnetic field and an ionized but neutral corpuscular stream was formulated in 1930 by Chapman and Ferraro (References 20 and 25) to explain SC's and the initial phase of magnetic storms and has subsequently been treated by them in additional detail (References 26 and 27). Recently, this problem has been approached by a number of investigators (References 21, 22, 28, 29, 30, 31, 32, and 33 among others) for cases of steady plasma flow and isotropic plasma pressure. Computations have been carried out for both two and three dimensional cases and in most cases it is assumed that the magnetic pressure just inside the cavity surface $B_s^2/8\pi$ is balanced by the plasma pressure just outside the cavity. The surface is in reality taken to be a thin current sheath having the necessary strength and geometry to identically cancel the geomagnetic field that would exist external to the same surface in the absence of a plasma pressure. Thus, the problem is formulated so that the geomagnetic field does not have a component normal to the surface at the boundary location. It is generally assumed that the plasma pressure inside the cavity surface is negligible and in nearly all computations the possible effects of an external field of solar-interplanetary origin are completely ignored.*

For a uniform solar stream with proton velocity v, mass m, and number density n, the equilibrium condition for the cavity surface is computed from

$$B_s^2/8\pi \ = \ 2 \, mnv^2 \, \cos^2 \zeta \, , \tag{1}$$

where ζ is the angle between the normal to the surface and the velocity vector of the stream prior to encountering the earth's field and B_s is the total magnetic field intensity at the boundary. Specular reflection of the incident plasma is assumed and although there is some concern over the factor 2 in the equation above (see References 22 and 29) it has been used by most investigators.

The computation of the surface geometry then becomes one of finding numerical solutions to the boundary value problem subject to additional approximations. The approximation

$$B_s \ = \ 2 \, fB_t \, , \tag{2}$$

where B_t is the component of the earth's dipole tangential to the surface, is often used to specify the condition that the field inside the cavity cannot have a component normal to the surface at the boundary.

---

*The exception to this is Dungey's (Reference 33) two-dimensional calculation for a selected orientation of an external interplanetary magnetic field.

For arguments regarding the value of f, usually taken to be unity or less, and the numerical techniques and approximations then employed, the reader should consult the references listed, and especially the work by Beard (Reference 29) and Spreiter and Briggs (Reference 22).

Cavity Geometry Relative to Cavity Models

In the preceding sections arguments have been advanced that the Region A magnetic fields can best be interpreted as fields within the geomagnetic cavity. The arguments are based almost entirely on: (1) the similarity between the Region A field direction and the field direction observed between 12 and 22 R_e (page 186); (2) the deduction that the Region A field intensities decrease with distance from the earth when importance is attached to the earth's daily rotation (pages 191 and 192); and (3) the absence of a detectable plasma flux when the field has the Region A orientation. If this interpretation is correct, the theoretical models can be compared with the measurements to check the degree of agreement.

Considering first the geometry of the cavity, it is apparent that the measurements support the theoretical prediction that the solar wind extends the geomagnetic field to great distances on the dark side of the earth. If, however, we then assume that the plasma velocity vector is directed exactly along the sun-satellite line, the dimensional agreement between theory and measurement becomes increasingly poorer with distance. This is illustrated in Figure 28 using Spreiter and Briggs's (Reference 22) computations of the cavity dimensions in equatorial and meridian planes for a typical observed plasma flux (References 3 and 6).* The fact that Region A fields are observed in intervals between 0600 and 1300 UT, March 27, as well as between 0600 and 1800 UT, March 26 (Figures 20 and 21), obviously requires, under the assumptions of radial plasma flow, that a symmetrical cavity be roughly conical rather than cylindrical at great distances along the trajectory. Also, rotating the position of the earth's dipole axis relative to a radial stream in the Spreiter and Briggs model does not appreciably alter the cavity dimensions shown in Figure 28. This further implies that the model calculations do not provide an explanation for the behavior of field intensities in Region A, which were discussed earlier. In general, from these and other arguments, it is apparent that dimensional agreement between the measurements and the models cannot be reached using the conditions that the plasma is directed along the sun-earth line and that the cavity formed is continuously symmetric relative to the earth-sun line. Assuming that the computations are basically correct for the assumptions made, there are a number of reasons why agreement might not be expected. The neglect of an external solar-interplanetary field in the model calculations is perhaps the most obvious, but until model calculations have been made either for the general case or a variety of selected cases the consequences of this neglect cannot be estimated with confidence. Second, although the plasma flux measurements are consistent with a flow directed in the sun-earth direction, flow from a direction to the west of the sun is not excluded (References 3 and 6). Third, the measurements do not exclude the possibility of plasma outside the observable energy range arriving from either the radial or other directions. It may, in fact, be essential to postulate a variable component of the solar stream arriving from a direction to the west of the sun to explain why the cavity moves back and forth across the satellite trajectory

---

*Beard's solution (Reference 29) gives substantially the same dimensions in the region of interest here.
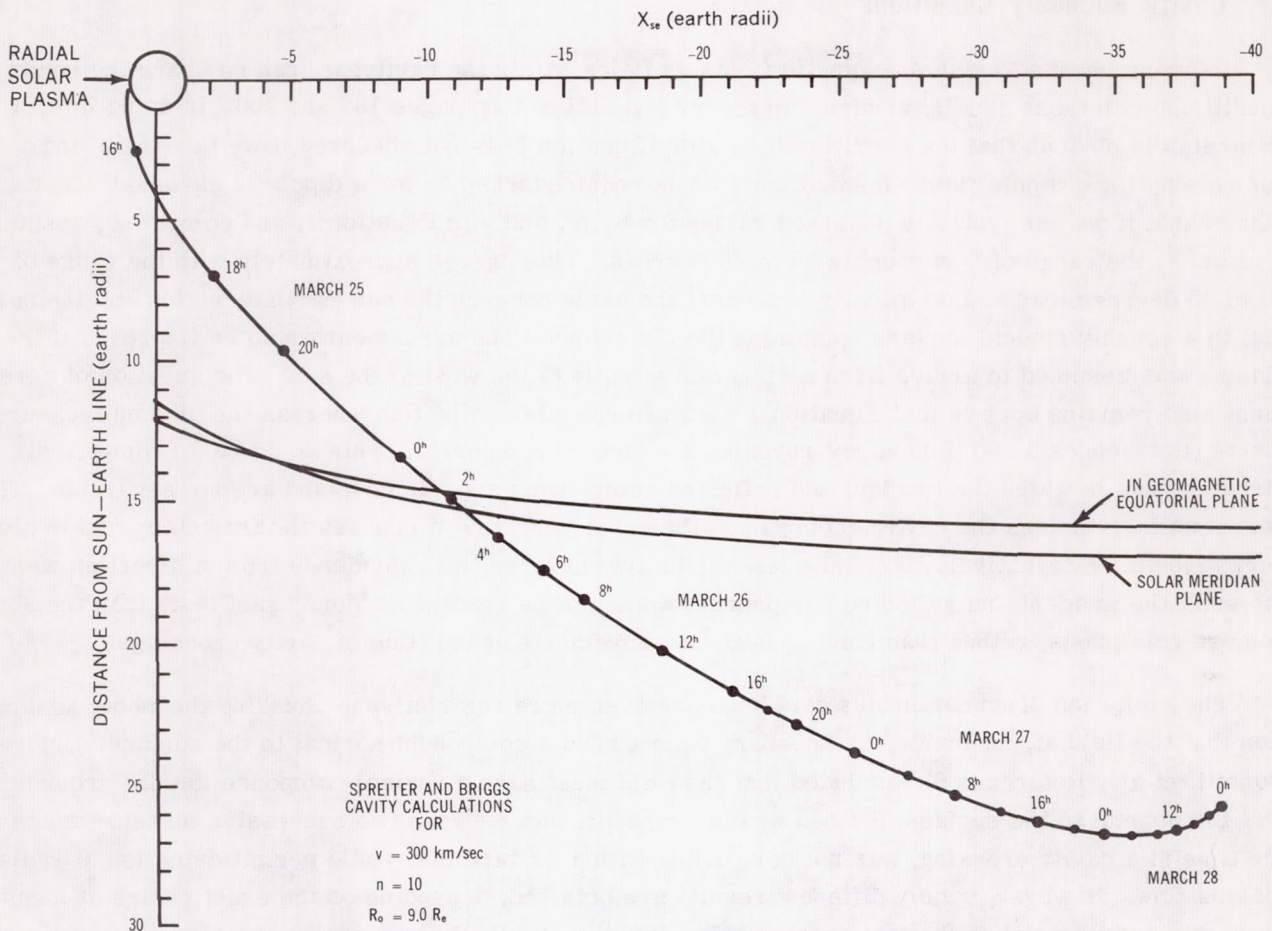
Figure 28—Cavity dimensions given by Spreiter and Briggs relative to trajectory dimensions.

between 0600 and 1300 UT, March 27, and 0600 and 1800 UT, March 26. An alternative explanation for the intermittent reappearance of Region A is that the degree of symmetric compression of the cavity differs between times when the satellite is inside or outside the cavity in response to changes in the solar wind pressure. This explanation appears to conflict with the fact that Region A fields are not observed during the periods of minimum magnetic activity at the earth's surface when we might expect the cavity to be the least compressed. This conflict may not exist, however, as the quiet magnetic periods occur within the 12-hour period in which Region A fields never appear. This may be attributed to a diurnal effect (see pages 189 and 191). Similarly, the conflict may not exist on the grounds that Region A fields do not appear after the SC.

These arguments do not lead to a consistent picture. They do, however, make it evident that relative to existing cavity models one must either postulate a non-radial component in the solar stream or postulate that the external field has a large effect on the cavity geometry. The alternative is to assume that the cavity calculations are wrong in not predicting a broad conical cavity back of the earth, even in the idealized formulation.

Cavity Boundary Conditions

Interpreting the Region A magnetic fields as fields within the cavity, we can compare the boundary conditions with those usually assumed in theory and outlined on pages 199 and 200. In doing this, it is immediately obvious that the condition $B_s = 2 fB_t$ (Equation 2) is not observed if we take $f \leq 1$ and compute B_t for a dipole field. Instead, an $f > 3$ is required when B_t for a dipole is assumed. On the other hand, if we use typically observed values for B_s, n, and v in Equation 1, and compute ζ, assuming a radial $\vec{v}$, the range of ζ is roughly 55 to 85 degrees. This agrees approximately with the range of 50 to 70 degrees that would typically represent the angle between the sun-earth direction and the normal to a roughly conical surface containing the trajectory. The agreement would be improved if the plasma was assumed to arrive from a direction slightly to the west of the sun. The question of agreement also remains open in that Equation 1 assumes specular reflection whereas the plasma measurements (References 3 and 6) have not revealed a reflected component. This could be a geometrical circumstance in which the incident and reflected components superimpose and are not separable. This seems unlikely unless the cavity geometry is the same each time it crosses the trajectory and is also very smooth. Alternatively, if ζ in Equation 1 is always large (i.e., incidence from a direction west of the sun), the incident and reflected components would not be resolved. More exact tests than the above require continuous, rather than time spaced, measurements at the time of cavity crossings.

The limitation of noncontinuous data becomes even more restrictive in checking the model assumption that the field at, but inside, the boundary cannot have a component normal to the surface. Bridge, Bonetti, et al. (Reference 6) concluded that the field must have a normal component on the grounds that the normal to the surface, defined by the cross-product between two successive measurements at the time of a cavity crossing, was not compatible with a surface that would permit detection of radial plasma flow. However, widely different results are obtained, depending on the exact choice of measurements and this makes the test questionable. We may similarly look at the cross-product of average vectors in Region A relative to Regions B and C, but this involves the assumption that the field external to the cavity is perfectly wrapped about the cavity surface without maintaining even a fractional resemblance to its original geometry. The assumption becomes untenable if the average distances from the cavity surface are large as might be expected from the duration of most of the intervals in which the field is in one of the three regions. In addition to these difficulties in using a cross-product, it involves in interpretation the assumption that the cavity has a rather simple symmetry which, though convenient for illustration purposes, may not be justified in view of the apparent diurnal behavior (Section 9) and various other features already discussed. As an illustrative example, the projection of Region B vectors in the X_{se}, Y_{se} plane of Figure 22 suggests that the field extended almost normal to a symmetric conical cavity; but if viewed from the sun ($Y_{se}Z_{se}$ plane), it is apparent that only a slight distortion of such a cavity would place the vectors in front (i.e., on the sunward side) of the assumed cavity.

Other arguments can be used that suggest that the field inside the cavity but near its surface is tangential to the surface. The most obvious is the fact that the Region A vectors (Figure 21) show only small changes in orientation from 22 to 41 R_e, and these changes appear to have a diurnal dependence. Another argument against having both a symmetric cavity and geomagnetic field lines crossing the cavity surface, is that it becomes exceedingly difficult to account for the total magnetic

field flux. To explain the observed field intensities in the case of a symmetric cavity, when no lines are allowed to cross the surface, it is necessary to assume that all lines of force intersecting the earth at latitudes of 72 degrees or higher extend through a plane perpendicular to the earth-sun line approximately 30 R_e behind the earth within the confines of the conical cavity. That is, only an insignificant fraction of the flux can pass through the equatorial plane between 10 and 30 or more R_e. Thus, unless the flux is highly concentrated near the cavity surface and not distributed throughout the volume back of the earth, it is not tenable to postulate both a symmetrical cavity and lines of force crossing the surface. It also seems unlikely that there would be two highly preferred directions, Regions B and C, for the field orientation outside the cavity if these fields were to be attributed to geomagnetic lines crossing the boundary. Similarly, if a significant fraction of the field intensity outside the surface was due to field sources inside the surface, we would expect to find a decrease in intensity in Regions B and C with distance, and this is not the case.

In summary, there is little reason to believe that the geomagnetic lines cross the surface and, indeed, observations indicate that they do not. Thus, it is not necessary to believe that the measurements contradict the common assumption that the geomagnetic lines do not extend into the highly conductive solar plasma. This does not preclude the existence of a sheath at the boundary in which mixing and diffusion occur as this must certainly take place within a finite volume. It suggests that the sheath thickness is small compared to the average distance from the boundary when the satellite is in one of the characteristic field configurations, Regions A, B, and C (Figures 19 and 20). As the measurements do not reveal either the distances from the boundary or the boundary thickness, we can only estimate that on the dimensional scale involved the average distances from the cavity could easily be several earth radii and at least several thousand kilometers, and thus very large compared to typical values computed for the boundary thickness, even for cases of surface instability. (See, for example, Reference 34.)

FIELDS EXTERNAL TO THE GEOMAGNETIC CAVITY

In an earlier section the Region B and C fields were interpreted as fields of solar-interplanetary origin whose orientations may be significantly affected by the proximity to the geomagnetic cavity. The degree of cavity influence was taken to be uncertain and could be negligible, especially between 1830 UT, March 26, and 0530 UT, March 27. Continuation of this interpretation of the measurements should reveal some of the properties of the solar wind and the behavior of the associated fields.

It is apparent that the field energy density is typically a factor of 5 to 10 less than the observed plasma energy density and thus it can be assumed that the field is carried by the solar wind. The measurements also suggest that the solar wind has both small and large scale variability. The small scale variability is suggested by the changes that take place between successive samples at 2-minute intervals. The large scale variability is suggested by the tendency for a given field configuration to persist for fractions of an hour to several hours and appears both as a movement of the cavity across the trajectory, typically transitions between Region A and Region C configurations, and as disruptions of the Region B configuration during the 12-hour period when plasma disappearance and Region A fields are not observed. The deviations from the Region B configuration, discussed on pages 193 and 194, are particularly important in interpreting the large scale structure in that each change away from

the Region B condition is accompanied by a shift to a higher energy plasma spectrum. This presents the possibility, when extrapolated to very quiet conditions, that a very weak solar wind is accompanied by a spiral field which at 1 AU lies roughly in the ecliptic plane at nearly right angles to the solar radial direction as predicted for this simple case by Parker (Reference 35) and others. The data suggests, however, that such a stable configuration may be quite rare and that to retain Parker's picture it would be closer to reality to view the interplanetary structure along the lines of a series of small "blast waves" from the sun (Parker, Reference 36). The interplanetary media would then be broken into annular regions moving outward from the sun and a typical annular width from the Explorer X data would be of the order 0.01 AU from $v(\Delta t)$, where Δt is the time interval for the region to cross the satellite and v is the observed plasma velocity. At the other extreme, the structure could be entirely filamentary with the individual filaments oriented roughly at the stream angle $\tan^{-1} (\omega r/v)$ with respect to the solar radial direction, where ω and r are, respectively, the sun's angular velocity and the distance from the sun. Filament dimensions would typically be $\omega r(\Delta t) \cos \left[\tan^{-1} (\omega r/v)\right]$ in this case, and thus not greatly different than 0.01 AU. With filaments of this small scale, agreement between filament orientation and field direction can hardly be expected as the range of observed velocities would certainly lead to intersecting flow between adjacent filaments in the space between the sun and the earth. Similarly, in a "blast wave" picture, the flow would necessarily involve higher velocity regions overtaking the lower velocity regions and the resulting field configuration can hardly be expected to fit any simple model. Thus, the data is obviously not definitive in selecting between "blast wave" or filamentary structures and similarly does not distinguish between these structures and others that might be visualized from a "magnetic bottle" (e.g., Reference 37) picture. The picture that does emerge is one of considerable structure in the solar wind under average conditions of solar activity. The correlations with surface magnetic activity also lead to this suggestion. The next question is whether or not these structures are related to minor solar events on the sun. As illustrated in Figure 14, the time intervals between Class 1 flares prior to the flight have some similarity to the observed duration of a given field configuration. Correlations cannot be justified, but the coincidence suggests that it might be worthwhile to attempt statistical correlations between numbers and locations of minor solar flares and occurrences of simultaneous world-wide magnetic field changes of the type discussed on pages 192 and 193. A correlation of this type would not be found by the usual techniques, as it requires detailed study of a large number of magnetograms from observatories widely distributed in longitude.

It may not be sufficient to look for events on the sun to explain the solar wind structure. Instead dimensions of the order 0.01 AU at distances of 1 AU may be related to a more fundamental and continuous property of the sun and solar corona. Some suggestion of this comes from McCracken's (Reference 38) deduction that scattering centers with dimensions of 0.01 AU could account for observed angular distributions in cosmic ray flare effects. Dimensions of 0.01 AU, or less, at distances of 1 AU are also indicated by extrapolating recent observations (Reference 39) of the scattering of radio emissions passing through the solar corona at distances out to 0.5 AU from the sun. These observations (Reference 39) are particularly suggestive in that a close correlation was also found between detection of scattering at great distances in equatorial regions (0.25 to 0.5 AU) and the areas and intensities of calcium plages. Thus, if the basic scattering structure is that of filaments which are extensions of visible solar rays and plage activity leads to greater density contrast between filaments there is a reasonable basis for suggesting that this is the type of structure observed by Explorer X.

From Figures 13 and 19, it is apparent that the solar stream from the Class 3 flare effectively displaced the existing field structure and the average field orientation (Figure 19) became more oriented in the ecliptic plane with time. The rather large angular deviations show, however, that the field within the stream was by no means highly regular and as was discussed on pages 196 through 198, we cannot assume that the SC represents a sharp stream boundary. Depending on the choice of origin of the stream, 1300 or 1503 UT (see pages 196 through 198), a minimum stream dimension corresponding to 4 to 6 hours in passage can be stated, but the maximum remains uncertain due to the loss of battery power.

It is also apparent that the ratio of field energy density to observed plasma energy density after the SC is essentially the same as observed during other periods when plasma was present between 22 and 40 R_e. Thus, if it is assumed that the proximity of the geomagnetic cavity does not affect the measurements after the SC, this may indicate that the Region B and C fields are not as affected by the cavity proximity as might be supposed on other grounds.

Comparison of the Region B and C fields with the measurements of Pioneer V (1960 α) does not show appreciable agreement in detail (References 40, 41, and 42). Field directions are not readily compared in that Pioneer V measured only the magnitude perpendicular to the spin axis and thus fields perpendicular to the ecliptic could not be distinguished from fields in the ecliptic plane normal to the radial solar direction (Reference 43). However, it is apparent in comparing magnitudes that the Explorer X components in the same plane would in general give values in excess of the 2.7 to 5.0 γ fields typically observed with Pioneer V. Similarly, Pioneer V apparently did not see evidence for large scale structure, except at times of magnetic storms, although the data intervals may in general have been too short for this to be apparent. Comparison of magnetic activity indices during the two flights also makes it clear that the Explorer X measurements prior to the SC occurred when the indices were comparable to those of the quiet days during the Pioneer V flight. Thus, differences are not readily explained in terms of the level of magnetic activity. Resolution of these differences can be attempted by assuming that the Region B and C fields show greater magnitude as a consequence of crowding of the field lines around the geomagnetic cavity; however, various features argue against this and the differences will best be resolved by future measurements.

ALTERNATIVE INTERPRETATIONS

At various points in the preceding discussion, alternative interpretations were presented, usually with respect to a particular problem, but no attempt was made to consider all possibilities. There are alternatives which would lead to grossly different interpretations that should be mentioned even though space will not permit extensive discussion. These are noted below:

1. If major differences in the plasma energy spectra existed between adjacent filaments in the solar wind, it is possible that the Region A field intervals could be solar wind filaments in which particle energies are greater than 5 kev. In this case, a cavity picture more consistent with theoretical cavity models could be obtained from the standpoint that a cylindrical surface, crossed once at 0530 UT, March 26, would be adequate and major diurnal distortions would not be indicated by the measurements. The principal difficulty is obviously the lack of observational evidence for higher energy plasma.

2. As in (1) above, in suggesting large velocity differences between adjacent filaments but instead treating the plasma-free regions as cool filaments, Parker (personal communication) has suggested that hot (solar wind observed) filaments and cool (solar wind not observed) filaments could be developed in adjacent columns low in the solar corona and continued outward to great distances with the hot filaments effectively drawing the fields outward in the cool filaments. Extending this further, we might suggest that the cool filaments superimpose with the earth's field to explain the similar orientation of Region A fields and the field between 12 and 22 R_e. The principal difficulty in explaining the observations is perhaps accounting for the regularity of the Region A fields.

3. As an alternative to explaining the transitions between Region A and Region C fields in terms of either movement of the entire cavity or differences in compression of a symmetrical cavity, it can be suggested that the cavity surface is highly unstable and irregular or that the surface exhibits long period oscillations. As noted on page 176, and previously illustrated (References 1 and 2), the measurements between 0530 and 1330 UT, March 26, typically show short period field fluctuations when plasma is observed that might be interpreted as an unstable surface behavior. Uncertainty arises in interpreting this as a typical behavior in that the same time interval coincides with an extended period of field fluctuations at the earth's surface as discussed on page 193.

4. W. I. Axford (personal communication) and Kellog (Reference 44), following the approach of Zhigulev (Reference 28), have proposed that the observed field changes can be explained by the existence of a collisionless shock front spreading outward in the form of a bow wave from a vertex position located several or more earth radii in front of the magnetosphere at the subsolar point. The existence of the shock considerably reduces the plasma bulk velocity, perhaps to random motion (W. I. Axford, personal communication), but the motion presumably again becomes radial at large distances behind the shock. The magnetic field behind the shock and outside the magnetosphere is presumably of solar-interplanetary origin but greatly modified by the presence of the shock. Comparison in any detail with the measurements is currently impossible as the postulated conditions have not been adequately developed from either an observational or theoretical approach.

5. As discussed on pages 181 through 184, the data does not suggest the existence of a symmetrical ring current at distances greater than 4 R_e. This does not preclude the existence of current systems within the cavity such as a "sheet" configuration in the equatorial plane extending over many earth radii. By careful selection of the distribution of current density and closing the circuit on the nightside of the earth, probably along field lines to high latitudes, a fit to the observations could probably be obtained. Explanation along these lines might also explain the outward spreading of the cavity back of the earth, the total flux required in the cavity, and other features which are difficult to explain in a model involving no external magnetic field, radial plasma flow, and a conically symmetric cavity. The rather highly selective current distribution required to fit the observations is the principal difficulty in seeking explanation along these lines.

DISCUSSION

The measurements taken in radiation belt regions are not inconsistent with a weak diamagnetic ring current below the magnetic shell intersecting the equator at 3.8 R_e. Questions regarding the

possible existence of meridional currents and the extension of the cavity field suggest that simple interpretations may not be adequate.

The measurements between 8 and 22 R_e and during periods when plasma was not observed between 22 and 41 R_e can be interpreted in terms of a large-scale cavity field that decreases in intensity with distance as $F(r_1) (r_1/r)^\chi$ with $0.6 < \chi < 1.0$ for $r_1 = 11.5 R_e$, $r > 11.5 R_e$, when it is assumed that the intensity observed depends on the position of the dipole axis relative to the solar stream.

At distances greater than 22 R_e, and prior to the SC, the field is typically oriented in one of three directions designated Regions A, B, and C. A distinctly different level of average field intensity is associated with each of the three orientations. The Region A fields correlate with the absence of detectable plasma and are interpreted as fields within the cavity. The Region B and C fields are observed only when plasma is observed. The occurrence of Region B fields coincides with both a different degree of magnetic activity on the earth's surface and a different position of the dipole relative to the solar stream than the A or C fields. This double correlation complicates interpretation as the relative importances are not separable.

World-wide changes in the magnetic field at the earth's surface characterized by small increases in the horizontal component are found to correlate with field changes at the satellite.

A change in field intensity at the satellite occurring 0 to 7 minutes after a SC at the earth's surface is identified as a SC effect. However, the direction of the field vector up to half an hour after the SC followed a slow shift in orientation that began abruptly 2 hours before the SC in coincidence with an abrupt change in the magnetic field at high latitudes at the earth's surface. This feature and others present questions regarding the possible importance of particles with energies greater than those measured suggest that these particles may arrive in advance of the lower energy plasma.

The cavity characteristics indicated by the measurements do not agree in detail with theoretical cavity models. Agreement might be obtained if it were assumed that the average solar stream was incident from a direction slightly to the west of the sun and above the ecliptic plane or if there was an intermittent component of the flow from this direction. Alternatively, agreement should probably not be expected as the theoretical models do not take into account the existence of a magnetic field outside the cavity.

On various grounds the fields measured external to the geomagnetic cavity are interpreted as fields of solar-interplanetary origin. Uncertainties arise in estimating the extent to which these fields are influenced by the proximity to the cavity.

The tendency for a given field condition to persist for fractions of an hour to several hours, which appears both as a movement of the cavity across the trajectory (typically transitions between Region A and Region C fields) and as disruptions of the Region B fields during a 12-hour period when plasma is always present, is interpreted in terms of structure in the solar wind. Dimensions of this structure would typically be of the order 0.01 AU. Arguments tend to favor the view that these structures may be filamentary extensions of coronal rays, but this is only one of several possibilities.

In addition to the points just cited, alternatives in interpretation have been noted to emphasize the lack of uniqueness that ensues from the limited state of knowledge of the interactions of plasma with weak magnetic fields, and from the restrictions of measurement along a single trajectory.

REFERENCES

1. Heppner, J. P., Ness, N. F. et al., "Magnetic Field Measurements with the Explorer X Satellite", in: *Proc. Internat. Conf. on Cosmic Rays and the Earth Storm, Kyoto, September 1961. II. Main Sessions,* Tokyo: Physical Society of Japan, 1962, pp. 546-552.

2. Ness, N. F., Skillman, T. L., et al., "Magnetic Field Fluctuation on the Earth and in Space", in: *Proc. Internat. Conf. on Cosmic Rays and the Earth Storm, Kyoto, September 1961. II. Main Sessions,* Tokyo: Physical Society of Japan, 1962, pp. 27-33.

3. Bridge, H. S., Dillworth, C., et al., "Direct Observations of the Interplanetary Plasma," in: *Proc. Internat. Conf. on Cosmic Rays and the Earth Storm, Kyoto, September 1961. II. Main Sessions,* Tokyo: Physical Society of Japan, 1962, pp. 553-560.

4. Finch, H. F., and Leaton, B. R., "The Earth's Main Magnetic Field—Epoch 1955.°," *Monthly Not. Roy. Astronom. Soc., Geophys. Suppl.* 7(6):314-317, November 1957.

5. Cain, J. C., Shapiro, I. R., et al., "Measurements of the Geomagnetic Field by the Vanguard III Satellite," NASA Technical Note D-1418, 1962.

6. Bridge, H. S., Bonetti, A., et al., "Explorer X Plasma Measurements," Paper presented at the 3rd Internat. Space Sci. Sympos., Washington, May 1962.

7. Dolginov, S. SH., and Pushkov, N. V., "On Some Results of Magnetic Field Investigations in Space," Paper presented at the 3rd Internat. Space Sci. Sympos., Washington, May 1962.

8. Dolginov, S. SH., Eroshenko, E. G., et al., "Magnetic Measurements with the Second Cosmic Rocket," in: *Artificial Earth Satellites,* 5:490-502, New York: Plenum Press, 1961.

9. Heppner, J. P., Stolarik, J. D., et al., "Project Vanguard Magnetic Field Instrumentation and Measurements," in: "Space Research," *Proc. 1st International Space Science Symposium, Nice, January 1960:* Amsterdam; North-Holland Publ. Co., 1960, 982-99.

10. Cain, J. C., Stolarik, J. D., et al., "Vanguard III Magnetic-Storm Measurements," Paper presented at 43rd annual meeting Amer. Geophys. Union, April 1962.

11. Cahill, L. R., "Study of the Outer Geomagnetic Field: Explorer XII," Paper Presented at the 3rd Internat. Space Sci. Sympos. Washington, May 1962.

12. Davis, L. R., "Low-Energy Trapped Protons," Paper presented at 43rd annual meeting Amer. Geophys. Union, April 1962.

13. Davis, L. R., "Low-Energy Trapped Protons," Paper presented at 43rd annual meeting Amer. Geophys. Union, April 1962.

14. Rossi, B., "Interplanetary Plasma" Paper presented at American Physical Society Meeting, New York, January 1962.

15. Smith, E. J., Coleman, P. J., et al., "Characteristics of the Extraterrestrial Current System: Explorer VI and Pioneer V," *J. Geophys. Res.* 65(6):1858-1861, June 1960.

16. Nishida, A., and Jacobs, J. A., "World-Wide Changes in the Geomagnetic Field," *J. Geophys. Res.* 67(2):525-540, February 1962.

17. Brown, R. R., Hartz, T. R., et al., "Large-Scale Electron Bombardment of the Atmosphere at the Sudden Commencement of a Geomagnetic Storm," *J. Geophys. Res.* 66(4):1035-1041, April 1961.

18. Hoffman, R. A., Davis, L. R., and Williamson, J. M., "0.1 to 5 Mev Protons and 50 Kev Electrons at 12 Earth Radii during Sudden Commencement on September 30, 1961," Paper presented at 43rd annual meeting *Amer. Geophys. Union*, Washington, April 1962.

19. Bryant, D. A., Cline, T. L., et al., "Cosmic Ray Observation in Space," Paper presented at the 3rd Internat. Space Sci. Sympos. Washington, May 1962.

20. Chapman, S., and Bartels, J., "Theories of Magnetic Storms and Aurorae" in *Geomagnetism,* Oxford: Clarendon Press, 1940.

21. Dungey, J. W., "The Steady State of Champam-Ferraro Problems in Two Dimensions," *J. Geophys. Res.* 66(4):1043-1047, April 1961.

22. Spreiter, J. R., Briggs, B. R., "Theoretical Determination of the Form of the Hollow Produced in the Solar Corpuscular Stream by Interaction with the Magnetic Dipole Field of the Earth," NASA Technical Report R-120, 1961.

    , Theoretical Determination of the Form of the Boundary of the Solar Corpuscular Stream Produced by Interaction with the Magnetic Dipole Field of the Earth," *J. Geophys. Res.* 67(1):37-51, January 1962.

23. Wilson, C. R., and Sugiura, M., "Hydromagnetic Interpretation of Sudden Commencements of Magnetic Storms," *J. Geophys. Res.* 66(12):4097-4111, December 1961.

24. Davis, T. N., "The Morphology of the Auroral Displays of 1957-1958. 2. Detail Analyses of Alaska Data and Analyses of High-Altitude Data," *J. Geophys. Res.* 67(1):75-110, January, 1962.

25. Chapman, S., and Ferraro, V. C. A., "A New Theory of Magnetic Storms. I. The Initial Phase," *J. Geophys. Res.* 36(2):77-97, June 1931; *J. Geophys. Res.* 36(3):171-186, September 1931; *J. Geophys. Res.* 37(2):146-156, June 1932; *J. Geophys. Res.* 37(4):421-429, December 1932.

, "A New Theory of Magnetic Storms. II. The Main Phase," *J. Geophys. Res.* 38(2): 79-96, June 1933.

26. Chapman, S., "Idealized Problems of Plasma Dynamics Relating to Geomagnetic Storms," *Rev. Modern Physics* 32(4):919-933, October 1960.

27. Ferraro, V. C. A., "Theory of Sudden Commencements and of the First Phase of a Magnetic Storm," *Rev. Modern Physics* 32(4):934-940, October 1960.

, "On the Theory of the First Phase of a Geomagnetic Storm: A New Illustrative Calculation Based on an Idealised (Plane not Cylindrical) Model Field Distribution," *J. Geophys. Res.* 57(1):15-49, March 1952.

, "An Approximate Method of Estimating the Size and Shape of the Stationary Hollow Carved Out in a Neutral Ionized Stream of Corpuscles Impinging on the Geomagnetic Field," *J. Geophys. Res.* 65(12):3951-3953, December 1960.

28. Zhigulev, V. N., "O iavlenii magnitnogo 'otzhatiia' potoka provodiashchei sredy," *Akademiia Nauk SSSR. Doklady* 126:521-523, 1959; and References cited therein.

29. Beard, D. B., "The Interaction of the Terrestrial Magnetic Field with the Solar Corpuscular Radiation. 2. Second-Order Approximation." *J. Geophys. Res.* 67(2):477-483, February 1962.

30. Hurley, J., "Interaction of a Streaming Plasma with the Magnetic Field of a Two-Dimensional Dipole," *Physics of Fluids* 4(7):854-859, July 1961.

31. Slutz, R. J., "The Shape of the Geomagnetic Field Boundary under Uniform External Pressure," *J. Geophys. Res.* 67(2):505-513, February 1962.

32. Midgley, J. E., and L. Davis, "Computation of the Bounding Surface of a Dipole Field in a Plasma by a Moment Technique," *J. Geophys. Res.* 67(2):499-504, February 1962.

33. Dungey, J. W., "The Interplanetary Field and Auroral Theory," in: *Proc. Internat. Conf. on Cosmic Rays and the Earth Storm, Kyoto, September 1961.* II. *Main Sessions,* Tokyo: Physical Society of Japan. 1962 pp. 15-19.

34. Parker, E. N., "Interaction of the Solar Wind with the Geomagnetic Field," *Physics of Fluids* 1(3):171-187, May-June 1958.

35. Parker, E. N., "Dynamics of the Interplanetary Gas and Magnetic Fields," *Astrophys. J.* 128(3): 664-676, November 1958.

36. Parker, E. N., "Sudden Expansion of the Corona Following a large Solar Flare and the Attendant Magnetic Field and Cosmic-Ray Effects," *Astrophys. J.* 133(3):1014-1033, May 1961.

37. Gold, T., "Plasma and Magnetic Fields in the Solar System," *J. Geophys. Res.* 64(11):1665-1674, November 1959.

38. McCracken, K. G., "The Cosmic-Ray Flare Effect. 3. Deductions Regarding the Interplanetary Magnetic Field," *J. Geophys. Res.* 67(2):447-458, February 1962.

39. Slee, O. B., "Observations of the Solar Corona out to 100 Solar Radii," *Monthly Not. Royal Astronom. Soc.* 123(3):223-231, 1961.

40. Coleman, P. J., Davis, L., and Sonett, C. P., "Steady Component of the Interplanetary Magnetic Field: Pioneer *V*," *Phys. Rev. Letters* 5(2):43-46, July 15, 1960.

41. Greenstadt, E. W., "Magnetic Storms in Interplanetary Space as Observed by Pioneer V," *Nature* 191(4786):329-331, July 22, 1961.

42. Coleman, P. J., Sonett, C. P., and Davis, L., "On the Interplanetary Magnetic Storm: Pioneer V," *J. Geophys. Res.* 66(7):2043-2046, July 1961.

43. Sonett, C. P., "Hyperwaves, Shock-Like Phenomena in the Outer Exosphere," in: *Proc. Internat. Conf. on Cosmic Rays and the Earth Storm, Kyoto, September 1961.* II. *Main Sessions,* Tokyo: Physical Society of Japan. 1962, pp. 528-531.

44. Kellog, P. J., "Flow of Plasma Around the Earth," *J. Geophys. Res.* 67(10):3805-3811, September 1962.

THE ORBITING SOLAR OBSERVATORY SPACECRAFT

by

F. P. Dolder, O. E. Bartoe,

R. C. Mercure, Jr., and R. H. Gablehouse

Ball Brothers Research Corporation,

Boulder, Colorado

and

J. C. Lindsay

Goddard Space Flight Center

SUMMARY

The first Orbiting Solar Observatory (1962 ζ1) was launched March 7, 1962, at 1606 UT from the Atlantic Missile Range, Cape Canaveral, Florida. This spacecraft was designed to point approximately 75 pounds of instruments at the sun with an accuracy of about 1 minute of arc. An additional 100 pounds of instruments are carried in a spinning section of the satellite which sweeps across the sun every 2 seconds. The total weight of the spacecraft is 458.3 pounds. In orbit, it is 92 inches in diameter and 37 inches in height. It carries data recording equipment that can store 90 minutes of data. Upon ground command, these data are played back over the spacecraft's transmission system in 5 minutes. The spacecraft is in an almost perfect 300-nautical-mile circular orbit inclined 32.8 degrees to the equator, and has worked perfectly since injection into orbit; at the present writing it has completed over 1000 orbits. The pointing system has functioned with an accuracy of approximately 2 minutes in azimuth angle and 2.5 minutes in elevation. The temperature inside the satellite has stabilized to 5°C; and excellent radio transmission has been received.

INTRODUCTION

Since the development of the high-altitude sounding rocket it has been possible for scientists to observe the sun from outside the main portion of the earth's atmosphere; however, sounding rockets allow only a fleeting glimpse of the sun and extended observations have not been possible. With the advent of the earth orbiting satellite, it was quickly recognized that long-term unimpeded solar observation was possible. One of the early programs initiated by NASA was the development of an Orbiting Solar Observatory to furnish an observing platform for solar studies. On March 7, 1962, at 1606 UT, OSO I (1962 ζ1) was launched from the Atlantic Missile Range by a Thor-Delta vehicle.

The OSO I spacecraft was designed to point approximately 75 pounds of instruments at the sun with an accuracy of about 1 minute of arc. An additional 100 pounds of instruments are carried in a spinning section of the satellite and sweep across the sun every 2 seconds.

The total weight of the spacecraft is 458.3 pounds; with the arms extended (Figure 1) it is 92 inches in diameter, 37 inches in height, and consists of two portions—the "wheel," the lower nine-sided cylinder with three arms attached; and the "sail," the fan-shaped structure mounted above the wheel, which carries the pointed instruments and the solar cell array. The sail is attached to the wheel by a shaft running through the wheel; the wheel is free to rotate with respect to the sail.

In order to provide attitude stability, the wheel is kept spinning at 30 rpm. This spin rate is measured by optical rate sensors and is controlled to within ± 5 percent by reaction jets (Figure 2) which use compressed N_2 gas. (The N_2 gas supply carried by the spacecraft is calculated to last at least six months.) The angular momentum of the spinning wheel produces great gyroscopic rigidity and the spin axis tends to remain fixed in inertial space. Although there are various disturbing torques which tend to precess the satellite, the precession rate is less than a degree per day. The angle between the solar vector and the spin axis is measured by optical error detectors; whenever the angle exceeds 3 degrees, a second set of reaction jets is used to precess the satellite until the pitch error is corrected. The spacecraft is free to precess in roll about the solar vector, but this rate is small.

The sail is free to rotate about the spin axis and is controlled by optical error sensors so that, during the sunlit portion of the orbit, the plane of the sail is perpendicular to the solar vector; this is accomplished by a servo motor on the sail's shaft which drives against the wheel (the azimuth
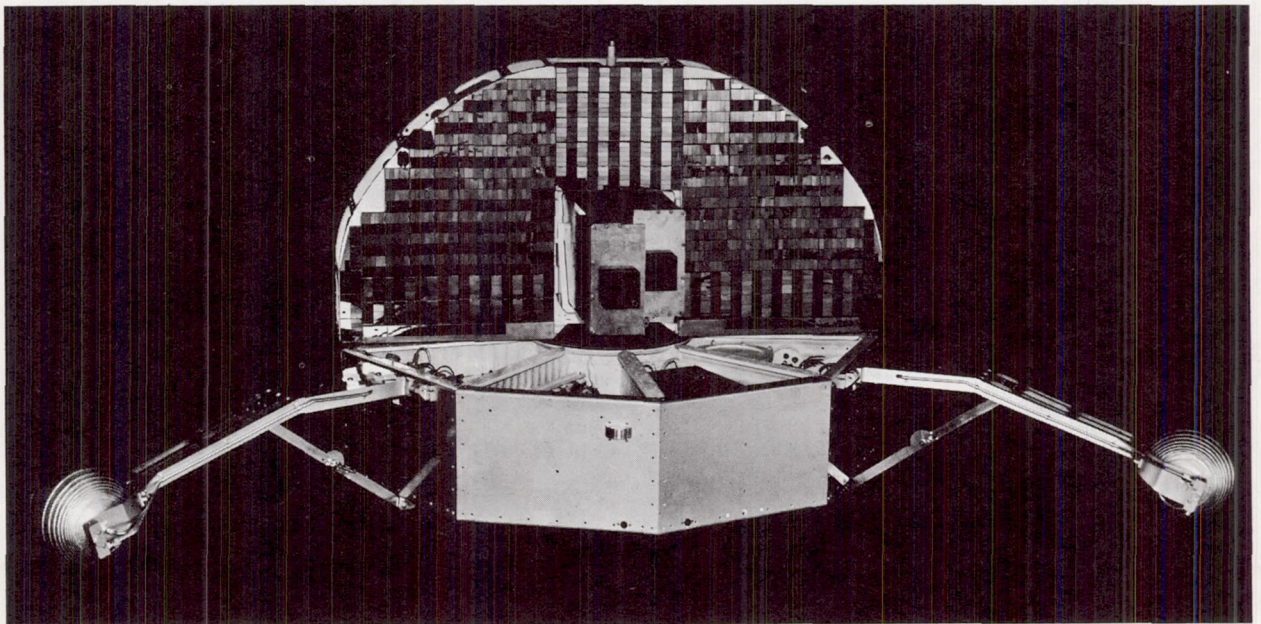

Figure 1—Rear view of the first Orbiting Solar Observatory (OSO I)
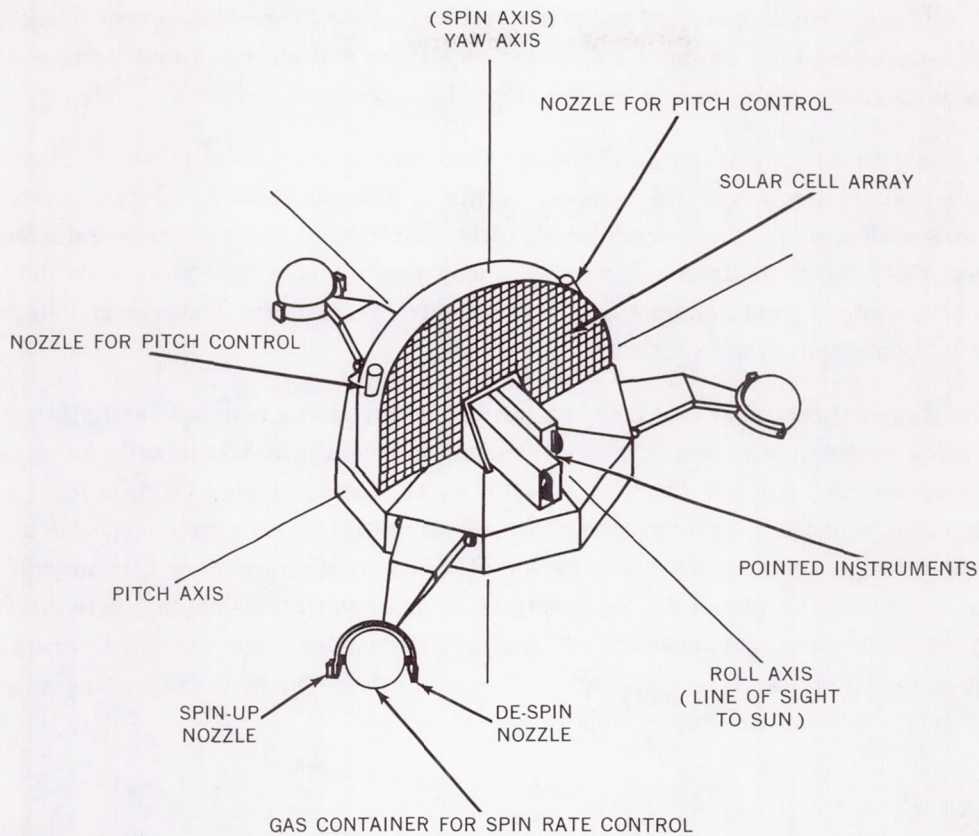
Figure 2—Attitude axes of the Orbiting Solar Observatory

servo). The accuracy of this alignment is 1 to 2 minutes of arc. In the center of the sail is a gimbal which is free to move in pitch with respect to the sail. The pointed experiments are carried in this gimbal. A second servo motor (the elevation servo), on the gimbal shift, is optically controlled to align the instruments to the sun, again with an accuracy of 1 to 2 minutes of arc. The servo systems derive their error signals from two sets of photoelectric sensors: one set mounted on the pointed instruments, and the second on the sail. The set mounted on the instruments senses the angles between the direction in which the instruments are pointing and the sun, producing a current output proportional to these angles; these detectors have limited fields of view but can measure angles of less than 1 minute. The set mounted on the sail is used to control the sail so that it is pointed at the sun within a few degrees. When this has been done, control is switched to the instrument detectors which will have the sun in their field of view. During the dark portion of each orbit, the servo systems are automatically turned off by a photoelectric switch; the sail is then allowed to spin with the wheel.

Each time the satellite passes from the dark to the sunlit portion of the orbit, the photoelectric switch turns on the servo systems. The azimuth servo stops the sail and aligns it so that the solar vector is normal to the plane of the sail. This is done under the control of the error detectors mounted on the sail. When the error detectors which are mounted on the instrument have the sun in

their field of view, control is switched from the sail detectors to the instrument detectors. These detectors then control both the azimuth and elevation servos and align the instruments accurately to the sun. This acquisition cycle takes approximately 45 seconds.

The azimuth and elevation servo systems are designed to use a total power of less than 4 watts (including the power used to drive the motors). This is accomplished by driving the azimuth and elevation motors with a pulse-width modulated power amplifier. The motors are driven by pulses which are always of maximum drive voltage but whose width varies depending upon the torque level required from the motor. This scheme eliminates power losses in the power transistors controlling the motors, since they are either saturated or cut off.

Low power consumption also requires that all bearings, motor brushes, and slip rings have very low friction. This presents a problem, since these components would ordinarily be sealed to protect them from the space environment; however, sealing results in too high a friction level and hence in higher power requirements. To overcome this, all slip rings, motor brushes, and bearings are operated exposed to the space environment. One of the most significant achievements during the OSO I development was the perfecting of treatments for these components which allow them to operate when exposed to the low pressure of the space environment for extended periods of time and still maintain acceptably low friction levels. The treatments have no outgassing products which might contaminate the scientific experiments.

EXPERIMENTS

The pointed instrument gimbal can carry 75 pounds of experiments in a space 38 x 8 x 8 inches. The OSO I spacecraft carries two pointed instruments which have a combined weight of 65.5 pounds. One is a 20.5 pound x-ray spectrometer which covers the spectral range from 30 to 400A. The second instrument, which weighs 45 pounds, consists of several different experiments: solar x-ray (20 to 100 kev and 1 to 8A) monitoring experiments, a gamma ray (0.510 Mev) monitoring experiment, an interplanetary dust particle experiment, and an experiment designed to monitor the aging of the photoelectric error sensors used in the spacecraft's servo system.

There are nine wedge-shaped compartments in the wheel. Of these, five are normally available for scientific instruments; a total weight of about 100 pounds can be accommodated. The other four compartments in the wheel are for the spacecraft's control, telemetry, data storage, and command systems; in OSO I, a sixth experiment shares one of these four compartments. The six experiments were furnished by the Goddard Space Flight Center and Ames Research Center of NASA, the University of Rochester, the University of California, and the University of Minnesota. The locations of these experimental packages and a brief description of each are shown in Figure 3. The total weight of the six wheel experiments in OSO I is 113 pounds.

Since the wheel spins at 30 rpm and its spin axis is normal to the solar vector, each experiment in the wheel sweeps the sun every 2 seconds. Also, the spacecraft slowly rolls about the solar vector because of external torques and hence, over a period of time, each wheel experiment will be able to

UNIVERSITY OF MINNESOTA
INTENSITY AND ANGULAR DISTRIBUTION
OF GAMMA RAYS (0.1-5 Mev)
WEIGHT 31.5 lb POWER 0.6 w

AMES RESEARCH CENTER
SURFACE EROSION STUDIES
WEIGHT 1.7 lb POWER 0.1 w

UNIVERSITY OF
CALIFORNIA
PROTON FLUX
ANALYZER ($E_p = 2$ Mev)
ELECTRON FLUX
ANALYZER ($E_e = 60$ kev)
WEIGHT 83 lb POWER 0.2 w

UNIVERSITY OF
CALIFORNIA
NEUTRON FLUX
MEASUREMENT
WEIGHT 26.2 lb Power 0.3 w

UNIVERSITY OF ROCHESTER
HIGH ENERGY GAMMA RAYS
(ABOVE 100 Mev)
WEIGHT 16.8 lb POWER 1.1 w

GODDARD SPACE FLIGHT CENTER
SOLAR RADIATION (4080-9800A)
GAMMA RAY ENERGIES (0.2-1.5 Mev)
SOLAR ULTRAVIOLET AND X RAY (1100-1205A)
WEIGHT 28.5 lb POWER 1.0 w

Figure 3—Experiments in the OSO I wheel

scan the entire celestial sphere. This is extremely useful for experiments that are intended to survey the sky or to compare the radiations and emissions of the sun with those from other regions of space.

The **OSO I** solar cell array delivers approximately 30 watts of power at 20 volts to the spacecraft during the time it is oriented to the sun. This power is used to operate the control system, telemetry, and experiments during the day, and to charge the nickel-cadmium batteries. During the dark period, the telemetry and wheel experiments operate from the storage batteries. Of the 30 watts, approximately 15 are used by the control and telemetry systems and 13 by the experiments; this allows 2 watts as a safety margin.

The telemetry system is FM-FM and has eight channels; six channels are assigned to the scientific experiments, one is used for monitoring the spacecraft's operation, and one is used for a reference oscillator. Each experimenter is assigned a channel. The output of each experiment is conditioned to 0 to 5 volts and is used to deviate a subcarrier oscillator. The outputs of the eight subcarrier oscillators are combined and then recorded by a magnetic tape recorder in the spacecraft that can record for 90 minutes. The reference oscillator referred to above is used for wow and flutter compensation of the tape recorder. Upon command from the ground, the tape can be played back in 5 minutes. When the tape is played back, the recorder output modulates a high power (1.75 watts)

FM transmitter. In the record mode, data are being stored on tape and the signals are also used to modulate a low power (250 milliwatt) transmitter so that real-time information is available. Each part of the telemetry system—subcarrier oscillators, tape recorders, and transmitters—is duplexed in the spacecraft; the spares can be substituted by ground command if the unit in operation fails.

Because of the increased speed of playback, the information rate into the tape recorder is limited. A total of 17.5 cps (square wave) of information bandwidth is available to the experimenters. On OSO I, this was divided as shown in Table 1. Even with these seemingly small data rates, a large amount of data is being collected by the experiments on OSO I.

Table 1
Telemetry Allocations for OSO I

Experiment	Bandwidth
Goddard X-ray Spectrometer	6
Goddard Gamma Ray Experiment	4
University of California Proton, Electron, and Neutron Experiment	3
University of Rochester Gamma Ray Experiment	2
Goddard Gamma Ray, X-ray, and Interplanetary Dust Experiment	1.5
University of Minnesota Gamma Ray Experiment	1
Spacecraft Monitoring Channel	1

The OSO I is equipped with a tone-type command system capable of accepting 10 commands which are used to initiate playback from the tape recorder, to interchange parts of the telemetry system, and to turn either all the wheel experiments or all the pointed experiments on or off. These last two commands are incorporated so that if too much power is being used or if the power supply is not developing the proper amount of power, the experiments can be turned off to allow the batteries to be charged and then turned on again.

The spacecraft's temperature is controlled passively by means of the absorptivity/emissivity ratio of the surface. This is done by either covering the various surfaces with paint having the proper ratio, or by highly polishing the surfaces. In order to find the correct ratio, a detailed mathematical analysis was made and the effects of changing the surface characteristics of the spacecraft were simulated on a digital computer.

SPACECRAFT PERFORMANCE

The actual performance of OSO I has been most gratifying. The spacecraft is in an almost perfect 300-nautical-mile circular orbit, inclined 32.85 degrees to the equator; the period is 96.15

minutes. At the time of injection, the spacecraft acquired the sun, and all control systems and experiments worked perfectly. At the present writing, the spacecraft has completed over 1000 orbits and a preliminary analysis has shown all spacecraft systems and all experiments to be functioning properly.

The pointing accuracy in azimuth (about the spin axis) has ranged from 0.5 to 1.8 minutes of arc. The power required to drive the azimuth motor is approximately 3 watts, slightly more than was expected. Figure 4 shows the observed azimuth error angle and the azimuth drive power.

The elevation error has ranged as high as 2.5 minutes of arc and the elevation drive power has been as high as 4 watts. This is also slightly higher than was anticipated, and is attributed to excessive torque on the instruments from two flexible electric cables from the instruments to the spacecraft's sail. These cables are colder than was anticipated and it is believed that they have become stiffer. Figure 4 shows the pitch angle of the spacecraft and the variation of the elevation error angle and drive power with time.

The rate of consumption of N_2 gas used to control the pitch angle and the spin rate is quite low. The spacecraft was injected into orbit with a pitch angle of about 3.5 degrees. The pitch control system corrected this to -1.0 degree, as it was designed to do, immediately after injection. No additional pitch gas was used until orbit 233, when again the pitch angle had increased to the allowable limit of 3 degrees. This amounted to a precession of about 0.25 degree per day. A third pitch correction was made during orbit 329. Between orbits 233 and 329, the precession rate averaged 0.67 degree per day. The rate of change of the pitch angle is expected to vary with time, since it is a function of the angle between the spin axis and the plane of the ecliptic. When the spin axis is normal to the ecliptic plane, there is no change in pitch attitude as the earth goes around the sun. When the spin axis is contained in the ecliptic plane the pitch, if not corrected, will change about 1 degree per day because of the earth's motion around the sun. With the observed rate of N_2 gas exhaustion, the gas supply should last more than six months.

The solar power supply appears to be working very well. The nickel-cadmium batteries are being properly charged and their voltage ranges from 20.4 volts at the end of the day to 18.5 volts at the end of the night. This voltage swing is as expected and indicates that the batteries are not being severely discharged during the night. The solar cell array is running slightly cooler than was expected, increasing the solar cell output by between 1 and 2 watts; therefore, the batteries are being kept well charged. Inside the wheel the temperature is 5°C, which compares very well with the design temperature, and is essentially constant throughout the orbit. The temperature excursions of the outer panels of the wheel do not exceed 12°C throughout the orbit. Thirty orbits were required to reach temperature equilibrium. The highest temperature reached on the solar cell array during the day is 60°C and at night the sail cools down to −38°C. The solar cell panel's rate of change of temperature as the spacecraft enters the sunlight is about 7 degrees per minute. A temperature monitor inside the Goddard x-ray spectrometer indicates a temperature of about 7°C with only about ±1 degree change over the orbit.

The FM-FM telemetry system of the spacecraft has been most satisfactory. The signals received at the ground stations during tape recorder playback have been strong and clean. A record
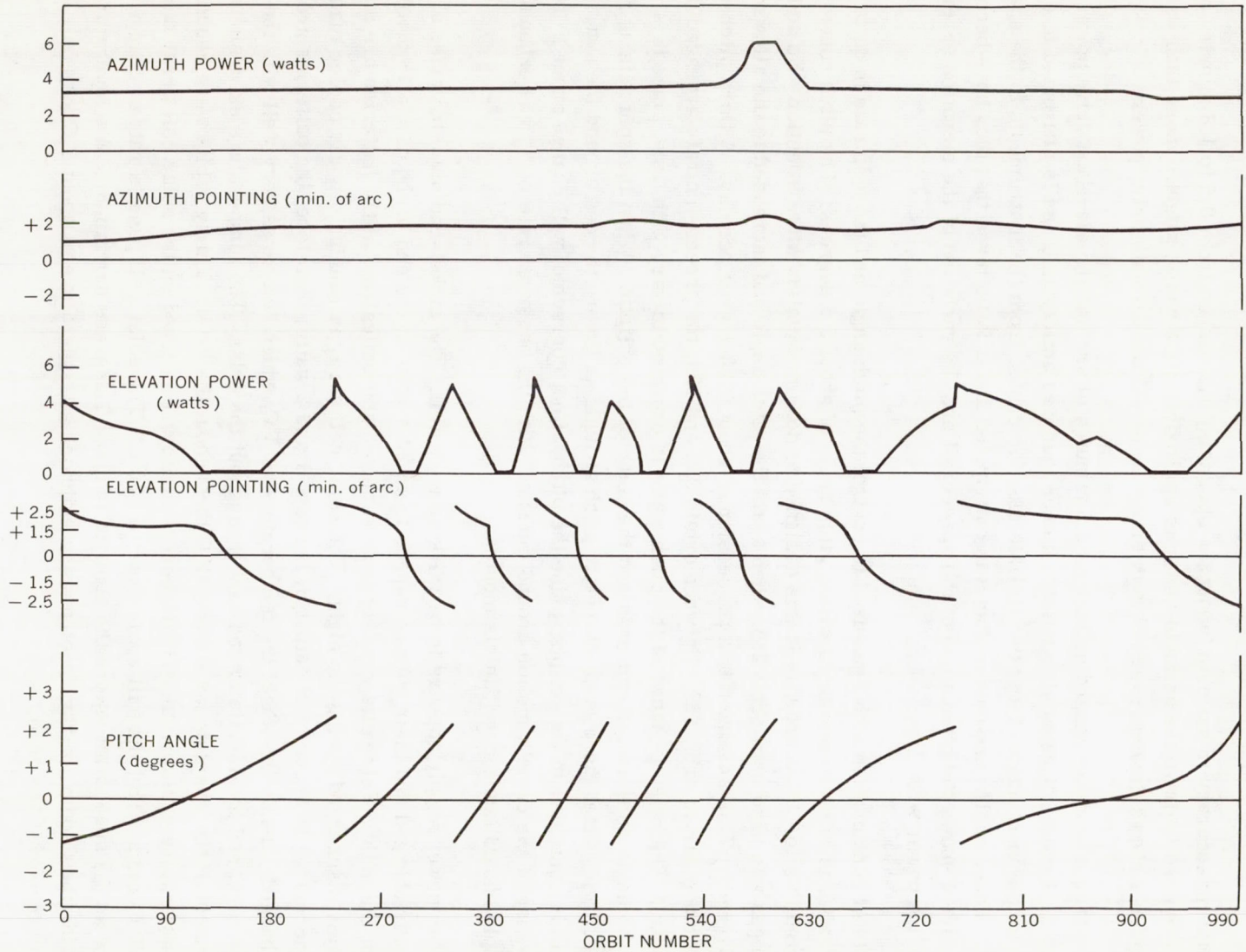
Figure 4—OSO I azimuth error angles

of a data transmission received at the Fort Myers, Florida, station compares favorably with one made in the laboratory during spacecraft checkout. It is possible to receive real-time data transmissions from the spacecraft in Boulder, Colorado. The signal is sufficiently good that information concerning the operation of the spacecraft and the experiments is routinely being gathered at Boulder.

The OSO I command system is functioning properly but has been found quite susceptible to spurious commands. This was not unexpected, since the same type of trouble occurred with the Explorer XI (1961 ν1) which has the same command system. Because of this possibility, the commands were structured so that nothing catastrophic to the spacecraft could occur if the command system did accept spurious commands. This difficulty has been an annoyance but has not compromised the spacecraft's operation.

SUMMARY

In summary, the OSO I was designed to provide a stabilized observing platform above the earth's atmosphere from which scientific observations of the sun and space could be performed. It is the first of a series of orbiting observatories which will progressively become more sophisticated, versatile, and useful. Operating experience with the OSO I has already given an observing time equivalent to that which would require nearly 10,000 Aerobee-Hi sounding rocket flights, at a fraction of the cost of such a rocket program. The first Orbiting Solar Observatory has successfully performed its mission and has ushered in a new era in astronomy and astrophysics.

COSMIC RAY EXPERIMENTS FOR EXPLORER XII (1961υ) AND THE ORBITING GEOPHYSICAL OBSERVATORY

by

George H. Ludwig and Frank B. McDonald

Goddard Space Flight Center

SUMMARY

The cosmic ray experiment on Explorer XII consisted of a Geiger counter telescope, a thin *CsI* scintillation counter, and a large-area scintillation counter telescope. The thin scintillation counter was connected to an 8-level integral analyzer. The large-area scintillation counter telescope, which measured the energy loss of the detected particle, was fed to a 32 channel differential pulse height analyzer with a storage capacity of 65,535 counts per channel. Both the Geiger counter telescope and single counter rates were telemetered. All information was multiplexed onto a single channel. Details of the instrumentation and the methods of encoding are discussed herein.

For the first Orbiting Geophysical Observatory mission, a new scintillation counter telescope has been developed which measures both energy loss and total energy. This furnishes excellent charge and energy resolution over an energy range from about 11 to 90 Mev per nucleon. Design details of this telescope and its associated electronic instrumentation are also presented.

INTRODUCTION

Measurements of the primary cosmic ray charge and energy spectra have been conducted for some time by means of balloon-borne instruments and nuclear emulsions. These measurements have been confined to the energy range above 65 Mev/nucleon since the lower energy particles cannot penetrate the atmosphere above the balloon, and thus cannot reach the detectors. Rocket probes could carry the instruments farther from the earth to extend these investigations to lower energies; however, the cosmic ray flux is so low that adequate data could not be accumulated during the brief trajectory to yield statistically meaningful results. The high apogee satellite offers the first good chance to investigate the lower energy region of the cosmic ray spectrum. Such a satellite must place the instruments well outside the earth's high intensity radiation belts for an appreciable period of time.

THE EXPLORER XII EXPERIMENT

Explorer XII (1961ν) was launched on August 16, 1961, into an orbit having an initial geocentric apogee of 83,600 km and perigee of 6700 km. This satellite contained a detector to investigate the energy spectrum of the total primary cosmic ray flux in the range from 3 to greater than 600 Mev/nucleon. It consisted of three detector arrays: a scintillation detector employing a thin crystal to investigate the spectrum in the 3 to 80 Mev/nucleon range; a double scintillator telescope array to perform a detailed differential analysis of the 100 to 600 Mev/nucleon portion; and a Geiger-Mueller counter telescope to measure protons having energies greater than about 28 Mev.

The Single Scintillation Detector

The configuration of the thin, single crystal detector is shown in Figure 1. A *CsI (Tl)* crystal 0.5 gm/cm² thick was used. A collimator was located around the crystal to define the geometry for all protons having energies less than about 400 Mev. The crystal was viewed by an RCA type C-7151 photomultiplier (PM) tube, which is a ruggedized version of the RCA 6199 tube. The detector was calibrated continuously by a small Pu²³⁹ alpha particle source mounted on the crystal; these particles lose about 3.5 Mev in the crystal. The high voltage power supply was located at the base of the PM tube. The complete assembly was encapsulated to form a rugged assembly capable of withstanding the launch environment and of operating throughout the pressure transition from one atmosphere to vacuum.

The characteristics of the detector are shown in Figure 2. Protons which enter the crystal through the thin foil (6.5 mg/cm² aluminum) and lose all their energy in the crystal fall along the curve A. The point of intersection of curves A and B represents particles which pass completely through the crystal but lose all their energy in the process. More energetic protons fall along curve B. As the particles become more and more energetic, less and less energy is lost due to the decreasing rate of energy loss. Minimum ionizing protons fall on the high energy, zero slope portion of the curve.
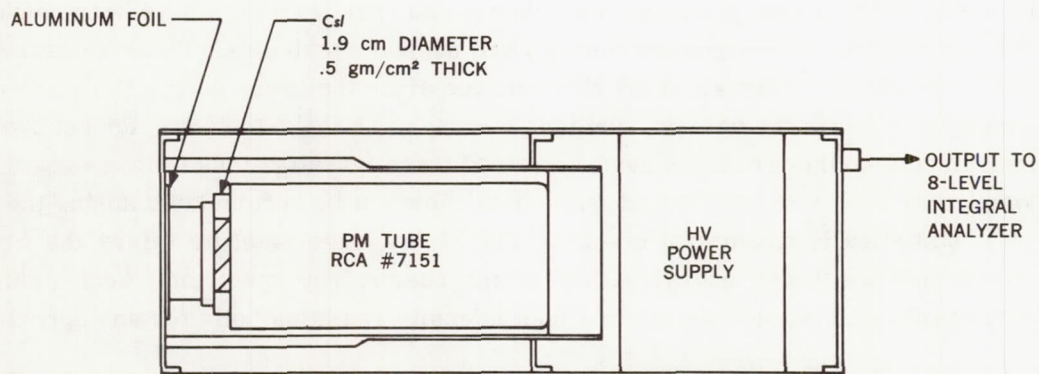

Figure 1—The thin scintillator counter assembly
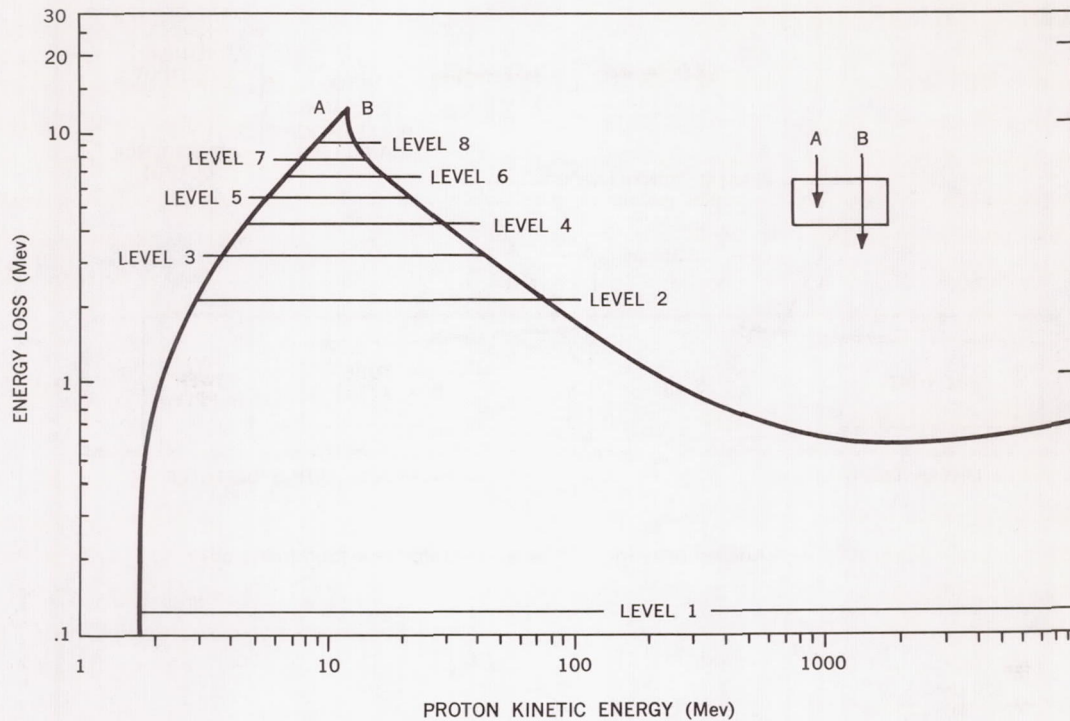
Figure 2—Proton energy loss in the thin scintillator as a function of energy

An eight-level integral pulse height analyzer was used with the detector; the pulse height thresholds are indicated in Figure 2. For each setting, all events resulting in an energy loss in the crystal greater than the threshold value were counted. Thus, all events counted while the analyzer was on level eight corresponded to protons of 9.4 to 13 Mev, all events counted on level seven to protons of 8 to 14 Mev, and so on. From a combination of this information with that from the other detectors and our previous knowledge of the spectrum, it is possible to determine the spectral distribution of particles down to approximately 3 Mev per nucleon.

The Double Scintillator Telescope

Since the amount of absorbing material needed to define the geometry for higher energy particles is excessive for use in satellites, a double scintillator telescope array (Figure 3) was employed for these particles. Two 0.975 gm/cm² disc shaped plastic scintillators were used in a telescope array having a geometric factor of 13.6 cm²-ster. The pulse from scintillator B was analyzed when a particle passed through scintillator A and into or through scintillator B. A curve similar to the one (Figure 2) for the single scintillator existed for this B scintillator — the protons which entered but did not penetrate the scintillator fell along an ascending curve A, and those which penetrated fell along a curve B.

The analysis of these events was performed by a 32 channel differential pulse height analyzer with a magnetic core memory. Figure 4 shows a spectrum obtained from this instrument during its flight.
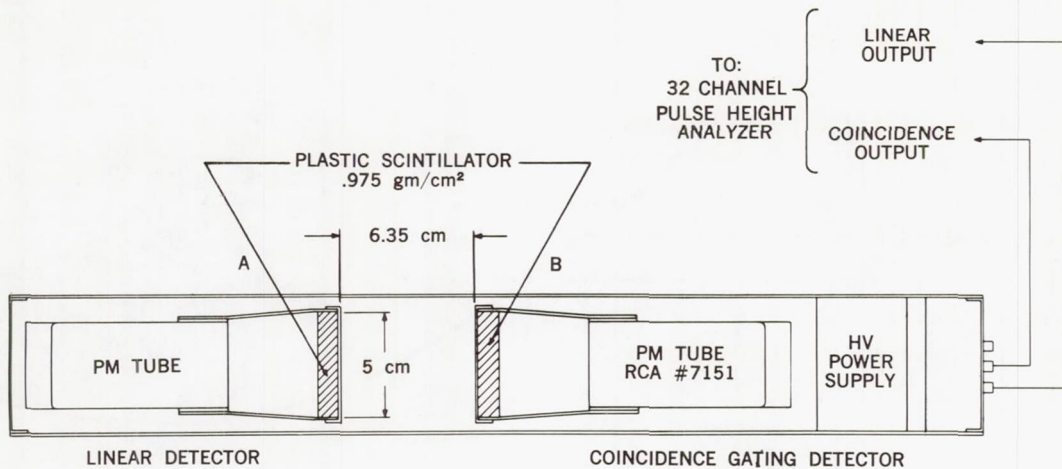
Figure 3—Outline drawing of the scintillator telescope assembly
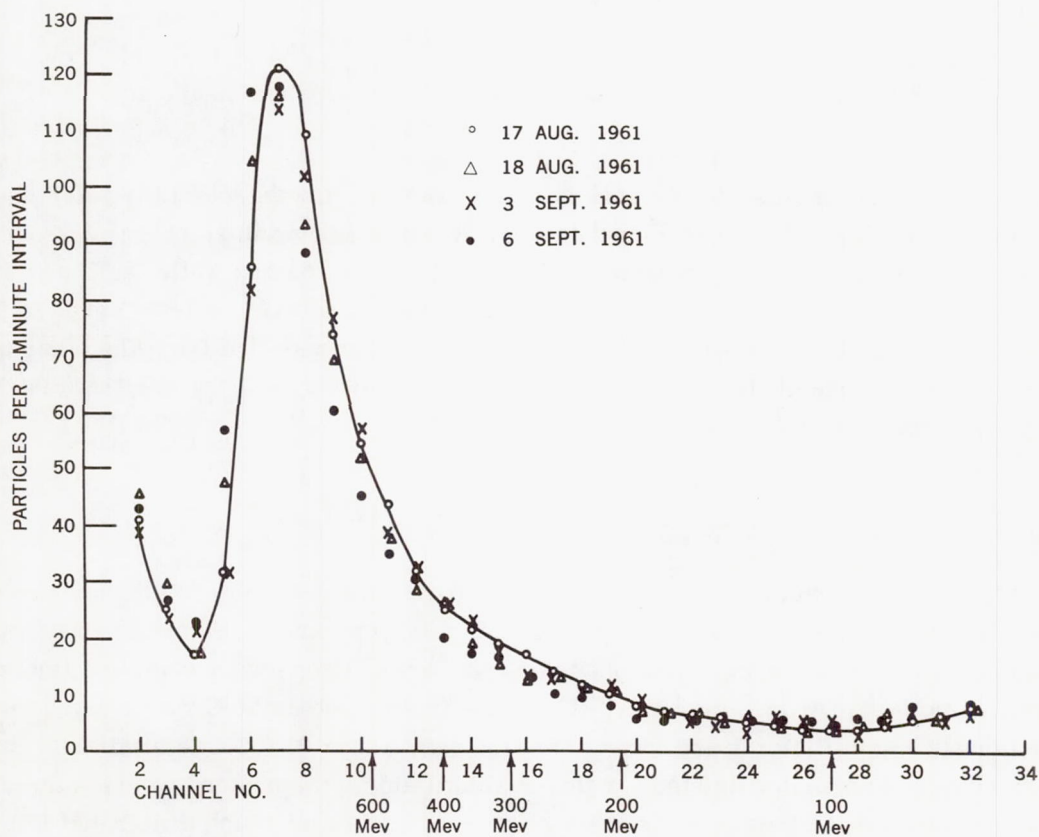
Figure 4—Scintillator telescope pulse height distributions obtained on four days during the flight of Explorer XII. The energies of protons which pass completely through the crystal and the analyzer channel number are superimposed on the abscissa

A large portion of the events (during solar quiet times) are minimum ionizing protons corresponding to an energy loss of about 1 Bev—thus, we find a peak in the spectrum at that energy which assists in calibrating the system. This peak is spread by the Landua spread of the minimum ionizing particles. The events registered in channels 2 through 4 are due to low energy particles. The failure of the curve to terminate at an energy loss corresponding to the intersection of curves A and B in Figure 2 is due to the alpha particle contribution. For this reason the useful lower energy limit of the detector is set at about 100 Mev. The upper limit is about 600 Mev, since protons of greater energy exhibit large statistical fluctuations in energy loss.

Figure 5—The GM counter telescope configuration

The GM Counter Telescope

A simple GM counter telescope was flown to determine the directional and omnidirectional cosmic ray intensities. The telescope threshold energies were 70 and 8 Mev for protons and electrons, respectively. The GM counters were disc shaped with effective diameters of 4.45 cm and depths of 1.0 cm. Figure 5 shows the configuration of the array, and the geometric factors are plotted as a function of proton energy in Figure 6. The efficiency of the telescope was 88 percent for minimum ionizing protons. It was operated in two modes: In the coincidence (telescope) mode, only particles entering both counters were counted. In the singles mode, all events from one GM counter were counted to obtain an approximation of the omnidirectional flux.

The Signal Conditioning Instrumentation

A signal conditioning system (Reference 1) processed the signals from the three detector arrays (Figure 7). The pulses from the single GM counter, the coincidence pulses from the GM counter telescope, and the thin scintillator pulses from the eight-level threshold discriminator were counted sequentially by a 15-stage binary scaler. At the beginning of the subcommutation cycle of the GM counter coincidence events were accumulated for about 1.6 seconds.


Figure 6—Geometric factor as a function of incident proton energy for both modes of operation of the GM counter telescope. The geometry is defined by a combination of the counter configuration and the absorbing material in the proton path
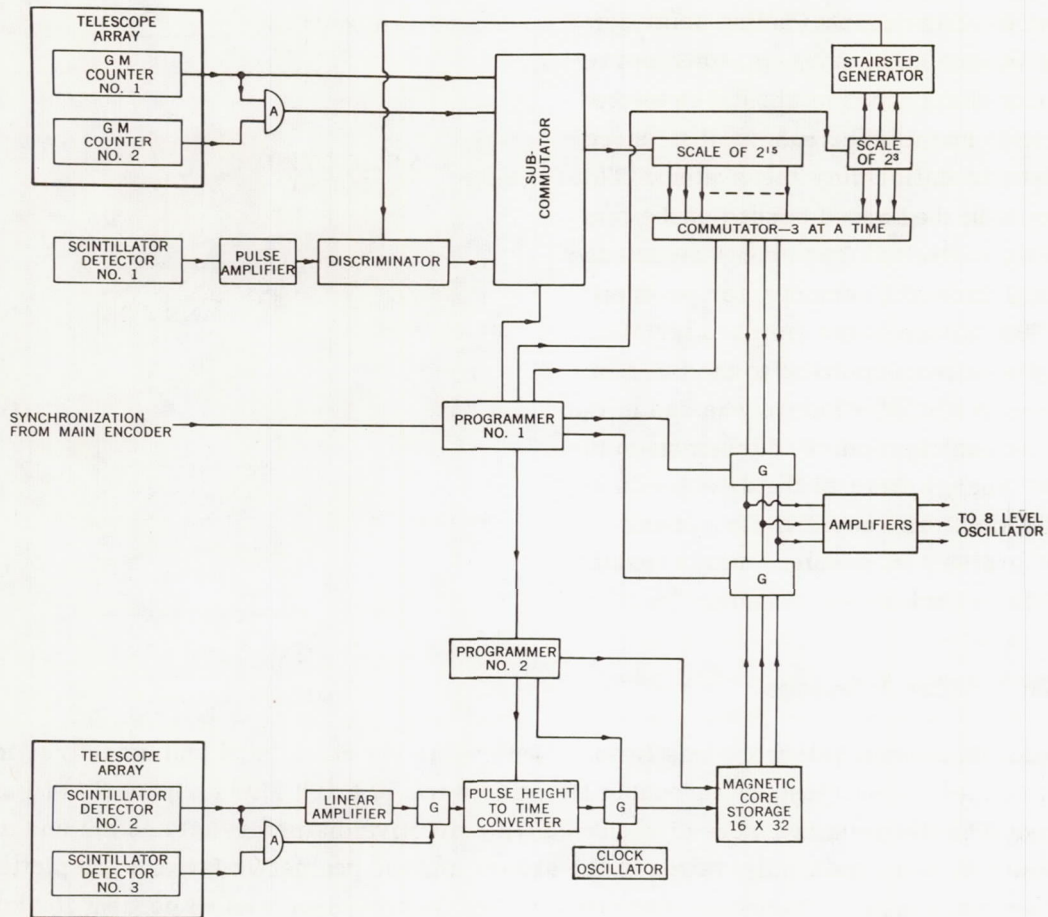
Figure 7—Block diagram of the Explorer XII cosmic ray experiment

During the next 0.96 second the scaler was read into the telemetry system for transmission to the ground by the 3-bits-at-a-time commutator. Then the single GM counter output was accumulated and read during similar intervals. The output of the thin scintillator detector, with the discriminator set at the first level, was accumulated and telemetered during the next 1.6 and 0.96 second intervals respectively; and this was repeated for discriminator levels two through eight. Thus a complete set of counting rates for these two detectors was obtained in 25.6 seconds. This entire sequence was repeated 12 times in slightly more than 5 minutes (307.2 seconds exactly).

While these rates were being measured, pulses from the double scintillator telescope were being analyzed. The analyzer included a linear amplifier to increase the amplitudes of the PM tube pulses; a linear gate to block all pulses not resulting from an acceptable coincidence event; a pulse height-to-time converter from which a pulse train consisting of a number of pulses proportional to the initial pulse amplitude was obtained for each event; and a storage system. At the end of the five minute analysis and storage interval, the pulse height spectrum was contained in a 32 channel by 16 bit magnetic core storage matrix. The count capacity for each channel was, therefore, $2^{16} - 1$ or 65,535 counts.

Following the accumulation of these data the "analyze and store" operation was terminated, the accumulation of counts from the GM counters and thin scintillator was interrupted, and the contents of the storage matrix were telemetered two bits at a time. The readout was repeated a second time; and this time the memory was erased when read. The first half of the erased memory was telemetered a third time so that the completeness of the erasure could be checked. The complete readout (2-1/2 times) required 102 seconds. Following the readout, the system reverted to the "analyze and store" mode, and the data system again telemetered the counting rates from the GM counters and thin crystal scintillator. The entire cycle, including the obtaining of the counting rates of the GM counters, the integral spectrum from the thin scintillator, and the differential spectrum from the scintillator telescope, was repeated every 6.66 minutes.
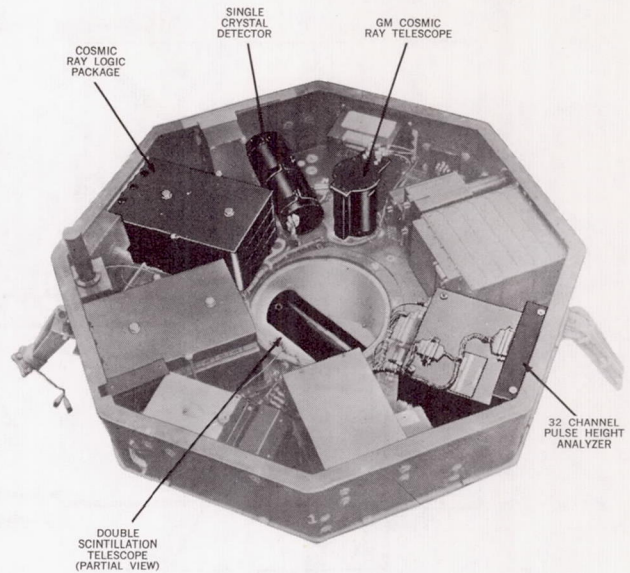

Figure 8—The Explorer XII instrument tray. The units comprising the cosmic ray experiment are darkened. Not shown are the solar paddles, cover, and magnetometer boom and coil assembly

The complete Explorer XII system described above, including the detectors, conditioning equipment, and pulse height analyzer, was fabricated in the form of five subassemblies weighing a total of 12.8 pounds, requiring about 1.4 watts of electrical power, and utilizing approximately 530 transistors. The subassemblies have been darkened in the photograph of the satellite instrument shelf (Figure 8). During the satellite's operating life (113 days) this equipment obtained a large amount of interesting new data about the primary cosmic rays and solar particles (References 2 and 3).

THE ECCENTRIC ORBITING GEOPHYSICAL OBSERVATORY (EGO) EXPERIMENT

An improved cosmic ray experiment is being prepared for launch aboard the first Eccentric Orbiting Geophysical Observatory (EGO) in mid-1963. This experiment will determine the relative abundances of nuclei of atomic numbers 1 through 8 (oxygen) and the energy spectrum for each, over the approximate energy range 11 to 90 Mev/nucleon. The experimental equipment employs scintillator crystals (Figure 9) to measure independently the rate of energy loss and total energy of each particle. A thin *CsI (Tl)* crystal A of 0.45 gm/cm² thickness (1 mm) measures a ΔE which is approximately proportional to the rate of energy loss. The particles which stop in the thick (9 gm/cm²)· scintillator B produce an output that is nearly proportional to $E-\Delta E$, where E is the initial energy of the particle. A guard scintillator C of thickness 0.8 gm/cm² surrounds the thick scintillator, and a coincidence circuit establishes the condition that each incident particle produce outputs from both the ΔE and $(E-\Delta E)$ scintillators, but not from the guard scintillator B, in order that it be analyzed. This establishes the geometry for the detector and ensures that energetic particles passing completely through the thick scintillator are not analyzed.
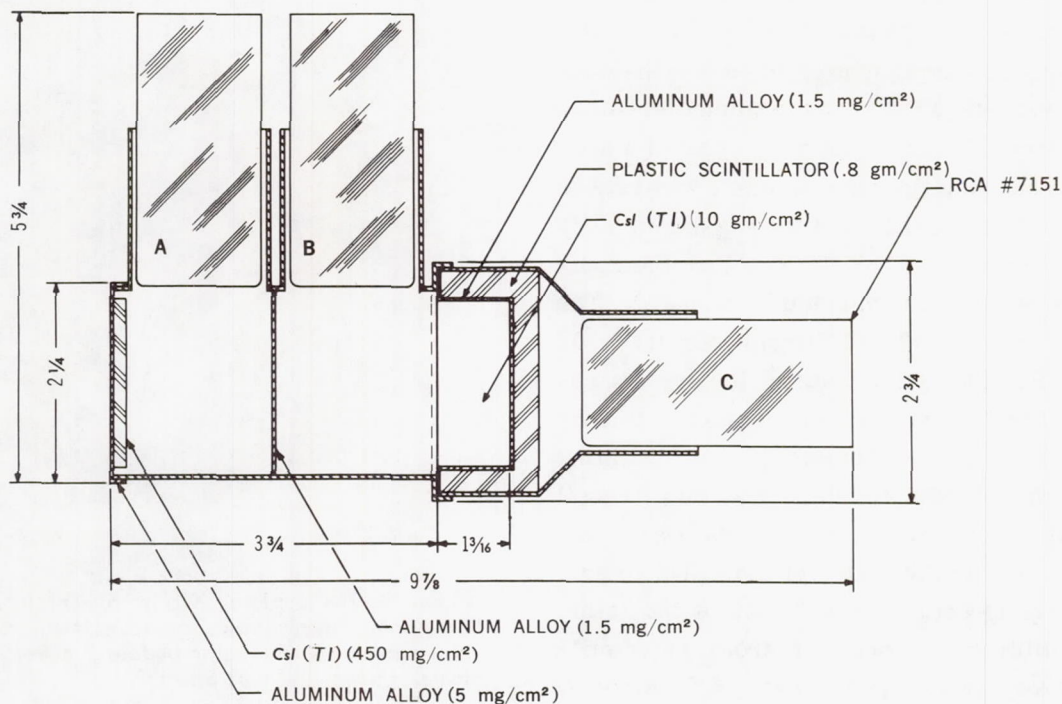
Figure 9—The EGO nuclear abundance detector configuration. The light from the two *CsI* crystals is diffusely reflected by internal white surfaces onto the photocathodes of the upper two PM tubes

The manner in which this detector determines the energy spectra of the individual nuclear constituents can be seen with the aid of Figure 10, in which the energy lost in the ΔE scintillator is plotted as a function of the energy lost in the (E-ΔE) scintillator for the various nuclei. In practice the measurements are scattered about the curves shown—this is due to Landau scattering, the variation in path length through the thin scintillator for different angles of incidence, the variation in light transmission between the crystals and the photocathodes of the PM tubes, and the uncertainties of the measurements of the PM tube pulse heights. These effects combine to produce approximately a 15 percent resolution, measured at the half height of a 0.5 Mev line. This resolution is adequate to separate electrons, protons, deuterons, tritons, alpha particles and lithium, beryllium, boron, carbon, nitrogen, and oxygen nuclei. The separation of the He_3 and He_4 lines is marginal, but may be possible if the two are approximately equal.

The two squares in Figure 10 indicate the areas in the ΔE vs. (E-ΔE) field covered by the EGO experiment. The lower energy region represents the ranges normally covered by the pulse height analyzers. However, if a pulse from either the ΔE or the (E-ΔE) crystal exceeds the upper bounds of this region, the gains of the amplifiers in the analyzers are automatically reduced. The field covered by this configuration is represented by the upper energy, or heavy nucleon, square. The terminations of the high energy ends of the curves results from the action of the guard scintillator. The energies at these termination points are those required for the particles to pass completely through the (E-ΔE) scintillator but not enter the guard scintillator.

230
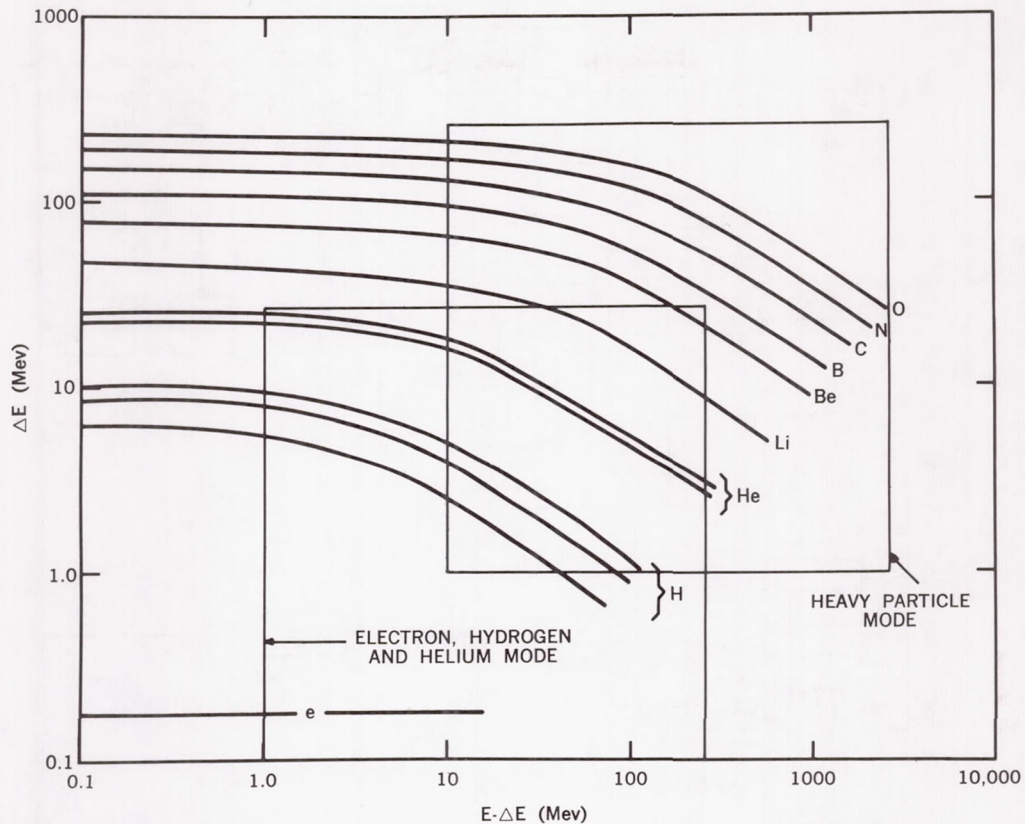
Figure 10—The energy loss in the thin ΔE crystal as a function of energy loss in the thick $(E-\Delta E)$ crystal. The two squares indicate the regions to be covered by the EGO experiment

In this experiment a rather high resolution analysis of the pulse heights from the ΔE and $(E-\Delta E)$ photomultiplier tubes is necessary. The system block diagram (Figure 11) shows the operation of the three dimensional (two parameter) 256 channel analyzer developed for this task. Scintillator pulses A, B, and C and a signal from a busy bistable multivibrator in the gate control circuit produce a gating signal at the coincidence circuit output if the A and B pulses are above the coincidence circuit threshold, the C pulse is below the threshold, and the busy bistable is in the "not busy" state. This coincidence pulse is then steered by the gain setting circuit: Normally the coincidence pulse passes to the pair of high gain linear gates; but if either the A or B pulse amplitudes exceed a threshold value, then the coincidence pulse is routed to the two low linear gates. A marker bit is telemetered with the data to indicate the gain setting for each event analyzed.

The A and B pulses are amplified, shaped, and delayed. The amplifiers are highly stable charge-input circuits employing very large amounts of feedback. Delay line shapers are employed to produce standard $2\,\mu$sec wide, squared pulses in order to remove the effects of changes in PM tube pulse characteristics. Additional pulse amplifiers are used in the high gain setting. The gate outputs charge the capacitors in the sweep circuits of the height-to-width converters. Sweep threshold detectors produce clock gating pulses, which permit numbers of clock pulses proportional to the amplitudes of the A and B pulses to emerge from the analyzers. Careful synchronization of the clock,
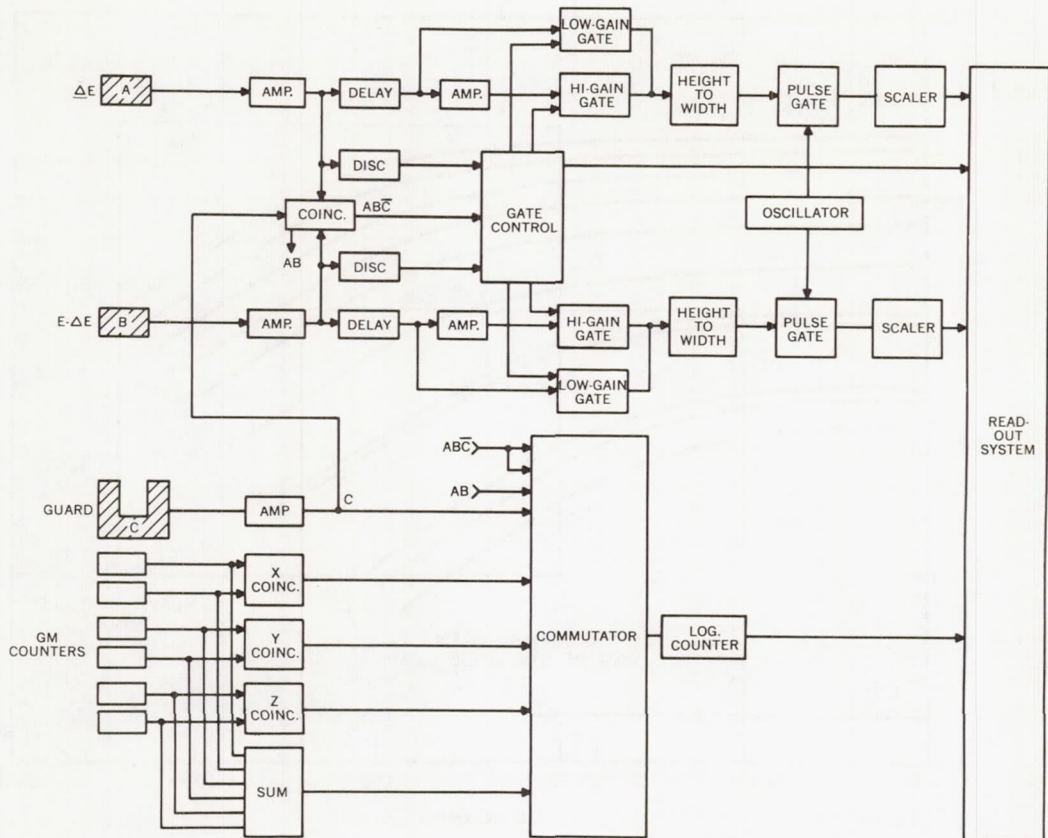
Figure 11—Block diagram of the EGO nuclear abundance experiment

busy bistable, and sweep circuit prevents jitter of the output pulse numbers. The busy bistable is set "busy" at the instant of occurrence of the clock pulse immediately following the charging of the sweep capacitor. At the same time, the clock pulse output gate is opened. The discharging of the sweep capacitor through a constant current generator is held off until this time; thus, the sweep always begins coincidently with the beginning of the first output clock pulse. The clock pulse output gate is closed when the sweep voltage reaches a threshold value.

The pulses from the clock pulse output gates are counted by two binary scalers. Eight stages are used, giving 256 channel pulse height resolution. Following the analysis of an acceptable event, binary numbers proportional to the A and B pulses reside in these scalers, and the busy bistable is in the busy state, holding off the analysis of additional events.

The data handling system in the EGO spacecraft is a PCM time-sharing system. Two main multipliers or commutators, located in two data system equipment groups (EG) are used. Each has 128 data inputs, corresponding to 128 nine-bit words in the telemetry frame. The words are entered into the equipment group designated by the signal on a switch signal line — the absence of a signal on this line means "feed EG 1" while the presence of a signal means "feed EG 2".

A number of lines connect the experiment to the data handling system. A data line is required for each equipment group to carry the serial binary data from the experiment to the data system. A shift

pulse line from each equipment group causes the bits at the experiment output to change in synchronism with the data system. Inhibit (or gating) signals from each telemetry word route the data from the experiment to the proper positions in the telemetry format.

For this experiment the data are entered into the data handling system by a shift register. When the data system is ready to begin accepting data, the contents of one of the two binary scalers are parallel-transferred into the shift register, and the scaler is reset. The contents of the shift register are then shifted serially into the data system in synchronism with the shift pulses. Then the contents of the other scaler are transferred and shifted. The contents of the two scalers are entered into adjacent words in the telemetry frame. Following the completion of this entry, the busy bistable circuit is reset to "not busy" and the system is free to accept another event for analysis.

Several auxiliary indicator bits are included in the data. The gain setting is entered into the ninth bit of the A binary scaler and, whenever either binary scaler overflows because an event occurs above or to the right of the low gain square of Figure 10, a "data error" bit is entered into the ninth bit of the B binary scaler. In addition, a data error is indicated if the data system attempts to read the binary scalers while an analysis is still in process. To prevent the beginning of an analysis while the data system is still reading the experiment, the busy bistable is set "busy" at the beginning of the readout if this has not already been done by the occurrence of an acceptable event in the analysis interval preceding the readout.

The EGO system will be capable of accepting and analyzing an event every second when the data are being recorded by the spacecraft data storage system. Operation at 8 or 64 events per second will occur whenever the data are transmitted directly to the ground receivers without on-board storage. The dead time of the analyzer itself is approximately $10 + 2N$ microseconds, where N is the higher of the two numbers produced in the binary scalers. Of course, the system is also dead whenever the busy bistable is "busy."

A secondary system is included in this experiment to provide additional information about the nuclear abundance measurements, and to provide an independent measurement of the flux of relatively high-energy particles by a simple monitoring detector. An eight position commutator sequentially connects eight sources to a scaler. The pulses from the first source are counted for a known period and the contents of the scaler are read into the data system. Then the pulses from the second source are counted and read, etc. The eight inputs are as follows: (1) The input is left open, to assist in establishing frame synchronization. (2) The C guard detector pulses are counted to allow measurement of high fluxes of charged particles which might effect the accuracy of the primary measurements, and to give a measurement of the omnidirectional intensity. (3) The coincidence circuit ABC pulse rate is measured to determine the number of events which would have been analyzed if the instrument had a zero dead time. (4) The AB coincidence events are counted to give a rough measurement of the directional intensity. (5), (6), (7) The X-, Y-, and Z-axes GM counter telescope rates, respectively, are measured. (8) The sum rate from the six GM counters is measured to give a rough measurement of the omnidirectional flux.

The GM counter array forms a simple monitoring instrument to check the validity of the primary detector's measurements, to allow direct comparisons of results obtained on other flights on which

similar arrays are flown, to provide measurements of the cosmic ray intensity, and to determine the directional characteristics of the cosmic rays. Each axis of this array is similar to the Explorer XII GM telescope described above and shown in Figure 6.

The scaler which counts these pulses has a rather unique quasi-logarithmic characteristic which provides a large dynamic range while retaining a fixed accuracy, with the use of only nine binary data bits. The word obtained from the scaler has two parts: a number consisting of N binary bits and an exponent consisting of E binary bits. The count capacity n_{max} of the circuit is, in general

$$n_{max} = 2^N \left(2^{2^E} - 1\right) .$$

In this case N = 5 and E = 4, so that $n_{max} = 2^{21} - 2^5 = 2,097,120$. This scaler is read by the space-craft data system in the same manner as the analyzer scalers described earlier.

This complete experiment is packaged in two assemblies, a cubical main package eight inches on a side, and a GM telescope package approximately $4 \times 4 \times 5.5$ inches. The total weight of the experiment is 10.5 pounds, and it requires 1.7 watts of power. The basic detector assembly has been flown on balloon flights several times during the past year to check its characteristics (Reference 4). These flights confirm the derivation of the detector parameters, and indicate that high resolution analysis of the charge spectrum will be possible.

CONCLUDING REMARKS

As more becomes known about a particular space phenomenon, experiments to study the phenomenon tend to assume a more complex character so that increasingly detailed information can be obtained. Because the cosmic rays have been investigated for many years, a great deal is already known about them. The experiments described in this paper were designed to increase the amount of detailed information about the energy and charge spectra of low energy cosmic rays. The Explorer XII instrument represents the first use of a medium-resolution differential analyzer and core memory system in space. The EGO system is an extension of this earlier work to make possible two parameter analysis with much higher resolution. It can be expected that instruments of this type will have wide application in space research as it becomes possible to make higher quality measurements of other phenomena.

ACKNOWLEDGMENTS

REFERENCES

1. U. D. Desai, R. L. Van Allen, and G. Porreca, "Explorer XII Rays," *Proc. 1962 National Telemetering Conf.*, Vol. I: Session 7, Article 5, May 1962, pp. 1-15

2. D. A. Bryant, T. L. Cline, U. D. Desai, and F. B. McDonald, "Cosmic Ray Observations in Space," To be published in Proc. Third Internat. Space Sci. Symp., May 1962

3. D. A. Bryant, T. L. Cline, U. D. Desai, and F. B. McDonald, "Explorer XII Observations of Solar Cosmic Rays and Energetic Storm Particles Following the Solar Flare of 28 September 1961," Geophys. Res. (in publication, 1962)

4. D. A. Bryant, G. H. Ludwig, F. B. McDonald, "A Scintillation Counter Telescope for Charge and Mass Identification of Primary Cosmic Rays," *IRE Trans. on Nuclear Science,* NS-9(3): June 1962